PTB bericht Diss-8
Wissenschaftliche Veröffentlichungen
November 2024

Dissertation

Mengdi Li

Experimental and kinetic modeling study on ammonia fuel blends from low to high temperatures

DOI 10.7795/110.20241024

ISSN 2941-1297
ISBN 978-3-944659-38-1

Physikalisch-Technische Bundesanstalt ■ Braunschweig und Berlin
Nationales Metrologieinstitut

Physikalisch-Technische Bundesanstalt

Dissertationen
PTB-Diss-8
Braunschweig, November 2024

Mengdi Li

Experimental and kinetic modeling study on ammonia fuel blends from low to high temperatures

DOI 10.7795/110.20241024

ISSN 2941-1297 2941-1297
ISBN 978-3-944659-38-1

https://doi.org/10.7795/110.20241024

Empfohlene Zitierweise/recommended citation

Mengdi L., 2024. *Experimental and kinetic modeling study on ammonia fuel blends from low to high temperatures.*
Dissertation, Technische Universität Carolo-Wilhelmina zu Braunschweig.
Braunschweig: Physikalisch-Technische Bundesanstalt.
PTB-Bericht Diss-8. ISBN 978-3-944659-38-1.
Verfügbar unter: https://doi.org/10.7795/110.20241024

Herausgeber:
Physikalisch-Technische Bundesanstalt
ISNI: 0000 0001 2186 1887

Presse und Öffentlichkeitsarbeit

Bundesallee 100
38116 Braunschweig

Telefon: (05 31) 592-93 21
Telefax: (05 31) 592-92 92
www.ptb.de

https://doi.org/10.7795/110.20241024

Experimental and kinetic modeling study on ammonia fuel blends from low to high temperatures

Von der Fakultät für Maschinenbau
der Technischen Universität Carolo-Wilhelmina zu Braunschweig

zur Erlangung der Würde

eines Doktor-Ingenieurs (Dr.-Ing.)
genehmigte Dissertation

von: Mengdi Li
geboren in: Shandong, China

eingereicht am: 09.07.2024
mündliche Prüfung am: 07.10.2024

Vorsitz: Prof. Dr.-Ing. Gabriele Raabe
Gutachter: Prof. Dr. rer. nat. Ravi Xavier Fernandes
Jun.-Prof. Dr.-Ing. Federica Ferraro
Dr. rer. nat. Kai Moshammer-Ruwe

2024

https://doi.org/10.7795/110.20241024

Abstract

The combustion of fossil fuels has significantly contributed to global warming and the subsequent rise in extreme weather events. Consequently, the pursuit of carbon-free alternative fuels has become imperative for future transportation and energy systems. Ammonia, in particular, offers advantages such as zero carbon emissions, compatibility with existing infrastructure, and ease of production from renewable energy sources. However, challenges such as high ignition temperature and low burning velocity hinder its independent use as a fuel. Blending NH_3 with reactive promoter fuels presents a feasible solution to enhance its combustion performance for specific applications. Nevertheless, recent studies have highlighted issues with low efficiency and high NO_x emissions when using ammonia fuel blends in conventional internal combustion engines (ICEs).

Given the limited generalizability of practical application results to other energy systems, there is a strong need to comprehend the fundamental reaction kinetics behind the oxidation of ammonia and ammonia fuel blends, which include ammonia oxidation reactions and cross-reactions between promoters and ammonia. Such understanding is critical for attaining high efficiencies and low emissions across various combustion facilities utilizing ammonia fuels. Fundamental combustion experiments with homogenous reactors (reactors without fluid dynamics effects) can play a key role in developing and validating intricate reaction mechanisms.

This study investigates the oxidation properties of NH_3/promoter fuel blends, with a specific focus on blending NH_3 with C_2-hydrocarbon fuels, i.e., ethane (C_2H_6), ethanol (C_2H_5OH), and dimethyl ether (DME, CH_3OCH_3). A wide range of temperatures (450 - 2500 K), pressures (1 - 40 bar), fuel blends ratios (1 - 50 %), equivalence ratios (ϕ = 0.5 - 2.0), and dilution ratios (70 - 95 %) have been explored by utilizing diverse facilities, including a jet-stirred reactor (JSR), a rapid compression machine (RCM), and a shock tube (ST). Based on obtained experimental data, namely ignition delay times and speciation data, a comprehensive chemical kinetic mechanism, PTB-NH_3/C_2 mech, was developed and validated. Consequently, kinetic analyses based on this mechanism were employed to identify the key reaction steps, with regard to comprehending combustion performances and optimizing combustion conditions for further development of the advanced ammonia combustion systems.

Experimental and simulation findings indicate that blending C_2-hydrocarbons can enhance ammonia's reactivity, e.g., decreasing the ignition delay times (IDTs) under RCM and ST conditions and lowering the oxidation onset temperature under JSR conditions. Detailed observations will be concisely discussed in the main text based on different temperature intervals. In brief, at low-to-intermediate temperatures (450 - 1180 K), speciation experiments under JSR conditions reveal three different oxidation regimes (1st, 2nd, and 3rd) for NH_3. Namely, the unique contribution of DME promotes NH_3 oxidation in the 1st regime (600 K), which only occurs in the NH_3/DME fuel mixtures due to the low-temperature combustion properties of DME. In the 2nd oxidation regime (900 K), NH_3 consumption is initiated by

https://doi.org/10.7795/110.20241024

the radicals from promoter fuels' chemistry, while the rapid NH_3 consumption in the 3rd oxidation regime (1050 K) is triggered by high temperatures. Both 2nd and 3rd oxidation regimes are generally observed across different C_2-hydrocarbon additives. Besides, the IDT measurements from RCM at intermediate temperatures (820 - 1120 K) demonstrate that C_2-hydrocarbon addition has a substantial effect on ammonia ignition, with the following promotional effects compared to other blended fuels: 5% C_2H_5OH > 5% CH_3OH > 5% C_2H_6 > 5% H_2 > 10% CH_4. At intermediate-to-high temperature (1320 - 1960 K) under ST conditions, speciation and IDT results from NH_3/C_2H_6 and NH_3/C_2H_5OH mixtures show comparable promotional effects on ammonia oxidation, as well as a reverse dependence of IDT at ST conditions compared to RCM conditions, namely IDT decreases as the equivalence ratios decrease in the high-temperature ST condition.

Finally, kinetic analyses based on PTB-NH_3/C_2 mech, have been employed to investigate the underlying reasons for C_2-hydrocarbon promotion and interpret the differences from the various conditions. This research contributes to advancing the understanding of NH_3/alkane/alcohol/ether fuel blend reaction kinetics and can serve as a valuable resource for further studies on ammonia combustion and its practical application.

https://doi.org/10.7795/110.20241024

Kurzfassung

Die Verbrennung fossiler Brennstoffe hat wesentlich zur globalen Erwärmung und zum Anstieg extremer Wetterereignisse beigetragen. Folglich ist die Suche nach kohlenstofffreien, alternativen Brennstoffen für zukünftige Verkehrs- und Energiesysteme zwingend erforderlich. Ammoniak (NH_3) bietet dabei Vorteile wie keine Kohlenstoffemissionen, Kompatibilität mit bestehender Infrastruktur und leichte Herstellung aus erneuerbaren Energiequellen. Allerdings stellen einige Eigenschaftenwie seine hohe Zündtemperatur und seine niedrige Brenngeschwindigkeit große Herausforderungen an seine unabhängige Nutzung als Brennstoff. Das Mischen von NH_3 mit reaktiven Promotorbrennstoffen stellt eine machbare und mögliche Lösung dar, um seine Verbrennungsleistung für spezifische Anwendungen zu verbessern. Dennoch haben jüngste Studien Probleme mit niedriger Effizienz und hohen NO_x-Emissionen bei der Verwendung von Ammoniak-Brennstoffgemischen in herkömmlichen Verbrennungsmotoren hervorgehoben.

Angesichts der begrenzten Verallgemeinerbarkeit der praktischer Anwendungsergebnisse auf andere Energiesysteme besteht ein großer Bedarf, die grundlegende Reaktionskinetik hinter der Oxidation von Ammoniak und Ammoniak-Brennstoffgemischen zu verstehen, die u.a. Ammoniak-Oxidationsreaktionen und Kreuzreaktionen zwischen Promotoren und Ammoniak umfassen. Ein solches Verständnis ist entscheidend für das Erreichen hoher Effizienz und niedriger Emissionen in verschiedenen Verbrennungstechnologien, die Ammoniak-Brennstoffe nutzen. Fundamentale Verbrennungsexperimente mit homogenen Reaktoren (Reaktoren ohne strömungsdynamische Effekte) können eine Schlüsselrolle bei der Entwicklung und Validierung komplexer Reaktionsmechanismen spielen.

Diese Arbeit untersucht die Oxidationseigenschaften von NH_3/Promotorbrennstoffgemischen, mit speziellem Fokus auf die Mischung von NH_3 mit C_2-Kohlenwasserstoffen. Dabei wurden Ethan (C_2H_6), Ethanol (C_2H_5OH) und Dimethylether (DME, CH_3OCH_3) als Promotoren gewählt. Ein breites Spektrum an Temperaturen (450 - 2500 K), Drücken (1 - 40 bar), Brennstoffmischungsverhältnissen (1 - 50 %), Äquivalenzverhältnissen (ϕ = 0,5 - 2,0) und Verdünnungsverhältnissen (70 - 95 %) wurde unter Nutzung verschiedener Reaktoren, einem Jet-Rührreaktor (JSR), einer Schnellverdichtungsmaschine (RCM) und einem Stoßrohr (ST), untersucht. Basierend auf den gewonnenen experimentellen Daten, sogenannten Zündverzugszeiten und Speziationsdaten, wurde ein umfassender chemischer Reaktionsmechanismus, PTB-NH_3/C_2 mech, entwickelt und validiert. Folglich wurden kinetische Analysen basierend auf diesem Mechanismus durchgeführt, um die Schlüsselreaktionen zu identifizieren, mit dem Ziel, die Verbrennungschemie besser zu verstehen und die Verbrennungsbedingungen zur Weiterentwicklung fortschrittlicher Ammoniak-Verbrennungssysteme optimieren zu können.

Experimentelle und Simulationsergebnisse zeigen, dass die Mischung von C_2-Kohlenwasserstoffen die Reaktivität von Ammoniak verbessern kann Hierzu werden detaillierte Beobachtungen im Haupttext

https://doi.org/10.7795/110.20241024

hinsichtlich unterschiedlicher Temperaturbereiche detailliert diskutiert. Bei niedrigen bis mittleren Temperaturen (450 - 1180 K) zeigen die Speziationsexperimente unter JSR-Bedingungen drei verschiedene Oxidationsregime für NH_3 abhängig vom entsprechenden Promoter. Die Zugabe von DME fördert die NH_3-Oxidation bereits bei 600 K (1. Oxidationsregime), aufgrund der Niedertemperatur-Verbrennungseigenschaften von DME. Im 2. Oxidationsregime (900 K) wird der NH_3-Abbau durch die Radikale aus der Chemie der Promotorenkraftstoffe initiiert, während der schnelle NH_3-Verbrauch im 3. Oxidationsregime (1050 K) durch hohe Temperaturen ausgelöst wird. Sowohl das 2. als auch das 3. Oxidationsregime werden allgemein bei der Zugabe von unterschiedlichen C_2-Kohlenwasserstoff-Additiven beobachtet. Darüber hinaus zeigen die IDT-Messungen durchgeführt in der RCM bei mittleren Temperaturen (820 - 1120 K), dass die Zugabe von C_2-Kohlenwasserstoffen einen wesentlichen Einfluss auf die Ammoniakzündung hat. im Vergleich zu anderen gemischten Brennstoffen: 5% C_2H_5OH > 5% CH_3OH > 5% C_2H_6 > 5% H_2 > 10% CH_4. Bei mittleren bis hohen Temperaturen (1320 - 1960 K) unter ST-Bedingungen zeigen Speziations- und IDT-Ergebnisse von NH_3/C_2H_6- und NH_3/C_2H_5OH-Gemischen vergleichbare reaktivitätssteigernde Effekte auf die Ammoniak-Oxidation sowie eine umgekehrte Abhängigkeit der IDTs unter ST-Bedingungen im Vergleich zu RCM-Bedingungen, nämlich dass die IDT mit abnehmenden Äquivalenzverhältnissen bei hohen Temperaturen abnimmt.

Kinetische Analysen auf der Grundlage des PTB-NH_3/C_2 mech wurden durchgeführt, um die Gründe für die Einflüsse der C_2-Kohlenwasserstoffe auf die Reaktivität des Ammoniaks zu untersuchen und die Unterschiede zwischen den verschiedenen Bedingungen zu interpretieren. Diese Forschungsarbeit trägt zu einem besseren Verständnis der Reaktionskinetik von NH_3/Alkan/Alkohol/Ether-Kraftstoffgemischen bei und kann als wertvolle Quelle für weitere Studien zur Ammoniakverbrennung und deren praktische Anwendung dienen.

https://doi.org/10.7795/110.20241024

Acknowledgment

I would like to express my sincere gratitude to my supervisor, Prof. Ravi Fernandes. I am truly grateful to him for bringing someone with a ‘German dream’ from Shanghai to Braunschweig and for his support and encouragement in my research work and daily life. I want to extend my thanks to my mentor, Dr. Kai Moshammer. Over the years, he’s been like a supportive big brother, teaching me patience and optimism in the midst of boring research. As a meticulous German scientist, he has imparted to me the values of scientific rigor and precision, which shape my research approach. But what stands out the most is that as a friend, his witty personality has made my time here truly enjoyable, and I believe being an interesting person is something he cherishes the most. I would also like to express my gratitude to Prof. Gabriele Raabe and Prof. Federica Ferraro for their invaluable contributions in reviewing my thesis.

I am grateful to all my colleagues, family, and girlfriend for their support and assistance in research and life over the years. I prefer not to list specific names here because the way all names are listed in acknowledgments always implies the end of the story, and that is not what I expect. It is ironic that over the past three decades, I have seldom expressed gratitude to my parents, especially my mother, Ms. Xiaofeng Zhang. Instead, I often blamed her for my character flaws and life's adversities. At times, I even dreamed about having wisdom 'professors' parents just like my friends. Yet, looking back on our time together, I realize how stupid I was. She is the one who always prepared breakfast before I woke up no matter how sleepy she was, always helped me clean up the mess after I messed up no matter how tired she was, and always encouraged me and believed in me no matter what time it was, is, or will be. Here, I want to express my heartfelt gratitude to my mother. She has always been a ‘professor’ in my life, teaching me to find joy in hardship and to chase my dreams relentlessly.

As I write here, I suddenly realize that my doctoral journey is finally coming to an end. After becoming a PhD candidate, the thoughts of ‘what science is’ always confuses me. I had a hard time defining it, but I guess publishing papers is obviously not what it's about, and maybe passionate brainstorming is more apt to my imagination of science. Honestly, I still don't know exactly what science is, but luckily I don't need to know what it is to get a PhD. Or maybe I do need to? Whatever.

In this era of carbon reduction and energy depletion, combustion is a research topic that many wish to run away. Those still in this field are gradually marginalized and forgotten. Nonetheless, that mass of light and heat is indeed our hope for humanity to get out of the earth and voyage the universe, so let's not lose faith. At the very end, with humble hope, this thesis endeavors to tell the whole story as comprehensively as possible, to serve as a tool for newcomers to this field, or perhaps as an obscure book in a pile of garbage that can burn and provide a short time warmth for the homeless. Finally, I hope I can always insist on my way and be pure and true, even though it may not be appropriate at times.

On April 23, 2024, in Braunschweig, Germany

https://doi.org/10.7795/110.20241024

Publication

Peer-reviewed publications

1. M. Li, K. Moshammer, Comparison of the effects of adding the isomers ethanol or dimethyl ether on ammonia oxidation chemistry, Fuel (2024), under review.

2. M. Li, D. Zhu, H. Karas, S. Agarwal, Z. Qu, K. Moshammer, R. Fernandes, B. Shu, NH_3/C_2H_6 and NH_3/C_2H_5OH oxidation in a shock tube: Multi-speciation measurement, uncertainty analysis, and kinetic modeling, Chemical Engineering Journal 498 (2024) 155041.

3. M. Li, X. He, D. Zhu, R. Fernandes, K. Moshammer, Experimental and kinetic modeling study of the autoignition and oxidation of ammonia/ethane mixtures in a rapid compression machine and a jet-stirred reactor, Combustion and Flame 256 (2023) 11–13.

4. X. He, M. Li, B. Shu, R. Fernandes, K. Moshammer, Exploring the Effect of Different Reactivity Promoters on the Oxidation of Ammonia in a Jet-Stirred Reactor, Journal of Physical Chemistry A 127 (2023) 1923–1940.

5. M. Li, D. Zhu, X. He, K. Moshammer, R. Fernandes, B. Shu, Experimental and kinetic modeling study on auto-ignition properties of ammonia/ethanol blends at intermediate temperatures and high pressures, Proceedings of the Combustion Institute 39 (2022) 511–519.

6. D. Zhu, Z. Qu, M. Li, S. Agarwal, R. Fernandes, B. Shu, Investigation on the NO formation of ammonia oxidation in a shock tube applying tunable diode laser absorption spectroscopy, Combustion and Flame 246 (2022) 112389.

7. M. Li, X. He, H. Hashemi, P. Glarborg, V.M. Lowe, P. Marshall, R. Fernandes, B. Shu, An experimental and modeling study on auto-ignition kinetics of ammonia/methanol mixtures at intermediate temperature and high pressure, Combustion and Flame 242 (2022) 112160.

Conference contributions

1. M. Li, K. Moshammer. Comparison of the effects of adding the isomers ethanol or dimethyl ether on ammonia oxidation chemistry. 40th International symposium - Emphasizing Energy Transition, 21th-26th July 2024, Milan, Italy, Poster.

2. M. Li, G. Lanza, R. Fernandes, K. Moshammer. Knowledge generation on combustion chemistry through automated database processing. 40th International symposium - Emphasizing Energy Transition, 21th-26th July 2024, Milan, Italy, Poster.

3. M. Li, G. Lanza, R. Fernandes, K. Moshammer. Knowledge generation on combustion chemistry through automated database processing. 27th International Symposium on Gas Kinetics and Related Phenomena, 14th-18th July 2024, Leeds, United Kingdom, Poster.

4. M. Li, D. Zhu, R. Fernandes, K. Moshammer. Experimental and kinetic modeling study of ammonia/ethane mixtures in a rapid compression machine and a jet-stirred reactor. 11th European Combustion Meeting, 26th-28th April 2023, Rouen, France, Poster.

5. M. Li. Experimental and modeling study on the reactive flow of ammonia fuel blends. Flow workshop Meeting, 16th February 2023, Braunschweig, Germany, Talk (onsite).

6. M. Li, D. Zhu, X. He, K. Moshammer, R. Fernandes, B. Shu. Experimental and kinetic modeling study on auto-ignition and oxidation chemistry of ammonia-ethanol mixtures. 26th International Symposium on Gas Kinetics and Related Phenomena, 28th August-1st September 2022, Rennes, France, Poster.

7. M. Li, D. Zhu, X. He, K. Moshammer, R. Fernandes, B. Shu. Experimental and kinetic modeling study on auto-ignition properties of ammonia/ethanol blends at intermediate temperatures and high pressures. 39th International symposium on combustion, 24th -29th July 2022, Vancouver, Canada, Talk (online).

https://doi.org/10.7795/110.20241024

Abbreviations and symbols

Abbreviation list

BPT	Burner plate temperature
CFD	Computational fluid dynamics
CL	Chemiluminescence
CS	Contact surface
CSTR	Continuously stirred tank reactor
CVCC	Constant volume combustion chamber
CVSR	Constant volume spherical reactor
CW-DFB	Continuous-wave distributed-feedback
DP	Dynamic Pressure
EI	Electron ionization
EOC	End of compression
est.	Estimation
FR	Flow reactor
FTIR	Fourier transform infrared spectroscopy
FWHM	Full width at half maximum
GC	Gas chromatography
HSC	High-speed camera
JSR	Jet-stirred reactor
ICE	Internal combustion engine
ICL	Interband cascade lasers
IDT	Ignition delay time
IE	Ionization energy
ISW	Incident shock wave
ini.	Initial
(TD)LAS	(Tunable diode) Laser absorption spectroscopy
LBV	Laminar flame velocitie
LDC	Laser diode controller
LIF	Laser induced fluorescence
LTC	Low-temperature combustion
MB(MS)	Molecular beam (mass spectrometry/mass spectrometer)
MCP	Microchannel plate
Mech	Mechanism
MFR	Micro flow reactor
NTC	Negative Temperature Coefficient
NUIG	National University of Ireland, Galway
PI	Photoionization
PLF	Premixed laminar flame
POF	Premixed opposed flame
PTB	Physikalisch-Technische Bundesanstalt

https://doi.org/10.7795/110.20241024

QCL	Quantum cascade laser
RCM	Rapid compression machine
RICS	Relative Ionization Cross Section
ROP(A)	Rate of production (analysis)
RSW	Reflected shock wave
SA	Sensitivity analysis
SC	Swirl combustor
ST	Shock tube
0D simulation	Simulation without spatial dependency but with time dependency
1D simulation	Simulation with dependency on one spatial dimension and time

Symbol list

A in Chapter 2	Device-specific proportionality factor
A in Chapter 3	Pre-exponential factor in Arrhenius form
A_w	Surface area of the RCM wall
a	Slope of c_m as a function of filament potential
a_v	Intensity of the absorbed light at the specific wavelength
b	Temperature exponent in Arrhenius form
C_0	Promoter fuel with zero carbon atom
C_1	Promoter fuel with one carbon atom
C_2	Promoter fuel with two carbon atom
c in Chapters 2.1	Instrument factor in mass spectrometry
c in Chapters 2.3	Sound speed
c_m	Mean value of the electron energy distribution
c_p	Isobaric heat capacity
c_v	Specific isochoric heat capacity
D	Dissociation energy
D_i	Mass discrimination factor of the species i
d	Length of the ion flight path
E	Energy
E''	Lower-state energy of the frequency v_{f0},
E_a	Activation energy
E_e	Electron energy
E_k	Kinetic energy
E_p	Potential energy
ΔE	Intercept of c_m as a function of filament potential
FKT	Empirical sample-dependent sampling function
e^-	Electron
f_{FC}	Franck-Condon factor
$f(E)$	Energy distribution of electrons or photons
h	Specific enthalpy per unit mass
h in Chapter 2.1.2	Planck's constant

https://doi.org/10.7795/110.20241024

$h\upsilon$	Photon energy
h_i	Enthalpy of the gas on different sides of the shock wave
I_0	Incident laser beam or Incident laser beam signal
I_b	Offset laser beam signal
I_t	Transmitted laser beam or Transmitted laser beam signal
k in Chapter 2.1.2	Proportionality constant representing factors related to the instrument
k in Chapter 3	Rate coefficient of reaction
k_B	Boltzmann’s constant
k_i	Original reaction rate constant of the ith reaction
k_v	Cross-section of the absorption
$k_{i/R}(E)$	Calibration factor of species i using R as reference species at energy E
L	Length of test gas medium
M	Molecule
M_s	Mach number
$M^{+\cdot}$	Singly charged cation
m	Mass
$\dot{m}$	Mass flow
m^2	Square meters
m/z	Mass-to-charge ratio
Δm	Mass difference
n_i	Amount of substance for species i
P	Pressure
P_c	End of compression pressure in RCM
P_{JSR}	Pressure in JSR
P_1	Initial pressure of test gas in ST
P_2	Pressure behind the incident shock wave
P_3	Pressure behind the contact surface
P_4	Initial pressure of high-pressure driver gas in ST
P_5	Pressure behind the reflected shock wave
Q	Volumetric flow rate
$\dot{Q}$	Net rate of the heat addition to the system
q	Charge of the particle
R	Universal gas constant
R_m	Mass resolution
ROP_i	Consumption or generation rate of species i
r	Bond lengths
S	Line-strength of the specific transition
$S_i(E)$ in Chapter 2	Signal intensity of species i in the mass spectrum at energy E
S_i in Chapter 3	Sensitivity coefficient
SW	Number of spectrum sweeps
T	Temperature
T_c	End of compression temperature in RCM

T_0	Initial temperature in RCM
T_1	Initial temperature of test gas in ST
T_2	Temperature behind the incident shock wave
T_3	Temperature behind the contact surface
T_4	Initial temperature of high-pressure driver gas in ST
T_5	Temperature behind the reflected shock wave
t_1/t_2	The starting and ending points of the investigation period
t_F	Time of the ion flight
Δt	Test time
U in Chapter 2.1.1	Internal energy
U in Chapters 2.1.2/3	Filament potential
U_v	Electric potential difference
u_s	Velocity of the incident shock wave
u_i	Specific internal energy per unit mass of species i
$u(j)$	Relative uncertainty of j
V	Volume
v	Velocity
v_f	Laser frequency
v_w	Velocity of the RCM wall
v_i	Velocity of the gas on different sides of the shock wave
vol%	Volume fraction
W_i	Molecular weight of species i
w	Standard deviation of electron energy distribution
$X(k_i)$	Predicted IDT or x_i with k_i
x_i	Mole fraction of species i
xs_i	Slope of σ_i near IE$_i$ for species i
Y_i	Mass fraction of species i
z	Species-specific constant in EI cross section
Z	Compression factor
$Z(T)$	Product of rotational, vibrational, and electronic partition function
$[C_i]$	Concentration of the species i
γ	Heat capacity ratio
δ_k	Absolute uncertainty of the factors k
σ_i	Ionization cross section of species i
τ in Chapter 2.1.1	Residence time
τ in Chapter 2.1.2	Volume integral elements in calculus
ρ	Density
ϕ	Equivalence Ratio
ϕ_v	Voigt line-shape function at frequency v_f
$\varphi(E)$	Number of ionizing particles at energy E
$\dot{\omega}_i$	Molar production rate
1st, 2nd, 3rd	First, Second, Third

Table of contents

https://doi.org/10.7795/110.20241024

https://doi.org/10.7795/110.20241024

1. Introduction

1.1 Motivation and background

In recent decades, the issue of global warming has emerged as one of the most pressing challenges facing humanity. The unprecedented increase in the concentration of greenhouse gases, particularly carbon dioxide (CO_2), methane (CH_4), nitrous oxide (N_2O), and fluorinated gases in the atmosphere has led to harmful changes in climate patterns worldwide [1]. The combustion of fossil fuels for energy production, transportation, and industrial processes has primarily contributed to this surge in greenhouse gas emissions. The effects of global warming are already evident, primarily manifested in rising surface and ocean temperatures leading to more frequent and severe extreme weather events, such as hurricanes, droughts, and wildfires, as well as the threat of rising sea levels to coastal communities worldwide.

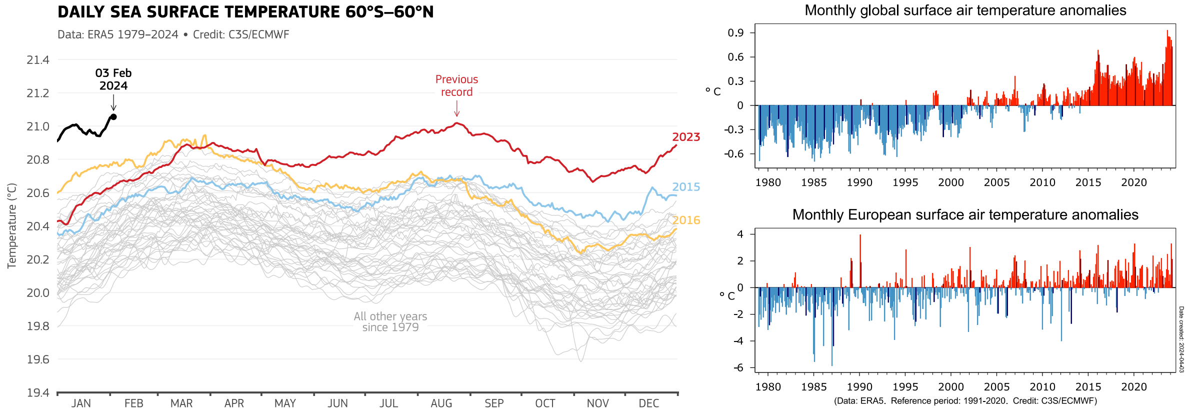

Fig. 1.1. Left). Daily sea surface temperature (°C) averaged over the extra-polar global ocean (60°S-60°N) for 2015 (blue), 2016 (yellow), 2023 (red), and 2024 (black line). All other years between 1979 and 2022 are shown with grey lines, Right). Global-mean and European-mean surface air temperature anomalies relative to 1991-2020 for all months from January 1979 to March 2024 with the darker colored bars denoting the March values [2].

Urgent action is required to mitigate these impacts and transition towards more sustainable energy sources. One promising solution is the adoption of zero-carbon alternative fuels. Among these alternatives, both ammonia (NH_3) and hydrogen (H_2) have become the focus of research as a carbon-free energy source to replace conventional fossil fuels. While hydrogen has garnered significant attention, ammonia offers distinct advantages in certain aspects.

Ammonia, with its zero carbon emissions during combustion, presents a viable alternative to traditional fossil fuels. Its production can be achieved through renewable energy sources, such as wind or solar power, making it a key player in efforts to decarbonize various sectors of the economy. Moreover, ammonia possesses an energy density comparable to fossil fuels and approximately 70% higher volumetric density than hydrogen. Its ease of liquefaction and narrow flammability limit makes it more

https://doi.org/10.7795/110.20241024

suitable for long-term energy storage and transportation. Additionally, ammonia infrastructure can leverage existing systems used in the fertilizer industry, offering a cost-effective solution for deployment at scale [3–6]. However, challenges such as its high ignition temperature (or long ignition delay time) and low burning velocity have hindered its independent use as a fuel source for combustion engines or other applications. To address these issues, blending ammonia with other fuels becomes necessary.

Recent studies [7] have highlighted the potential of blending ammonia with reactive promoters in internal combustion engines (ICEs) to improve ammonia combustion performance. Nevertheless, it still faces the problem of low efficiency and high NO_x emissions. Moreover, the applicability of experimental findings to different engine configurations remains uncertain. To address these challenges, a combined approach of numerical simulations and experimental investigations is being employed to interpret the underlying characteristics of ammonia combustion. The aim is to achieve high efficiency and minimize NO_x emissions across various combustion facilities utilizing ammonia fuel.

Computational fluid dynamics (CFD) and reaction dynamics are key players in these numerical simulations, which are used to predict fluid flows and chemical processes, respectively. This research will primarily focus on the latter, i.e. implementing a reliable reaction mechanism model. In the field of combustion research, fundamental combustion experiments with homogenous reactors (reactors without fluid dynamics effects) are indispensable tools for developing and validating intricate mechanisms. Over the past few decades, tremendous experimental data have been consistently available, typically including the ignition delay times (IDT), laminar flame velocities (LBV), and speciation. The former two parameters reflect the global process of chemical reactions in the system and interpret the combustion behaviors of the fuel within a heat engine. They can also serve as validation targets for testing the overall performance of a reaction mechanism. On the other hand, speciation data can test the specific subsets of the mechanism related to the individual species and improve the predictability of the model.

In previous studies, a series of fundamental experiments have delved into the impact of various promoters (C_0-H_2/O_3, C_1-CH_4/CH_3OH) on ammonia oxidation. Utilizing diverse facilities, including the jet-stirred reactor (JSR), flow reactor (FR), rapid compression machine (RCM), and shock tube (ST), the ammonia fuel blends under a wide range of temperatures (450 - 2500 K), pressures (1 - 40 bar), fuel blends ratios (1 - 50%), equivalence ratios (ϕ = 0.5 - 2.0), and dilution ratios (70 - 95 %) have been explored [8–11]. These studies aim to investigate the effect of different promoters on ammonia oxidation under various conditions and to develop and validate reliable reaction mechanisms by building an exhaustive database on ammonia combustion.

However, due to the hierarchical properties of the reaction mechanism and the need to broaden the mechanism's predictability for ammonia blends with molecules larger than C_0-C_1 compounds, it is necessary to further develop and validate sub-mechanisms involving ammonia and other basic molecules such as alkanes, alcohols, and ethers. Therefore, the present work builds on the previous studies' foundation by extending the blending fuels to C_2-hydrocarbon, namely C_2H_6/C_2H_5OH/ CH_3OCH_3. Notably, all results for NH_3/C_2-hydrocarbon fuel mixtures are from the present work. Detailed experimental conditions can be found in Table 1.1. Subsequently, the mechanism undergoes continuous updates, evolving towards the PTB-NH_3/C_2 mech based on the expanding database. This validated and persuasive mechanism is then utilized for kinetic analysis to identify the key reaction steps, comprehend combustion mechanisms, optimize combustion conditions, and further develop the advanced combustion system.

Table 1.1. Details of the NH_3/C_2-hydrocarbon mixtures and experimental conditions studied in this work.

Mixture	$x_{promoter}$ in fuel	Condition (T, P, ϕ)	Measurement/Facility
NH_3/C_2H_6	10 - 50 %	700 - 1180 K, 1 bar, 0.5 - 2.0	Speciation / Jet-stirred reactor
NH_3/C_2H_5OH	10 - 50 %	700 - 1180 K, 1 bar, 0.5 - 2.0	
NH_3/CH_3OCH_3	10 - 50 %	450 - 1180 K, 1 bar, 0.5 - 2.0	
Pure NH_3	-	700 - 1170 K, 1 bar, 0.5	
Pure C_2H_6	-	700 - 1170 K, 1 bar, 1.0	
Pure C_2H_5OH	-	700 - 1080 K, 1 bar, 1.0	
Pure CH_3OCH_3	-	453 - 923 K, 1 bar, 0.35	
NH_3/C_2H_6	1 - 10 %	890 - 1110 K, 20/40 bar, 0.5 - 2.0	Ignition delay time / Rapid compression machine
NH_3/C_2H_5OH	1 - 10 %	820 - 1120 K, 20/40 bar, 0.5 - 2.0	
NH_3/C_2H_6	5 - 20 %	1320 - 1960 K, 2.4 - 3.1 bar, 0.5 - 2.0	Speciation & Ignition delay time / Shock tube
NH_3/C_2H_5OH	5 - 20 %	1320 - 1920 K, 2.4 - 3.1 bar, 0.5 - 2.0	

1.2 Literature review

The increasing interest in using ammonia as a promising alternative to fossil fuels is evident in the growing number of combustion-related experimental and simulated studies on ammonia in recent years. The corresponding combustion experiments have been conducted across various facilities, including shock tubes, rapid compression machines, constant volume combustion chambers, burners, jet-stirred reactors, and flow reactors. These studies not only examine combustion characteristics but also contribute to validating and refining chemical kinetic mechanisms. Reviewing the literature over the past few years reveals a shift in the focus of investigations, transitioning from pure NH_3 to NH_3 fuel blends. This transition could be attributed to the need to enhance the reactivity of pure ammonia by blending with other fuels, thus facilitating its practical application.

The investigations concerning pure NH_3 and NH_3/C_0-C_1 fuel blends have been thoroughly documented in previous work [12]. Therefore, the literature review will exclusively focus on the study of the NH_3/C_2 mixture, which serves as the primary focus of this current work. As of April 2024, the details of the NH_3/C_2 experiments, including the studied mixtures (blending ratio), facilities, conditions (temperature T, pressure P, and equivalence ratio ϕ), diagnostic techniques, and targets, are summarized in Table 1.2.

Table 1.2 indicates that only limited systematic investigations into the combustion properties of ammonia/C_2 blends have been reported in the literature, particularly the IDT at intermediate temperatures (under RCM conditions) and speciation data. For instance, apart from our published study [13] (part of this work) on oxidation properties of ammonia/ethane fuel blends in RCM (for IDT) and JSR (for speciation) conditions, only one heat flux burner experimental work on LBV [14] for NH_3 with ethane (2 cases) and other alkanes, and an IDT study [15] for NH_3 with natural gas and ethane (2 cases) in ST conditions are currently available in the literature.

Table 1.2. Experimental studies for measuring ignition delay times and speciation of NH_3/C_2 fuel Blends.

Author, year, Ref.	Fuel mixtures ($x_{promoter}$ in fuel)	*Facility*: Condition (T, P, ϕ)	Diagnostic (target)
Chen et al., 2022, [14]	NH_3/C_2H_6 (10/50 %)	*HFB*: 298 K (ini.), 1 atm, 0.65 - 1.6	BPT (LBV)
Li et al., 2023, [13] (part of this work)	NH_3/C_2H_6 (1 - 50 %)	*RCM*: 890 - 1110 K, 20/40 bar, 0.5/1.0/2.0; *JSR*: 700 - 1180 K, 1 bar, 0.5/1.0/2.0	DP (IDT); EI-MBMS (NH_3, C_2H_6, H_2, CH_4, C_2H_4, NO_2, CO, NO, HCN, CH_2O, HNCO, CH_3CHO)
Jiang et al., 2024, [15]	NH_3/C_2H_6 (8.8/29.4 %)	*ST*: 1200 - 1800 K, 1 atm, 1.0	DP (IDT)
Wang et al., 2021, [16]	NH_3/C_2H_5OH (20 - 80 %)	*HFB*: 298 - 448 K (ini.), 1 atm, 0.7 - 1.6	BPT (LBV)
Ronan et al., 2022, [17]	NH_3/C_2H_5OH (25 - 75 %)	*CVCC*: 423 K (ini.), 1 bar, 0.8 - 1.3	HSC (LBV)
Li et al., 2022, [18] (part of this work)	NH_3/C_2H_5OH (1 - 10%)	*RCM*: 820 - 1120 K, 20/40 bar, 0.5/1.0/2.0	DP (IDT)
Li et al., 2023, [19]	NH_3/C_2H_5OH (5 - 30%)	*ST*: 1250 - 1980 K, 0.14/1.0 MPa, 0.5/1.0/2.0	OH* CL (IDT)
Yang et al., 2024, [20]	NH_3/C_2H_5OH (20 - 80%) Energy fraction	*CVCC*: 400 - 500 K (ini.), 0.5 - 1.5 MPa, 0.8 - 1.3	HSC (LBV)
Zheng et al., 2024, [21]	NH_3/C_2H_5OH (37.5 %)	*ST*: 1367 - 1514 K, 1.9 - 2.2 bar, 1.2	LAS (NH_3, NO, CO, CO_2, H_2O)
Wei et al., 2024, [22]	NH_3/C_2H_5OH (40 - 95 %)	*SC (Swirl combustor)*: 298 - 303 K (ini.), 101.3 kPa, 0.25 - 0.53	CL (OH*) Testo 350 (CO, NO_x)
Dai et al., 2021, [23]	NH_3/CH_3OCH_3 (2/5 %)	*RCM*: 610 - 1180 K, 10 - 70 bar, 0.5/1.0/2.0	DP (IDT)
Issayev et al., 2022, [24]	NH_3/CH_3OCH_3 (5 - 50%)	*RCM*: 649 - 950 K, 20/40 bar, 0.5/1.0; *CVSR*: 300 K, 1/3/5 bar, 0.8 - 1.3	DP (IDT) HSC (LBV)
Xiao and Li, 2022, [25]	NH_3/CH_3OCH_3 (20 - 80%)	*CVCC*: 298 K (ini.), 0.1 - 0.5 MPa, 0.7 - 1.4	HSC (LBV)
Murakami at al., 2022, [26]	NH_3/CH_3OCH_3 (50 - 85%)	*MFR*: 400 - 1300 K. 1 atm, 0.5/1.0/1.2	Weak flame responses
Jin et al., 2023, [27]	NH_3/CH_3OCH_3 (20 - 80%)	*ST*: 1150 - 1950 K, 0.14/1.0 MPa, 0.5/1.0/2.0	OH* CL (IDT)

https://doi.org/10.7795/110.20241024

Zhu et al., 2023, [28]	NH_3/CH_3OCH_3 (50%)	*JSR*: 500 - 1100 K, 1 atm, 0.2/1.0	PI-MS (NH_3, H_2O, N_2O, NO, NO_2, C_2H_6O, CH_2O, CO, CO_2, CH_4, H_2O_2) GC (N_2, H_2, CO, CO_2, CH_4)
Yin et al., 2023, [29]	NH_3/CH_3OCH_3 (20 - 80%)	*JSR*: 800 - 1250 K, 1 atm, 0.5/1.0/2.0	GC (O_2, H_2, CO, CO_2, CH_4, CH_3OCH_3) NO_x analyzer and FTIR (NO, NH_3)
Chen and Gou, 2023, [30]	NH_3/CH_3OCH_3 (10 - 50%)	POF: 298 K (ini.), 1 atm	Extinction limits of the diffusion flames
Jiang et al., 2024, [31]	NH_3/CH_3OCH_3 (5 - 50%)	*ST*: 690 - 1810 K, 1.2/10 atm, 1.0	OH* CL (IDT)
Li et al., 2022, [32]	NH_3/C_2H_4 (5 - 30 %)	*PLF burner*: 500 - 1730 K, 1 atm, Constant O_2 flow (1.811 L/min)	LIF (PAH formation)

HFB: heat flux burner, RCM: rapid compression machine, JSR: jet-stirred reactor, ST: shock tube, CVCC: Constant volume combustion chamber, SC: swirl combustor, CVSR: constant volume spherical reactor, MFR: micro flow reactor, POF: premixed opposed flame, PLF: premixed laminar flame,

BPT: burner plate temperature, DP: dynamic pressure, EI/PI-(MB)MS: photoionization/electron ionization (molecular beam) mass spectrometry, HSC: high-speed camera, CL: chemiluminescence, LAS: laser absorption spectroscopy, Testo 350: electrochemical gas sensor, GC: gas chromatography, FTIR: Fourier transform infrared spectroscopy, LIF: laser induced fluorescence,

ini.: initial

Unlike the ethane case, there have been relatively more studies of two NH_3/C_2H_6O-isomers fuel blends. In specific, Wang et al. [16] initially employed the heat flux method to measure the LBVs of the ammonia/ethanol/air mixture. Their results showed that blending alcohols with ammonia has a similar effect to adding ammonia to simple fuels like hydrogen and methane in enhancing the laminar burning velocity. Subsequently, Ronan et al. [17] and Yang et al. [20] expanded LBV measurements using a high-speed camera under CVCC conditions. Moreover, the auto-ignition properties of these blends have been investigated by our group in RCM conditions ([18], part of this work), as well as by Li et al. [19] in ST conditions. Similarly, Dai et al. [23] were the first to combine DME with ammonia in an RCM to explore the auto-ignition properties of ammonia/DME mixtures. A slightly later study by Issayev et al. [24] demonstrated that blending DME can increase the reactivity of the mixture by increasing the flame speed and shortening the ignition delay. Their investigations were then extended to high-temperature ST conditions to study IDTs by Jin et al. [27] and Jiang et al. [31], as well as a higher DME content in a CVCC reactor to study LBV by Xiao and Li [25].

Recently, advancements in combustion diagnostic techniques, such as chemiluminescence, laser diagnostics, gas chromatography, and mass spectrometers, have led to a shift from conventional global parameter measurements like IDT or LBV to more detailed speciation profiles. As shown in Table 1.2, Zheng et al. [21] utilized laser absorption spectroscopy (LAS) in a shock tube to analyze the species profiles of NH_3, NO, CO, CO_2, and H_2O in the oxidation of NH_3/C_2H_5OH mixtures. In NH_3/DME studies, Zhu et al. [28] and Yin et al. [29] employed PI-MS as well as GC, NO_x-analyzer, and FTIR, respectively, to collect more comprehensive species information. Furthermore, certain studies have delved into flame stability [22,26,30] as well as emission characteristics [32], which have deviated from the scope of this work and will not be elaborated upon.

It is apparent that only a limited number of studies provide detailed experimental speciation data and global validation targets (e.g., IDTs). Moreover, in most of the current studies, the chemical influence of the respective promoters on ammonia is interpreted and discussed individually, and not compared with each other. For these reasons, there is a need to supplement research on NH_3/C_2 mixtures and to discuss the oxidation differences across various promoters and under different conditions. This is crucial for the development and validation of chemical kinetic models for the oxidation of ammonia/hydrocarbon fuel blends.

1.3 Structure of Dissertation

Chapter 1 introduces the motivation and background for this dissertation and provides a literature review of the relevant research. The basic knowledge and methods for the experiment and simulation as well as the major achievements of this work will be discussed in the next five chapters detailedly.

Chapter 2 describes three different apparatuses experimentally and theoretically, categorized based on their working temperature intervals from low to high. Furthermore, an uncertainty analysis will be conducted for each specific device, i.e., JSR-MBMS, RCM, ST-LAS.

Chapter 3 presents the theoretical basis of the reaction dynamic and the development of the PTB-NH_3/C_2 mech Mechanism. In addition, the introduction of 0D simulation methods for reproducing the measurements in the JSR, RCM, and ST will be elaborated in this chapter.

Chapter 4 presents experimental low-to-intermediate temperature observations of NH_3/C_2H_6 mixtures, and NH_3/C_2H_6O-isomers mixtures, which are measured in a JSR-MBMS setup. The updated mechanism PTB-NH_3/C_2 mech proposed in Chapter 3 gives satisfactory predictions for all species measured in the current work. Comprehensive kinetic analyses are then conducted to investigate the effect of ethane, ethanol, and DME addition on NH_3 oxidation.

Chapter 5 presents the auto-ignition properties of NH_3/C_2H_6 and NH_3/C_2H_5OH fuel blends at intermediate temperatures and elevated pressures. These IDT measurements are conducted in an RCM. The developed PTB-NH_3/C_2 mech mechanism can reproduce the measurements of IDT very well for both mixtures. Furthermore, sensitivity and reaction pathway analyses are performed to investigate the impact of ethane and ethanol addition on the ammonia auto-ignition.

Chapter 6 presents the oxidation of both NH_3/C_2H_6 and NH_3/C_2H_5OH mixtures at intermediate-to-high temperatures and intermediate pressures. Time-resolved NH_3, NO, and CO profiles of both mixtures are

https://doi.org/10.7795/110.20241024

measured in the ST-LAS setup. The mechanism PTB-NH_3/C_2 mech can satisfactorily predict the ignition delay times and speciation profiles for both mixtures. In addition, comprehensive kinetic analyses are performed to investigate the underlying chemical reason for the measurements.

Finally, Chapter 7 summarizes the major conclusion of this work and proposes the outlook for future research.

2. Theoretical Basis and Experimental Method

In this chapter, three different apparatuses will be introduced experimentally and theoretically according to their working temperature interval from low (450 K) to high (1960 K). Additionally, an uncertainty analysis will be performed for each specific device. Schematics and photographs of all experimental facilities are shown in either the main text below (cf. Figures 2.1-2.2 and Figure 2.7/2.10) or the Appendix (cf. Figures A2.1-A2.5).

2.1 Low-to-intermediate temperatures measurements

2.1.1 Jet-stirred reactor (JSR)

The measurements at low-to-intermediate temperatures (450 - 1180 K) were made at PTB by coupling a jet-stirred reactor (JSR) with a time-of-flight molecular-beam mass spectrometer (MBMS). Specifically, the JSR is a continuously-flow stirred tank reactor system [33] used for speciation measurement from ambient temperature to around 1300 K. It is generally operated at atmospheric pressure but is sometimes utilized for elevated pressures up to 100 bar, especially for supercritical conditions [34]. In the reactor, the stirred mixing achieves spatial homogeneity throughout the reactor when it is operated at a steady state for the entire residence time. The stirring is established by utilizing four turbulent jets issued from the nozzles of the injectors [35]. The average residence time (τ) of the gas mixture in the reactor is equal to the reactor volume (V) over the volumetric flow rate (Q) [36], as shown in Eq. 2.1.

$$\tau = \frac{V}{Q} \qquad \textit{Eq. 2.1}$$

The following equations can describe a continuous JSR system under steady conditions [12]. Eq. 2.2 indicates that the inlet mass is identical to the outlet mass. Eq 2.3 considers the influence of the different compositions between the inlet and outlet gases on the variations in species mass fraction, Eq 2.4 and Eq 2.5 specify the constant volume and temperature of the reactor, and Eq. 2.6 states that the change in internal energy is equal to the obtained heat energy and enthalpy (h) change in the system, subtracting the work done by the system.

$$\frac{dm}{dt} = \dot{m}_{in} - \dot{m}_{out} = 0 \qquad \textit{Eq. 2.2}$$

$$\frac{d(mY_i)}{dt} = \dot{m}_{in}Y_{i,in} - \dot{m}_{out}Y_{i,out} + V\dot{\omega}_i W_i \qquad \textit{Eq. 2.3}$$

$$\frac{dV}{dt} = 0 \qquad \textit{Eq. 2.4}$$

$$\frac{dT}{dt} = 0 \qquad \textit{Eq. 2.5}$$

$$\frac{dU}{dt} = mc_v\frac{dT}{dt} + \sum_i u_i m\frac{dY_i}{dt} + u\frac{dm}{dt} = -P\frac{dV}{dt} + \dot{Q} + \dot{m}_{in}h_{in} - \dot{m}_{out}h_{out} \qquad \textit{Eq. 2.6}$$

https://doi.org/10.7795/110.20241024

In the given equations, m represents the mass of the entire system, $\dot{m}$ is the mass flow, Y_i is the mass fraction of species i, V denotes the volume of the system, $\dot{\omega}_i$ is the molar production rate, W_i is the molecular weight, T is the system temperature, U is the internal energy of the system, u_i represents the specific internal energy per unit mass for species i, c_v is the specific isochoric heat capacity, P is the system pressure, $\dot{Q}$ is the net rate of the heat added to the system, and h is the enthalpy per unit mass.

A comprehensive description of JSR and MBMS used in this study can be found in [11,13]. In summary, the jet-stirred reactor is constructed from quartz and adopts a spherical structure with a diameter of 40 mm and a volume of approximately 32.5 cm^3, of which the design is based on Dagaut et al. [35] (cf. Figure 2.1). During experiments, adjustments to the gas phase mixture composition within the reactor are made using separate mass flow controllers (MKS GM50). For liquid fuels, such as ethanol, the flow rate is regulated using a syringe pump (Cetoni Nemesys S). As the reactor temperature increases, the flow rates of each component are adjusted using the mass flow controllers and syringe pump to maintain a constant residence time. To prevent pre-oxidation within the reactor, fuel gases, with argon serving as a carrier gas, are introduced into the premixing chamber via a capillary, while the oxidizer and diluent enter through the inlet tube located outside the capillary. The unmixed gases in the premixing chamber then access four inclined nozzles oriented in different directions, facilitating flow stirring to achieve homogenous mixing. The reactor temperature is controlled using a heating tape wrapped around the outer surface of the reactor and regulated by a temperature controller (HT61 Horst) up to 1180 K. The thermocouple is positioned between the heating tape and the reactor rather than inside the reactor in case the inserted thermocouple may disturb the gas mixing and cause catalytic reactions. To ensure accurate pressure maintenance within the reactor, a vacuum throttle valve (MKS T3BIB) coupled with a manometer (MKS Baratron) is placed at the outlet of the JSR chamber.

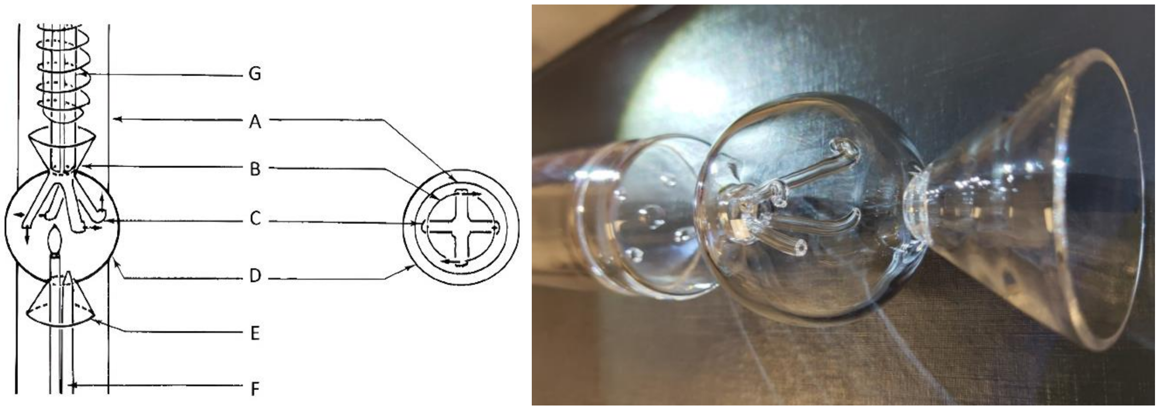

Fig. 2.1. a) The schematics of the reactor: A. external tube; B. convergent cone; C. injectors; D. spherical quartz reactor; E. divergent cone; F. sampling sonic probe and thermocouple probe; G. capillary surrounded by the preheating resistor [35], *b) the photo of the reactor.*

2.1.2 Molecular beam mass spectrometry (MBMS)

Between the JSR and the mass spectrometer (MS) is a three-stage molecular beam (MB) setup. This setup comprises a quartz nozzle, the first skimmer, and the second skimmer, each with orifice diameters of 0.1 mm, 0.5 mm, and 2.0 mm, respectively. As shown in Figure 2.2, the pressures behind the nozzle and two subsequent skimmers are vacuumed into ~1 mbar (1st pumping stage), ~1E-4 mbar (2nd pumping stage), and ~1E-6 mbar (3rd pumping stage), respectively. A similar MB setup has been investigated by the simulated work of Chen et al. [37]. The authors reached a consistent conclusion regarding the relative pressure reduction at each stage, affirming the successful formation of the MB through the observation of elevated Mach numbers. The generated MB, by preventing further reactions within the ionization region, enables the ongoing reactor chemistry to be imaged.

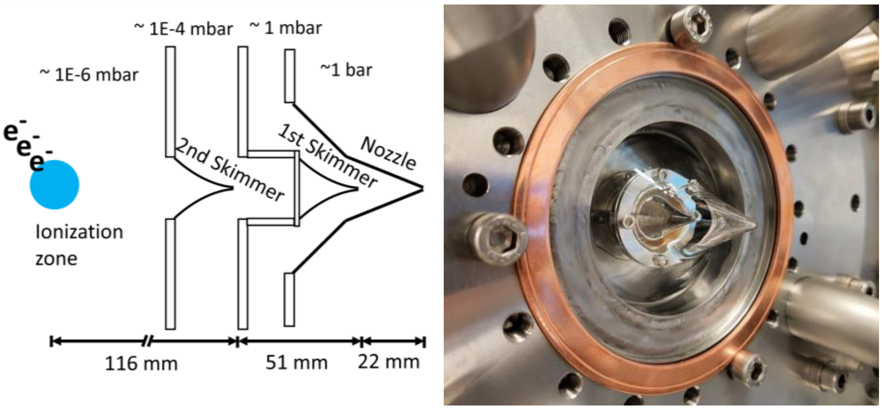

Fig. 2.2. a) The schematics and b) the photo of the molecular beam setup [12].

These output gases from the reactor are extracted through this setup, forming a molecular beam. This molecular beam is subsequently guided straight to the ionization zone within the mass spectrometer (MS), where the molecules undergo ionization. The continuous ionization process can be typically categorized into two types, i.e., electron ionization (EI, by electron beam) used in this study and photoionization (PI, by vacuum ultraviolet radiation), as represented by the following equations.

$$M + e^- \rightarrow M^{+\cdot} + 2e^- \qquad \textit{Eq. 2.7}$$

$$M + hv \rightarrow M^{+\cdot} + e^- \qquad \textit{Eq. 2.8}$$

In this process, the neutral molecule (M) acquires energy from electrons (e^-) or photons (with the energy of hv), subsequently undergoing electron loss (e^-) to transform into a singly charged cation ($M^{+\cdot}$). The minimum required energy to ionize the M in its electronic and vibrational ground states is defined as the ionization energy (IE), which varies from different molecules. In practice, there are still some unexpected events accompanying the desirable process, such as electronically excited neutrals resulting from the non-ionizing electron-neutral interactions or dissociation/fragmentation of the ionized molecules due to the high energy. Figure 2.3 illustrates the transitions from the neutral to the ionic state for a diatomic molecule, providing valuable insights into the ionization process [38].

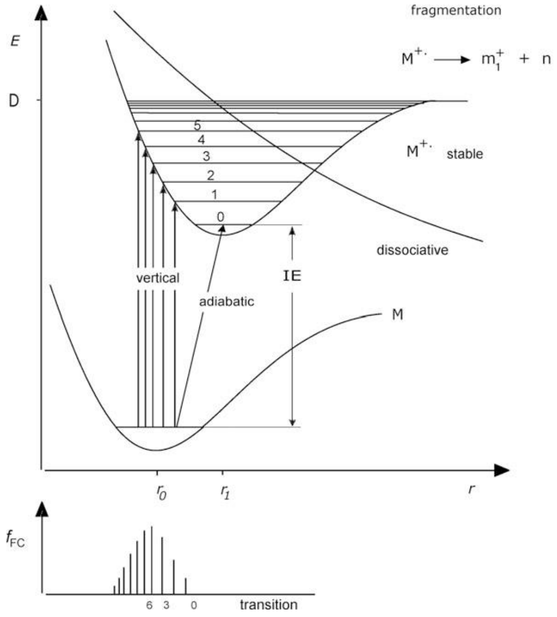

Fig. 2.3. The upper part illustrates the vertical and adiabatic transitions from the neutral to the ionic state for a molecule. The lower part schematically displays the distribution of Franck-Condon factors (f_{FC}) for various transitions [38].

In diagrams where energy is depicted on the ordinate and bond length on the abscissa, as well as the given Franck-Condon factor (f_{FC}) in the lower subplot, which indicates that the probability of a specific transition from the neutral ground state to a particular vibrational level of the ion. Normally, f_{FC} reaches the maxima where the electronic wave functions of both the ground state and excited state have maximum overlap. [38]. These ions with internal energies below the dissociation energy (D) maintain stability, while fragmentation will occur at energy levels exceeding D. Moreover, according to the Franck-Condon principle [39,40], electronic transitions occur at a significantly faster rate than the time required for nuclei to reach their new equilibrium positions. This phenomenon ensures that the positions of the atoms and thus bond lengths (r) remain unaltered during ionization, and such transitions are represented as vertical energy transitions (cf. Figure 2.3). While the energy is slightly higher than the minimum required energy IE, i.e., adiabatic energy transitions in Figure 2.3 where the ionization of the neutral in its vibrational ground state would yield the radical ion also in its vibrational ground state. Discrepancies between adiabatic and vertical energy can introduce errors in ionization energies ranging from 0.1 to 0.7 eV. Throughout this study, ionization energy consistently denotes the adiabatic energy transition, unless explicitly specified otherwise. However, achieving quantitative energy transfer for ionization during collisions is a low-probability event, resulting in a nearly negligible ionization efficiency when electrons carry only the adiabatic IE of the neutral. A slight increase in electron energy leads to a gradual improvement in ionization efficiency. Each molecular species i has a unique ionization efficiency curve determined by its ionization cross section (σ_i), which represents the ionization probability by the particles (typically electrons or photos) at a given energy level, often measured in square meters (m^2). It can also be analogized to the region that the electron or photon must traverse for the effective ionization of the neutral. For the electron ionization used in this study, the cross section can be established through either experimental methods [41–43] or theoretical calculations using the binary-encounter Bethe model [44]. It can be described by Eq. 2.9 [45] as the energy range near IE.

$$\sigma_i(E_e) = \begin{cases} xs_i(E_e - IE_i)^z \, , & E_e > IE \\ 0 & , \, E_e < IE \end{cases} \qquad \textit{Eq. 2.9}$$

Where the E_e represents the electron energy, xs_i denotes the slope of σ_i near IE$_i$ for species i, and z is a species-specific constant normally assumed to be 1. It should be noted that most available literature values represent total ionization cross sections and do not consider the fragmentation of the corresponding species [46].

In the ionization region of the mass spectrometer, there are two stages of ion extraction configuration by deploying a pulsed and (E_1) a constant (E_2) electric field in the 1st and 2nd stages, respectively, which were proposed by Wiley and Mclaren [47]. The molecules are bombarded by the electron beam and converted to ions in the 1st stage, and further extracted as well as accelerated in the 2nd stage. The acceleration results in having the same kinetic energy as any other ion that has the same charge, and therefore, each ion's velocity will depend only on its mass (or mass-to-charge ratio). These ions will further enter the flight tube and drift in a field-free region. Consequently, the lighter ions reach the detector with a short flight time, while heavier ions take longer. According to Eq. 2.10-2.12, the same recorded flight time (t_F) can correspond to specific ionized molecules with the same mass (m).

$$E_p = qU_v = E_k = \frac{1}{2}mv^2 \qquad \textit{Eq. 2.10}$$

$$v = \frac{d}{t_F} \qquad \textit{Eq. 2.11}$$

$$t_F = \frac{d}{\sqrt{2U_v}}\sqrt{\frac{m}{q}} = k\sqrt{\frac{m}{q}} \qquad \textit{Eq. 2.12}$$

Here, the E_p is potential energy, q is the charge of the particle, and U_v is the electric potential difference (also known as set voltage). In effect, the potential energy is converted to kinetic energy (E_k) which can be determined through the particle's mass (m) and velocity (v). The v can be determined in a time-of-flight tube since the length of the path (d) of the ion flight is known and the time of the ion flight (t_F) can be measured using a transient digitizer or time-to-digital converter. k is a proportionality constant representing factors related to the instrument settings and characteristics. Eq. 2.12 reveals more clearly that the time of ion flight varies with its mass-to-charge ratio m/z (or mass m due to the same charge

q). Hence, the consistent initial timing of the ion flight becomes more paramount. This is effectively accomplished by utilizing the pulsed electric field (spatial correction) within the two-stage extraction.

However, in practical applications, the ions often do not possess precisely the same kinetic energy when they leave the ionization region. The discrepancy can be attributed to the inconsistent initial kinetic energy of the neutral species. Consequently, ions with identical masses may exhibit different velocities, leading to a broader signal in the final spectrum. To solve this issue, Mamyrom et al. [48] implemented a reflectron setup in the time-of-flight mass spectrometer that can reverse the trajectories of ions in appropriate electric reflecting fields. The ions with higher kinetic energy penetrate deeper into the reflecting field, which increases their flight distance and thus minimizes the discrepancy of flight time. The combination of both two-stage ion extraction and reflectron can significantly enhance the mass resolution (R_m), which can be quantified by Eq. 2.13. It indicates that two equally intense but not entirely separated signals at a distance Δm (the full width at half maximum (FWHM) of a signal) in the spectrum can still be distinguished.

$$R_m = \frac{m}{\Delta m} \qquad \textit{Eq. 2.13}$$

The integrated and corrected ion signal intensity of species i at a specific energy (E) for our time-of-flight mass spectrum can be described by the following equation [46]:

$$\begin{aligned} S_i(E) &= x_i \cdot \varphi(E) \cdot SW \cdot D_i \cdot c \cdot FKT \cdot \int \sigma_i(\tau) \cdot f(E-\tau) d\tau \\ &= A \cdot x_i \cdot \varphi(E) \cdot D_i \int \sigma_i(\tau) \cdot f(E-\tau) d\tau \end{aligned} \qquad \textit{Eq. 2.14}$$

In this equation, x_i represents the mole fraction of the species i, $\varphi(E)$ is the number of ionizing particles (photons or electrons), SW is the number of spectrum sweeps, D_i is the mass discrimination factor, c is an instrument factor, and FKT is an empirical sample-dependent sampling function, which describes the influence of the temperature on the measured signal intensity [49]. $\sigma_i(E)$ represents the ionization cross section at energy E, and $f(E)$ is the energy distribution of the ionizing particles. The device-specific proportionality factor A is a combination of SW, c, and FKT. When comparing signals to a reference species R (usually argon), Eq. 2.14 simplifies to:

$$\frac{S_i(E)}{S_R(E)} = \frac{x_i}{x_R} \cdot \frac{D_i}{D_R} \cdot \frac{\int \sigma_i(\tau) \cdot f(E-\tau)\, d\tau}{\int \sigma_R(\tau) \cdot f(E-\tau)\, d\tau} = \frac{x_i}{x_R} \cdot k_{i/R}(E) \qquad \textit{Eq. 2.15}$$

where $k_{i/R}(E)$ represents the species- and energy-dependent calibration factor for the species i and the reference species R (Argon used in this work).

The mass spectrometer utilized at PTB is a custom-made orthogonal reflectron time-of-flight mass spectrometer (OTF12, Stefan Kaesdorf). Its remarkable mass resolution, reaching up to 4000, is achieved through the integration of a reflectron in conjunction with a two-stage Wiley-dMcLaren ion extraction method. Following the passage of ions through the field-free zone within the flight tube, they

https://doi.org/10.7795/110.20241024

are detected by a microchannel plate manufactured by Photonis Inc. and counted by a multiple-event time digitizer (MCS6A, FAST ComTec.). The recorded ion counts are subjected to fitting by a Gaussian function and then integrated to yield the flight-time signal intensity for each species. This fitting procedure becomes essential when multiple species are closely positioned, rendering them indistinguishable from the current mass resolution.

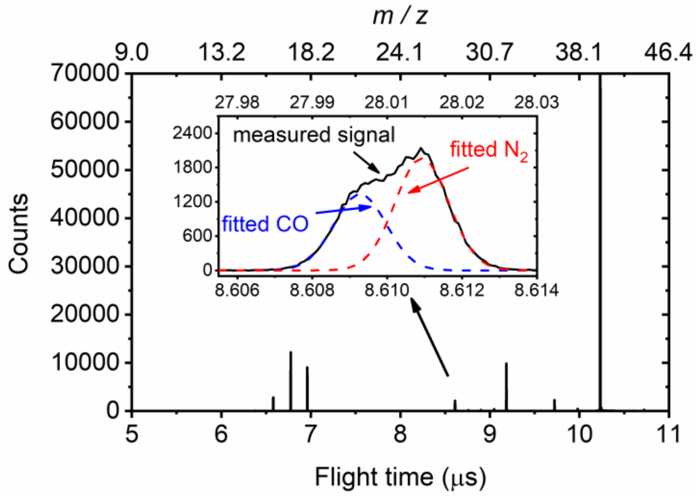

Fig. 2.4. An example of a time-of-flight spectrum [12].

An instance of this occurs with the species CO (m/z = 27.9949u) and N_2 (m/z = 28.0061u), which possess extremely similar exact masses. The signals from these molecules exhibit some overlap in the spectrum, as illustrated in the inset of Figure 2.4. Through Gaussian fitting, it becomes possible to separate and reconstruct the individual signals from the combined signal. This fitting process is implemented using a Matlab code from previous work [12]. The spectrum signals were then converted to the mole fractions of each species individually with the help of x_R (mole fraction of reference species R) and corresponding $k_{i/R}$, which can be obtained through direct calibration or a convolution procedure (indirect calibration). Further details of these calibration methods can be found in the main text below.

Practically, to locate the species in the time-of-flight spectrum, a second-order polynomial representing the connection between the flight time and the mass is provided (cf. Eq. 2.16)

$$m = a_2 t_F^2 + a_1 t_F + a_0 \qquad \textit{Eq. 2.16}$$

where t_F is the sum of the flight times through the entire trajectory, encompassing the two-stage extraction, the field-free drift, and the reflectron. This polynomial is determined by fitting the signal peak positions to the exact molecular masses of known species, such as those found in the inlet gas (fuel, O_2, and Ar), as well as some common intermediates or products (H_2, CO, CO_2, H_2O, N_2). The inclusion of more species in the fitting process results in more precise polynomial coefficients. A dependable equation can help to identify unknown species based on their flight times.

https://doi.org/10.7795/110.20241024

2.1.3 Uncertainties of JSR measurement

According to Eq. 2.15, the determined mole fractions from JSR-MBMS are expressed as a dependent function of the spectrum signals intensity (S_i, S_{Ar}), calibration factors ($k_{i/R}$), and argon mole fraction (x_{Ar}). Consequently, the uncertainty associated with the species mole fractions $u(x_i)$ can be computed through the propagation of uncertainties from these individual parameters. Previously developed data evaluation routines and uncertainties for converting mass spectrometric signals of individual species into mole fractions have been extensively reported in the literature [46,50] and therefore only the key aspects should be summarized here.

It found that the determining factor for the uncertainty of the signal intensity $u(S_i)$ is not the electron energy, ionization potential, species, or its concentration, but rather the resulting recorded ion counts. The signal exhibits good stability with less than ±8% uncertainty once the S_i reaches 5000 counts. It is noteworthy that the majority of detected species in the study can attain this threshold. However, the difficult-to-detect intermediate species with less intense signals are adversely affected by lower repeatability of the signal intensities, and consequently, the uncertainty for such species is significantly higher than for easily detectable species. Besides, the inconsistent signal ratio S_i/S_{Ar} should be considered in the overall uncertainty assessment, with its uncertainty arising from three distinct aspects. Firstly, it is affected by the uncertainty of the signal for both Ar and the species i. A second source of $u(S_i/S_{Ar})$ stems from changes in the instrument's state, such as heating current and MCP (Microchannel plate) voltage. The remaining part of that originates from variations in the sample itself, specifically inconsistent pressures and mole fraction ratios. Given that the first source has already been included in the $u(S_i)$, the last two variations are combined and summarized as the uncertainty related to inconstancy, $u(inconstancy)$, which is obtained from calculations with a maximum range of ±19.2%.

2.1.3.1 Direct calibration

The uncertainty, $u(k_{i/R})$, is contingent upon the selected calibration method. In the case of inlet gas and intermediate products with stable existence, the calibration factor can be directly determined (cf. Eq. 2.17) from cold gas measurements by introducing the analyzed mixture (fuel, O_2, and Ar) or a known binary calibration gas (e.g., 5%CO+95%Ar mixture). To stabilize the components, this process must be conducted under conditions that ensure the absence of combustion reactions. SAfixed electron energy E (filament potential U of 20 eV) is applied in this work to achieve the balance between proper signal intensity and weak fragmentation. The subsequent -(20 *eV)* will be omitted, for instance, S_i instead of $S_i(20\ eV)$. The overall $u(k_{i/R,direct})$ can be calculated according to Eq. 2.18.

$$k_{i/R,direct} = \frac{S_i}{S_R} \cdot \frac{x_R}{x_i} \qquad \text{Eq. 2.17}$$

$$u\left(k_{i/R,direct}\right) = \sqrt{u(x_i)^2 + u(x_R)^2 + u(S_i)^2 + u(S_R)^2 + u(inconstancy)^2} \qquad \text{Eq. 2.18}$$

https://doi.org/10.7795/110.20241024

Where the uncertainty of the inlet mole fraction $u(x_i)$ and $u(x_R)$ is consistent with that of the mass flow controller, specifically ±1% in the study. For the liquid ethanol, the flow rate uncertainty from the Cetoni syringe pump is also ±1%. In summary, the uncertainty of the direct calibration factor $u\left(k_{i/R,direct}\right)$ is determined to be in the range of ±11.4% - ±22.3%. It is important to note that the calibration gas sample is typically delivered using the same molecular-beam setup used in the combustion experiment, the effect of mass discrimination (D_i) has already been factored into the direct calibration factor, as indicated in Eq. 2.15.

The calibration factor of the main species, such as fuel, oxidizer, and major product can be calculated from the element balance as well. For instance, in the combustion of NH_3/C_2H_6 fuel mixture, the amount of substance, such as n_N, n_C, n_O, n_H, and n_{Ar} are known from the initial conditions based on the element balance (cf. Eq. 2.19). The main exhaust gas composition in the outlet of the reactor will contain combustion products (such as N_2, CO, CO_2, and H_2O) and residual inlet gas (such as Ar, O_2, and fuel from incomplete combustion). With an introduced calibration factor $k_{co/co_2,direct}$, the used element balance can be concluded as follows.

$$\begin{cases} n_N = n_{NH_3,in} = n_{NH_3,out} + 2n_{N_2,out} \\ n_C = 2n_{C_2H_6,in} = 2n_{C_2H_6,out} + n_{CO,out} + n_{CO_2,out} \\ n_O = 2n_{O_2,in} = 2n_{O_2,out} + n_{H_2O,out} + n_{CO,out} + 2n_{CO_2,out} \\ n_H = 6n_{C_2H_6,in} + 3n_{NH_3,in} = 6n_{C_2H_6,out} + 3n_{NH_3,out} + 2n_{H_2,out} + 2n_{H_2O,out} \\ n_{Ar} = const. \\ n_{CO,out} = \frac{S_{CO}}{S_{CO_2} \cdot k_{CO/CO_2,direct}} \cdot 2n_{CO_2,out} \end{cases} \quad \textit{Eq. 2.19}$$

Here, the calibration factor $k_{co/co_2,direct}$ was established through an independent calibration measurement. Eq. 2.20 is then applied to obtain the respective calibration factor for the main species *i*.

$$k_{i/Ar} = \frac{S_i}{S_{Ar}} \cdot \frac{n_{Ar}}{n_i} \quad \textit{Eq. 2.20}$$

Once all the k_i were known, the Ar mole fraction can be calculated through Eq. 2.21. Notably, the overall number of molecules in the reactor will expand as the reaction proceeds, leading to a gradual decrease in the actual mole fraction of Ar as the temperature rises. For this, the x_{Ar} should be solved for each temperature (*T*).

$$x_{Ar}(T) = \left(1 + \sum_i \frac{S_i(T)}{S_{Ar}(T)} \cdot \frac{1}{k_{i/Ar}}\right)^{-1} \quad \textit{Eq. 2.21}$$

In general, it is advisable to include all species with mole fractions exceeding 1% in Eq 2.21. The calibration factors for the main species can be obtained from element balance, whereas for other species, calibration factors can be determined through either direct cold gas calibration or indirectly through the methods outlined below. The calculated $u(x_{Ar})$ is up to ±1% [50], which is consistent with the uncertainty of the inlet mole fraction $u(x_i)$ and $u(x_R)$ from the mass flow controller.

https://doi.org/10.7795/110.20241024

2.1.3.2 Convolution method

In the case of species that cannot be accessed directly from a test gas mixture, such as radicals or unstable species, the calibration factors must be determined indirectly. This can be achieved either through a convolution procedure or by employing the method of Relative Ionization Cross Section (RICS) [51]. The convolution method, which involves combining functions, is likely used to model or analyze the ionization process in situations where both the ionization energy (IE) and the ionization cross section $\sigma_i(E)$ are functions of the electron energy. The assessment of the energy distribution of ionizing electrons particles $f(E)$ confirmed that it could be approximated by a Gaussian distribution with a mean value of c_m and standard deviation of w, which can be expressed by Eq. 2.22 [45,46]

$$f(E_e)=\frac{1}{\sqrt{2\pi w^2}}\exp\left(-\frac{(E_e-c_m)^2}{2w^2}\right) \qquad \textit{Eq. 2.22}$$

where the w represents the width (one standard deviation) of the energy distribution of the electrons (1.0 ± 0.1 eV). However, the effect of the thermal distribution leads to the deviations between the selected value U of the electron acceleration voltage (nominal filament potential) and the resulting mean value c_m of the kinetic energy distribution of the electrons, i.e., an energy offset ΔE (cf. Eq. 2.23, a linear function of the filament potential at the selected filament heating current) [45]. For the device used in this study, both the slope a and the standard deviation w are stable and determined to be 1.05 and 0.9, respectively.

$$c_m = aU + \Delta E \qquad \textit{Eq. 2.23}$$

By integrating Eq. 2.9, Eq. 2.22, and Eq. 2.23 into Eq. 2.14, the signal S of a species i at the nominal filament potential (U) can be simulated by the following equation:

$$\begin{aligned} S_{i,conv}(U) &= A \cdot x_i \cdot \varphi(U) \cdot D_i \cdot \int_{IE}^{\infty} xs_i(E - IE_i) \cdot \frac{1}{\sqrt{2\pi w^2}} \exp\left(-\frac{(E-aU-\Delta E)^2}{2\omega^2}\right) dE \\ &= A \cdot x_i \cdot \varphi(U) \cdot D_i \cdot xs_i \left\{\frac{aU+\Delta E-IE_i}{2}\left[1 - erf\left(\frac{IE_i-aU-\Delta E}{\sqrt{2}w}\right)\right] + \frac{w}{\sqrt{2\pi}} exp\left[\frac{-(aU+\Delta E-IE_i)^2}{2w^2}\right]\right\} \end{aligned} \qquad \textit{Eq. 2.24}$$

As shown in Eq. 2.24, the signal becomes a function of U in the form of convolution. The definite integral ranges from the IE to positive infinite since the electron ionization cross section below IE is zero. Note that the device-specific proportionality factor A and the energy offset ΔE are less stable over time and fluctuate. As a result, their determination becomes necessary for each measurement series. This process involves fitting Eq. 2.24 to the energy scan of a species with a known concentration and cross-section (near IE_i) slope xs_i. Typically, a mixture of CO, CO_2, and Ar is employed to derive three fits from a single scan. The mean values (A and ΔE) obtained from these fits are then employed to simulate signals for any species of interest at a given mole fraction x_i by utilizing literature values [52,53] for xs_i and IE_i. The uncertainty of the simulated signal from convolution procedure $u(S_{i,conv,simulated})$ is determined to be in the range of ±28.3% - ±49.0%. It should be noted that the simulated signal has to take into account

https://doi.org/10.7795/110.20241024

the mass discrimination factor D_i, which has an uncertainty of ± 20% for the device used in this study [50]. By specifying a x_i consistent with the molar fraction of Ar (x_R), the calibration factors $k_{i/R,conv}$ can be obtained using Eq. 2.25. The total uncertainty $u(k_{i/R,conv})$ is finally determined to be in the range of ±29.4% - ±53.2% [50] based on Eq. 2.26.

$$k_{i/R,conv}(U) = \frac{S_{i,conv,simulated}(U)}{S_R(U)} \cdot \frac{x_R}{x_i} = \frac{S_{i,conv,simulated}(U)}{S_R(U)} \qquad Eq.\ 2.25$$

$$u(k_{i/R,conv}) = \sqrt{u(x_R)^2 + u(S_{i,conv,simulated})^2 + u(S_R)^2 + u(inconstancy)^2} \qquad Eq.\ 2.26$$

2.1.3.3 RICS method

As the RICS approach was not utilized in this study, only a brief overview will be provided here. The application of the RICS method is restricted to molecules with known species-specific ionization energy (IE) and ionization cross section at 70 eV ($\sigma(70\ eV)$). By Eq. 2.27, it assumes that for molecules with chemical similarities, the cross-section ratio of two species, *i* and *j*, at a given distance *b* to their ionization threshold IE is equivalent to their cross-section ratio at 70 eV [51].

$$\frac{\sigma_i(E_1 = IE_i + b)}{\sigma_j(E_2 = IE_j + b)} = \frac{\sigma_i(70\ eV)}{\sigma_j(70\ eV)} \quad or \quad \sigma_i(E_1) = \sigma_j(E_1 + IE_j - IE_i) \cdot \frac{\sigma_i(70\ eV)}{\sigma_j(70\ eV)} \qquad Eq.\ 2.27$$

Based on Eq. 2.14 and Eq.2.27, the measured signal of unknown species $S_i(U)$ can be approximately simulated using the signal of a known chemically similar species $S_j(U)$, as depicted in Eq. 2.28 [50].

$$S_{i,RICS}(U) = \frac{x_i}{x_j} \cdot \frac{D_i}{D_j} \cdot \frac{\varphi(U)}{\varphi(U + IE_j - IE_i)} \cdot S_j(U + IE_j - IE_i) \cdot \frac{\sigma_i(70\ eV)}{\sigma_j(70\ eV)} \qquad Eq.\ 2.28$$

Therefore, the calibration factor of a species *i* relative to the reference *R* (Ar) can be expressed as follows:

$$\begin{aligned} k_{i/R,RICS}(U) &= \frac{S_{i,RICS}(U)}{S_R(U)} \cdot \frac{x_R}{x_i} \\ &= \frac{1}{S_R(U)} \cdot \frac{x_R}{x_i} \cdot \frac{x_i}{x_j} \cdot \frac{D_i}{D_j} \cdot \frac{\varphi(U)}{\varphi(U + IE_j - IE_i)} \cdot S_j(U + IE_j - IE_i) \cdot \frac{\sigma_i(70\ eV)}{\sigma_j(70\ eV)} \\ &= \frac{x_R}{x_j} \cdot \frac{S_j(U + IE_j - IE_i)}{S_R(U)} \cdot \frac{\varphi(U)}{\varphi(U + IE_j - IE_i)} \cdot \frac{\sigma_i(70\ eV)}{\sigma_j(70\ eV)} \end{aligned} \qquad Eq.\ 2.29$$

Here, assuming that the mass discrimination factor from the similar species is roughly consistent (namely $D_i \approx D_j$). The calibration factor can be estimated from the energy scan of a chemically similar reference substance *j*. The overall uncertainty of the calibration factor $k_{i/R,RICS}$ varies within the range of ±51.2% to ±205%, depending on the selected reference species *j*.

2.1.3.4 Overall uncertainty

Depending on the different calibration methods, the overall uncertainty for the species mole fraction ($u(x_i)$) can be estimated by following Eq. 2.30.

https://doi.org/10.7795/110.20241024

$$u(x_i) = \sqrt{u(x_{Ar})^2 + u(S_i)^2 + u(S_{Ar})^2 + u(k_{i/Ar})^2} \qquad Eq.\ 2.30$$

Table 2.1 summarizes the uncertainties of the calibration factor and the mole fractions. It should be noted that the uncertainties in Table 2.1 are based on the peak value of species signals. Besides, the 8% of the $u(S_i)$ and $u(S_{Ar})$ in the calculated equation applies when the signal intensity exceeds 5000 counts. For species with very low concentrations, where the signal intensity is lower, the uncertainty increases accordingly. The uncertainty of the temperature is ±2.5%. Both uncertainties for mole fractions (shaded areas, B-Spline) and that for temperature (horizontal error bars) are illustrated in the results figures.

Table 2.1. Detailed uncertainties of species mole fractions and the applied calibration method.

Species and applied calibration method	$u(k_{i/Ar})$	$u(x_i)$
Direct calibration: NH_3, C_2H_6, C_2H_5OH, CH_3OCH_3, H_2, C_2H_4, CH_4, CO, NO, NO_2	±22.4%	±29.2%
Convolution: HCN, CH_2O, HNCO, CH_3CHO, CH_2O_2, $C_2H_4O_2$, CH_3NO_2	±53.2%	±56.5%
Estimated calibration: HONO	±200%	±202%

2.2 Intermediate temperatures measurements

2.2.1 Rapid compression machine (RCM)

The investigation at intermediate temperature and elevated pressures was also conducted in a rapid compression machine (RCM) at PTB. RCMs are predominantly employed for assessing autoignition properties, meanwhile, some attempts to combine the machine with diagnostic techniques such as laser absorption, gas chromatography (GC), and fluorescence spectroscopy to visualize the ongoing chemical process [54]. Here, this study will exclusively concentrate on the ignition delay time.

The details of RCM have been described in [8,10], and only a brief description is given here. Typically, an RCM is employed to replicate a simplified adiabatic compression stroke of an internal combustion engine by eliminating the complexities associated with engine operating conditions, e.g., intricate swirl bowl geometry, cycle-to-cycle variation, and the presence of residual gas. It can be equipped with a single piston or dual opposed pistons [55], which is driven by a falling weight or high-pressure driver gases. The high-temperature and elevated-pressure environment at the end of compression (EOC) triggers the chemical reactions. To establish a constant volume reaction chamber and minimize the deviations between each measurement, the fast-moving piston must stop at the EOC and lock in its final position. In addition, due to the high-speed piston motion, the ordinary flat piston will also bring a huge discrepancy by creating a roll-up vortex, which results in a mixing of pockets of cold gas from the boundary layer with the hot gases in the core region (cf. Figure 2.5).

https://doi.org/10.7795/110.20241024

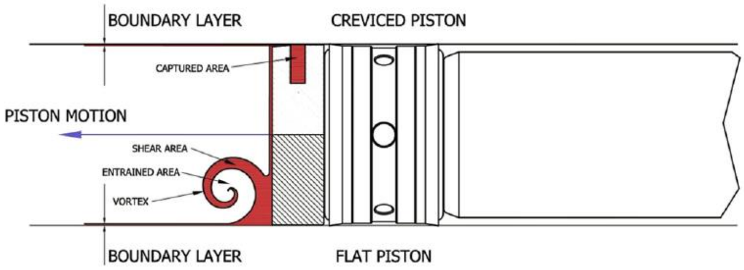

Fig. 2.5. The lower part illustrates the creation of a roll-up vortex due to piston motion during the compression stroke. The upper part shows the containment of the boundary layer through a crevice [56].

As shown in Figure 2.5, introducing a crevice on the side of the piston can potentially eliminate the intricate fluid mechanics and undesired mixing with near-wall cold gases within the combustion chamber. This contributes to the establishment of a well-defined homogenous zone within the RCM [57]. Once the impact of vortex roll-up is suppressed, the influence of heat loss is effectively limited to the boundary layer, and therefore, an adiabatic core has been established at the end of compression [58,59], which is known as the "adiabatic core hypothesis". It has been observed that large discrepancies in measurements arise under similar conditions because of temperature inhomogeneity within the reaction chamber and the lack of heat loss characterization for the associated experiments [60–63]. For this, these mixtures within the adiabatic core will be the investigation target in RCM measurements and can be reproduced in the simulation as a closed adiabatic reactor with constrained volume. The equations Eq. 2.2-2.4 and 2.6 are modified to fit this system, as shown in Eq. 2.31 to Eq. 2.34. Note that all symbols, except the wall surface area (A_w) and wall speed (v_w) in these equations, have been previously defined in Eq. 2.2-2.6 and will therefore be omitted here.

$$\frac{dm}{dt} = 0 \qquad \textit{Eq. 2.31}$$

$$m\frac{dY_i}{dt} = V\dot{\omega}_i W_i \qquad \textit{Eq. 2.32}$$

$$\frac{dV}{dt} = A_w v_w(t) \qquad \textit{Eq. 2.33}$$

$$\frac{dU}{dt} = mc_v\frac{dT}{dt} + \sum_i u_i m\frac{dY_i}{dt} = -P\frac{dV}{dt} + \dot{Q} \qquad \textit{Eq. 2.34}$$

Where Eq. 2.31 reveals the mass of the whole system remains constant in a closed RCM system. Eq. 2.32 denotes that the mass of each species *i* varies according to the production rate by corresponding reactions. Eq. 2.33 indicates the volume of the reactor is constrained by the wall surface area and its speed. An ideal RCM system has no enthalpy change, so the change of the internal energy is equal to the heat added to the system minus the work done by the system.

https://doi.org/10.7795/110.20241024

In RCM experiments, the initiation of ignition is characterized by a swift pressure increase within the reaction chamber, a parameter directly measured via a pressure transducer. To mitigate thermal shock, the transducer has been covered by a thin silicone layer. Figure 2.6 depicts a typical pressure profile for both a reactive ammonia/ethane blend (black line) and its non-reactive counterpart (red dashed line). The initial peak in the reactive pressure curve indicates the end of compression (EOC). It is succeeded by a gradual pressure drop because of heat losses to the reaction chamber wall, until the pressure re-arises. The moment of the maximum pressure derivative during this rise is defined as the ignition onset. The ignition delay time (IDT) is defined as the period between EOC and ignition onset. The thermal conductivity, specific heat capacity, and diffusion coefficient of nitrogen (N_2) are similar to those of oxygen (O_2), which minimizes the impact on the system's thermodynamic and kinetic properties when nitrogen replaces oxygen. Therefore, non-reactive measurements were conducted by substituting the O_2 content of the mixture with an equal amount of this inert gas (N_2), facilitating the characterization and accurate simulation of non-ideal effects, particularly heat loss within the device.

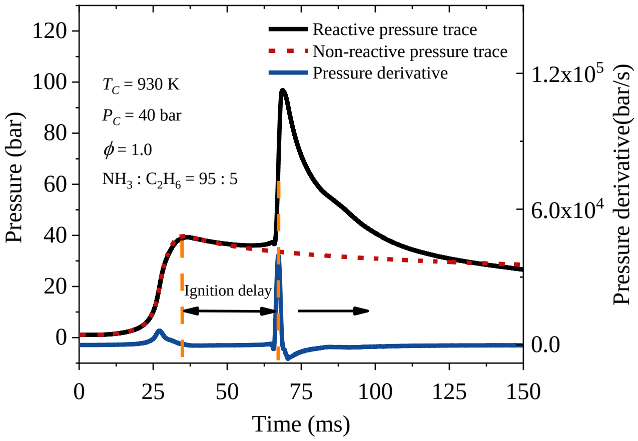

Fig. 2.6. Typical pressure profiles with respect to time for a reactive and a non-reactive NH_3/C_2H_6 mixture and the corresponding derivative profile for the reactive mixture [13].

However, measuring temperature directly in an RCM remains challenging since the intrusion of a thermocouple disrupts the homogeneous reactor core, and those non-intrusive temperature measurements introduce large uncertainties. In this work, the temperature at the EOC (T_c) is determined by incorporating the adiabatic core hypothesis [64] and applying the following equation:

$$\ln\frac{P_c}{P_0} = \int_{T_0}^{T_c} \frac{\gamma(T)}{\gamma(T)-1}\frac{dT}{T} \qquad \textit{Eq. 2.35}$$

where the initial temperature (T_0) and pressure (P_0) of the mixture within the combustion chamber are denoted, respectively. $\gamma(T)$ represents the temperature-dependent heat capacity ratio (γ), equivalent to the ratio of heat capacity at constant pressure to that at constant volume (c_p/c_v). Since the compression ratio and mixture composition are constant, the desired T_c is realized by adjusting the T_0 of the gas mixtures within the combustion chamber using heating tapes.

https://doi.org/10.7795/110.20241024

The RCM setup at PTB comprises three main components: a pneumatically driven chamber, a hydraulically braked chamber, and a combustion chamber. Notably, a creviced-designed piston is utilized to ensure the formation of a homogeneous reacting core during the compression stroke [65], with the geometric compression ratio maintained at 20.93. Pressure measurements are conducted using a Kistler (601H) pressure sensor coupled with a Kistler (Type 5018) charge amplifier, and data are recorded using a Spectrum Instrumentation data acquisition card (M2i.3016-Exp). The sampling frequency is set at 200 kHz, with a digital resolution of 0.00488 V and no filtering applied. Before preparing the mixtures, a passivation technique is employed to mitigate the adsorption effects of ammonia on the system wall by saturating the entire system with pure ammonia [18]. All test mixtures (purity: NH_3 > 99.999%, C_2H_6 > 99.95%, O_2 > 99.999%, N_2 > 99.999%, Ar > 99.999%, Linde; C_2H_5OH > 99.9%, Supelco), are initially prepared in three 3.785 L stainless-steel tanks (two for reactive mixtures and one for non-reactive mixtures) at room temperature, ensuring precise control of the partial pressures of each gas component (uncertainty < 0.25%) via an MKS manometer (Baratron 627). To achieve the desired temperature range (T_c), adjustments are made to the N_2/Ar ratio in the dilution, ensuring a suitable heat capacity ratio for the mixture. Both reactive and non-reactive gas mixtures are allowed to homogenize for a minimum of 12 hours before measurements. During experiments, measurements are repeated three times for each test condition to minimize deviations in the recorded data.

2.2.2 Uncertainties of RCM measurement

In the present work, the temperature at EOC (T_c) is taken as the reference for reporting ignition delay time (IDT), and therefore the respective uncertainties of both T_c and IDT should be considered here. According to Eq. 2.35, the calculated T_c is dependent on the initial pressure and temperature, the compressed pressure, and the specific heat ratio of the mixture components. An error propagation analysis (cf. Eq. 2.36) is therefore required to determine the contributions of these factors to the uncertainty in calculating the T_c.

$$\begin{gathered}
u(T_c) = \sqrt{\left(\frac{\partial T_c}{\partial P_0}\delta_{P_0}\right)^2 + \left(\frac{\partial T_c}{\partial P_c}\delta_{P_c}\right)^2 + \left(\frac{\partial T_c}{\partial T_0}\delta_{T_0}\right)^2 + \left(\frac{\partial T_c}{\partial \gamma}\delta_{\gamma}\right)^2} \\
\frac{\partial T_c}{\partial P_0} = \frac{C_p(T_0)\cdot T_c}{C_p(T_c)\cdot T_0} \\
\frac{\partial T_c}{\partial P_c} = \frac{R\cdot T_c}{C_p(T_c)\cdot P_c} \\
\frac{\partial T_c}{\partial T_0} = \frac{R\cdot T_c}{C_p(T_c)\cdot P_0} \\
\frac{\partial T_c}{\partial \gamma} = \frac{T_c}{\gamma(\gamma-1)}\ln\frac{T_c}{T_0}
\end{gathered} \qquad \textit{Eq. 2.36}$$

The absolute uncertainties δ_k of the factors k, namely P_0, P_c, T_0, and γ have been extensively documented in our previous works [8] and only presented here in Table 2.2. Overall, the $u(T_c)$ is ±1.1% at 40 bar and ±1.4% at 20 bar, which is an approximate variation of ±10 K for both 40 and 20 bar cases, considering their different temperature range. He et al. [8] highlighted that the primary contributor to the total $u(T_c)$ for this device is the error in the compressed pressure measurement, directly proportional to the full range of its pressure signal amplifier. By reducing the full range of the amplifier, the $u(T_c)$ was minimized to ±0.5%, roughly ±5.5 K under various pressures for the measurement of NH_3/C_2H_5OH fuel blends. Furthermore, the uncertainty of the IDT $u(IDT)$ is derived from the repeatability (5%) in the measurements. The uncertainties for IDT (vertical error bars) and for T_c (horizontal error bars) are illustrated in the results figures.

Table 2.2. The uncertainty and partial derivatives of the independent parameters [8,13].

k	δ_k	Apparatus
P_0	0.25% of the reading	Manometer, Baratron 627
P_c	0.513 bar at 40 bar 0.256 bar at 20 bar	Pressure transducer, Kistler 601H (Linearity: $\leqslant \pm 0.5\%$ FS)
T_0	0.01 K	Thermal resistor, Pt-100
γ	0.0017	Manometer, Baratron 627 [8]

2.3 Intermediate-to-high temperatures measurements

2.3.1 Shock tube (ST)

Observations at intermediate-to-high temperature conditions were performed by a shock tube (ST) integrated with tunable diode laser absorption spectroscopy (TDLAS) at PTB. This study quantifies the highly time-resolved NH_3, NO, and CO profiles and characterizes the rapid ignition events at high temperature, namely IDT within 2 microseconds, based on the peak position of CO. Details of the apparatus have already been published several times [66–69], so that only a concise outline of the most important properties of the system is given here. Typically, shock tubes are constructed with thick walls, often made of stainless steel, and feature either rectangular or circular cross-sections [70]. They are separated into driver and driven sections by a diaphragm, which is made of aluminum or polymer sheet. The driver section is filled with high-pressure driver gas (T_4, P_4 in Figure 2.7) to initiate the ignition of test gas (T_1, P_1 in Figure 2.7) inside the driven section by introducing a shock wave. To obtain a stronger shock wave, the gases with low molecular mass, such as helium (He) and H_2, are selected as the driver gas because of their high sound speed (c) and low heat capacity ratio (γ).

Figure 2.7 illustrates the schematics of the shock tube, providing valuable insights into the temperature and pressure distribution. During the experiment, the driver gas is introduced into the driver section until the diaphragm ruptures and then expands into the driven section. The driver gas and test gas do not merge, but a separating surface, the contact surface (CS), is formed between the two gases. Simultaneously, an incident shock wave (ISW) is generated at the front of the driver gas and propagates into the driven section. The ISW travels through the test gas, leading to an increase in both temperature and pressure behind the wave (T_2, P_2). Since the propagation speed of CS is lower than that of ISW, the later arriving CS carrying the cold driver gas will cool the previously heated test gas ($T_3<T_2$, $P_3=P_2$).

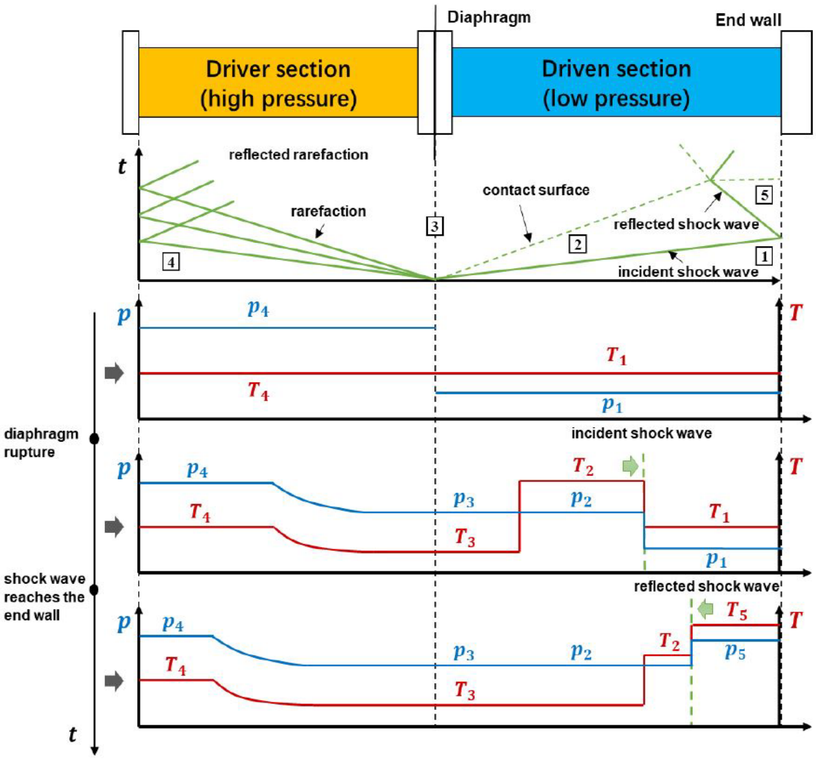

Fig. 2.7. The x–t diagram and operational principle of a shock tube [71,75].

As the ISW reaches the end wall of the driven section, a reflected shock wave (RSW) forms and transfers back to the driver section. In this process, the temperature and pressure of test gas undergoes a second surge (T_5, P_5). It is noteworthy that the generation of the RSW counteracts the effect of the ISW on the test gas, causing the velocity of gas behind the reflected wave to drop to zero. This contributes to the establishment of a homogenous and quasi-instantaneous region near the end wall of the driver section, where surface effects and transport processes behind the reflected wave can be neglected.

However, the duration of this region (Δt, or test time) only maintains a limited period because of disturbances from two aspects. The first arises from the interaction between the CS and RSW, which introduces either expansion waves or reflected waves towards the end wall of the driven section, depending on the properties of the gases. Besides, a series of expansion waves propagate towards the driver section after the rupture of the diaphragm. These expansion waves are reflected by the end wall of the driver section and travel back to the driven section. Consequently, the shock-heated test gas in the homogenous region experiences strong quenching upon the arrival of these expansion waves. Note that, there is no such issue in an RCM system but heat loss to the cold wall needs to be considered, thus its experimental duration can be designed for up to 150 ms. The investigation at ST conditions will only focus on examining the combustion process within the homogenous region during the test time *Δt*, which is approximately 1-2 ms based on our shock tube geometry.

The temperature (*T*), pressure (*P*), and density (ρ) of the test gas behind the ISW can be determined through the Rankine-Hugoniot equations [72,73] in 1D shock-wave coordinates [74]. For this, the shock fixed coordinate is utilized here instead of the laboratory fixed coordinate, and the conversion relationship between them is illustrated in Figure 2.8.

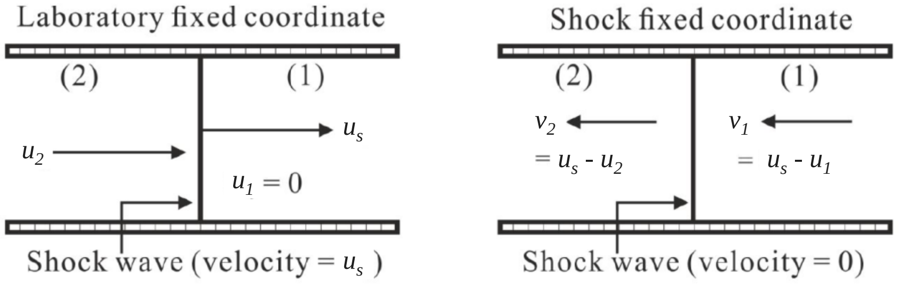

Fig. 2.8. One-dimensional laboratory fixed (left) and shock fixed (right) coordinates (v_1 is equal to the velocity of the incident shock wave u_s).

In the shock fixed coordinate system, the Rankine-Hugoniot conditions can be expressed as follows.

$$\rho_1 v_1 = \rho_2 v_2 \quad (Conservation\ of\ Mass) \qquad \text{Eq. 2.37}$$

$$\rho_1 v_1^2 + p_1 = \rho_2 v_2^2 + p_2 \quad (Conservation\ of\ Momentum) \qquad \text{Eq. 2.38}$$

$$\frac{1}{2} v_1^2 + h_1 = \frac{1}{2} v_2^2 + h_2 \quad (Conservation\ of\ Energy) \qquad \text{Eq. 2.39}$$

Where *v_i* and *h_i* represent the velocity and enthalpy of the gas on different sides of the shock wave, respectively. The mixture is assumed to obey the ideal gas law so that the equations of state (Eq. 2.39, *R* is the universal gas constant) and enthalpy (Eq. 2.40) can be written as:

$$p = \rho R T \qquad \text{Eq. 2.39}$$

$$h = c_p T = \frac{\gamma}{\gamma - 1} R T \qquad \text{Eq. 2.40}$$

By integrating the Eq. 2.39 and Eq. 2.40 into the Rankine-Hugoniot equations (Eq. 2.37 to Eq. 2.39), the temperature, pressure, and density can be obtained by the following equation:

$$\frac{T_2}{T_1} = 1 + \frac{1(\gamma - 1)}{(\gamma - 1)^2} \cdot \frac{\gamma M_s^2 + 1}{M_s^2} \cdot (M_s^2 - 1) \qquad \text{Eq. 2.41}$$

$$\frac{P_2}{P_1} = 1 + \frac{2\gamma}{\gamma - 1} \cdot (M_s^2 - 1) \qquad \text{Eq. 2.42}$$

$$\frac{\rho_2}{\rho_1} = \frac{(\gamma + 1) M_s^2}{(\gamma - 1) M_s^2 + 2} \qquad \text{Eq. 2.43}$$

Where the Mach number M_S can be determined by the ratio between the velocity of the incident shock wave (u_S) and the speed of sound (*c*) at the given condition (namely temperature *T₁* and molar mass *M* of the test gas), as shown in below.

$$M_S = \frac{u_S}{c} = \frac{u_S}{\sqrt{\frac{\gamma R T_1}{M}}} \qquad \textit{Eq. 2.44}$$

A comparable derivation method can be employed to calculate the state of the test gas behind the reflected shock wave (RSW).

$$\frac{T_5}{T_1} = \frac{\left[2(\gamma-1)M_S^2+(3-\gamma)\right]\left[(3\gamma-1)M_S^2-2(\gamma-1)\right]}{(\gamma-1)^2 M_S^2} \qquad \textit{Eq. 2.45}$$

$$\frac{P_5}{P_1} = \frac{2\gamma M_S^2-(\gamma-1)}{\gamma+1} \cdot \frac{(3\gamma-1)M_S^2-2(\gamma-1)}{(\gamma-1)M_S^2+2} \qquad \textit{Eq. 2.46}$$

$$\frac{\rho_5}{\rho_1} = \frac{P_5}{P_1} \cdot \frac{T_5}{T_1} \qquad \textit{Eq. 2.47}$$

The shock tube at PTB is composed of a 3.5-meter driver section and a 4.5-meter driven section, which are partitioned by aluminum diaphragms. The inner diameter of the tube is 70 mm. To minimize surface effects, the inner surface has been electropolished. An MKS manometer is positioned at the top of the driven section, near the diaphragm placement, to measure the initial filling pressure within the driven section. Additionally, a Wika manometer is installed at the end of the driver section to measure the burst pressure of the diaphragm.

Before preparing the mixtures, the mixing tank undergoes vacuuming by using a turbo-molecular pump (Leybold) overnight until reaching a pressure of 1×10^{-7} mbar. When initiating the mixture preparation process, a small quantity of the target gas is first used to flush the pipes twice, effectively cleaning any residual gas. Subsequently, the mixtures are stirred using a magnetic stirrer (cyclone 300 ac, Büchiglasuster) for a minimum of two hours to ensure uniformity.

To address the adsorption effects of NH_3, a passivation procedure is implemented: the mixture is introduced into the driven section until reaching the target initial pressure and held for 2 minutes before being vacuumed to 1.5 mbar. This procedure is repeated twice before filling the formal mixture [66,67]. Meanwhile, the driver sections are evacuated to 1×10^{-3} mbar before each measurement.

A 90 µm thick aluminum sheet serves as the diaphragm, with helium employed as the driver gas for all measurements. Five pressure sensors (603CAB, Kistler) are deployed for pressure measurements. Four of them are positioned at an equal distance of 500 mm along the tube axis to facilitate shock velocity calculations. The fifth pressure sensor is installed on the end wall to monitor the pressure behind RSW. Three charge amplifiers (5018A, Kistler) are utilized to process the pressure signals. The first three pressure sensors are combined and connected to a single charge amplifier, while the fourth and fifth

https://doi.org/10.7795/110.20241024

sensors are connected to separate charge amplifiers. Pressure signals are recorded using a data acquisition card (M2i.4964-Exp, Spectrum). The pressure (P_5) and temperature (T_5) behind RSW are computed according to the one-dimensional shock equations (Eq. 2.45 to Eq. 2.47). To visualize the process occurring behind RSW, two Zinc Selenide (ZnSe) windows are installed at the same plane as the fourth pressure transducer for laser measurements. Further details regarding laser absorption spectroscopy will be summarized below.

2.3.2 Tunable diode laser absorption spectroscopy (TDLAS)

TDLAS presents numerous advantages over conventional spectroscopic techniques, including enhanced resolution, heightened sensitivity, swift response times, and applicability to remote measurements. In practical applications, it adjusts the output wavelength of the diode laser to match the absorption line of the target gas molecules. The gas concentration is then analyzed based on the absorption of the target gas molecules. Figure 2.9 depicts the typical schematics of a TDLAS measurement. As the incident laser beam I_0 at frequency v_f passes through the uniform test gas medium of length L, after a certain amount of absorption, diminishing the light intensity to a transmitted beam I_t, the ratio between I_t and I_0 follows the Beer-Lambert law (Eq. 2.48).

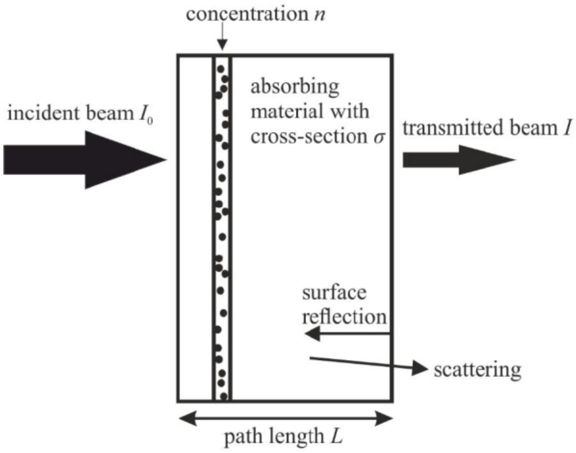

Fig. 2.9. The schematic of an absorption measurement [75].

$$\frac{I_t}{I_0} = \exp(-Px_i\phi_v SL) = \exp(-a_v) \qquad \textit{Eq. 2.48}$$

where P represents the total pressure, x_i is the mole fraction of the absorbing species i, and ϕ_v is the Voigt line-shape function [76] at frequency v_f, which combines both temperature and collisional broadening. S is the line-strength of the specific transition and is a function of temperature according to:

$$S(T) = S(T_0)\frac{Z(T_0)}{Z(T)}\left(\frac{T_0}{T}\right)\cdot\exp\left[-\frac{hcE''}{k_B}\left(\frac{1}{T}-\frac{1}{T_0}\right)\right]\frac{1-\exp\left(\frac{hcv_{f0}}{k_BT}\right)}{1-\exp\left(\frac{hcv_{f0}}{k_BT_0}\right)} \qquad \textit{Eq. 2.49}$$

where $S(T_0)$ represents the line strength at a reference temperature T_0, E'' is the lower-state energy of the frequency v_{f0}, and h, c, k_B are Planck's constant, speed of light and Boltzmann's constant, respectively. $Z(T)$ is defined as the product of rotational, vibrational, and electronic partition functions and can be fitted approximately by a third-order polynomial [77]. All parameters in Eq 2.49 at the reference temperature T_0 can be measured in a static cell or obtained from the HITRAN database, where T_0 is consistently set to 296 K [78,79]. Notably, the coefficients of the $Z(T)$ polynomial are temperature- and molecule-dependent and therefore should be determined for each target species.

In Eq. 2.48, the combination of $Px_i\phi_v SL$ is defined as absorbance (a_v) [66,67]. This indicates that the intensity of the absorbed light at the specific wavelength (reciprocal of the specific frequency v_f) is proportional to the concentration (x_i) of the target molecules. By measuring the absorbed light intensity (absorbance), the concentration of the target species can be interpreted. Practically, a reference laser signal I_0 and an offset signal I_b were recorded before conducting each shock, combining with the transmitted signal I_t during the test time Δt, the absorbance $\alpha(v)$ can be calculated following the Beer-Lambert law.

$$a_v = -\ln\left(\frac{I_t - I_b}{I_0 - I_b}\right) \qquad \textit{Eq. 2.50}$$

In this work, three lasers running in fixed-wavelength modes for simultaneous NH_3, NO, and CO quantification were coupled to the shock tube. To get the absolute species mole fraction from absorbance, line-by-line data, and absorption cross-sections are two commonly used methods. For the quantification of NO and CO, the line-by-line method was used according to the variation of Eq. 2.48. (cf. Eq. 2.51) [66,67]:

$$x = \frac{a_v}{P\phi_v S(T)L} \qquad \textit{Eq. 2.51}$$

Because of the difficulty in obtaining $S(T)$ through line-by-line data of the current NH_3 spectrum, which involves six very close transition lines, the absorption cross-section-based method was used to get the absolute NH_3 mole fraction by Eq. 2.52 [69]:

$$x = \frac{a_v k_B T}{P k_v L} \qquad \textit{Eq. 2.52}$$

where k_v is the absorption cross-section. The absorption cross-section method is frequently used to quantify absolute mole fractions at elevated temperatures and pressures, particularly in conditions as well as spectral ranges where the line-by-line parameters are neither possible nor feasible. The absorption cross-section, k_v, is defined as Eq. 2.53 [80]. It can be determined by an absorption cross-section experiment using a known binary calibration gas (NH_3/Ar) in the shock tube under elevated temperatures and pressures. Since the working pressure of the shock tube is maintained at 1-3 bar, the compression factor Z is assumed to be 1.

https://doi.org/10.7795/110.20241024

$$k_v = a_v \cdot \frac{Zk_BT}{xPL} \qquad \textit{Eq. 2.53}$$

In the present work, the used Mid-IR NH_3 laser, centered at 1084.61 cm^{-1}, is a continuous-wave distributed-feedback quantum cascade laser (CW-DFB-QCL, Alpes Lasers). Its operation is controlled by a QCL driver (ITC4005QCL, Thorlabs) [69]. Additionally, both the Mid-IR NO and CO lasers are continuous-wave distributed-feedback interband cascade lasers (CW-DFB-ICL, Nanoplus). The NO lase, centered at 1915.76 cm^{-1}, is driven by a modular laser diode controller (LDC-3900, ILX Lightwave) [66–68]. Meanwhile, the CO laser, centered at 2059.91 cm^{-1}, is driven by a modular laser diode controller (PRO8000 equipped with LDC8002 and TED8020, Thorlabs) [81]. As shown in Figure 2.10, the three laser beams are combined into the shock tube with a path length of 7 cm through two concave mirrors (CM508-200-M01, Thorlabs). To discriminate against thermal emissions from shock-heated gases, specific bandpass filters (FB9000-500, Thorlabs; L0167215 and L0200593, Laser Components) are positioned in front of three photodetectors (PVI-4TE-5, PVI-4TE-6, PVI-4TE-10.6, VIGO). Furthermore, one branch of the laser beam is directed into a wavemeter (671B, Bristol Instruments) to precisely characterize the wavenumber. Both the pressure and laser signals are recorded using a data acquisition card (20 MS/s, Spectrum M2i.4964-Exp).

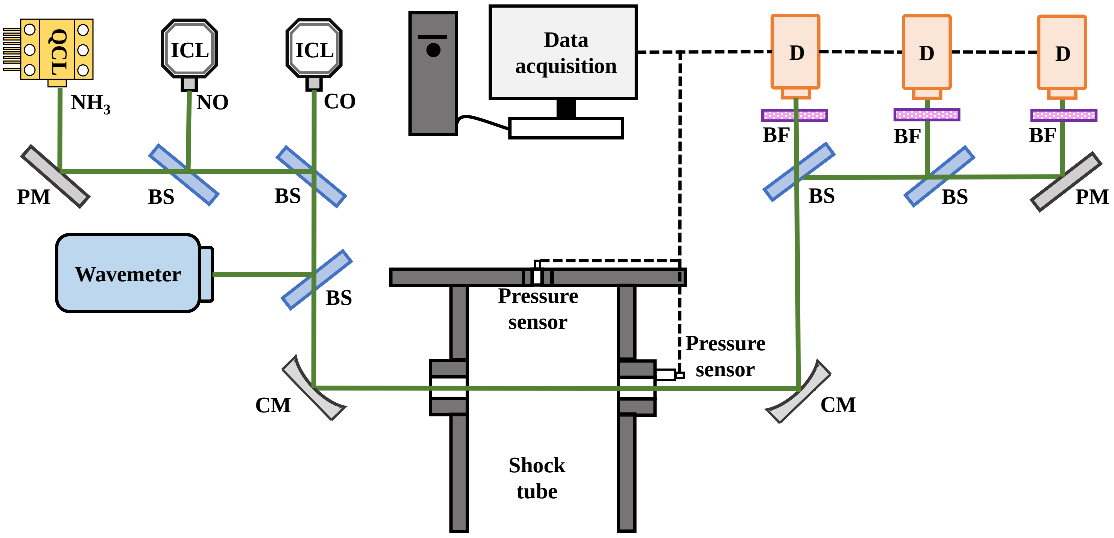

Figure 2.10. Schematic of the experimental setup (QCL: Quantum Cascade Laser; ICL: Interband Cascade Laser; PM: Plane Mirror; BS: Beam Splitter; CM: Concave Mirror; BF: Bandpass Filter; D: Detector) [82].

Figure 2.11 shows the typical pressure profile, raw laser signals, absorbance, and species mole fraction of stoichiometric NH_3/C_2H_6 mixtures (T_5 = 1514 K, P_5 = 2.78 bar). In the figure, two distinct rises in pressure signify the arrival of the incident shock wave and the reflected shock wave. The laser signals are synchronized with the sharp pressure rise at the arrival of the reflected shock wave, defining time zero. Subsequently, a discernible pressure increase, attributed to heat release during the oxidation process, becomes evident after an induction time of approximately 150 μs.

https://doi.org/10.7795/110.20241024

The raw laser signals exhibit variations and schlieren effects, providing a visual representation of the shock front's passage. These variations align seamlessly with the pressure profile. Before the incident shock wave, the NH_3 laser signal intensity approaches zero due to the strong absorbance of NH_3 as the reactant. Conversely, NO and CO laser signals experience a decrease in intensity during the oxidation process, reflecting the generation of these species.

By Equation 2.50, the conversion of raw laser signals to absorbance is demonstrated in Figure 2.11b. The concurrent tracking of NH_3 consumption and CO and NO production serves as a reliable indicator of the entire oxidation process. Additionally, applying Eq. 2.51-2.52, the absorbances are transformed into species mole fractions, as depicted in Figure 2.11c. Noteworthy is the synchronicity between the rapid decline in NH_3 and the swift generation of NO and CO. Drawing from our prior investigation [81], where the CO peak consistently aligned with the steepest pressure rise, we maintain the proposed definition of ignition delay time in this study. This definition entails measuring the time interval between the arrival of the reflected shock wave (P_5, T_5) and the peak value in CO mole fraction, marking the onset of ignition.

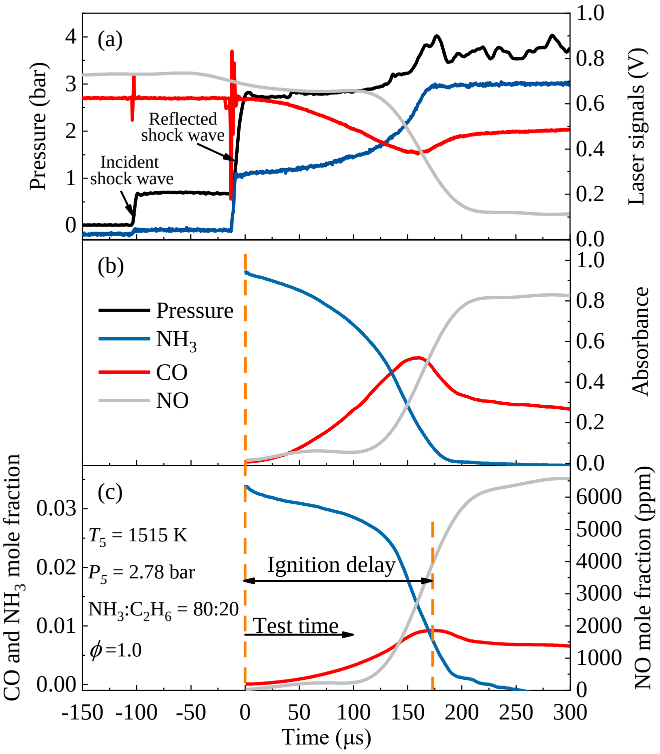

Fig. 2.11. a) Typical pressure profile and laser signals; b) Absorbances; c) Species mole fractions (NH_3:C_2H_6 = 80:20, ϕ = 1.0, T_5 = 1514 K, P_5 = 2.78 bar) [82].

2.3.3 Uncertainties of ST measurement

Given the relatively low dilution ratio (90%) in the experiments, the rise in pressure and temperature cannot be ignored. In the current study, these effects on the absorption coefficient have been carefully considered. The dynamic pressure was measured by the fourth pressure transducer (cf. chapter 2.3.1) with an uncertainty of 1.5% based on the manufactory datasheet of the pressure sensor. Following the method from previous work [67], which has been validated in recent studies of Alturaifiet al. [83] and He et al. [84], the dynamic temperature was obtained from the prediction of chemical modeling constrained by measured pressure profiles, with an uncertainty of 2.2%. The path length is 7 cm with an uncertainty of 1.1% [66,67]. All required spectroscopic parameters of the three lasers such as pressure broadening coefficients or cross-sections can be found in our previous studies [68,69,81].

$$u(x_i) = \sqrt{u(P)^2 + u(T)^2 + u(L)^2 + u(a_v)^2 + u(Spectroscopy\ parameters)^2} \qquad Eq.\ 2.54$$

Error propagation analysis is not applicable in this case, as there are coefficients (e.g., Z) that cannot be accurately formulated retroactively. Accordingly, uncertainties of the mole fractions (x_i) of NO, CO, and NH_3 were calculated based on the root sum squared method (cf. Eq. 2.54), as shown in Table 2.3. The uncertainty of IDTs depends on the start point of time zero which is determined from the pressure profile according to the value of P5, and also depends on the position of CO peak. According to the root mean squared method, the uncertainty of IDT turns out to be 5.92%, including 2.8% uncertainty in (P_5), 1.5% uncertainty in dynamic pressure (P), and 5% uncertainty in CO absorbance profiles.

Table 2.3. Uncertainty budgets of species mole fraction.

Contributing factors	Uncertainty of NO (%)	Uncertainty of CO (%)	Uncertainty of NH_3 (%)
Dynamic pressure (P)	1.5	1.5	1.5
Dynamic temperature (T)	2.2	2.2	2.2
Path length (L)	1.1	1.1	1.1
Absorbance (a_v)	5	5	1
Spectroscopy parameters	19.8	7.2	11
Mole fraction	20.7	9.2	11.5

https://doi.org/10.7795/110.20241024

3. Theoretical Basis and Simulation Method

This chapter will present the theoretical basis of the reaction dynamic (cf. chapter 3.1) and the development of the PTB-NH_3/C_2 mech Mechanism (cf. chapter 3.2). In addition, the introduction of 0D simulation methods for reproducing the measurements in the jet-stirred reactor (JSR), the rapid compression machine (RCM), and the shock tube (ST) will be elaborated in chapter 3.3.

3.1 Reaction dynamics

The reaction dynamic is the study of the molecular-level mechanism of elementary chemical and physical processes. Its objective is to reveal the underlying kinetics behind chemical transformations. This field is also applicable to understanding combustion. It is noted that combustion is a highly intricate thermochemical process involving the conversion of a fuel with an oxidizer into products with the release of energy. This process typically proceeds by a series of elementary steps, also known as elementary reactions, which can be classified into five categories: chain initiation, chain propagation, chain branching, chain inhibition, and chain termination reactions, based on their specific type of reaction. The involved species in reactions can exist as either stable molecules or radicals. To elucidate the overall reaction proceeds of specific fuel combustion, a reaction mechanism comprising a kinetic collection of necessary fuel-specific elementary reactions has therefore been proposed. In practice, the thermodynamic properties of the system state such as enthalpy, entropy, and heat capacity should be incorporated into the mechanism. Additionally, for these combustion systems involving transport processes, it is crucial to consider the diffusion coefficients, viscosities, and thermal conductivities of the species as well. The thermodynamic properties of the reactants and products play a decisive role in determining the equilibrium and reaction direction, while reaction kinetics provide insights into the reaction rates [85].

The temperature dependence of a rate constant k for each elementary reaction can be described by the modified Arrhenius equation [86,87], Eq. 3.1. It can be determined through experimental methods, theoretical calculations, or estimation by drawing analogies to reactions with chemical similarity [88].

$$k = AT^b \cdot \exp\left(\frac{-E_a}{RT}\right) \qquad \textit{Eq. 3.1}$$

where A is referred to as the pre-exponential factor, b is the temperature (T) exponent, E_a is the activation energy, and R is the universal gas constant. Note that some rate constants follow a fall-off curve [89], which is constrained by both low- and high-pressure limits [90], indicating that their rate constants are also pressure-dependent.

In the domain of combustion research, fundamental combustion experiments, which decouple the chemistry from other processes such as flow dynamics, are indispensable tools for developing and validating intricate mechanisms. Over the past few decades, tremendous experimental data have been consistently available, which normally include the global process reflection such as ignition delay times (IDT) and laminar flame velocities (LBV), as well as the molecule-scale process information from speciation. Such data can either be used to test the overall performance of a mechanism for a specific fuel or validate the subsets of the mechanism related to identified species. Additionally, combining these experimental data with mechanisms can lead to a better understanding of the underlying chemical information. To gain a more persuasive mechanism for broad conditions, adjustments to certain elementary reaction rates can be made within a reasonable range (uncertainty bounds of k). Typically, kinetic analyses of the mechanism such as rate of production analysis (ROPA) and sensitivity analysis (SA) can identify these reactions by locating the most contributing and sensitive reactions.

In the present work, the SA for the ignition delay time and speciation was carried out based on a brute-force method. In particular, the rate constant for each reaction is changed successively, and the sensitivity coefficient (S_i) defined by Eq. 3.2 is the evaluated value [13].

$$S_i = \frac{X(2k_i)-X(k_i)}{X(k_i)} \qquad \textit{Eq. 3.2}$$

where k_i is the original reaction rate constant of the ith reaction; $X(k_i)$ is the predicted IDT or $x_{species}$ (mole fraction of specific species, e.g., x_{NH3}) with k_i, and $X(2k_i)$ is the predicted IDT or $x_{species}$ with the doubled k_i. In this case, the reaction with a higher absolute S_i has a more significant influence on IDT or $x_{species}$. For ignition delay time as well as fuel and oxidizer speciation, a negative value of S_i indicates the promotion of the ignition or $x_{fuel/oxidizer}$ consumption while a positive value implies an inhibiting effect. However, for speciation of all intermediate species (e.g., x_{CH3NO2}), a negative value signifies inhibition of its formation, while a positive value indicates promotion of its formation. To compare the results of the sensitivity analysis from different reactions, sensitivity coefficients are normalized to the maximum absolute value ($S_i/|S_i|_{max}$). It should be noted that SA will only identify the most sensitive reactions, but the contributions of these reactions may not always be substantial.

Additionally, the ROPA provides the contribution of each reaction to the net production or destruction rates of a species. This helps identify key intermediate species and facilitates an understanding of the reaction progression. For each species i of interest, its ROP can be described by Eq. 3.3.

$$ROP_i = \frac{d[C_i]}{dt} = \frac{[C_i]_{t2}-[C_i]_{t1}}{t_2-t_1} \qquad \textit{Eq. 3.3}$$

Here, $[C_i]$ is the concentration of the species i. t_1 and t_2 indicate the starting and ending points of the investigation period, respectively. The negative value indicates the consumption of species i, while the positive value indicates the formation of species i.

Once obtaining validated and persuasive mechanisms, they can be utilized for kinetic analysis to identify the key reaction steps, comprehend combustion mechanisms, optimize combustion conditions, and further develop the advanced combustion system. It therefore becomes more crucial to thoroughly

https://doi.org/10.7795/110.20241024

investigate the underlying details of ammonia combustion by establishing a dependable mechanism with various validations.

3.2 Mechanism development

The comprehensive chemical kinetic model, PTB-NH_3/C_2 mech has been systematically developed for ammonia fuel blends ranging from hydrogen to major C_2-hydrocarbons and represents the results of extensive research conducted by the author's group in recent years [10,11,13,18]. Notably, all results for NH_3/C_2-hydrocarbon fuel mixtures are from the present work. In summary, the base kinetics for the nitrogen (incl. ammonia) sub-mechanism is derived from Dai et al. [23], and the sub-mechanism of the promoter fuel is taken from the NUIG 1.1 model [91]. Moreover, a new subset describing ammonia/C_2-hydrocarbon interactions is introduced, accompanied by updates to certain elementary reactions in the mechanism based on the new experimental data. The thermodynamic and transport files of NUIG 1.1 are merged into the model to simulate the thermodynamic properties and transport processes in combustion.

More specifically, the sub-mechanism of the nitrogen chemistry from Dai et al. [23] is an updated version of the Glarborg mechanism [88]. In the original Glarborg mechanism, it can be divided into three parts as follows: reactions of amines, cyanides, and C_1-C_2 hydrocarbon/nitrogen interactions. The key amine sub-mechanism includes NH_2+NO/NO_2/OH, NH_2/NNH + O_2 reactions, and the reactions on the ONNH potential energy surface which were derived from the theoretical work of Klippenstein et al. [92]. Dai et al. [23] modified some rate constants for H_2NO reactions and adopted new rate coefficients for the reactions $NH_3(+M)=NH_2+H(+M)$, $NH_3+HO_2=NH_2+H_2O_2$, $NH_3+O_2=NH_2+HO_2$, and $HNO(+M)=H+NO(+M)$ from Stagni et al. [93] as well as those from the HONO/HNO_2 subset of Chen et al. [94]. In the Dai model, the CH_3CN subset from Alzueta et al. [95], methylamine subsets from Glarborg et al. [96], and a new subset of ammonia/DME cross-reactions were adopted, which was found to be essential for the oxidation of NH_3/C_2-hydrocarbon in the following modeling study. Given that the entire NUIG mechanism is a large model up to C_7-hydrocarbons, this work employs only the C_0-C_2 sub-mechanism from the NUIG model to minimize simulation time while ensuring the accuracy of the simulations. The selected sub-mechanism is mainly drawn from the CH_4/C_2H_6/C_2H_4 sub-mechanisms from Baigmohammadi et al. [97]. Besides, it incorporates the H_2/CO reactions from Kéromnès et al. [98], the C_1-C_2 reactions from Metcalfe et al. [99], and additional C_2H_5OH/CH_3OH reactions from Zhang et al. [100] and Burke et al. [101]. Both sub-mechanisms have been validated against specific targets (IDT, LBV, and speciations) for two individual fuels across a wide range of conditions. However, merging only these two sub-mechanisms still lacks the accuracy to predict the combustion of ammonia fuel blends.

Previous studies [10,18] have shown that incorporating or adjusting the rate constants for interactions between ammonia and the promoter fuel (hydrocarbon) system can significantly enhance predictions for

https://doi.org/10.7795/110.20241024

NH_3 fuel blends. On the other hand, kinetic analysis can also be used to further optimize the mechanism. To establish a more convincing mechanism for both global validation targets (IDT in this work) and species measurements, a novel subset (R1-R17) with reactions between species in the nitrogen sub-mechanism and those in the promoter fuels sub-mechanism has been introduced. Furthermore, some elementary reactions (R18-R23) were adjusted based on the kinetic analysis of the mechanism. Details of these reactions can be found in Table 3.1.

Table 3.1. The parameters of the updated reactions. Rate constants are listed in the form $A*T^b*exp(-E_a/RT)$*. Units are calories,* cm^3*, mol, and second.*

Elementary reactions	*A*	*b*	E_a	Source
1. $C_2H_6+NH_2=C_2H_5+NH_3$	9.00×10^{1}	3.46	5600	Mebel and Lin [102], k*2.0
2. $C_2H_4+NH_2=C_2H_3+NH_3$	1.56×10^{13}	0	13408	Siddique et al. [103]
3. $C_2H_6+NO_2=C_2H_5+HONO$	6.50×10^{14}	0	41400	Rasmussen et al. [104]
4. $C_2H_6+NO_2=C_2H_5+HNO_2$	6.00×10^{14}	0	33200	Rasmussen et al. [104]
5. $C_2H_5+NO_2=C_2H_5O+NO$	1.10×10^{13}	0	0	$k_{CH3+NO2}$ est. [105]
6. $CH_3OH+NH_2=CH_3O+NH_3$	1.80×10^{1}	3.34	4757	Ab-initio calculation [10]
7. $CH_3OH+NH_2=CH_2OH+NH_3$	1.40×10^{0}	3.61	4824	Ab-initio calculation [10]
8. $C_2H_5OH+NH_2=CH_3CHOH+NH_3$	1.07×10^{-1}	4	2893.5	Li et al. [18]
9. $C_2H_5OH+NH_2=C_2H_5O+NH_3$	3.15×10^{-1}	3.84	2244.5	Li et al. [18]
10. $C_2H_5OH+NH_2=CH_2CH_2OH+NH_3$	4.50×10^{1}	3.46	5600	$k_{C2H6+NH2}$ est. [102]
11. $C_2H_5OH+NH_2=C_2H_5+NH_2OH$	1.91×10^{34}	-6.34	68800	RMG database [106]
12. $CH_3CHOH+NO=HNO+CH_3CHO$	6.60×10^{12}	0	0	$k_{C2H5O+NO}$ est. [107]
13. $CH_3CHOH+NO_2=HONO+CH_3CHO$	1.70×10^{12}	0	0	$k_{C2H5O+NO2}$ est. [108]
14. $CH_3CHOH+NO=NO_2+C_2H_5$	1.60×10^{12}	0	-755	$k_{C2H5O2+NO}$ est. [109]
15. $C_2H_5O_2+NO=NO_2+C_2H_5O$	1.60×10^{12}	0	-755	$k_{C2H5O2+NO}$ est. [109]
16. $CH_2O+NH_2=HCO+NH_3$	3.15×10^{3}	3.00	3770	Zhu et al. [28]
17. $CH_3+NO_2=CH_3O+NO$	5.60×10^{14}	-0.5	0	Matsugi and Shiina [110]
18. $NO+HO_2=NO_2+OH$	2.31×10^{12}	0	-497	Baulch et al. [111], k*1.1
19. $CH_3+HO_2=CH_4+O_2$	2.00×10^{3}	2.83	-3700	Zhu and Lin [112], k*1.1
20. $CH_3CHO+H=CH_3CO+H_2$	7.59×10^{5}	2.40	1905	Mendes et al. [113], k*1.1
21. $C_2H_5OH+HO_2=CH_3CHOH+H_2O_2$	1.89×10^{-5}	5.26	6500	Zhang et al. [100], k*0.9
22. $CH_3OCH_3+OH=CH_3OCH_2+H_2O$	1.95×10^{7}	1.89	-366	Carr et al. [114]
23. $CH_3OCH_3+HO_2=CH_3OCH_2+H_2O_2$	2.00×10^{13}	0	16500	Zhao et al. [115]

est.: estimation

The H-abstraction reaction of C_2H_6 by NH_2 (R1) is derived from the study of Mebel and Lin [102], who adjusted their calculated rate constant based on the experiments in the temperature ranges of 300 - 500 K (k(theor) = (0.75 - 1.18) ∗k(exp)), 598 - 973 K (k(theor) = (1.12 - 1.41) ∗k(exp)), and 1500 - 1900 K (k(theor) = (3.7 - 5.6) ∗k(exp)). However, using its original rate constant in the model results in an overestimation of the IDTs for the studied NH_3/C_2H_6 mixtures. This indicates that the rate constant does not fit the experimental conditions studied (900 - 1200 K). To improve the agreement with the experiment, the pre-exponential factor (A) was adjusted by a factor of 2. It is important to point out that this modification of the rate constant should be considered an 'engineering modification' [23] that compensates for other shortcomings in the mechanism. This modification is not based on a deeper scientific understanding but rather serves as an empirical adjustment to improve mechanism performance under specific conditions. A similar approach has been also used for the rate constant of other reactions (R18-R21). For instance, the rate constant of $NO+HO_2$ reaction (R18) was summarized by Baulch et al. [111] based on the experimental measurements and review studies, while most of the studies were carried out at temperatures close to 300 K. The A-factor of R18 was multiplied by 1.1 within its given ±15% uncertainty, which contributes to a more accurate prediction in NH_3/C_2H_6 auto-ignition. The same adjustments were made to determine the calculated rate constants of the reactions CH_3+HO_2 (R19) and CH_3CHO+H (R20). Besides, the H-abstraction reaction of C_2H_5OH by HO_2 (R21), derived from Zhang et al. [100], exhibited overestimated reactivity for the studied NH_3/C_2H_5OH mixtures. In the present study, we suggest that this rate constant may be reduced by 10% to get a better agreement.

The rate coefficients for the H-abstraction from C_2H_4 by NH_2 (R2) are drawn from the recent theoretical work by Siddique et al. [103]. They computed the reaction rate constants of alkenes/NH_2 and fit them to an Arrhenius equation over a temperature range of 300 - 2000 K. The rate coefficients of R3 and R4 are adopted from the evaluation study of Rasmussen et al. [104], who compared the proposed rate coefficients of NO_x/alkane from Yamaguchi et al. [116] and Chan et al. [117] based on their experimental data. Another NO_2 reaction (with C_2H_5, R5) has been estimated by analogy to CH_3+NO_2. In addition, a novel subset with reactions between species in the nitrogen sub-mechanism and those in the methanol/ethanol sub-mechanism (R6-R15) has been added, which is either from ab initio calculations or analogy estimations. In this subset, the amino radicals (NH_2) are prone to abstract the H-atom from the alcohol and the intermediates of alcohol, where the NH_2+CH_3OH/C_2H_5OH reactions (R6-R10) appear to be very sensitive to predict the experimental data of NH_3/alcohol mixtures. Furthermore, the H-abstraction reaction of CH_2O by NH_2 (R16) is based on the recent work by Zhu et al. [28]. The rate coefficient of the reaction $CH_3+NO_2=CH_3O+NO$ (R17) was experimentally determined by Matsugi and Shiina [110]. The rate coefficients for the CH_3OCH_3 reactions with OH (R22) and HO_2 (R23) were adopted from the Wang-model [118], which originates from the theoretical study of Carr et al. [114] and Zhao et al. [115].

https://doi.org/10.7795/110.20241024

Given that some elementary reactions in nitrogen and hydrocarbon sub-mechanisms have been adjusted, it is necessary to revalidate the updated mechanism against previous measurements for both pure fuels and ammonia/C_{0-1} blend mixtures at the investigated conditions. As shown in Figure 3.1, the model still predicts well for these fuels and fuel blends. Further detailed comparisons between simulations and experimental data concerning ammonia/C_2 fuel blends are presented in chapters 4-6 below. In summary, the PTB-NH_3/C_2 mech can reasonably capture the observed global validation targets (IDT) and speciation measurements for ammonia/C_2 fuel blends across various conditions.

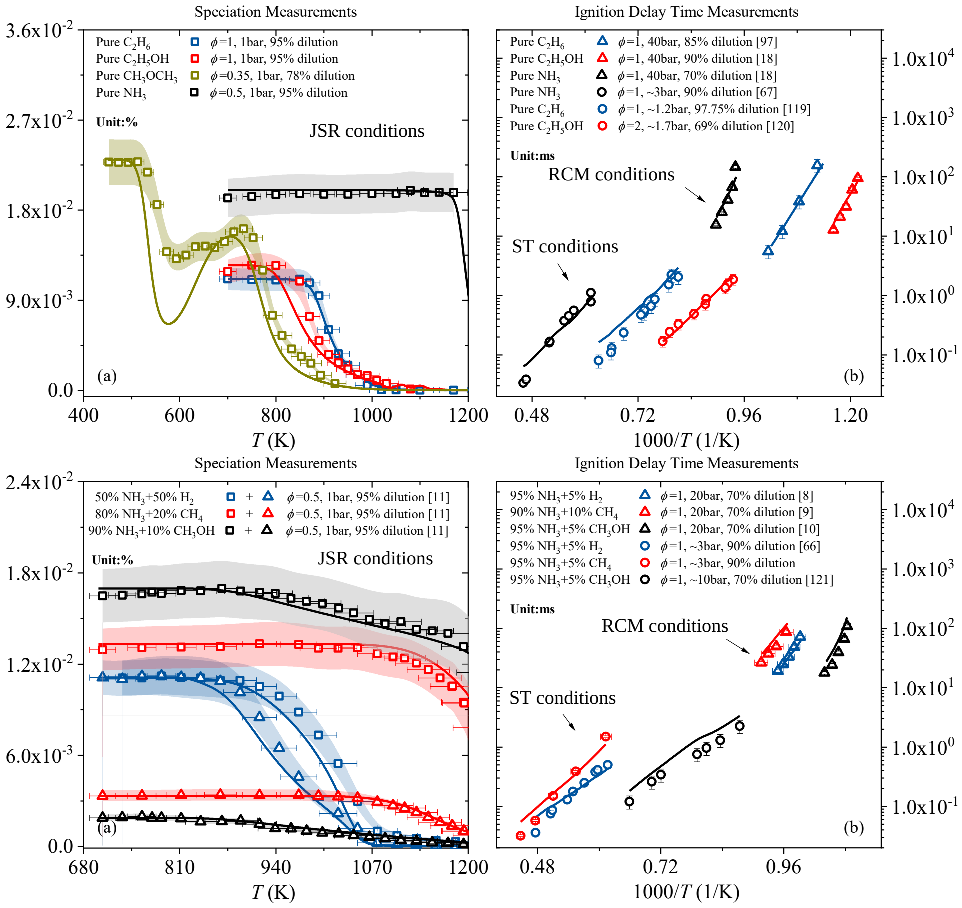

Fig. 3.1. Comparison of the measurements (symbols) and simulations (lines) for a) speciations and b) ignition delay times of pure fuels, c) speciations, and d) ignition delay times of NH_3/C_{0-1} fuel blends. The uncertainties of the IDT (error bars) and mole fraction (shaded area, B-Spline) measurements are indicated on all species. Note that, except for a few cases that have been marked with citations [8–11,18,66,67,97,119–121], *most of the validation data is from the present work.*

3.3 Simulation method

3.3.1 JSR modeling

A perfectly stirred reactor under a fixed temperature and pressure for the JSR simulations was performed by an in-house Cantera code on the Matlab program, which is mainly developed based on Cantera's

Continuously Stirred Tank Reactor (CSTR) template. As shown in Table 3.2, this setup includes five components: inlet mixture, mass flow controller, jet-stirred reactor, pressure control valve, and exhaust gas. Correspondingly, five Cantera functions are used to represent them: two *Reservoirs* to introduce the upstream inlet mixture and downstream exhaust gas, respectively; an *IdealGasReactor* with energy equation disabled to implement a reactor with constant temperature; a *MassFlowController* between the inlet mixture and the reactor to regulates the residence time of the mixture in the reactor; and a Valve between the reactor and the exhaust gas to maintain a constant pressure. The simulated end time for JSR simulation is set to 50 seconds to achieve a steady-state solution.

Table 3.2. The main components of JSR and the corresponding functions of Cantera.

Components of JSR	Functions of Cantera
Inlet mixture	*Reservoir*
Mass flow controller	*MassFlowController*
Jet-stirred reactor	*IdealGasReactor*
Pressure control valve	*Valve*
Exhaust gas	*Reservoir*

3.3.2 RCM modeling

A homogeneous reactor with a constrained volume was established via an in-house Cantera code to perform the RCM simulations. This reactor considers the energy equation to reproduce the temperature and pressure conditions in the adiabatic core of the reaction chamber. The pressure of the core gas varies due to the volume change by the piston movement in the compression phase and the heat loss from the boundary layer to the cylinder wall. Thus, a volume profile was generated using the adiabatic core assumption [122] by applying the pressure trace of a non-reactive mixture under identical conditions of the corresponding reactive mixtures (cf. Figure 2.6) to account for the effects from the compression phase and the heat losses. Furthermore, the present heat loss modeling approach ensures that along with the pressure history, the temperature history of the adiabatic core is also correctly simulated, where the difference between the T_c of the simulation and that of the corresponding experiment is smaller than ~5 K.

Table 3.3 depicts three Cantera functions employed to simulate the main components in the RCM experiments. Unlike an upstream reservoir in the JSR modeling, the initial composition, temperature, and pressure of the inlet mixture are directly defined in the *IdealGasReactor*. A *Wall* function located between the reaction chamber and the outside environment (*Reservoir*) describes the piston movement, which is constrained by the volume profile. For instance, the time derivative of the volume, representing the rate of volume variation, is applied as the speed of the wall. Besides, the simulated end time is limited

https://doi.org/10.7795/110.20241024

by the duration of the volume profile. The simulated IDTs are obtained from the simulated pressure trace applying the same definition as for the experimental measurements.

Table 3.3. The main components of RCM and the corresponding functions of Cantera.

Components of RCM	Functions of Cantera
Reaction chamber	*IdealGasReactor*
Piston	*Wall*
Environment	*Reservoir*

3.3.3 ST modeling

The IDT and speciation simulations for the ST were carried out in a constant volume reactor, constructed using the in-house Cantera code. The reaction region near the end wall (cf. chapter 2.3.1) is still implemented by the function of *IdealGasReactor*, while the *Wall* function is absent between the ambient environment (*Reservoir*) and reaction region due to no volume changes considered here. The details of the main components of ST and the corresponding functions of Cantera are shown in Table 3.4.

Table 3.4. The main components of ST and the corresponding functions of Cantera.

Components of ST	Functions of Cantera
Reaction region	*IdealGasReactor*
Environment	*Reservoir*

However, in the case of dynamic temperature prediction (cf. chapter 2.3.2), a *Wall* function is introduced between the *IdealGasReactor* and environmental *Reservoir* similar to the RCM model. This *Wall* is constrained by using the measured pressure profile as input, allowing the dynamic temperature profile to be calculated from the prediction of mechanisms. Then, the real-time pressure and temperature values for each data point were used to convert the measured absorbance to the concentration of CO, NO, and NH_3. Note that, even if the pressure is constrained, the predicted temperatures may differ when using different mechanisms, and sometimes they may even not align with the reactivity timing [83]. For instance, the moment of temperature sharp rise that also occurs in ignition events does not coincide with the moment of pressure rise. In most cases, our mechanism can accurately predict the reactivity timing. For those rare cases of inconsistency, careful modifications to the dynamic temperatures have been made based on the measured pressures. Besides, such modifications are also considered in the uncertainty analysis.

4. The experimental and kinetic study of NH_3/C_2 fuel blends oxidation at atmospheric pressure and low-to-intermediate temperatures

This chapter will present experimental low-to-intermediate temperatures (450-1180 K) and atmospheric pressure (1 bar) measurements of $NH_3/C_2H_6/O_2/Ar$ mixtures in chapter 4.2, and $NH_3/C_2H_5OH/O_2/Ar$ as well as $NH_3/CH_3OCH_3/O_2/Ar$ mixtures in chapter 4.3, which are measured in a jet-stirred reactor (JSR) with a time-of-flight molecular-beam mass spectrometer (MBMS). The mechanism PTB-NH_3/C_2 mech proposed in chapter 3, gives satisfactory predictions for all species measured in the current work. Comprehensive kinetic analyses are then conducted to investigate the effect of ethane, ethanol, and DME addition on NH_3 oxidation. Part of the results are already published in ref. [13].

4.1 Introduction and Motivation

In previous studies, several additives including C_0 (H_2) and C_1 (CH_4, CH_3OH) fuels co-fired with NH_3 were investigated, and a combustion database covering various conditions of ammonia fuel blends was developed accordingly [8–11]. However, there is still a gap in research on ammonia blended with C_2 fuels, such as ethane (C_2H_6), the most basic alkane. Since ethane is the main non-methane compound in natural gas and has been utilized as a mature fuel for combustion engines and energy supply [123,124], the combination of ammonia with ethane is also a feasible option for developing alternative energy solutions. On the other hand, oxidation and pyrolysis of C_2H_6 play an important role in the hierarchy of hydrocarbon fuel reaction mechanisms [125,126]. Therefore, it is necessary to complement and enrich the database of studies on NH_3/C_2H_6 blends, which is critical to developing and validating the chemical kinetic models for nitrogen/ammonia/hydrocarbon oxidation. To the authors' best knowledge, there are only a few theoretical computational studies on $NH_2+C_2H_6$ cross-reactions, an experimental work about NO_x production from ammonia/ethane mixtures in the thermally stabilized burner, as well as an IDT study for NH_3 with natural gas (2 cases with ethane) in ST conditions are currently available in the literature [15,103,127]. Therefore, more global validation targets (cf. IDT studies in chapters 5 and 6), and specifically, the speciation measurements of NH_3/C_2H_6 mixtures are extremely valuable and urgently needed for the model development and ammonia practical application.

In addition, ethanol (C_2H_5OH) and dimethyl ether (DME, CH_3OCH_3) are also chosen as ammonia fuel promoters due to their importance as alternative fuels with potential applications in sustainable energy systems. Ethanol is widely used in internal combustion engines and has a well-established production infrastructure, while DME is a promising diesel fuel substitute with clean combustion characteristics. Both fuels are of great interest in the field of renewable energy and emissions reduction. Therefore, this study is also concerned with the influence of the two isomeric fuels C_2H_5OH and CH_3OCH_3 on ammonia oxidation in a temperature range between 450 K to 1180 K at 1 bar. Despite their identical chemical molecular formula, these two promoters have significantly different properties in terms of their combustion chemistry which has made them interesting for kinetic studies as a mixture component to NH_3 [17–19,23,28,29,128,129]. However, in most of these studies, the chemical influence on ammonia of the respected promoters is only interpreted and discussed individually and not compared with each other and only a few studies provide detailed experimental speciation data.

In this work, temperature-dependent mole fraction profiles of $NH_3/C_2H_6/O_2/Ar$, $NH_3/C_2H_5OH/O_2/Ar$, and $NH_3/CH_3OCH_3/O_2/Ar$ mixtures are experimentally measured in a jet-stirred reactor (JSR) which is coupled to a molecular-beam mass spectrometer allowing the detection of many species involved in the oxidation reactions. The speciation measurements are undertaken at atmospheric pressure (1 bar) and low-to-intermediate temperatures (700 - 1180 K for ethane cases and 450 - 1180 K for ethanol/DME cases). The developed mechanism PTB-NH_3/C_2 mech proposed in chapter 3, gives satisfactory predictions for all species measured in the current work. Detailed kinetic analysis is performed to analyze and compare the effect of ethane, ethanol, and DME addition on NH_3 oxidation. Attention is also paid to the intersystem-crossing chemistry of species originating from the ammonia and the alkane/alcohol/ether sub-chemistry. The chemical insights presented here will support the development of future models for ammonia/promoter fuels combustion and help to a more detailed understanding of their chemical interactions.

4.2 NH_3/C_2H_6 fuel blends

4.2.1 Experimental results and mechanism validation

Figure 4.1 illustrates the mole fractions of species during the oxidation of NH_3/C_2H_6 stoichiometric mixtures with various C_2H_6 mole fractions under JSR conditions. For better comparisons, the CH_3CHO mole fractions in Figure 4.1l are multiplied by a factor of 20. As shown in Figure 4.1a, the temperature window of NH_3 consumption decreases as the C_2H_6 content increases. Specifically, the NH_3 in the mixture with 50% C_2H_6 begins to be consumed at ~850 K, but is not rapidly until the temperature reaches ~1020 K, and then mainly consumed at 1070 K. This phenomenon can be concluded as a two-stage (two-regime) oxidation that the first happens between ~850 - ~1020 K, and the second stage is over ~1020 K. To better characterize the two-stage oxidation, Figure 4.2 provides the conversion rates of NH_3 at different temperatures. As shown in Figure 4.2a, NH_3 is also consumed by two-stage oxidation in mixtures with other different C_2H_6 mole fractions, e.g., in the case of 20% C_2H_6 (first stage: above ~930 K ~1070 K, and second stage: above ~1070 K), and for 10% C_2H_6 (first stage: ~950 - ~1100 K, and second stage: above ~1100 K). Similar findings of two-stage oxidation have been investigated in our IDT studies of NH_3/CH_3OH [10], indicating that the fuel-promoting participant is oxidized at constant low temperatures to generate a pool of reactive O/H radical, leading to the radical-initiated NH_3 consumption (first stage). When the temperature rises high enough to the second stage, a temperature-initiated NH_3 consumption occurs.

https://doi.org/10.7795/110.20241024

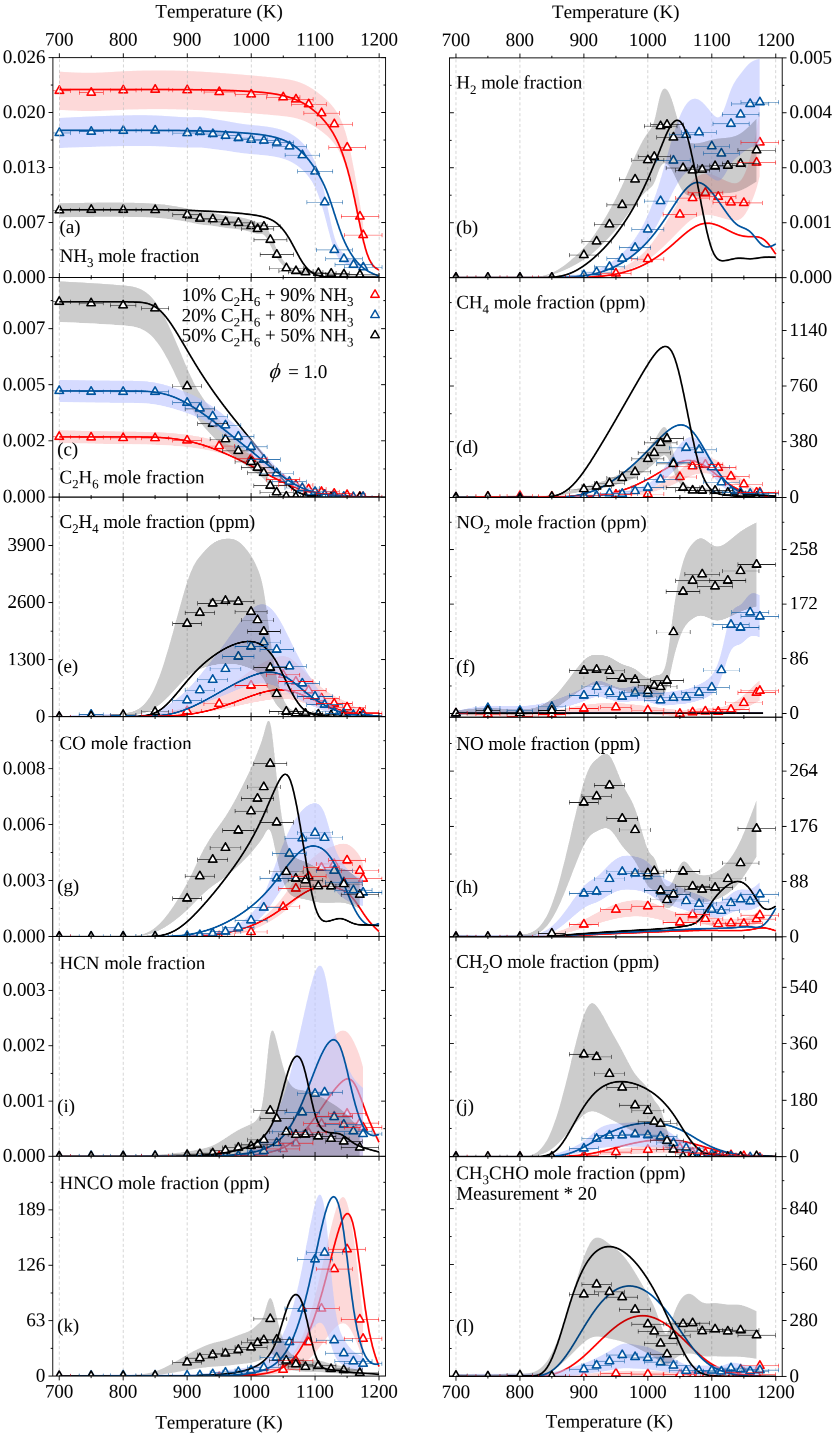

Fig. 4.1. Comparison of the measured (symbols) and simulated (lines) speciation profiles for a) NH_3, b) H_2, c) C_2H_6, d) CH_4, e) C_2H_4, f) NO_2, g) CO, h) NO, i) HCN, j) CH_2O, k) HNCO, l) CH_3CHO at P_{JSR} = 1 bar, ϕ = 1.0, and different C_2H_6 mole fractions in fuel. The error bars of T_{JSR} (horizontal) and mole fraction (shaded area, B-Spline) are indicated on all species.

Notably, the mole fractions of C_2H_6 and its corresponding carbon intermediates do not exhibit such two-stage oxidation. Figure 4.1c and Figure 4.3a exhibit that C_2H_6 is consumed at the same onset temperature (~850 K) with varying ethane content, with most of the consumption (~83%) occurring at the same time as the first stage of NH$_3$ oxidation. In addition, it is more evident from the adjusted conversion of C$_2$H$_6$ (cf. Figure A4.1 in the Appendix) that the first stage of NH$_3$ under different conditions always occurs after a small amount of C$_2$H$_6$ is consumed. For example, a certain percentage of C$_2$H$_6$ (~2 - 4%) of the whole fuel is oxidized, providing sufficient reactive O/H radicals to initiate the first stage of NH$_3$ consumption. Besides, the higher C$_2$H$_6$ content in the mixture, the more carbon and hydrogen atoms are introduced into the overall system, leading to the higher peak mole fractions of the intermediates H$_2$, C$_2$H$_4$, CH$_4$, NO$_2$, CO, NO, HCN, CH$_2$O, and CH$_3$CHO (cf. Figures 4.1b, 4.1d-4.1j, and 4.1l), except for HNCO (cf. Figure 4.1k). Furthermore, higher C$_2$H$_6$ mole fraction will also shift the peak positions to lower temperatures, which is consistent with the pattern observed in the measured NH$_3$ profiles. The NO and NO$_2$, especially in the mixture with 50% C$_2$H$_6$ are formed in two stages as shown in Figures 4.1f/4.1h. The first formation occurs during the first stage of NH$_3$ consumption, and the second formation initiates at relatively high temperatures (mainly above 1050 K) coinciding with the high-temperature consumption of NH$_3$. Similar NO formation was observed by Tang et al. [130] and He et al. [11] in JSR ammonia measurements as well as by Zhu et al. [66] in a flow reactor measurement, and all their models cannot predict it. Furthermore, two nitrogenous intermediates, HNCO (isocyanic acid) and HCN (hydrogen cyanide) tend to form more rapidly in the second stage, which is considered (discussed in chapter 4.2.2) to be an important pathway for the NH$_3$ oxidation under JSR conditions. Note that at 50% C$_2$H$_6$ in the fuel, the mole fraction of HNCO increases significantly in the first stage.

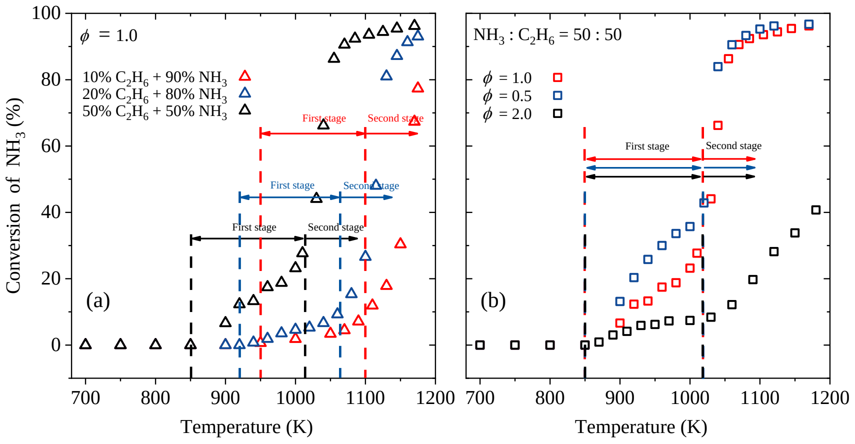

Fig. 4.2. Conversion ratio of NH$_3$ for (a) different C$_2$H$_6$ mole fractions in fuel, at P_{JSR} = 1 bar, ϕ = 1.0; and (b) different equivalence ratio (ϕ), at P_{JSR} = 1 bar, with 50% C$_2$H$_6$ in fuel.

Figure 4.4 compares the respective oxidation species for mixtures with 50% C$_2$H$_6$ in fuel at different equivalence ratios. It can be seen that all measured NH$_3$ profiles (cf. Figures 4.4a and 4.4b) with different ϕ show similar two-stage consumption. For instance, the temperature interval for the two-stage oxidation remains the same for different equivalence ratios. Specifically, the onset of the first stage of NH$_3$ consumption is always around 850 K, and then the second stage of consumption begins at around 1020 K. However, unlike the complete ammonia consumption under fuel-lean and stoichiometric conditions, almost 60% of ammonia under fuel-rich conditions cannot be consumed at the highest temperature of the system (1180 K). Since C_2H_6 is more reactive than NH_3, C_2H_6 can even capture enough oxygen under fuel-rich conditions to carry out the reaction, therefore, as shown in Figures 4.4c and 4.3b, most C_2H_6 can be depleted below ~1100 K.

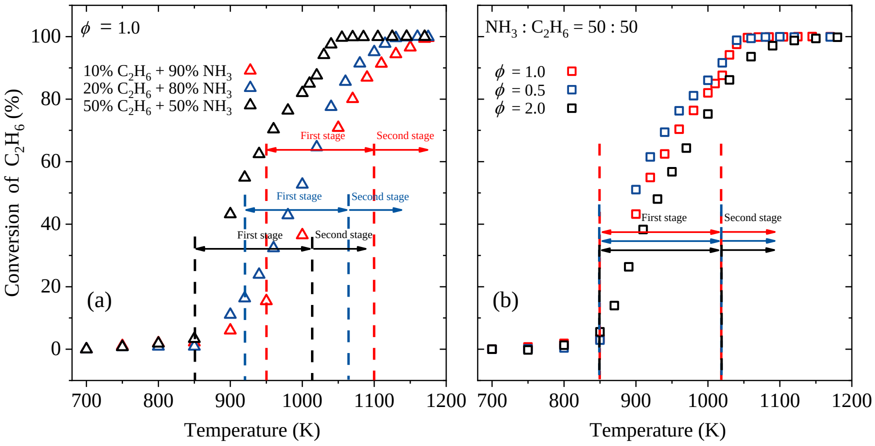

Fig. 4.3. Conversion ratio of C_2H_6 for (a) different C_2H_6 mole fractions in fuel, at P_{JSR} = 1 bar, ϕ = 1.0; and (b) different equivalence ratio (ϕ), at P_{JSR} = 1 bar, with 50% C_2H_6 in fuel.

Along with the NH_3 and C_2H_6 consumption, H_2, CO, CH_4, and C_2H_4 (cf. Figures 4.4b, 4.4d-4.4e, and 4.4g) begin to form at ~850 K and reach the peak mole fractions by ~1050 K. For the mixrues at fuel-lean and stoichiometric conditions (ϕ = 0.5, 1.0), most of the intermediate are readily consumed, whereas at high equivalence ratio (ϕ = 2.0), more intermediates are produced, which compete with NH_3 for oxygen, resulting in a less pronounced depletion of NH_3 in the second stage (~1020 K). Figures 4.4i and 4.4k show that the peak mole fractions of the oxygenated intermediates i.e., CH_2O and CH_3CHO, decrease with lower equivalence ratios, and both aldehydes are completely consumed at ~1080 K. Besides, no significant correlation between NO mole fractions and equivalence ratios has been found in the first formation stage (cf. Figure 4.4h). A possible reason for this is that the heterogeneous reactions of NH_3 with the reactor wall lead to the first formation of NO, which can not be reproduced by the respective models [11,66,130]. But for the second formation stage at higher temperatures, the mole fraction of NO decreases with increasing equivalence ratio. More specifically, at ϕ = 0.5 and 1.0, a large amount of NO is formed at higher C_2H_6 mole fractions and only a minor NO formation appears at ϕ = 2.0. The reason may be that with enough oxygen in the reaction system (ϕ = 0.5 and 1.0), the formation of NO is favored at relatively high temperatures, while under fuel-rich conditions NO acts as an oxidizer. Similar phenomena were found in both stages of NO_2 formation, suggesting a potential correlation between NO and NO_2 formation, which will be discussed in chapter 4.2.3. The patterns of the hydrocarbon-nitrogen species mole fraction, like HCN and HNCO under different ϕ conditions are similar to those under different C_2H_6 contents, where these species are formed faster in the second stage of NH_3 consumption.

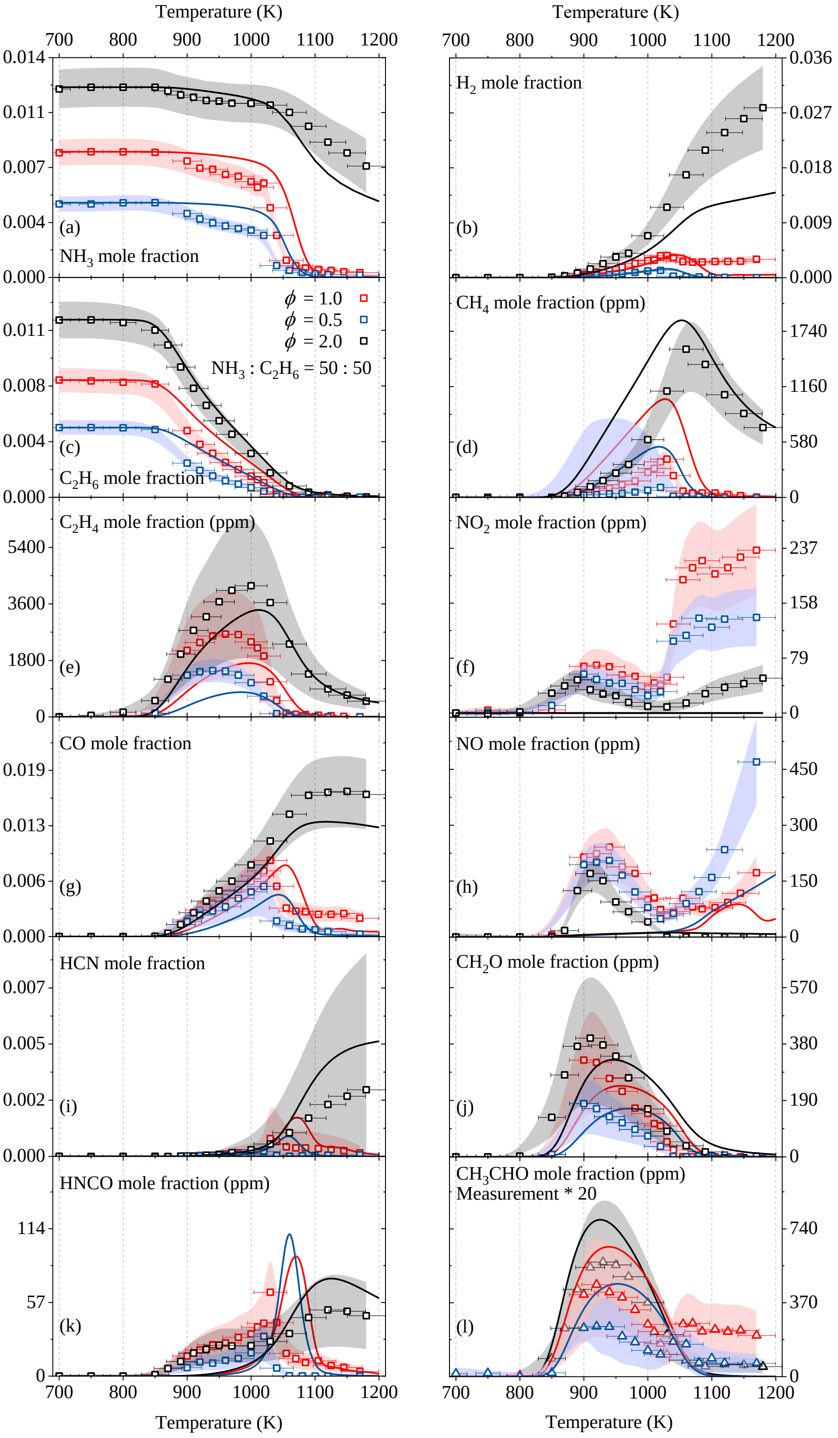

Fig. 4.4. Comparison of the measured (symbols) and simulated (lines) speciation profiles for a) NH_3, b) H_2, c) C_2H_6, d) CH_4, e) C_2H_4, f) NO_2, g) CO, h) NO, i) HCN, j) CH_2O, k) HNCO, l) CH_3CHO at P_{JSR} = 1 bar, with 50% C_2H_6 in fuel, and different equivalence ratios (ϕ). The error bars of T_{JSR} (horizontal) and mole fraction (shade area, B-Spline) are indicated on all species.

Figures 4.1 and 4.4 show the comparisons between the experimental and simulated mole fractions of the species in JSR conditions. Overall, the model can capture the two-stage NH_3 oxidation for all mixtures with varying C_2H_6 contents (cf. Figure 4.1a) and equivalence ratios (cf. Figure 4.4a). However, for the mixture with 50% C_2H_6 under fuel-lean and stoichiometric conditions (cf. Figure 4.4a), it underpredicts the ammonia consumption in the first stage. A similar underestimation can be found for C_2H_6, which might result in a smaller predicted radical pool and thus slow down the NH_3 oxidation, leading to the observed deviations in the NH_3 simulations. The model reproduces the H_2 measurements in the initial formation stage (cf. Figures 4.1b and 4.4b) but starts to underestimate its mole fraction from 1050 K, which is more pronounced under fuel-rich conditions. Similar results are obtained for the formation of CO (cf. Figures 4.1g and 4.4g), i.e., the model underpredicts CO mole fraction as temperature increases. For CH_4 and C_2H_4 mole fractions (cf. Figures 4.1d-e and 4.4d-e), the simulations accurately characterize the temperatures at peak mole fractions but overestimate the peak values of C_2H_4 and overestimate those of CH_4, especially in the fuel mixture with 50% C_2H_6. According to the reaction pathway analysis (presented in chapter 4.2.2), it indicates that there are two primary paths for the oxidation of C_2H_6: $C_2H_6 \rightarrow C_2H_5 \rightarrow CH_3CHOH \rightarrow CH_3CHO \rightarrow CH_3CO \rightarrow CO(CH_3) \rightarrow CO_2$, and $C_2H_6 \rightarrow C_2H_5 \rightarrow C_2H_4 \rightarrow CH_2O \rightarrow HCO \rightarrow CO \rightarrow CO_2$. The deviations between experiments and simulations for C_2H_4 as well as CH_4 suggest that the model exaggerates the fraction of $C_2H_5 \rightarrow CH_3CHOH$ pathway and underestimates the path to C_2H_4, leading to more CH_3 and less C_2H_4, which is the primary source of CH_4. For the same reason, the simulated peak values of CH_2O and CH_3CHO (cf. Figures 4.1j/l and 4.4j/l) are about five times lower and twenty times higher than the measured results, respectively. Additionally, as seen in Figures 4.1f/h and 4.4f/h, the model does not adequately reproduce the formation of NO_2 and NO, which could be the result of a shortcoming in the NO_x-hydrocarbon sub-mechanism (cf. chapter 4.2.2). According to the modeling results, the production trajectories of two nitrogenous intermediates HCN and HNCO (cf. Figures 4.1i/k and 4.4i/k) are in agreement with the measured data, while their amounts are not accurately predicted. This discrepancy may be due to an overestimation of the CH_3 formation, which makes the reaction $CH_3+NH_2=CH_3NH_2$ (and consequently, $CH_3NH_2 \rightarrow CH_2NH_2 \rightarrow CH_2NH \rightarrow H_2CN \rightarrow HCN$) more pronounced.

4.2.2 Kinetic analysis

Figure 4.5a shows the sensitivity analysis (SA) for x_{NH3} at 1060 K, 1 bar, and $\phi = 1.0$, including the fifteen most sensitive elementary reactions for different C_2H_6 contents to interpret the ongoing chemistry from different measurements. Regarding the sensitivity analysis for JSR measurements at atmospheric pressure, a broad range of C_2H_6 contents in fuel are selected, including 0% (pure ammonia), 1%, 10%, and 50%. It should be noted that the mechanism works effectively under all conditions and that it is expected that the mechanism will be able to replicate the JSR measurements in the case of a low (1%) C_2H_6 level. As shown in Figure 4.5a, low ethane content in the mixture significantly leads to more sensitive reactions to consume NH_3, not only the interaction of $NH_2+C_2H_6$ but also those related to $NH_2+C_2H_4/CH_3$, $H+O_2$, and HCO, which are absent from pure ammonia oxidation at JSR conditions. On the other hand, the H radical takes the place of HO_2 (cf. Figure 4.6b for an example of the RCM condition) as the primary source of OH in the NH_3 oxidation process at JSR conditions. This is

https://doi.org/10.7795/110.20241024

demonstrated by the fact that the channel of HO_2 production from H becomes an inhibiting reaction, whereas the reaction $H+O_2=O+OH$ exhibits the most enhancing effects. The reactions of H ($H+O_2=O+OH$) and NH_3 ($NH_3+O_2=NH_2+HO_2$) remain the most promoting and inhibiting reactions for NH_3 consumption in the mixture containing 10% C_2H_6, respectively.

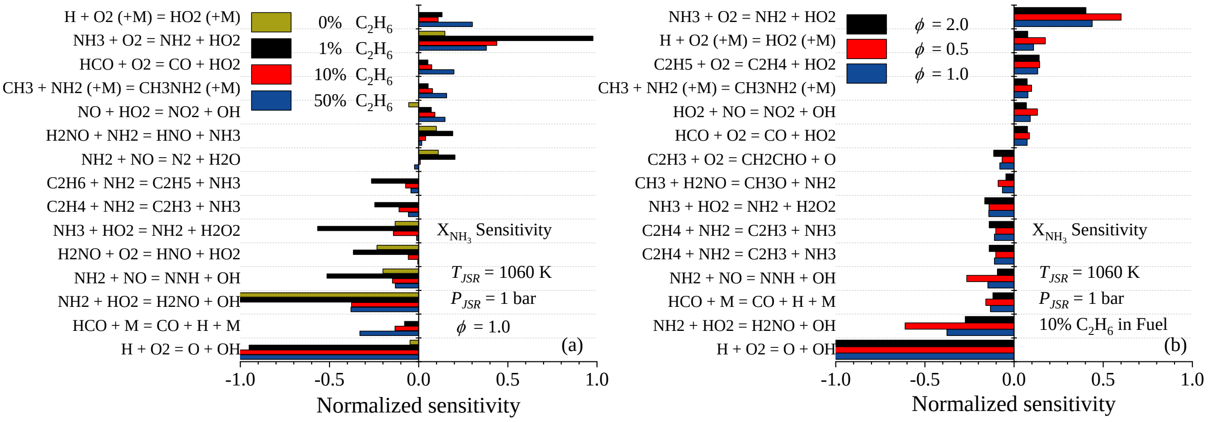

Fig. 4.5. Sensitivity analysis of NH_3 mole fraction at 1060 K and 1 bar a) for the stoichiometric mixture with different C_2H_6 fractions b) for the mixture with 10% C_2H_6 fractions under different equivalence ratios (ϕ). The negative value indicates promotion of the NH_3 consumption while a positive value implies the inhibiting effect.

In addition, the two reaction channels of NH_2+NO and the chain-branching reaction of $H_2NO+O_2=HNO+HO_2$ show less influence on NH_3 oxidation. Instead, the reactions related to HCO and CH_3 exhibit higher sensitivities since more HCO and CH_3 have been transformed from ethane at 1060 K in the mixture with higher C_2H_6 contents. When the proportion of C_2H_6 in the mixture is increased to 50%, the chemistry of C_2H_6 becomes dominant in the oxidation of NH_3. For instance, the oxidation as well as decomposition of HCO are one of the most promoting and inhibiting reactions, respectively. Furthermore, the chain-terminating channel $CH_3+NH_2(+M)=CH_3NH_2(+M)$ exhibits a more inhibitory influence. Along with the reactions related to C_2H_6, more H radicals are generated in the radical pool. These radicals subsequently react with O_2, initiating the most dominant branching reactions ($H+O_2(+M)=HO_2(+M)$ and $H+O_2=O+OH$). Regardless of the C_2H_6 mole fraction in the fuel, the reactions of $NH_2+HO_2=H_2NO+OH$ and its reversed reaction of $NH_3+O_2=NH_2+HO_2$ play a crucial role in the ammonia oxidation process. Consequently, the branching ratio of these two channels is important for the final simulation results. To assess the effect of equivalence ratios (ϕ) on the chemistry, a sensitivity analysis for x_{NH3} in the mixture with 10% C_2H_6 is performed at various ϕ ranging from 0.5 to 2.0. As depicted in Figure 4.5b, the sensitivity analysis of x_{NH3} demonstrates no obvious differences across the various ϕ.

All measurements and simulations of NH_3 mole fraction in NH_3/C_2H_6 mixtures display a two-stage NH_3 consumption characteristic within the investigated temperature range. To comprehensively understand the underlying chemical reason, the sensitivity of important reactions as a function of temperature is conducted (cf. Figure 4.6). This analysis includes the sensitivity of x_{NH3} and IDT to compare the sensitive reactions of different processes (NH_3 consumption in the JSR and ignition delay time in the RCM) within their respective temperature windows. As previously mentioned, in the mixture with 10% C_2H_6, NH_3 consumption can be roughly divided into two stages, with the first stage occurring between ~950 and ~1100 K, and the second stage appearing above ~1100 K. Figure 4.6a illustrates that reactions related to HO_2 dominate at temperatures below 950 K. On one hand, the reaction of HO_2+NH_2 directly forms more OH radicals. On the other hand, HO_2 abstracts the H-atom from C_2H_6 and NH_3 to generate H_2O_2, and its subsequent decomposition into two OH radicals enhances the reactive radical pool as well. However, it is not sufficient to initiate NH_3 oxidation until the chain-branching reaction of $H+O_2=OH+O$ becomes dominant, with its sensitivity at 950 K increased by ~110% compared to that at 900 K. This is because the reaction between H and O_2 generates a great level of reactive radicals, triggering the early radical-initiated NH_3 consumption in the first stage. With increasing temperature, the effect of HO_2-related reactions exhibits less significant, particularly evident for the reactions $NH_2+HO_2=H_2NO+OH$ and $NH_3+O_2=NH_2+HO_2$, whose sensitivities decrease over ~62.3% and ~61.3% at 1100 K compared to 950 K, respectively. As the temperature of 1100 K, the high temperature enhances molecules collision frequency, i.e. increases the energy of the system, to overcome the activation energy barrier (E_a) of the most reactions related to NH_3, leading to rapid temperature-initiated NH_3 consumption in the second stage. Between 1100 K and 1180 K, the majority of NH_3 is consumed, and the reaction of $H+O_2(+M)=HO_2(+M)$ becomes the most inhibiting reaction as it suppresses the chain-branching reaction of $H+O_2=O+OH$.

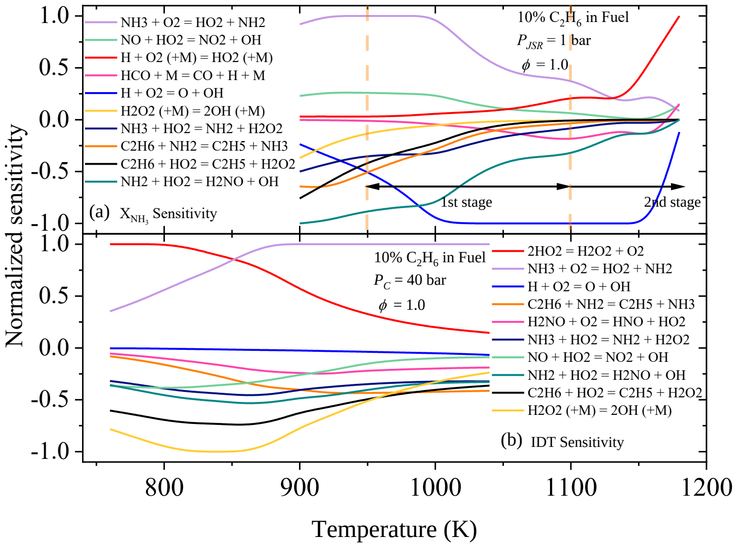

Fig. 4.6. Sensitivity analysis of a) NH_3 mole fraction at the JSR condition and b) IDT at the RCM condition for the mixture with 10% C_2H_6 fractions under different temperatures. The negative value indicates the promotion of the ignition or x_{NH3} consumption while a positive value implies an inhibiting effect.

The temperature-dependent sensitivity analysis for the IDTs (cf. Figure 4.6b) reveals that the reactions related to HO_2 dominate the auto-ignition process across the entire temperature range. Conversely, the reaction of $H+O_2$ demonstrates no influence on this process, suggesting that for the NH_3/C_2H_6 mixture, HO_2 and H radicals govern the characteristic of the NH_3 consumption process in the JSR and the auto-ignition process in the RCM via generating OH radicals, respectively. This is further supported by the sensitivity analysis of the OH radical at two different conditions (RCM: 40 bar and 960 K; JSR: 1 bar and 1060 K) in Figure A4.2 in the Appendix. As seen in Figure 4.6, C_2H_6-related reactions participate in ammonia oxidation over a broad temperature range in both RCM and JSR conditions. This chemical behavior demonstrates that the ethane additive leads to a more reactive ammonia fuel mixture.

Figure 4.7 presents the reaction pathway analysis for the stoichiometric mixture with 10% C_2H_6 at JSR conditions (1060 K and 1 bar). The species beside an arrow represent the reaction partners of the species at the arrow's tail, and the percentage number indicates their contribution to the reaction channels. Overall, NH_3 is primarily consumed by OH radicals (81.1%) and O radicals (10.4%), leading to the formation of NH_2 radicals. Most NH_2 radicals prefer to engage in the reactions with other major components and convert back to NH_3 (73.3%). However, a small fraction of NH_2 radicals (17.0%) will undergo further consumption through the pathway of $H_2NO \rightarrow HNO \rightarrow NO \rightarrow N_2$ or the reaction with CH_3 (5.9%), followed by the subsequent reaction pathway of $CH_3NH_2 \rightarrow CH_2NH_2 \rightarrow CH_2NH \rightarrow H_2CN \rightarrow HCN$. More than half of HCN (52.2%) is oxidized by O radicals to form NCO, which will further react with NH_3 or C_2H_6 to generate HNCO. Additionally, HNCO formation partly stems from the reaction of NH_2+CO. These generated HNCO species are either converted back to NCO (88.5%) or eventually transformed into CO_2 (11.5%). It is noteworthy that the reaction pathway through CH_3NH_2 significantly influences the NH_3 consumption process at JSR conditions. Meanwhile, the interaction between NH_2 and C_2H_6 plays an important role in facilitating the oxidation of C_2H_6 (cf. Figures A4.3 and A4.4 in Appendix). Its product C_2H_5 will further undergo two main pathways, i.e., $C_2H_5 \rightarrow C_2H_4 \rightarrow CH_2O \rightarrow HCO \rightarrow CO \rightarrow CO_2$, and $C_2H_5 \rightarrow CH_3CHOH \rightarrow CH_3CHO \rightarrow CH_3CO \rightarrow CO(CH_3) \rightarrow CO_2$. These pathways introduce numerous reactive radicals such as H, HO_2, and OH into the radical pool, triggering the promotion reactions for NH_3 oxidation, such as $H+O_2=O+OH$. As mentioned above, the model overstates the proportion of the second pathway of $C_2H_5 \rightarrow CH_3CHOH$ and underestimates the pathway to C_2H_4. This discrepancy results in less C_2H_4, CH_2O and more CH_4, CH_3CHO in the predicted results compared to the measurement (cf. Figure 4.1). The presence of CH_3CO, originating from the second pathway, leads to an increase in the CH_3 content of the radical pool, which further combines with NH_2, namely the inhibition reaction of $CH_3+NH_2=CH_3NH_2$. This impediment becomes more pronounced with the increasing amount of C_2H_6 in the mixture, which could explain the overestimation of both NH_3 and C_2H_6 mole fractions in the mixture with 50% C_2H_6 content (Figures 4.4a and 4.4c). The analysis of the reaction pathway highlights the significant role of OH radicals in the entire reaction path. Particularly in the initial reaction, nearly 81.8% of NH_3 is consumed by OH radicals, suggesting that more OH radical

https://doi.org/10.7795/110.20241024

yields can boost the consumption of NH_3. This can also be supported by a rate of production (ROP) analysis (cf. Figure A4.3).

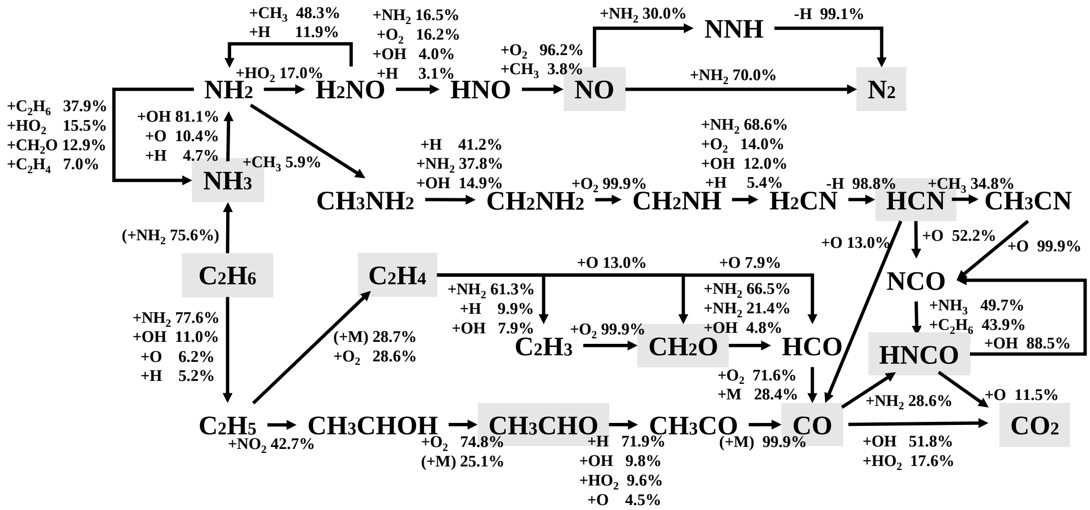

Fig. 4.7. Reaction pathways for the oxidation of the mixture with 10% C_2H_6 fractions at T_{JSR} = 1060 K, P_{JSR} = 1 bar, ϕ = 1.0, and a residence time of 1 s. Numbers indicate the ratio of the rate of a specific reaction to the total consumption rate of a species at the beginning of an arrow. Repeated reactions are shown in the bracket. Species experimentally measured are highlighted in grey.

The ROP analysis reveals that NH_3 is mostly consumed by the reactions of NH_3+O/OH at temperatures exceeding 1070 K. In particular, these consumption rates significantly increase during the second temperature-initiated NH_3 consumption stage, where the elevated temperature provides sufficient energy to overcome the activation energy barriers of these reactions. When the temperature is below 1070 K during the first consumption stage, NH_3 consumption is primarily driven by the reactions of NH_2+OH/O/H/CH_3. This indicates that introducing C_2H_6 not only provides the relevant reactive radicals (e.g., O, H, and OH) but also introduces the interactions between NH_2 and hydrocarbons (e.g., CH_3). Additionally, the ROP of OH and H radicals (cf. Figures A4.5 and A4.6) indicates that C_2H_6-related reactions contribute to a more pronounced radical pool at relatively low temperatures. For instance, the decompositions of C_2H_5, HCO, and CH_3O generate H radical. These H radicals, in turn, contribute to the formation of OH radicals through reactions such as O_2+H=O+OH, and its subsequent reactions of C_2H_6/NH_3+O=C_2H_5/NH_2+OH. (cf. Figure A4.5). The involvement of formed OH radicals in both two NH_3 consumption stages leads to a more reactive ammonia fuel mixture.

4.2.3 NO_x analysis

As depicted in Figures 4.1f/h and 4.4f/h, the mechanism exhibits shortcomings in predicting the mole fraction of both NO and NO_2. Therefore, a rate of production (ROP) analysis is conducted for NO/NO_2 at 940 K (first stage) and 1200 K (second stage), as illustrated in Figure A4.7. Surprisingly, the ROP of

https://doi.org/10.7795/110.20241024

$CH_3CHOH+NO=C_2H_5+NO_2$ (R14) demonstrates a significant impact on NO and NO_2, i.e., R14 predominantly converts NO into NO_2 at both temperatures.

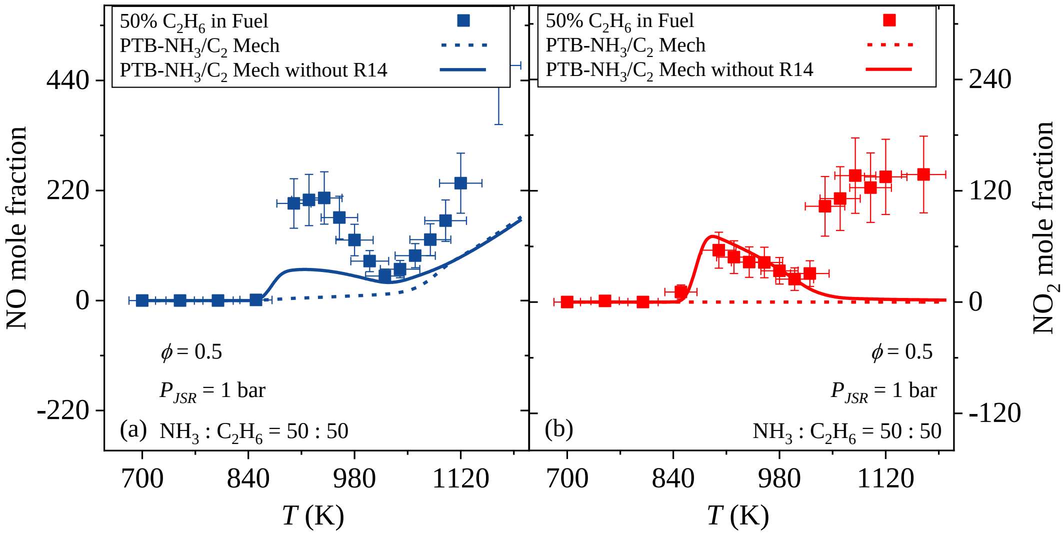

Fig. 4.8. Comparison of the measurements (symbols) and simulations (lines) for a) NO mole fraction profile and b) NO_2 mole fraction profile from JSR. The error bars of the measurements are indicated on all mixtures.

After eliminating R14 from the mechanism, there is an improvement in predicting NO and NO_2 mole fractions (cf. Figure 4.8). Nevertheless, the model is still unable to simulate NO_2 production during the second stage, i.e., at temperatures above 1050 K. A new ROP analysis is performed based on the mechanism without R14, as shown in Figure 4.9. At 940 K, the major formation of NO_2 is attributed to the consumption reaction of NO, specifically, $NO+HO_2=NO_2+OH$ (R18). In the meantime, NO_2 can undergo conversion into HNO_2 and HONO through reduction reactions with C_2H_6/NH_2. Subsequently, both isomers (HNO_2/HONO) decompose to NO. At 1200 K, reaction R18 remains dominant for NO_2 formation, whereas an equivalent amount of NO_2 is consumed through the reaction of $NO_2+H=NO+OH$. This phenomenon could explain the underpredicted concentration of NO_2 in the second stage. Unlike the ROP of NO_2, the significance of reaction R18 at 1200 K exhibits a negligible effect on NO formation. Instead, the reactions $HNO+H=NO+H_2$ and $NH_2+NO=N_2+H_2O$ become more important. In addition, the contribution of $NH_2/NH/N+NO/O_2$ reactions is more pronounced at 1200 K compared to 940 K. It is noted that the prediction of the ignition delay time under RCM conditions becomes worse when R14 is removed, and the reason for this is currently unknown. Therefore, we decided to keep R14 in the mechanism.

4.2.4 Conclusion

The speciation of NH_3/C_2H_6 fuel blends has been measured in this work using a jet-stirred reactor coupled with molecular beam mass spectrometry (JSR-MBMS). The experimental results indicate that the addition of C_2H_6 to NH_3 significantly enhances the reactivity of ammonia oxidation. The newly developed model (PTB-NH_3/C_2 mech) successfully captures the effects of ethane fraction and equivalence ratio on the speciation and demonstrates reasonable accuracy across broad conditions.

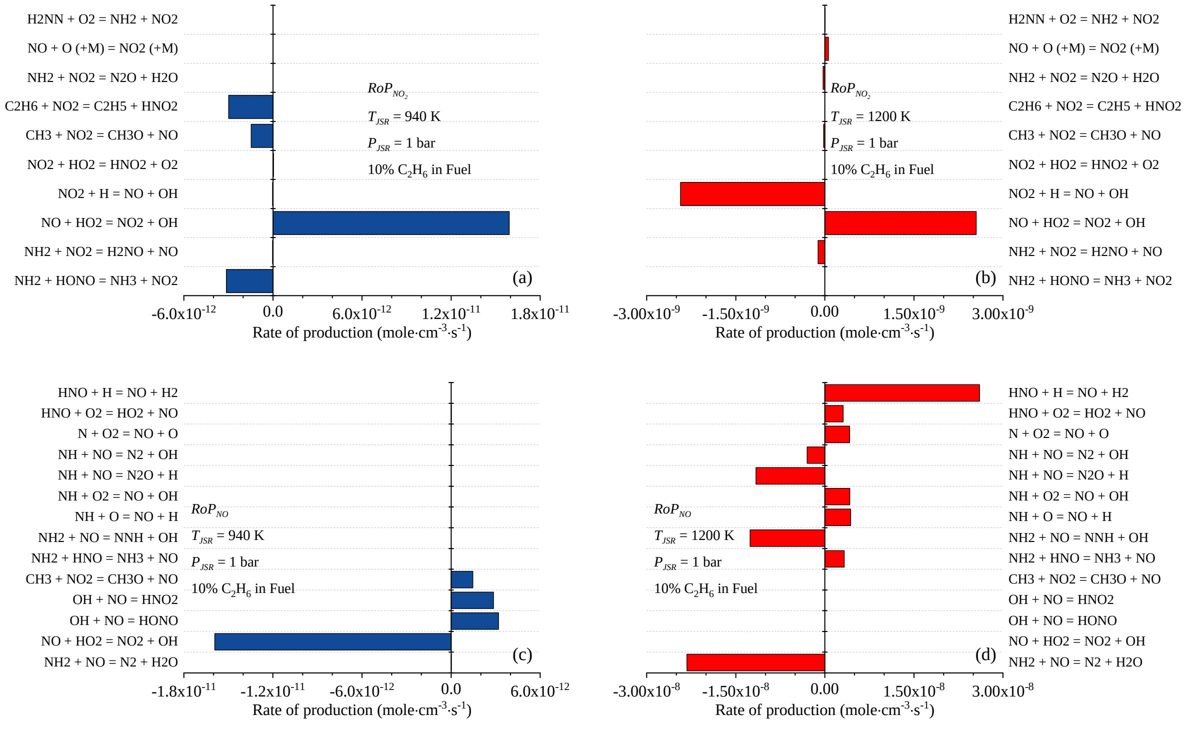

Fig. 4.9. Rate of production analysis for a) NO_2 at 940 K, b) NO_2 at 1200 K, c) NO at 940 K, and c) NO at 1200 K for the stoichiometric mixture with 10% C_2H_6 fraction. The positive value represents the formation of NO_2/NO, and the negative value represents the consumption of NO_2/NO. The ROP is based on the original PTB-NH_3/C_2 mech without R14.

The kinetic analysis shows that at JSR conditions, even a small amount of ethane (1% C_2H_6) in the mixture can increase the number of sensitive reactions for NH_3 oxidation through the intersystem cross-reactions and the involvement of subsequent hydrocarbon species, notably, the direct reactions of NH_2+C_2H_6/CH_3/C_2H_4 as well as the related reaction of HCO. These reactions/species are not present in the pure ammonia oxidation at the same temperature range. At different temperatures, it is observed that under JSR conditions, the chain-branching reaction H+O_2=OH+O generates a significant number of reactive radicals. This process triggers the first stage of radical-initiated NH_3 consumption (e.g., 950 - 1100 K for the 10% C_2H_6). As temperature increases beyond a certain level (e.g., 1100 K for the 10% C_2H_6), the activation energy barrier (E_a) for most NH_3-related reactions is surpassed, resulting in rapid temperature-initiated NH_3 consumption in the second stage. In addition, the reactions related to HO_2 dominate the auto-ignition process (under RCM conditions) across the temperature range, whereas the reaction involving H+O_2 exhibits negligible influence on this process (cf. Figure 4.6). This observation suggests that for the NH_3/C_2H_6 mixtures, H and HO_2 radicals generate OH radicals, which is the dominant radical to consume NH_3 in all the conditions investigated, to determine the characteristic of the NH_3 consumption process in the JSR and the auto-ignition process in the RCM, respectively. The involvement of C_2H_6-related reactions contributes to a more reactive radical pool already at relatively low temperatures through the decompositions of C_2H_5/HCO/CH_3O to provide H radical. These H radicals further form OH radicals via reactions such as O_2+H=O+OH, and its subsequent reactions of C_2H_6/NH_3+O=C_2H_5/NH_2+OH (cf. Figure A4.5). The formed OH participates in both stages of NH_3 oxidation, resulting in a more reactive ammonia fuel mixture.

The analysis of NO_x formation employs a refined mechanism (PTB-NH_3/C_2 mech without the reaction of CH_3CHOH+NO=C_2H_5+NO_2). It was found that at 940 K, the primary formation of NO_2 is attributed to the reaction of NO+HO_2=NO_2+OH (R18). At higher temperatures, such as 1200 K, the reaction R18 remains dominant for NO_2 formation, whereas an equivalent amount of NO_2 is consumed through the reaction of NO_2+H=NO+OH. This may explain the underpredicted concentrations of NO_2 in the second stage. Additionally, the ROP analysis for NO reveals that reactions such as NH_2+NO=N_2+H_2O and HNO+H=NO+H_2 become more significant at elevated temperatures.

4.3 NH_3/C_2H_6O-isomers fuel blends

4.3.1 Experimental results and mechanism validation

Experimental mole fraction profiles of all quantified species for NH_3/C_2H_5OH and NH_3/CH_3OCH_3 mixtures at all investigated conditions are provided in Figures 4.10 and 4.11 (different C_2H_6O fractions) in the main text below and Figures A4.8 and A4.9 (different equivalence ratios) in the Appendix.

It becomes obvious that the addition of the two isomeric fuels affects ammonia oxidation differently. Specifically, three oxidation regimes (named hereafter as 1st, 2nd, and 3rd oxidation regimes), as well as an NTC behavior, can be observed for DME addition, but only two consumption stages (2nd and 3rd oxidation regimes) occur for the case of ethanol, which is similar to ethane case. This phenomenon will be discussed and analyzed in detail in chapter 4.3.2 whereas this chapter focuses on general observations. Generally, Figure 4.10 reveals that as the C_2H_5OH content in the mixture increases, NH_3 is completely consumed at lower temperatures under the investigated conditions, while the majority of C_2H_5OH is still consumed within the same temperature interval (800 - 1100 K). This suggests that the (less reactive) ammonia does not influence the (more reactive) ethanol oxidation. With higher C_2H_5OH content, more carbon and hydrogen atoms are introduced into the system, leading to higher peak mole fractions of the intermediate species (H_2, C_2H_4, CH_4, CO, CH_2O, and CH_3CHO), except for species that result from an intersystem-crossing N–C chemistry, i.e., HCN and HNCO (cf. Figures 4.10i and 4.10k). These nitrogenous intermediates form rapidly at temperatures above 1000 K, and their formation shows no correlation with the mole fraction of C_2H_5OH. Besides, both HCN and HNCO were already identified as crucial intermediates for NH_3 oxidation under JSR conditions in our previous NH_3/C_2H_6 study [13]. Notably, NO_2 and NO levels are also elevated, which is due to the introduction of a more active radical pool by C_2H_5OH, facilitating the conversion of NH_3 to NO_x. Furthermore, all peak positions of

https://doi.org/10.7795/110.20241024

intermediate species shift to lower temperatures with higher initial C_2H_5OH content consistent with the observed NH_3 profiles.

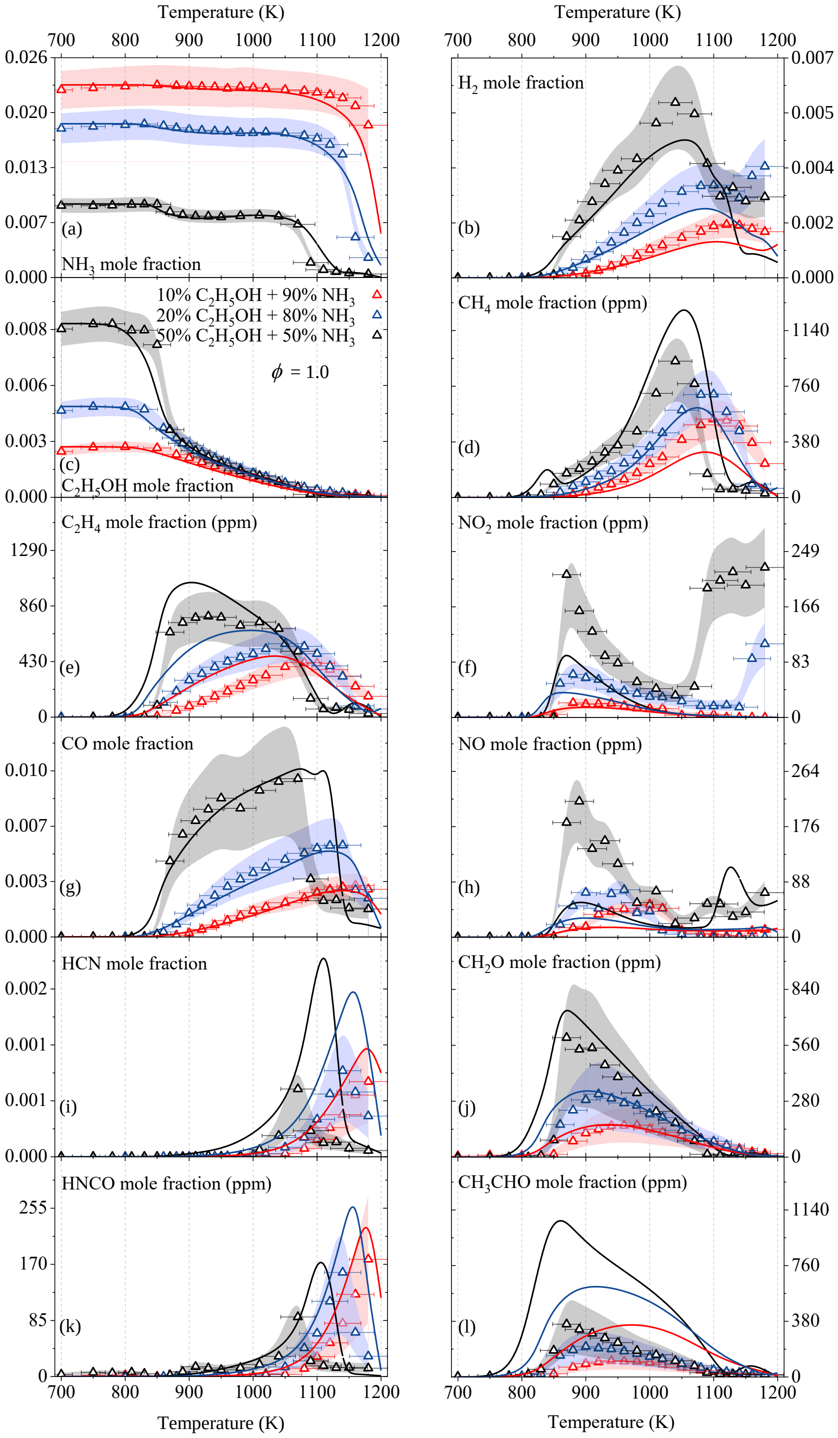

Fig. 4.10. Comparison of the measured (symbols) and simulated (lines) mole fraction profiles of a) NH_3, b) H_2, c) C_2H_5OH, d) CH_4, e) C_2H_4, f) NO_2, g) CO, h) NO, i) HCN, j) CH_2O, k) HNCO, l) CH_3CHO at P_{JSR} = 1 bar, $\phi = 1.0$, and different C_2H_5OH mole fractions in fuel. The error bars of T_{JSR} (horizontal) and mole fraction (shaded area, B-Spline) are indicated on all species.

https://doi.org/10.7795/110.20241024

In Figure A4.8, the speciation data from the mixture with 50% C_2H_5OH in the fuel is shown for different equivalence ratios. All the measured NH_3 profiles with different ϕ reveal a similar two-stage consumption model. Regardless of the equivalence ratios, consistent temperature windows are observed for the onset and rapid consumption of ammonia,i.e., NH_3 consumption begins around 850 K, followed by rapid consumption starting from the temperature of around 1050 K. Note that more than half of the ammonia at the fuel-rich conditions ($\phi = 2.0$) remain unconsumed at the highest measured temperature (1180 K), while most of the C_2H_5OH is depleted already below ~1100 K even under fuel-rich conditions. This phenomenon is attributed to the higher reactivity of C_2H_5OH, allowing it to capture sufficient oxygen and support its consumption. The intermediates C_2H_4, CH_4, CO, CH_2O, and CH_3CHO generated by promoter-fuel chemistry begin to form and reach their peak mole fractions before the rapid consumption of NH_3. For the fuel-lean and stoichiometric conditions ($\phi = 0.5$, 1.0), most intermediate species are fully consumed within the measured temperature range whereas at $\phi = 2.0$, these intermediates must compete with NH_3 or among themselves for oxygen, leading to the presence of unconsumed CH_4, C_2H_4, and CO. Since a portion of H_2 is derived from the consumption of NH_3 and these intermediates, the H_2 concentration continues to rise in the fuel-rich condition. The NO/NO_2 mole fractions formed from the mixtures with different equivalence ratios almost overlap at around 900 K, while at temperatures higher than 1050 K, the NO and NO_2 formation exhibits different trends depending on the equivalence ratios. In particular, at $\phi = 0.5$ and $\phi = 1.0$, a considerable amount of NO is formed, exhibiting higher mole fractions under fuel-lean conditions, with only a minor amount formed at $\phi = 2.0$. The mole fraction patterns of the nitrogenated hydrocarbon species HCN and HNCO under different ϕ resemble those under different C_2H_5OH contents, i.e., they are formed more pronounced as the temperature is higher than 1000 K.

Figure 4.11 illustrates the species mole fractions during the oxidation of NH_3/CH_3OCH_3 stoichiometric mixtures with varying CH_3OCH_3 mole fractions in the JSR. It should be noted that CH_2O_2 and $C_2H_4O_2$ are crucial intermediates (cf. chapter 4.3.2.1) in the DME oxidation process. In contrast, C_2H_4 and CH_3CHO are less pronounced in the mass spectra as they are not typical intermediates from DME oxidation. Therefore, C_2H_4/CH_3CHO, which are shown in the ethanol case, are replaced by $CH_2O_2/C_2H_4O_2$ in the DME case, as depicted in Figures 4.11i and 4.11k. To obtain a better comparison, the measurements of $C_2H_4O_2$ in Figure 4.11k are multiplied by a factor of 5.

As shown in Figure 4.11a, NH_3 can be completely consumed at lower temperatures as the molar fraction of DME increases. Meanwhile, most of the DME is consumed between 850 K and 1100 K and shows a poor correlation with ammonia concentration. Besides, the variations in peak mole fraction of the intermediate species (cf. H_2, CH_4, NO_2, CO, NO, CH_2O, HCN, and HNCO in Figure 4.11) and their peak position for different DME contents follow the same pattern as observed in the NH_3/C_2H_5OH mixtures. The study of Moshammer et al. [131,132] concluded that the formation of $C_2H_4O_2$ and CH_2O_2 both indicate the involvement of typical DME low-temperature oxidation pathways. In the present work (cf. Figure 4.11k), the $C_2H_4O_2$ formation appears at both 600 K and 900 K. In contrast, CH_2O_2 (formic acid) peaks only in the low-temperature oxidation regime (at 600 K), giving evidence that the 2nd O_2-addition of the DME chemistry is involved in the overall chemistry of the fuel mixture [131,132]. Further details will be discussed in chapter 4.3.2.1.

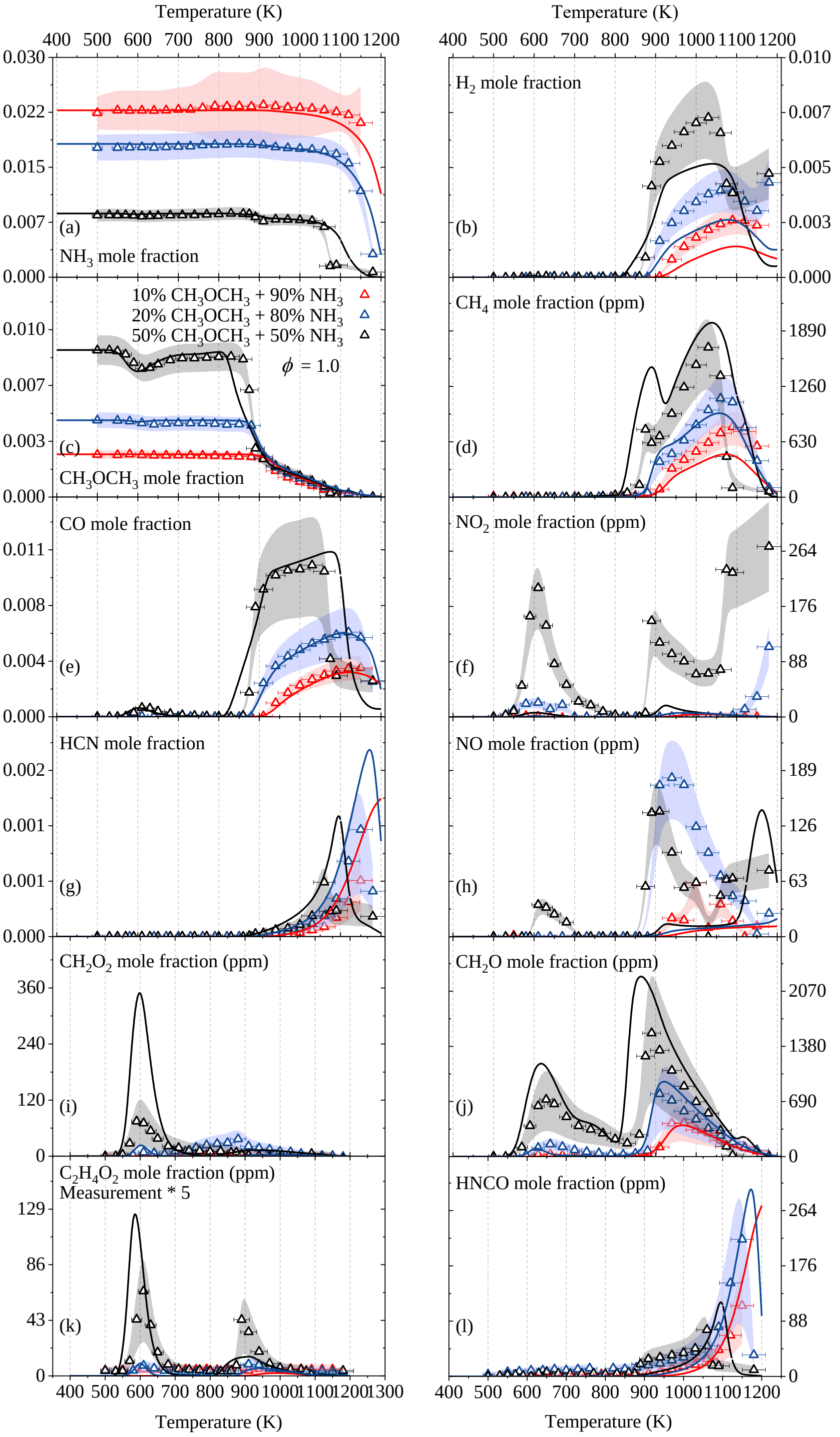

Fig. 4.11. Comparison of the measured (symbols) and simulated (lines) mole fraction profiles of a) NH_3, b) H_2, c) CH_3OCH_3, d) CH_4, e) CO, f) NO_2, g) HCN, h) NO, i) CH_2O_2, j) CH_2O, k) $C_2H_4O_2$, l) HNCO at

P_{JSR} = 1 bar, ϕ = 1.0, and different CH_3OCH_3 mole fractions in fuel. The error bars of T_{JSR} (horizontal) and mole fraction (shaded area, B-Spline) are indicated on all species.

At different equivalence ratios (ϕ) for the mixture with 50% DME in fuel, as depicted in Figure A4.9, all NH_3 mole fractions exhibit low-temperature oxidation behavior at 600 K, as well as a two-stage consumption model at temperatures above 850 K, which is consistent with the two-stage from NH_3/C_2H_5OH cases. Besides, 67% of the ammonia at ϕ = 2.0 cannot be consumed at the highest temperature of the system due to the lack of oxygen. The peak mole fractions of the intermediates related to DME, e.g., CO, CH_2O, and $C_2H_4O_2$ also increase with higher equivalence ratios. But for the CH_2O_2, there is no significant correlation observable between its mole fraction and the equivalence ratio at 600 K. When the temperature is above 850 K, the intermediates from NH_3 and DME oxidation, such as H_2, CH_4, CO, CH_2O, NO, HCN, and HNCO, still follow the pattern observed in the C_2H_5OH case, except for NO_2 at ϕ = 2.0, which is not generated at 1050 K.

All the speciation data from NH_3/C_2H_5OH and NH_3/CH_3OCH_3 mixtures has been utilized to validate the developed PTB-NH_3/C_2 mechanism. Detailed comparisons between simulations and experimental data can be found in Figures 4.10 and 4.11 (different C_2H_6O fractions) in the main text and Figures A4.8 and A4.9 (different equivalence ratios) in the Appendix. Generally, the model can reasonably capture the observed features (different oxidation stages) and mole fractions with some discrepancies, particularly in the NO/NO_2 chemistry. For example, no NO_2 formation is predicted in the third oxidation regime. Besides, it slightly overestimates (most of the simulations are still within the associated uncertainty of the temperature) the mole fractions of C_2H_5OH and CH_3OCH_3 for the mixtures with 50% C_2H_6O-isomer in fuel in the temperature range of 800 - 900 K. Accordingly, this overestimation extends to their respective intermediates $C_2H_4O_2$ and CH_3CHO. Such phenomenon could be attributed to the inadequacy of the hydrocarbon sub-mechanism since the same is found for the pure C_2H_5OH and CH_3OCH_3 fuel mixtures (cf. Figure 3.1). It should be noted that the model is sufficient in predicting the underlying chemistry even if there are some discrepancies existing.

Interestingly, both simulated and measured CH_4 show a small peak at temperatures between 850 and 900 K, as can be seen for example for the mixture with 50% promoters (cf. Figures A4.8 and A4.9). In this temperature range, ethanol and DME exhibit faster consumption rates compared to the range of 900 K to 1180 K, as depicted in Figure A4.10. Specifically, almost 70% of C_2H_5OH or CH_3OCH_3 will be consumed within 850 - 900 K, while the remaining 30% of the conversion occurs above 900 K. This might be explained by a near-constant OH radical concentration above 900 K due to the reactions of $NO+HO_2=NO_2+OH$ (from ammonia sub-chemistry) and $H_2+OH=H+H_2O$, as it will be explained detailed in chapter 4.3.2.2. However, the same phenomenon can also be observed in pure C_2H_5OH and CH_3OCH_3 (cf. Figure 1). Meanwhile, during this transition between these two different consumption rates, the mole fraction of CH_4 shows a certain degree of decline and then increases again. According to

https://doi.org/10.7795/110.20241024

the ROP analysis of CH_4 (cf. Figure A4.11 in Appendix), the reactions of CH_3+CH_2O/HO_2= CH_4+HCO/O_2 are responsible for the CH_4 variations. However, it is still hard to explain the different consumption rates of CH_3OCH_3/C_2H_5OH, which requires further investigation. Since this paper will primarily focus on NH_3 and its interactions with promoter fuels, this topic will not be elaborated further.

4.3.2 Kinetic analysis of the three oxidation regimes

Based on the above discussion, a general conclusion can be drawn: In the case of both NH_3/C_2H_5OH and NH_3/CH_3OCH_3 mixtures, their oxidations exhibit different stages similar to that observed in the NH_3/C_2H_6 study from Ref. [13]. Interestingly, the addition of the two isomeric fuels affects ammonia oxidation differently as mentioned above. Whereas three oxidation regimes (named hereafter as 1st, 2nd, and 3rd oxidation regimes), as well as an NTC (Negative Temperature Coefficient) behavior, can be observed for DME addition, only two consumption stages (2nd and 3rd oxidation regimes) occur for the case of ethanol. This phenomenon constitutes the primary focus of the following kinetic analysis within this section. A comprehensive kinetic analysis is performed to analyze and compare the effect of ethanol and DME addition on NH_3 oxidation across various oxidation regimes. To keep clear the subsequent analysis will focus only on the fuel-lean case (ϕ = 0.5). However, similar conclusions can also be drawn for the other conditions measured.

For better comparing the different impacts of ethanol and DME addition on NH_3 oxidation, Figure 4.12 depicts the temperature-dependent mole fraction profiles of NH_3 together with the corresponding co-fuels ethanol and DME (Figures 4.12a and 4.12b), respectively, as well as of the intermediate species NO_2 and CH_2O for both cases (Figures 4.12c and 4.12d). As mentioned above, the introduction of the two isomeric fuels has varying effects on ammonia oxidation, specifically the 1st low-temperature (600 K) oxidation regime that occurs during the oxidation of the NH_3/DME mixture. Interestingly, both the 2nd and 3rd oxidation regimes appear at comparable temperatures for both fuels, i.e., at 900 K and 1050 K, respectively.

4.3.2.1 First oxidation regime

The consumption of ammonia through oxidation around 600 K could only be observed when adding DME. Similar observations were made by Zhu et al. [28]. The authors concluded that under the studied conditions the NH_3 oxidation is promoted through the OH radicals produced from the DME low-temperature chain-branching reactions. The same conclusions can be drawn for the conditions measured here. Previous DME studies by Moshammer et al. [131,132] showed that DME undergoes typical low-temperature oxidation pathways through first O_2-addition and second O_2-addition. According to their findings, the CH_3OCH_2 radical reacts with O_2 (first O_2-addition), resulting in the formation of CH_2OCH_2OOH radicals. During the low-temperature combustion (LTC), this radical can combine with another molecular O_2 (second O_2-addition) forming the keto-hydroperoxide ($HOOCH_2OCHO$), which leads to the production of two OH radicals and further conversion to CH_2O_2 (formic acid, OHCHO, cf.

https://doi.org/10.7795/110.20241024

Figures 4.11i and A4.9i). However, when the temperature exceeds that temperature range, DME is more likely to follow other pathways after the first O_2-addition, producing $C_2H_4O_2$ (methyl formate, CH_3OCHO, cf. Figures 4.11k and A4.9k), 1,3-dioxetane, or two formaldehydes with one OH radical. It is clear that the reactivity of the system increases by providing one more OH radical from the second O_2-addition, and the detection of its unique product CH_2O_2 can be used to identify the involvement of the second O_2-addition. Similarly, the measurement of $C_2H_4O_2$ gives evidence of the involvement of the first O_2-addition. From the mass spectrometric signal on m/z=64.016 u (CH_4O_3), a main fragment from the keto-hydroperoxide [132], a species profile can be extracted (cf. Figure A4.12), which peaks at 600 K, indicating an active low-temperature chemistry of DME.

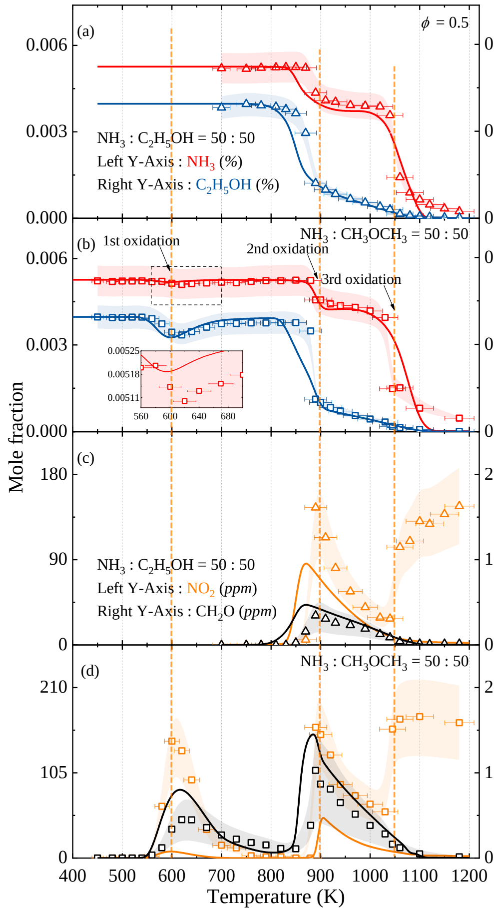

Fig. 4.12. Experimental (symbols) and simulated (lines) mole fraction profiles of NH_3 and the respective co-fuel as well as the intermediate species NO_2 and CH_2O for (a, c) NH_3/C_2H_5OH or (b, d) NH_3/CH_3OCH_3 mixtures. Uncertainties for mole fractions are illustrated by shaded areas and for temperature exemplary error bars are shown.

Interestingly, with a higher initial DME mole fraction (50% DME content in fuel) in the fuel-rich mixtures (ϕ = 2.0, cf. Figure A4.9), the NH_3 oxidation at low temperature (600 K) is likely to be more extensive compared to the fuel-lean conditions. One possible explanation might be that the NH_3 fraction in the fuel undergoes consumption primarily through reaction with OH or other radicals whereas DME

https://doi.org/10.7795/110.20241024

follows oxidation through the addition of molecular oxygen in this temperature range available in high amounts independent from the equivalence ratio. As a result, a fuel-rich mixture with a higher initial DME mole fraction exhibits increased reactivity and introduces more OH radicals from the second O_2-addition path, triggering more NH_3 oxidation within the 1st oxidation regime. For the mixtures with 10% and 20% DME in fuel (cf. Figure 4.11), it shows a slightly pronounced NH_3 consumption, as corroborated by the NO/NO_2 formation in this regime. It can be speculated that lower DME content does not generate sufficient OH radicals during the LTC to initiate extensive NH_3 oxidations, which can further be supported by the low peak mole fraction of CH_2O_2 in the 1st oxidation regime.

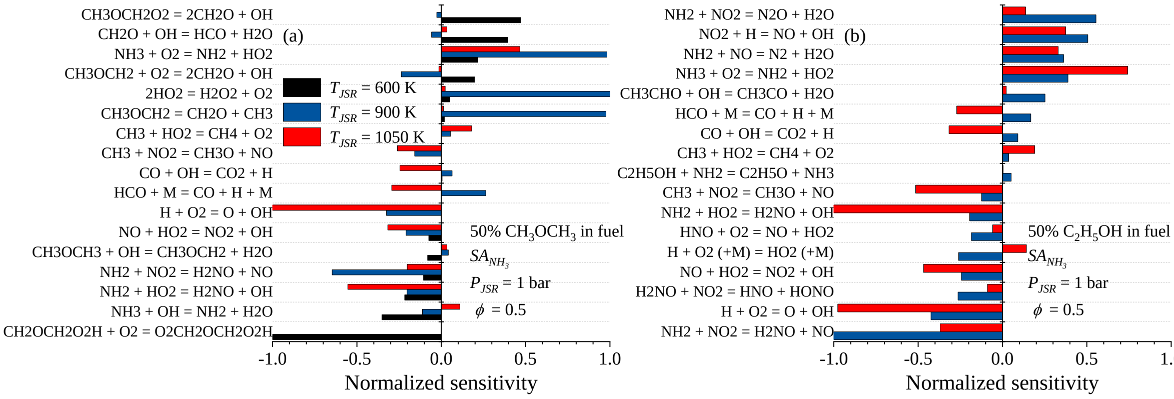

Fig. 4.13. Sensitivity analyses of NH_3 mole fraction for (a) NH_3/CH_3OCH_3 mixture and (b) NH_3/C_2H_5OH mixture at different temperatures. The negative value indicates promotion of the NH_3 consumption while a positive value implies the inhibiting effect.

Figure 4.13a shows the sensitivity analysis (SA) of NH_3 at 600 K (black bars) demonstrating the importance of DME low-temperature kinetics for the consumption of NH_3. In particular, the second O_2-addition reaction $CH_2OCH_2O_2H+O_2=O_2CH_2OCH_2O_2H$, which leads to the formation of the keto-hydroperoxide and further to the production of two OH radicals, shows the highest sensitivity for the promotion of the NH_3 consumption. The high sensitivity of the reaction $NH_3+OH=NH_2+H_2O$ reveals the importance of the OH radicals for the oxidation of ammonia at the first oxidation stage. According to the sensitive analysis, the reaction $CH_3OCH_2O_2=2CH_2O+OH$ is the most sensitive inhibiting reaction. This reaction is well-known for causing the reduction of OH radicals in the low-temperature chemistry of DME and becomes even more important with increasing temperature being responsible for its NTC phenomenon. As the OH radical concentration is the key player for NH_3 consumption, the NTC phenomenon is also reflected in the ammonia profile at low temperatures.

While in many cases for DME and ethanol addition to hydrocarbon fuels, the chemistries of the individual fuel components do not interact [133], it is worth analyzing the potential entanglement of the NH_3 chemistry with the chemistry of the oxygenated hydrocarbon because both kinds of fuels produce different small radicals (e.g. NH_2, NO_2, CH_3, etc.). In the low-temperature oxidation regime, only very weak signals at m/z=27.011 u (HCN) and 61.016 u (CH_3NO_2) that result from such intersystem-crossing

https://doi.org/10.7795/110.20241024

chemistry could be experimentally detected but not quantified due to low signal intensities. However, some potential N–C species like CH_3NH_2 and CH_3ONH_2 may not be identified due to overlapping strong signals from other species. The model (cf. Figure 4.14b) only predicts the formation of CH_3NO_2.

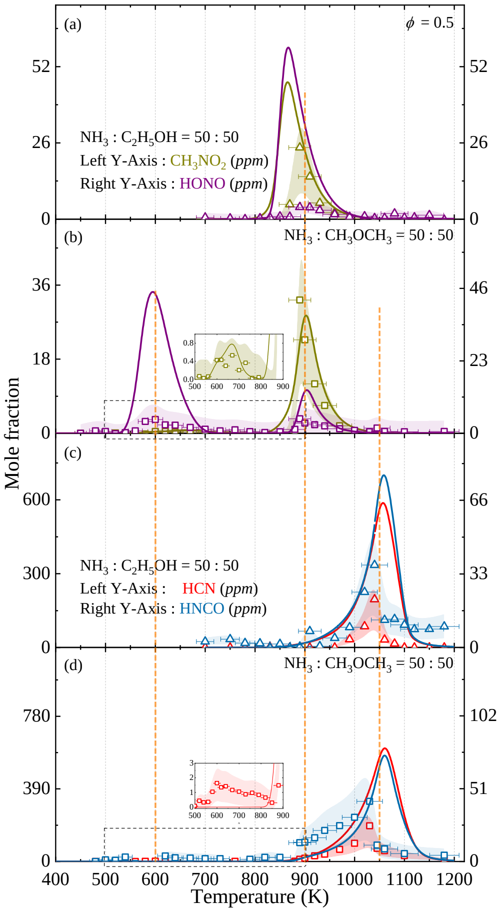

Fig. 4.14. Experimental (symbols) and simulated (lines) mole fraction profiles of intermediate species CH_3NO_2, HONO, HCN, and HNCO for (a, c) NH_3/C_2H_5OH or (b, d) NH_3/CH_3OCH_3 mixtures. Uncertainties for mole fractions are illustrated by shaded areas and for temperature exemplary error bars are shown.

According to the rate of production (ROP) analysis at 600 K (cf. Figure A4.13), CH_3NO_2 is exclusively formed through the reaction of CH_3 with NO_2, whereas the CH_3 radical is produced via CH_3OCH_2=CH_3+CH_2O and CH_3OCO=CH_3+CO_2 (cf. Figure A4.14). The latter reaction is part of a reaction channel that results from the first O_2-addition to the DME fuel radical and sequential decomposition of CH_3OCH_2OO to CH_3OCHO (methyl formate) and further to CH3OCO. Methyl formate was also measured and quantified experimentally (cf. Figures 4.11k and A4.9k). The SA for CH_3NO_2 at 600 K (cf. Figure A4.15) shows the second O_2-addition reaction as the most sensitive reaction, underlining the importance of this low-temperature reaction channel for the production of CH_3NO_2.

4.3.2.2 Second oxidation regime

As mentioned above, the addition of both fuels leads to NH_3 consumption at around 900 K. The sensitivity analyses for NH_3 depicted in Figure 4.13a (for the addition of DME) and Figure 4.13b (addition of ethanol) reveal similar promoting reactions to be important. The highest sensitivities are attributed to reactions that are related to the ammonia sub-mechanism or the H_2/O_2 chemistry, i.e., $NH_2+NO_2=H_2NO+NO$ and $NH_3+O_2=HO_2+NH_2$ as well as $H+O_2=O+OH$, respectively. In the case of DME addition, the DME-specific reactions forming OH radicals such as $CH_3OCH_2+O_2=2CH_2O+OH$ also show a slight promoting effect, while in the case of ethanol, reactions connected to the alcohol chemistry seem to be less important. Also, for the inhibiting effect, it becomes obvious that DME-related reactions are much more sensitive than the respective reactions related to the alcohol chemistry in the ethanol case, indicating a stronger influence of DME-specific chemistry on ammonia consumption.

While the sensitivity analysis only provides information about the potential significance of individual reactions, the reaction path analyses depicted in Figure 4.15 provide much more details about the ongoing chemistry. It can be seen that NH_3 consumption for both promoter fuels follows an identical chemical sequence, namely via $NH_3 \rightarrow NH_2 \rightarrow H_2NO \rightarrow HNO \rightarrow NO \rightarrow NO_2 \rightarrow N_2O \rightarrow N_2$, which mainly is initiated by NH_3 reacting with OH radicals forming NH_2, in particular, 99.5% of the reactions for ethanol addition and 99.2% for DME addition, respectively.

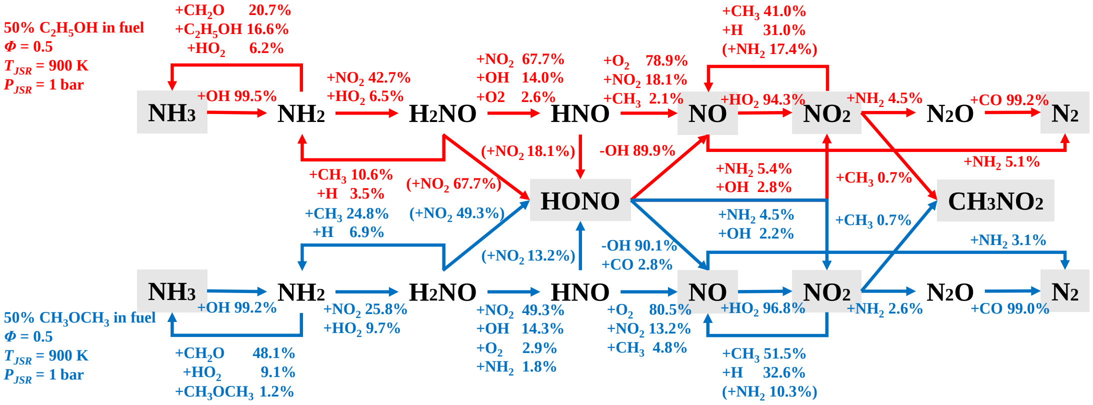

Fig. 4.15. Reaction pathways of NH_3/C_2H_5OH *(red) and* NH_3/CH_3OCH_3 *(blue) mixtures at second oxidation regime (*T_{JSR} *= 900 K,* P_{JSR} *= 1 bar,* $NH_3:C_2 = 50:50$, $\phi = 0.5$ *and a residence time of 1s). Numbers indicate the ratio of the rate of a specific reaction to the total consumption rate of a species at the beginning of an arrow. Repeated reactions are shown in the bracket. Species experimentally measured are highlighted in grey.*

A temperature-dependent rate of production analyses for OH (cf. Figure 4.16) reveals that in the second oxidation regime, the DME chemistry competes with the NH_3 chemistry, and OH consumption is slightly dominated by the reaction $CH_2O+OH=HCO+H_2O$ and the direct reaction of the fuel with OH ($CH_3OCH_3+OH=CH_3OCH_2+H_2O$). Only at temperatures above 960 K, NH_3 chemistry becomes more important and the reaction $NH_3+OH=NH_2+H_2O$ dominates the reaction process. For ethanol addition,

https://doi.org/10.7795/110.20241024

the reactions $C_2H_5OH+OH=CH_3CHOH+H_2O$, $CH_2O+OH=HCO+H_2O$, and $NH_3+OH=NH_2+H_2O$ compete. However, the ethanol chemistry is not dominating the OH consumption as it is observed for the DME chemistry which is consistent with the conclusions of the sensitivity analyses above. It should be noted that at 900 K a large part of the NH_2 radicals react with CH_2O, HO_2, CH_3CH_2OH/CH_3OCH_3 and revert to NH_3 (43.5% for the addition of ethanol and 58.4% for the DME case, respectively).

As shown in Figure 4.15, a second reaction pathway exists that proceeds through nitrous acid (HONO) via $HONO \rightarrow NO_2$ and $HONO \rightarrow NO \rightarrow NO_2$ making HONO a key species in NO and NO_2 formation in the second oxidation regime. The model can only qualitatively predict the mole fraction profiles of both species and HONO chemistry should be addressed in future studies to improve the prediction of NO_x chemistry in ammonia oxidation. In addition, HONO decomposes into NO and OH radicals and thus enhances the radical pool further initiating the consumption of NH_3. He et al. [11] found that the HONO-related reaction routine can be activated uniquely by adding methanol to ammonia through the reaction of CH_3OH with NO_2 and consequently, it enhances the reactivity significantly. A similar reaction could be imagined with the addition of ethanol, but the respective experimental HONO mole fraction profiles (cf. Figure A4.16 in the Appendix) do not indicate such an effect, as they peak at the same concentration level regardless of the additive.

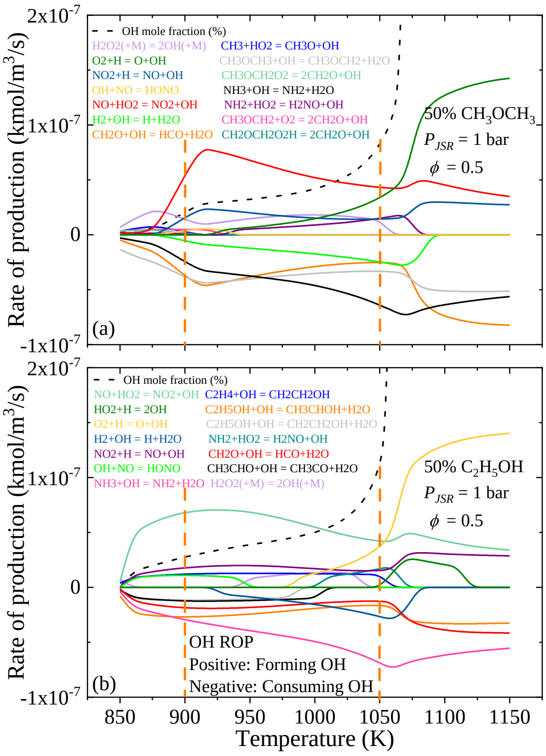

Fig. 4.16. Rate of production analysis of OH radical for (a) NH_3/CH_3OCH_3 and (b) NH_3/C_2H_5OH mixture at different temperatures. The negative value represents consuming OH, and the positive value represents forming OH.

https://doi.org/10.7795/110.20241024

Also, for the second oxidation regime, the N–C chemistry remains weak. Again, CH_3NO_2 could be detected experimentally and shows higher concentrations than at low temperatures. From Figure 4.15 it becomes obvious that CH_3NO_2 is again formed through the reaction of CH_3 with NO_2. As we can see from Figure A4.14, in the case of DME, the production rate of CH_3 radical via $CH_3OCH_2=CH_3+CH_2O$ is significantly higher compared to that at the first oxidation regime. However, for the ethanol case, the CH_3 radical is mainly formed through $CH_3CO(+M)=CH_3+CO(+M)$ and $CH_3CHO+OH=CH_3+HOCHO$ as well as $C_2H_5O(+M)=CH_3+CH_2O(+M)$ (cf. Figure A4.17).

Notably, NH_3 reactivity decreases significantly in both cases before the temperature reaches the third oxidation regime (cf. Figure 4.12). This effect can be connected to a near-constant OH radical concentration caused by a slight decrease in the rate of production of the OH productive reaction $NO+HO_2=NO_2+OH$ and an increase in the activity of the OH-consuming reaction $H_2+OH=H+H_2O$ (cf. Figure 4.16).

4.3.2.3 Third oxidation regime

The third oxidation regime initiates at 1050 K for both NH_3/C_2H_5OH and NH_3/CH_3OCH_3 mixtures. A similar phenomenon has been explored in the context of fast temperature-initiated NH_3 consumption by adding ethane [13]. As the temperature increases, it generates sufficient energy to overcome the activation energy barrier (E_a) of most NH_3-related reactions, thereby triggering rapid NH_3 consumption. Hence, the consumption of NH_3 is determined by reactions related to N-species and is not dependent on the respective C_2 fuels and their chemical functional groups. The similarity in the reaction pathway analysis (see Figure 4.17) validates these findings. Additionally, the SA analyses at 1050 K (cf. Figure 4.13) highlight the reactions of $H+O_2=O+OH$, $NH_2+HO_2=H_2NO+OH$ as well as $NH_3+O_2=HO_2+NH_2$ indicating that these reactions play more crucial roles in promoting and inhibiting the NH_3 consumption for both additives. In addition to OH radicals, O radicals from the $H+O_2$ reaction can also facilitate the NH_3 oxidation through $NH_3+O=NH_2+OH$ within the third regime (cf. Figure A4.18).

Meanwhile, the reversed path of NH_2+HO_2 provides more recycled NH_3 (cf. Figure 4.17). Interestingly, the H-radical production reactions $HCO+M=CO+H+M$ and the subsequent reaction $CO+OH=CO_2+H$ (cf. Figure 4.13) exhibit a promoting effect for NH_3 consumption in contrast to their hindrance in the second regime. This discrepancy might arise from the involvement of generated H radicals in a more vigorous $H+O_2$ reaction in the third oxidation regime, which not only compensates for the OH consumption from the CO+OH reaction but also intensifies the OH/O radical pool.

The N–C chemistry tends to play a more important role in the third oxidation regime as indicated by the intermediate species HCN and HNCO and their corresponding mole fraction profiles (cf. Figures 4.14 and 4.17). The reaction pathway analysis reveals that approximately 11% of NH_2 undergo reaction with CH_3, proceeding through the subsequent pathway $CH_3NH_2 \rightarrow CH_2NH_2 \rightarrow CH_2NH \rightarrow H_2CN \rightarrow HCN \rightarrow$

https://doi.org/10.7795/110.20241024

CH_3CN→NCO→HNCO and accumulate N–C species like HCN/HNCO. It is noteworthy that this pathway is absent in the second oxidation regime. Nonetheless, the remaining NH_2 radicals would prefer to participate in the reactions with other major components and revert to NH_3 (54.4% for the C_2H_5OH case and 57.9% for the CH_3OCH_3 case), about one-fourth of these radicals will be further consumed through the typical NH_2 oxidation steps like seen in the second oxidation regime, namely NH_2→H_2NO→HNO→NO→NO_2→ N_2O→N_2, but without the formation of HONO.

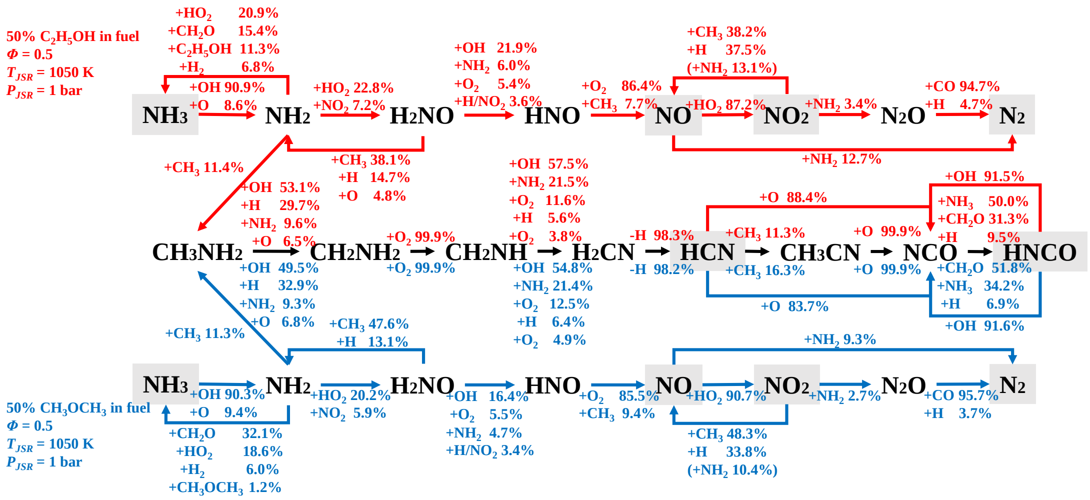

Fig. 4.17. Reaction pathways of NH_3/C_2H_5OH (red) and NH_3/CH_3OCH_3 (blue) mixtures at third oxidation regime (T_{JSR} = 1050 K, P_{JSR} = 1 bar, $NH_3:C_2$ = 50:50, ϕ = 0.5 and a residence time of 1s). Numbers indicate the ratio of the rate of a specific reaction to the total consumption rate of a species at the beginning of an arrow. Repeated reactions are shown in the bracket. Species experimentally measured are highlighted in grey.

4.3.3 Conclusion

This study explores the NH_3 oxidation in the presence of the C_2-hydrocarbon additives ethanol (C_2H_5OH) and DME (CH_3OCH_3) across various temperatures. The developed mechanism PTB-NH_3/C_2 mech can satisfactorily reproduce the speciation profiles. The investigation reveals that the addition of both fuels influences ammonia oxidation differently, with three oxidation regimes (1st, 2nd, and 3rd) as well as an NTC behavior observed for CH_3OCH_3 but only two regimes (2nd and 3rd) for C_2H_5OH.

The 1st oxidation regime highlights the unique role of CH_3OCH_3 in promoting NH_3 consumption at 600 K as well as the subsequent NTC phenomenon, through specific low-temperature kinetics and the influence of OH radical production. In the 2nd regime, the DME chemistry exhibits more importance in ammonia oxidation by competing for OH radicals with the NH_3 chemistry, which is less significant in the ethanol case. Nonetheless, NH_3 consumption with both promoter fuels follows identical chemical reaction paths initiated by the reaction of NH_3+OH. Moreover, nitrous acid HONO at 900 K tends to be a key species in NO and NO_2 formation. The 3rd oxidation regime is characterized by rapid NH_3

https://doi.org/10.7795/110.20241024

consumption primarily governed by NH_3 chemistry and independent from the promoter fuel. Unlike the weak detection of CH_3NO_2 in the 1st and 2nd regimes, the N–C chemistry (HCN and HNCO) is more pronounced at 1050 K.

In summary, the study observes distinct NH_3 consumption regimes that are differently influenced by the two isomeric promoters, emphasizing the importance of fuel-specific chemistry, temperature, and N–C species in NH_3 oxidation. The results provide valuable insights for future model development and studies on NH_3 combustion.

5. The experimental and kinetic study of NH_3/C_2 fuel blends auto-ignition at high pressures and intermediate temperatures

This chapter presents the auto-ignition properties of NH_3/C_2H_6 (chapter 5.2) and NH_3/C_2H_5OH (chapter 5.3) fuel blends at intermediate temperatures (820 - 1120 K) and elevated pressures (20 and 40 bar). These ignition delay times (IDT) measurements are conducted in a rapid compression machine (RCM). The developed PTB-NH_3/C_2 mech mechanism can reproduce the measurements of IDT very well for both mixtures. Furthermore, sensitivity and reaction pathway analyses are performed to investigate the impact of ethane and ethanol addition on the ammonia auto-ignition. Part of the results are already published in refs. [13,18].

5.1 Introduction and Motivation

Despite ammonia presenting several benefits as an alternative fuel, its practical implementation remains a challenge due to its low burning velocity and elevated auto-ignition temperature. The solution here to overcome these issues is to blend ammonia with C_2-hydrocarbon fuels as additives, such as ethane (C_2H_6) and ethanol (C_2H_5OH). This work explores the fundamental combustion chemistry to gain insights into the blending effects of NH_3 with additives. The speciation measurements from the last chapter can test the specific subsets of the mechanism related to the individual species and improve the predictability of the model. However, in this chapter, the focus will be on ignition delay times (IDTs) from a rapid compression machine (RCM). The importance of these IDTs is that they can reflect the global process of chemical reactions within the system, and interpret the combustion behaviors of fuel within the heat engine. Furthermore, IDT serves as an essential target for validating the overall performance of reaction mechanisms.

Here, ethanol is incorporated into the ammonia to specifically examine its impact. Ethanol is chosen because, among other fuels, it possesses a better antiknock quality because of its higher octane number and can greatly reduce soot formation due to its oxygen content. Moreover, alcohol can be generated through power-to-x technology using renewable energy sources, offering the advantage of carbon-neutrality. In our previous study [10], methanol demonstrated high efficiency in facilitating ammonia oxidation. Given that ethanol is extensively utilized, either as an additive in gasoline or directly as a mono fuel for vehicles [134], the combination of NH_3 and C_2H_5OH is, therefore, a promising option for developing carbon-neutral energy solutions.

A comprehensive investigation on the ignition properties of NH_3/C_2H_5OH blends has been barely reported in the literature. Haputhanthri et al. [135] attempted to enhance the solubility of ammonia/gasoline blends by incorporating ethanol. Their finding revealed that the addition of 10 vol% ethanol increases the ammonia solubility from 4.5 vol% to 11 vol%. This ammonia-enrich mixture leads to increased torque and power output in the engine compared to the use of pure gasoline. However, this

https://doi.org/10.7795/110.20241024

research primarily focuses on the blending of gasoline and ammonia, with ethanol mainly serving as an emulsifier. In terms of fundamental research, Wang et al. [16] recently conducted measurements of the laminar burning velocities (LBVs) of NH_3/CH_3OH/air and NH_3/C_2H_5OH/air using the heat flux method. The results indicated that the addition of alcohols to ammonia has a comparable effect to their addition to other fuels such as hydrogen and methane on enhancing the LBV. Subsequently, they developed a novel kinetic mechanism validated based on experimental results. Recently, Li et al [19] measured the ignition characteristics of NH_3/C_2H_5OH mixtures in a shock tube condition. However, the test temperatures of Wang et al. [16] and Li et al. [19] were either below 448 K or higher than 1250 K, and the pressure range was within 1 atm to 10 bar, which deviates from the actual application condition of modern energy systems. As of now, there is no other study that investigated the auto-ignition properties of NH_3/C_2H_5OH fuel blends at elevated pressures and intermediate temperatures. In the previous chapter, a detailed introduction was undertaken regarding the necessity of employing ethane as a co-firing fuel in the process of ammonia oxidation, which will be omitted here for brevity.

In the present work, the auto-ignition properties of NH_3/C_2H_6 as well as NH_3/C_2H_5OH fuel blends close to engine operating conditions are explored for the first time. Specifically, the ignition delay times for both two blends were measured in a rapid compression machine (RCM) covering temperatures between 820 and 1120 K, equivalence ratios (ϕ) of 0.5, 1.0, and 2.0, and pressures of 20 and 40 bar. Besides, the mechanism (PTB-NH_3/C_2 mech) has been validated based on this data, which reproduces the measurements of IDT very well for most conditions. Additionally, kinetic analyses were conducted to enhance comprehension and illustration of the ignition process. Overall, this chapter work provides new experimental data (IDTs) as well as the underlying chemical information that can benefit combustion research in the field of ammonia-based fuel applications.

5.2 NH_3/C_2H_6 fuel blends

5.2.1 Experimental results and mechanism validation

The measured IDTs of the NH_3/C_2H_6 stoichiometric mixtures with varying C_2H_6 mole fractions are depicted in Figure 5.1. Additionally, results from pure NH_3 and the mixture containing 1% C_2H_5OH in fuel are included for comparison. Detailed variations with ethane mole fraction under fuel-lean and fuel-rich (ϕ = 0.5, 2.0) conditions can be found in Figures A5.1-A5.2 in the Appendix. In general, the measured IDTs generally follow the typical Arrhenius temperature dependence, suggesting a positive enhancement in ignition with higher temperatures. It is observed that blending C_2H_6 significantly influences ammonia ignition, namely, the mixtures become more reactive with more ethane content in fuel compared to pure ammonia. For instance, the addition of 1% C_2H_6 to a mixture at 40 bar reduces the ignition temperature from ~1065 K for pure ammonia to ~980 K while maintaining an overall IDT of about 105 ms. As the C_2H_6 mole fraction increases to 5% and 10%, the enhancement by adding more ethane becomes less, similar to observations in other NH_3 fuel blend studies [10]. Compared with the ignition enhancement by C_2H_6, the addition of 1% C_2H_5OH in the mixture reduces the ignition temperature by an additional ~25 K due to a higher reactivity of C_2H_5OH than C_2H_6. To evaluate the reactivity-enhancing characteristics of ethane relative to other promoters, the measured IDTs have been compared with those of various ammonia/promoter mixtures [8–10] (cf. Figure A5.3 in the Appendix). It shows that the additives promote the reactivity in the following order: 5% C_2H_5OH > 5% CH_3OH > 5% C_2H_6 > 5% H_2 > 10% CH_4.

In addition, the effect of pressure on IDTs is illustrated in Figure 5.1 by utilizing different EOC pressures, specifically 20 and 40 bar. As expected, an increase in pressure from 20 to 40 bar results in an increase in reactivity along with a shorting of the IDTs, since higher pressures generate higher collision frequency. However, as the C_2H_6 content in the mixture increases, the effect of pressure on IDTs becomes less significant, which is consistent with observations for other ammonia fuel blends [10].

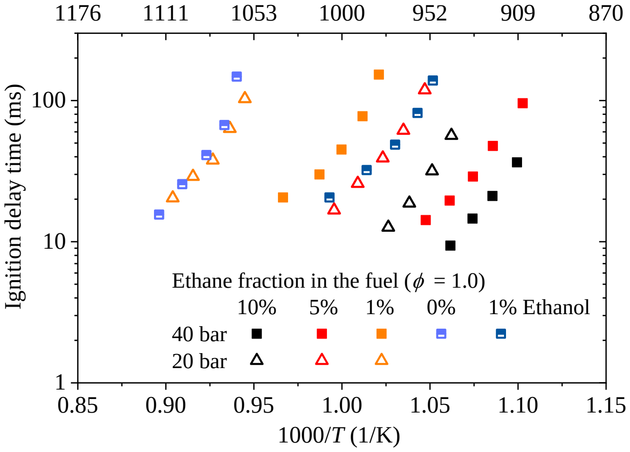

Fig. 5.1. Measured ignition delay times of NH_3/C_2H_6 mixtures with different C_2H_6 mole fractions in fuel at 20/40 bar and $\phi = 1.0$. Comparative mixtures with pure ammonia and 1% C_2H_5OH in fuel at 40 bar and $\phi = 1.0$.

Figure 5.2 illustrates the relationship between IDTs and equivalence ratio (ϕ) for different C_2H_6 fractions in the mixture, excluding the mixture with 1% C_2H_6 in fuel at 20 bar and $\phi = 2.0$ due to the ignition onset temperature could not be achieved under this condition. As depicted in Figure 5.2c, in the case of the mixture with 1% C_2H_6, raising the equivalence ratio from 0.5 to 2.0 leads to an extended IDT, consistent with the IDT dependence on ϕ for pure ammonia [136] and pure ethane [97]. When the fraction of C_2H_6 is increased to 5%, the IDTs for the different equivalence ratios are very close and nearly overlap at both pressures. An opposite trend is found in the mixture with 10% C_2H_6, where fuel-rich mixtures exhibit more reactive, leading to shorter IDTs compared to the fuel-lean case. This phenomenon has been noted in other ammonia/promoter mixtures studies when the content of the promoter in fuel reaches a certain level (20% H_2 [8], 20% CH_4 [9], 5% CH_3OH [10], 5% C_2H_5OH, 25% DME [24], 5% DEE [137], 10% Diesel [138]). It is noteworthy that for ammonia/methane mixtures [9], 20% CH_4 fractions in fuel still exhibit a shorter IDT at a lower equivalence ratio, but the overall measurements at 40 bar start to shift

https://doi.org/10.7795/110.20241024

to the opposite trend when compared to the 10% CH_4 condition. This suggests that an inverse dependence of IDT on ϕ can also be observed if the CH_4 content in fuel is further increased.

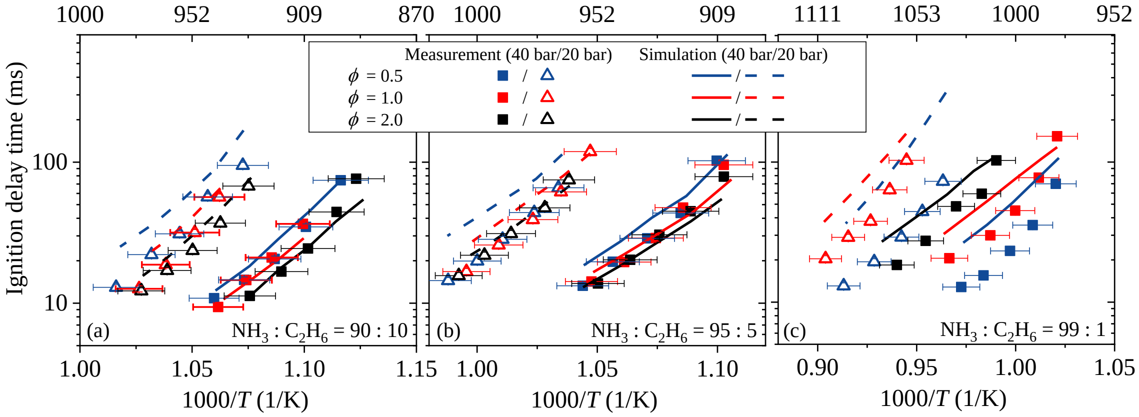

Fig. 5.2. Comparison of the measured (symbols) and simulated (lines) ignition delay times for the mixtures with a) 10% C_2H_6, b) 5% C_2H_6, and c) 1% C_2H_6 in fuel. The error bars of T_c (horizontal) and IDT (vertical) are labeled for all mixtures (vertical error bars of IDT in this Figure are hidden inside the symbol).

The PTB-NH_3/C_2 mechanism has been validated against the auto-ignition data from the RCM. As depicted in Figure 5.2, the mechanism satisfactorily predicts the IDTs and the corresponding slope of the curve for the mixtures containing 10% C_2H_6 at most of the pressures and equivalences ratios. But for the 20 bar condition, it tends to slightly underestimate the reactivity of the fuel-lean mixtures, leading to a longer ignition delay. In the case of the mixtures with 5% C_2H_6 in fuel, there is a similar agreement between simulations and experimental data. The simulated IDT values closely match the measurements under most conditions, but the IDTs at lower pressure and equivalence ratio (20 bar, $\phi = 0.5$) are overpredicted. At 1% ethane mole fraction, the mechanism exhibits an overprediction of the IDT, particularly for fuel-lean mixtures, with a deviation of exceeding a factor of three. Besides, a reduced slope for simulated IDT-1/T curves becomes evident at 40 bar. It can be observed that the predictive ability of the mechanism for fuel-lean mixtures appears to be unsatisfactory, particularly when the NH_3 content is high. The reason for this discrepancy could be attributed to the inadequacy of correct oxygen/nitrogen chemistry, which requires further investigations. Recently, Stagni et al. [93] found that there is a significant uncertainty in the theoretical assessment of important ammonia reactions, such as $NH_3+O_2=NH_2+HO_2$. Another discrepancy between measurements and predictions occurs for relatively long IDTs, specifically, at higher pressures and equivalence ratios (40 bar, $\phi = 1.0, 2.0$), the simulated IDTs are shorter than the measured values. This phenomenon may be due to that part of the heat loss is not reflected in the volume profile of the non-reactive gas mixture and becomes more pronounced in the case of longer heat loss processes (due to the longer IDT) and higher collision frequencies between the wall and reactants (due to the higher P_c and ϕ). Furthermore, the mechanism satisfactorily replicates the dependence of IDT on ϕ in various fuel mixtures, except for the case of 5% C_2H_6 in fuel, where

https://doi.org/10.7795/110.20241024

discrepancies between different equivalence ratios are evident in the simulations while the experimental measurements almost overlap.

5.2.2 Kinetic analysis

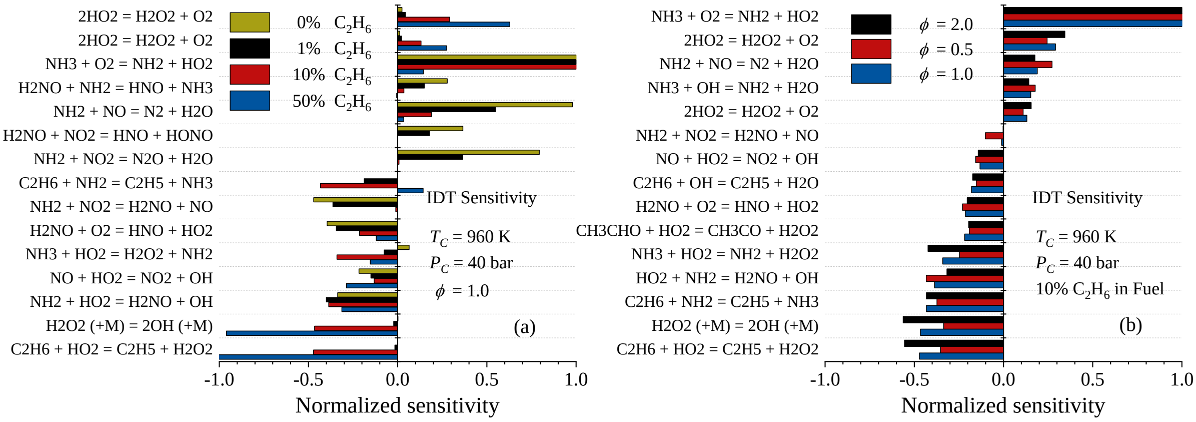

Fig. 5.3. Sensitivity analysis of IDT at 960 K and 40 bar a) for the stoichiometric mixture with different C_2H_6 fractions b) for the mixture with 10% C_2H_6 fractions under different equivalence ratios (ϕ). A positive value of the sensitivity coefficient indicates inhibition of the ignition while a negative value implies a promotion effect.

The sensitivity analysis based on the PTB-NH_3/C_2 mechanism is conducted for IDT at 960 K and 40 bar (typical RCM conditions). For better comparison with the JSR condition from Figure 4.5 in Chapter 4, the consistent 0% (pure ammonia), 1%, 10%, and 50% C_2H_6 content has been applied here. As shown in Figure 5.3a, the ammonia-related reactions such as NH_3+O_2, NH_2+NO_2/NO/HO_2, and H_2NO+NH_2/NO_2/O_2 remain the dominant chemistry of IDTs in the mixture containing 1% C_2H_6. In addition, the interaction between the ammonia and the promoter-fuel system, i.e., NH_2+C_2H_6 becomes effective in enhancing auto-ignition, which could be the underlying reason for the lower ignition temperature compared to pure ammonia. As the C_2H_6 content increases to 10%, the NH_3+O_2 reaction remains the most inhibiting, but its product HO_2 initiates reactions with NH_3, NH_2, NO, and C_2H_6, leading to increased OH levels in the radical pool directly or indirectly (via the H_2O_2 decomposition), thereby promoting ignition. Importantly, these promoting reactions involving HO_2 amplify their effects with higher C_2H_6 fraction. A recent study by Klippenstein and Glarborg [139] has pointed out that the peroxy (HO_2) radicals serve as the primary chain carrier at intermediate temperatures and high pressures, and its reaction with NH_2 plays a pivotal role in ammonia auto-ignition. The H-abstraction of C_2H_6 by HO_2 and the H_2O_2-decomposed reaction into OH are most significant when 50% C_2H_6 is added to the mixture. Simultaneously, under this condition, the duplicated self-reaction of HO_2 replaces NH_3+O_2 as the most inhibitory reaction. These changes in sensitivities suggest that with 50% C_2H_6 in fuel, the chemistry of the promoter (ethane) completely governs the ignition process. Additionally, owing to the increased HO_2 levels resulting from C_2H_6-related reactions, the NH_3/NH_2/NO+HO_2 reactions continue

https://doi.org/10.7795/110.20241024

to play a significant role in ignition enhancement. It is indeed intriguing that the interaction between NH_2 and C_2H_6 exhibits an opposing hindrance. This could be attributed to NH_2 competing with HO_2 for C_2H_6, thereby reducing the highly reactive radical H_2O_2 as well as the OH (generated from H_2O_2), consequently hindering ignition. With the current fuel mixing ratio (50%NH_3+50%C_2H_6), OH radicals are more likely to be generated by the decomposition of H_2O_2 rather than by other HO_2-related reactions. It is evident that the inclusion of C_2H_6 in the mixture would lead to either a direct reaction with NH_3 or the provision of additional OH radicals to enhance the ammonia ignition. According to the SA at different equivalence ratios (cf. Figure 5.3b), the promoted reaction $NH_2+NO_2=H_2NO+NO$ holds relatively high significance for ignition delay times (IDTs) in the fuel-lean mixture. This observation is consistent with the conclusion that NO_x (nitrogen oxide) is recognized as a typical product of high-temperature and rich-oxygen environments. Therefore, those large deviations observed at fuel-lean conditions, as depicted in Figure 5.2, may partly stem from the imperfection in the NO_x-related reactions within the mechanism, and thus require further study. Apart from that, the SA of the IDT shows no significant differences between the various equivalence ratios.

When comparing the sensitivity analysis results from jet-stirred reactor (JSR) conditions (cf. Figure 4.5a in chapter 4.2.2), the reaction of $NO+HO_2$ surprisingly shows different effects on the auto-ignition at RCM conditions. This may be due to the fact that the HO_2 radicals serve as the primary direct source of OH during the auto-ignition process at RCM conditions, i.e., elevated pressures and intermediate temperature. Its direct reaction of HO_2+NO produces OH radicals, which in turn facilitate the reaction. On the other hand, during the NH_3 consumption process at the atmospheric pressure of JSR conditions, the H radical takes over from HO_2 as the primary source of OH through a reaction like $H+O_2=O+OH$. The reaction of HO_2+NO does not directly consume NH_3 like the promoted reactions of NH_3/NH_2+HO_2. Instead, it consumes HO_2 leading to an enhancement of the inhibitory channel $H+O_2(+M)=HO_2(+M)$ and thereby weakening the reactive OH and O radicals formation (via $H+O_2=O+OH$) to diminish the overall reactivity of the system. Additional kinetic analysis of NH_3/C_2H_6 mixtures at RCM conditions as well as its comparisons to other conditions are presented in chapters 4.2.2 and 5.3.2.

5.2.3 Conclusion

This chapter presented the ignition delay times of NH_3/C_2H_6 fuel blends under RCM conditions, which results indicated that the blending of ethane into ammonia can significantly increase the reactivity of the ammonia fuel leading to a lower auto-ignition temperature. Besides, the mechanism (PTB-NH_3/C_2 mech) has been validated against all the measurements and its predictions display reasonable accuracy.

From the sensitivity analysis, the interaction of $NH_2+C_2H_6$ becomes effective in enhancing auto-ignition, which may be the underlying reason for the lower ignition temperature compared to pure ammonia. Compared with the SA at JSR conditions (cf. chapter 4.2.4), notable changes are observed in the dominant reactions of the NH_3 oxidation at RCM conditions. Specifically, only the chemistry related to

https://doi.org/10.7795/110.20241024

pure ammonia, such as the reactions of NH_3+O_2, NH_2+HO_2/NO_2/NO, and H_2NO+ O_2/NO_2, is found to be dominant for the auto-ignition of the mixture with a low amount (1%) of C_2H_6. On the other hand, the HO_2 radical instead of the H radical plays an important role and its related reactions dominate the auto-ignition process across a wide temperature range (cf. Figure 4.6). Such phenomenon appears more obvious in the case of 50% C_2H_6 (cf. Figure 5.3), e.g., the reaction of C_2H_6+HO_2, the decomposition of H_2O_2 into OH as well as the duplicated self-reaction of HO_2 becomes the most promoting and inhibiting reactions, respectively, while the important reaction of H+O_2 from JSR conditions show no influence in the autoignition process at RCM conditions.

5.3 NH_3/C_2H_5OH fuel blends

5.3.1 Experimental results and mechanism validation

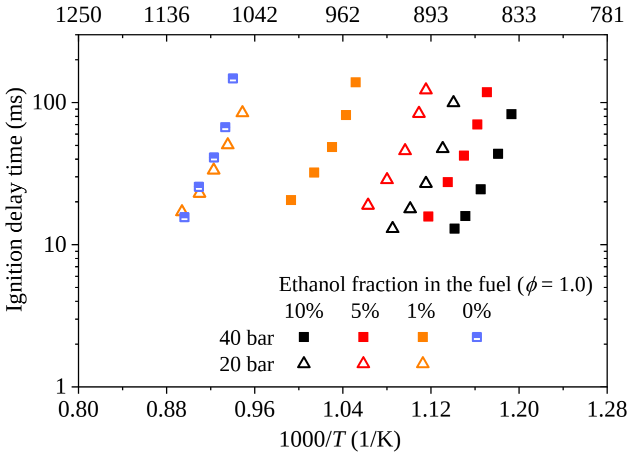

Fig. 5.4. Measured ignition delay times of NH_3/C_2H_5OH mixtures with different C_2H_6 mole fractions in fuel at 20/40 bar and ϕ = 1.0.

Figure 5.4 depicts the IDTs of NH_3/C_2H_5OH stoichiometric mixtures with varying C_2H_5OH mole fractions in fuel. Across all measurements, a typical Arrhenius temperature dependence is observed, where the IDT increases with decreasing temperature. It is clear that the addition of ethanol drastically promotes ammonia reactivity. As mentioned above, even a 1% C_2H_5OH addition can decrease the ignition temperature by around 110 K at 40 bar as compared to pure ammonia, which promotion is more effective than that observed case of 1% C_2H_6 addition. However, this promotion diminishes as the ethanol content elevates in the fuel. For example, the ignition temperature decreases by a further 100 K with 5% C_2H_5OH, but only by another 25 K with 10% C_2H_5OH in fuel. Note that, the efficiency of C_2H_5OH as a promoter is higher than that of H_2 and CH_4 by a factor of 5 and 10, respectively. In Specific, it takes 5% H_2 or 10% CH_4 (cf. Figure A5.3) to achieve a similar reduction of the ignition temperature of ammonia by around 100 K under the same pressure and ϕ [8,9]. Similar to the ethane cases, higher pressure increases collision frequency in the system, thereby accelerating ignition processes. For instance, to achieve the same ignition delay time, the stoichiometric mixture with 10% C_2H_5OH must

https://doi.org/10.7795/110.20241024

reach 877 K at 20 bar, but only 837 K at 40 bar. This effect is more pronounced in mixtures with lower C_2H_5OH content in the fuel. Similar phenomena can also be observed in the cases of ϕ = 2.0 (Figure A5.4) and ϕ = 0.5 (Figure A5.5).

Figures 5.5a and 5.5b illustrate that the IDTs of the mixtures containing 10% and 5% C_2H_5OH in fuel decrease with increasing equivalence ratios (ϕ) at both 40 and 20 bar, similar to the behavior of pure ethanol in fuel (Figure A5.6). This suggests that ethanol dominates the ignition process under such conditions. However, the mixture with 1% C_2H_5OH in fuel (Figure 5.5c) exhibits an inverse dependence of IDT on ϕ. This behavior is consistent with the measured IDTs of pure NH_3 reported by He et al. [8] and Dai et al. [140], indicating that the reactivity of this mixture is dominated by ammonia chemistry.

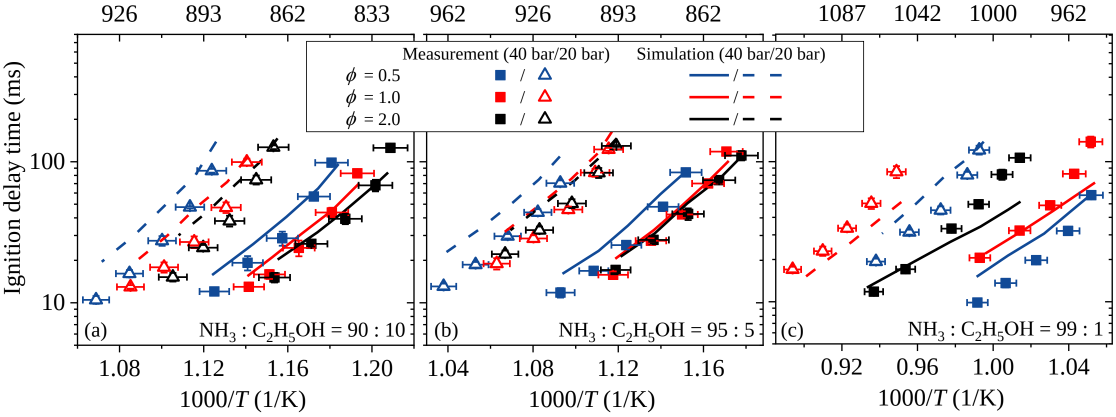

Fig. 5.5. Comparison of the measured (symbols) and simulated (lines) ignition delay times for the mixtures with a) 10% C_2H_5OH, b) 5% C_2H_5OH, c) 1% C_2H_5OH in fuel. The error bars of T_c (horizontal) and IDT (vertical) are labeled for all mixtures (vertical error bars of IDT in this Figure are hidden inside the symbol).

The modeling results based on the PTB-NH_3/C_2 mechanism are also compared with the measured IDTs in Figure 5.5. Generally, the simulations broadly agree with the measurements regarding IDTs and the slope of IDT-1/T curves. However, in the case of mixtures containing 1% C_2H_5OH in fuel (Figure 5.5c) the mechanism tends to overestimate the reactivity for stoichiometric and fuel-rich mixtures (ϕ = 1.0, 2.0). For example, it overestimates the ignition delay by a factor of two when the measurements are around 100 ms. In addition, a smaller slope of simulated IDT-1/T curves is observed at 40 bar and ϕ = 1.0, 2.0 conditions. A further discrepancy between the simulations and measurements appears in the mixture where the fuel contains 5% and 10% C_2H_5OH. In this case, the simulated IDTs are slower than those of the measurements at ϕ = 0.5. Nonetheless, the new mechanism can satisfactorily replicate the ϕ-dependence of IDT for various fuel mixtures. It also greatly increases prediction accuracy due to the addition of cross-reactions between the ammonia and ethanol. If these reactions are eliminated, the model is unable to predict any mixture ignition, such as the particular conditions such as 5% C_2H_5OH in fuel (cf. Figure A5.7). Such significance of the cross-reaction involvement for achieving reasonable simulation results has also been noted and verified in [23,24,141]. Furthermore, based on the results of this work as well as those reported in [141], it appears that the interaction of nitrogen compounds with hydrocarbons affects the accuracy of simulated results more than the interaction of oxygenated hydrocarbon with hydrocarbon mixtures. To determine these differences requires further research, which is beyond the scope of this work.

5.3.2 Kinetic analysis

To obtain a better understanding of the kinetic effects of introducing C_2H_5OH on the auto-ignition properties of NH_3/C_2H_5OH mixtures, Figure 5.6a displays the 15 most sensitive elementary reactions based on PTB-NH_3/C_2 mechanism at $T_c = 960$ K, $P_c = 40$ bar, $\phi = 1.0$ and different C_2H_5OH fractions in the mixture.

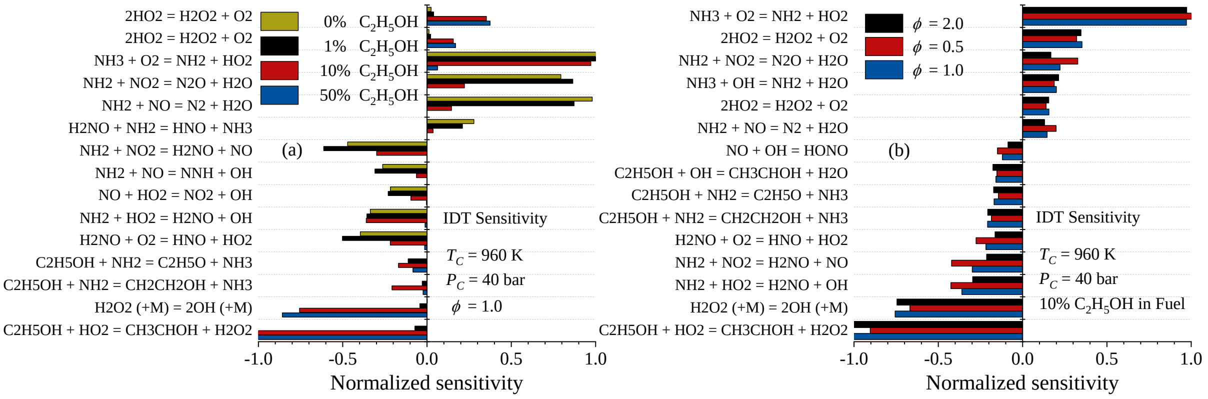

Fig. 5.6. Sensitivity analysis of IDT at 960 K and 40 bar a) for the stoichiometric mixture with different C_2H_5OH fractions b) for the mixture with 10% C_2H_5OH fractions under different equivalence ratios (ϕ). A positive value of the sensitivity coefficient indicates inhibition of the ignition while a negative value implies a promotion effect.

Among the four different C_2H_5OH fractions, there is a significant variation in the dominant reactions. In the mixture with 1% C_2H_5OH, the four most ignition-enhancing reactions are $NH_2+NO_2=H_2NO+NO$, $H_2NO+O_2=HNO+HO_2$, $NH_2+HO_2=H_2NO+OH$ and $NH_2+NO=NNH+OH$, while the reactions $NH_3+O_2=NH_2+HO_2$, $NH_2+NO_2=N_2O+H_2O$ and $NH_2+NO=N_2+H_2O$ act as the primary inhibiting factors. This reveals that the branching ratio of the NH_2+ NO_2/HO_2 reactions has a significant effect on the predictions. Comparable findings are observed in the condition of pure ammonia. As a result, the dominance of NH_3 chemistry in the mixture is consistent with the experimental findings mentioned earlier that the mixture containing 1% C_2H_5OH exhibits the same ϕ-dependence performance as neat NH_3. As the C_2H_5OH fraction rises to 10%, the chain-terminating reaction of $NH_3+O_2=NH_2+HO_2$ remains the most inhibiting. In addition, the chemistry of ignition promotion reactions shifts from that of NH_3 to that of C_2H_5OH. For example, notable effects in the current mixture are observed from the H-abstraction of C_2H_5OH by HO_2 and the decomposition of H_2O_2 into OH radicals. Additionally, the

https://doi.org/10.7795/110.20241024

reactivity of the mixture is substantially enhanced by the interactions between NH_3 and C_2H_5OH, specifically $C_2H_5OH+NH_2=C_2H_5O+NH_3$ and $C_2H_5OH+NH_2=CH_2CH_2OH+NH_3$. This further supports the importance of cross-reactions between the two fuels in accurately reproducing the IDTs of the NH_3/C_2H_5OH blends. The influence of ammonia-related reactions on the auto-ignition process diminishes further as the C_2H_5OH fraction increases to 50%, suggesting C_2H_5OH dominance in the chemistry. The two most promoting reactions remain consistent with the 10% C_2H_5OH condition, while the most inhibiting reaction changes to $2HO_2=H_2O_2+O_2$. Additionally, a sensitivity analysis has been also carried out with various equivalency ratios given the non-negligible deviation between measurements and simulations at fuel-lean conditions (cf. Figure 5.6b). However, the results show negligible overall changes between different equivalence ratios with only a few conditions exhibiting negligible differences, therefore further investigations are required.

In addition to the sensitivity analysis, the reaction pathways for the NH_3/C_2H_5OH stoichiometric mixture with 10% C_2H_5OH in fuel at 960 K and 40 bar were investigated, as shown in Figure 5.7. Meanwhile, the important reaction pathways relating to the NH_3/C_2H_6 mixture at the same condition were also presented. Particularly, the definitive onset of the ignition in this work, namely the location of the maximum derivative of pressure was selected as the investigated point. It should be noted that the reaction path at the beginning of the pressure rise, namely the oxidation occurrence, follows the consistent pathway at JSR condition, i.e., via $NH_2 \rightarrow H_2NO \rightarrow HNO \rightarrow NO(\rightarrow NO_2) \rightarrow N_2O \rightarrow N_2$ (cf. Figure 4.17). However, this pathway is no longer pronounced in the present analyzed reaction time, since more reactive radicals like OH radicals have been produced and the temperature/pressure has reached a higher level (above 110 bar and 2600 K). On the other hand, most additives (C_2H_5OH/C_2H_6) and C-intermediates have been consumed before this stage leading to an increased number of OH/O/H radicals in the radical pool. These radicals ultimately facilitate the reaction process of NH_3 and increase the reactivity of NH_3/C_2 mixtures compared to pure ammonia, which can be confirmed by the participating species alongside the reaction arrows.

From Figure 5.7, the elevated ambient temperatures at the investigated point eliminate the different chemical influences between ethanol and ethane, resulting in a similar reaction pathway. In brief, both ammonia are primarily consumed by OH radicals (72.9% in the ethanol case and 71.6% in the ethane case) to form one of the most critical radicals NH_2, which will further be converted into H_2N_2 and NH. The NH radicals undergo the subsequent reactions to form H_2N_2, N, HNO, and NO, which then proceed through different pathways such as $NH \rightarrow N \rightarrow N_2$, $NH \rightarrow N_2H_2 \rightarrow NNH \rightarrow N_2$ or $NH \rightarrow N(HNO) \rightarrow NO(NO_2) \rightarrow N_2O \rightarrow N_2$. Surprisingly, in the ethane case, more than 42.2% of NH converts to N_2H_2, while only 22.9% of that participates in this conversion for the ethanol case. As discussed in the previous chapter, the N–C chemistry has a notable impact on the oxidation of the NH_3/C_2 mixture, particularly the combination of NH_2 and CH_3. This reaction initiates the pathway of $CH_3NH_2 \rightarrow CH_2NH_2 \rightarrow CH_2NH \rightarrow H_2CN \rightarrow HCN$

https://doi.org/10.7795/110.20241024

in the initial oxidation regime, leading to the accumulation of N–C species, e.g., HCN. These accumulated HCN species will continue to be involved in the subsequent oxidation process of the mixture. For example, at the investigated stage, HCN undergoes further conversion via HCN→CN→NCO→HNCO→CO.

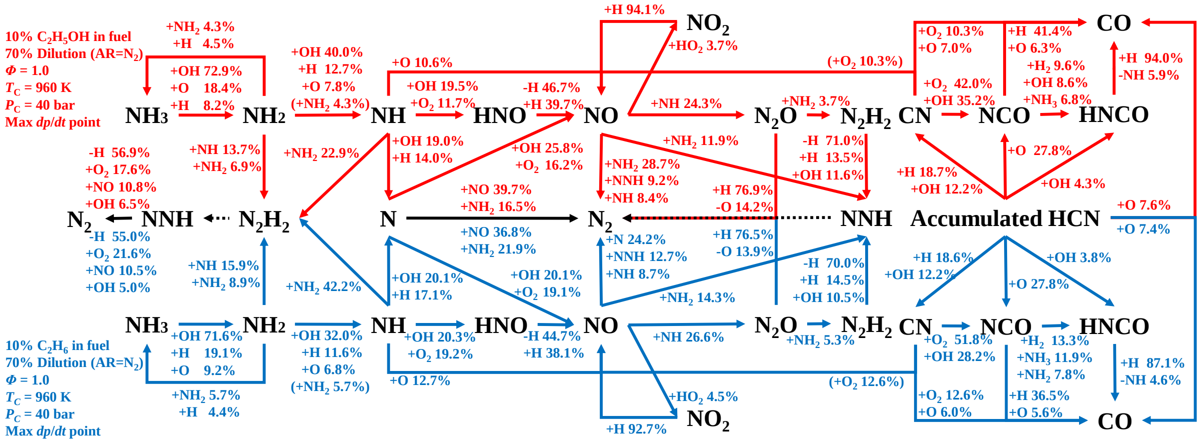

Fig. 5.7. Reaction pathways of NH_3/C_2H_6 (blue) and NH_3/C_2H_5OH (red) mixtures at the location of the maximum derivative of pressure (T_c = 960 K, P_c = 40 bar, $NH_3:C_2$ = 90:10, ϕ = 1.0). Numbers indicate the ratio of the rate of a specific reaction to the total consumption rate of a species at the beginning of an arrow. Repeated reactions are shown in the bracket.

5.3.3 Conclusion

The ignition delay times (IDTs) of NH_3/C_2H_5OH fuel blends have been investigated in an RCM facility at intermediate temperatures between 820 and 1120 K, elevated pressures of 20 and 40 bar, three C_2H_5OH mole fractions ranging from 1% to 10%, and three equivalence ratios of 0.5, 1.0 and 2.0. The results of the experiment demonstrate that adding ammonia to ethanol can significantly increase its reactivity. In particular, 1% ethanol exhibits much higher promotion efficiency when compared to the same amount of ethane. The dependence of IDTs on the equivalence ratio (ϕ) displays different trends. For example, the IDTs of the mixture containing 10% and 5% C_2H_5OH in fuel decrease with an increase of ϕ, whereas mixtures containing 1% C_2H_5OH in fuel show an opposite trend.

The PTB-NH_3/C_2 mech replicates the measurements of IDT very well across various conditions. It is emphasized that the inclusion of cross-reactions between the two fuels is required to obtain reasonable simulations. Further analyses of the sensitivity and reaction pathway are conducted for a better understanding of the influence of C_2H_5OH on the auto-ignition of NH_3/C_2H_5OH mixtures. According to the modeling results, the addition of ethanol enriches the O/H radical pool and provides N–C intersystem pathways, which will greatly accelerate the auto-ignition process.

6. The experimental and kinetic study of NH_3/C_2 fuel blends oxidation at intermediate pressures and intermediate-to-high temperatures

This chapter will present the oxidation of both NH_3/C_2H_6 and NH_3/C_2H_5OH mixtures at intermediate pressures (2.4 - 3.1 bar) and intermediate-to-high temperatures (1320 - 1960 K). Time-resolved NH_3, NO, and CO profiles of both mixtures are measured in a shock tube (ST) using laser absorption spectroscopy (LAS). The mechanism PTB-NH_3/C_2 mech can overall satisfactorily predict the ignition delay times and speciation profiles for both mixtures. In addition, comprehensive kinetic analyses are performed to investigate the underlying chemical reason for the measurements. Part of the results are already published in refs. [82].

6.1 Introduction and Motivation

The integration of a shock tube with in-situ and non-invasive laser absorption spectroscopy (LAS) proves potential in capturing speciation profiles within microseconds, facilitating examination of high-temperature combustion chemistry. Nevertheless, there is a scarcity of studies focusing on speciation measurements for ammonia and ammonia fuel blends in shock tubes. Alturaifi et al. [142–144] coupled LAS to the shock tube for NH_3, N_2O, and H_2O measurements during ammonia pyrolysis and oxidation. He and Zheng et al. [21,84,145] utilized LAS to measure NH_3, NO, CO, CO_2, H_2O, and temperature of ammonia oxidation in the shock tube. Zhu et al. [66,67] quantified time-resolved NO profiles for pure NH_3 and NH_3/H_2 mixtures. These shock tube-LAS measurements have strongly improved the understanding of high-temperature combustion chemistry.

To expand the NH_3/C_2-promoters fuel blends database and refine the mechanism at high-temperature, this chapter employs LAS to quantify time-resolved NH_3, NO, and CO profiles of NH_3/C_2H_6 and NH_3/C_2H_5OH mixtures in the shock tube. Speciation profiles of NH_3/C_2H_6 mixtures are reported for the first time. While a prior shock tube study reported speciation information for one specific NH_3/C_2H_5OH mixture (1% NH_3/0.6% C_2H_5OH, $\phi = 1.2$, $T_5 = 1367 - 1514$ K, $P_5 = 1.9 - 2.2$ bar) [21], the present study designs a consistent experimental matrix comprising ten mixtures, spanning a temperature range of 1317 - 1957 K at around 2.8 bar, including 5 - 20% C_2H_6/C_2H_5OH in the fuel, three equivalence ratios (0.5/1.0/1.5), and a fixed argon dilution ratio of 0.9. Additionally, the updated mechanism PTB-NH_3/C_2 mech is validated against the measured high-temperature measurements. Detailed kinetic analysis is performed based on the PTB-NH_3/C_2 mech.

6.2 NH_3/C_2H_6 and NH_3/C_2H_5OH fuel blends

6.2.1 Experimental results and mechanism validation

Figure 6.1 illustrates the IDTs of all experimental cases. As depicted in this figure, the experimental IDTs exhibit a typical Arrhenius temperature dependence, i.e., the IDT increases with decreasing

https://doi.org/10.7795/110.20241024

temperature. The promotional effect of adding either C_2H_6 or C_2H_5OH on ammonia ignition is consistently observed. For instance, at 1450 K, the IDT is three times shorter when 20% C_2H_6 is added compared to the case with 5% C_2H_6. Besides, adding the same percentage of C_2H_6 or C_2H_5OH, the IDTs of the mixtures are quite close to each other, which means that the promotional effect of adding either C_2H_6 or C_2H_5OH on ammonia ignition is identical. In the previous chapter, the promotional effect of C_2H_5OH was notably stronger than that of C_2H_6 at rapid compression machine (RCM) conditions (40 bar, ~ 1000 K). The difference in promotional effect is decreasing with the increase of temperature as observed in the present study. This difference provides indications on selecting appropriate promoters at different temperature regimes.

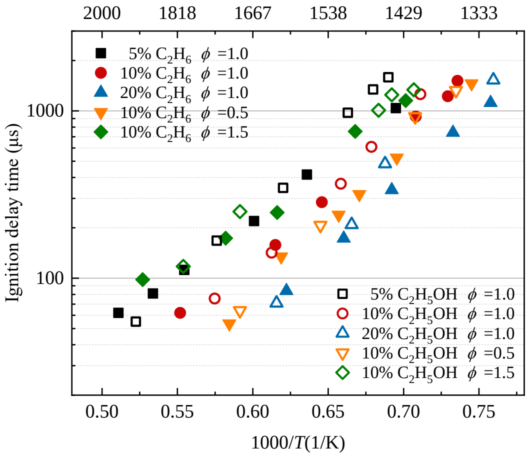

Fig. 6.1. Measured ignition delay times of NH_3/C_2 mixtures for different C_2 mole fractions in fuel and different equivalence ratios (ϕ).

The dependence of IDTs on equivalence ratios for both mixtures remains consistent, i.e., IDT decreases as the equivalence ratios decrease. This effect is more obvious on the fuel-rich side, where the IDTs difference between fuel-rich (ϕ = 1.5) and stoichiometric mixtures (ϕ = 1.0) is larger than that of stoichiometric (ϕ = 1.0) and fuel-lean (ϕ = 0.5) mixtures. The same ϕ-dependence of IDTs has been observed by Li et al. [19], with similar temperatures (1250 - 1980 K), pressures (~ 1.4 bar), and Ar dilution ratio (~ 92%) for NH_3/C_2H_5OH oxidation in a shock tube. On the other hand, this trend contrasts with the results obtained in the RCM, where fuel-rich mixtures exhibited shorter IDTs. In fact, at the low-temperature regimes (< 1500 K) in Figure 6.1, a decreasing difference in IDTs among different equivalence ratios can also be found. This indicates that if the temperature further decreases, the ϕ-dependence of IDTs might reverse as observed in the RCM conditions (cf. chapters 5.2.1 and 5.3.1). Since the pressure ranges between RCM and ST studies are quite different, to individually examine the effect of pressure and temperature on the ϕ-dependence of IDTs, we performed simulations for 12 cases at different pressure, temperature, and equivalence ratio combinations, as shown in Figure A6.1 in the Appendix. The simulations reveal a reverse equivalence ratio dependency at different temperatures regardless of pressure. Therefore, the contrasting trend is primarily attributable to temperature differences. Further discussions will be presented later in the kinetic analysis part.

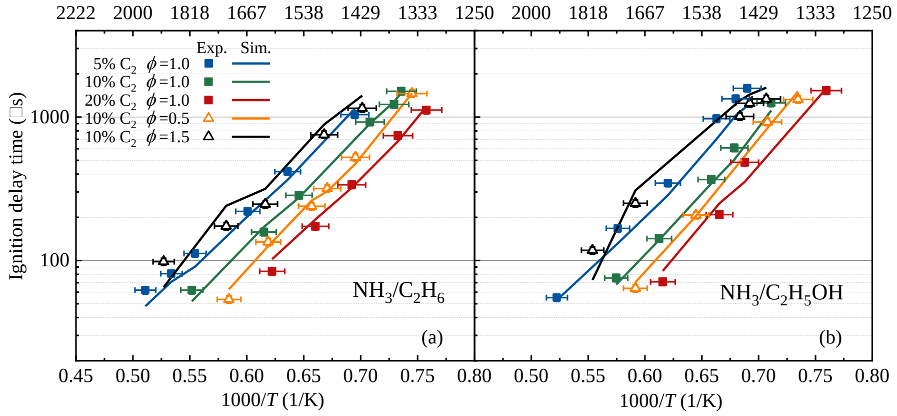

Fig. 6.2. Comparison between experimental (symbols) and simulated (lines) IDTs. The error bars of T_5 (horizontal) and IDT (vertical) are indicated on all mixtures (The vertical error bars of IDT in this Figure are hidden inside the symbol).

Figure 6.2 compares the experimental IDTs with the modeling based on the updated mechanism. Generally, the simulations are broadly in agreement with the measurements for both NH_3/C_2H_6 and NH_3/C_2H_5OH mixtures, capturing the trends in IDTs and the slope of IDT-1/T curves. The ϕ-dependence of IDTs is also reproduced by the updated mechanism.

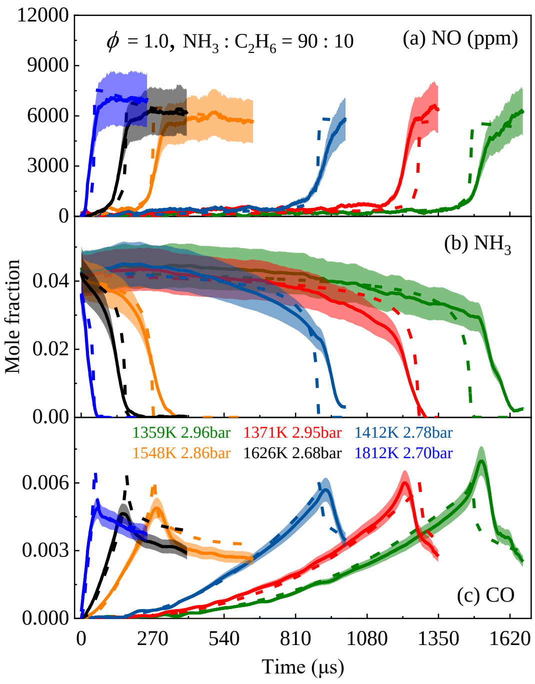

Fig. 6.3. Comparison between experimental and predicted species mole fraction for NH_3/C_2H_6 mixture (NH_3:C_2H_6 = 90:10, ϕ = 1.0, Solid lines: experiments, Dashed lines: simulations, Uncertainties are marked by shadows).

https://doi.org/10.7795/110.20241024

Furthermore, the comparison of experimental and predicted speciation profiles is conducted, with examples shown in Figure 6.3 and Figure 6.4. The uncertainties are indicated by shadows. Detailed comparisons for other mixtures are available in the Appendix (Figures A6.2-A6.9). All speciation profiles were truncated before the arrival of the contact surface.

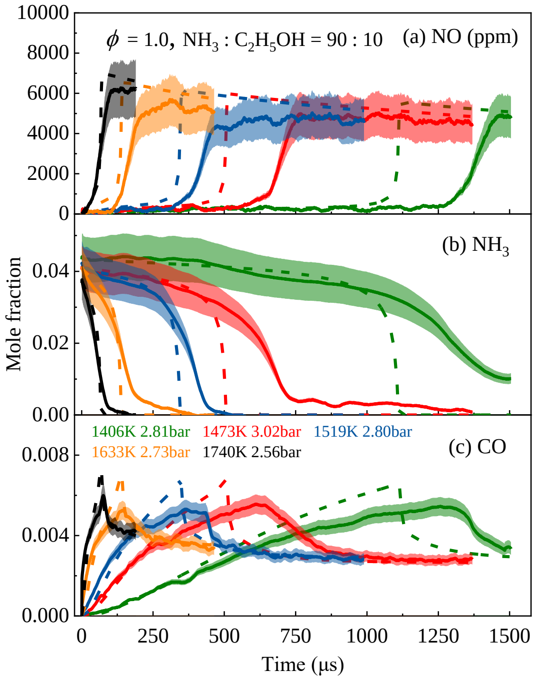

Fig. 6.4. Comparison between experimental and predicted species mole fraction for NH_3/C_2H_5OH mixture (NH_3:C_2H_5OH = 90:10, ϕ = 1.0, Solid lines: experiments, Dashed lines: simulations, Uncertainties are marked by shadows).

The simulations successfully replicate the shapes of experimental results for both NH_3/C_2H_6 and NH_3/C_2H_5OH mixtures. In most cases, the slow consumption of NH_3 before ignition can be very well captured, whereas the NH_3 consumption after ignition is sharper in simulation than observed in experiments. For NO profiles, the formation occurs and then levels off at a certain plateau. The temperature and equivalence ratio dependency on the maximum NO value can be reproduced by the mechanism, i.e., the peak NO decreases with a decrease in temperature and with an increase in equivalence ratios. These observations are consistent with our previous measurements on NO for pure NH_3 and NH_3/H_2 mixtures in the shock tube [66,67]. The predictions on NO values are satisfactory for most cases considering the uncertainties of the experiments, except for NH_3/C_2H_6 fuel-rich mixtures (cf. Figure A6.5), where the predicted NO is lower than the experimental values. The formation of CO initiates immediately with the oxidation process and continues to rise until it reaches a peak value. In most mixtures, CO tends to decrease due to the conversion of CO into CO_2. However, for fuel-rich mixtures (cf. Figure A6.5 and Figure A6.9), CO reaches its peak and then remains almost unchanged. This phenomenon is also predicted by the simulations. Compared to NO, the peak value of CO is less

https://doi.org/10.7795/110.20241024

sensitive to temperatures. The mechanism can overall satisfactorily predict the CO values except for fuel-rich mixtures where the simulations over-predict the CO peak by a factor of around 1.4.

In summary, the mechanism can well reproduce the shapes and temperature or equivalence ratio dependencies of the experimental results. The predictions in absolute values are generally satisfactory. Nevertheless, addressing observed discrepancies, especially in fuel-rich mixtures, is crucial to enhance the predictive accuracy of the mechanism. Further investigations and potential refinements are warranted to bring the model's predictions into closer alignment with experimental observations.

6.2.2 Kinetic analysis

Based on the mechanism of PTB-NH_3/C_2 mech, sensitivity and reaction pathway analysis have been performed. Figure 6.5 illustrates the most sensitive reactions of ignition for both NH_3/C_2H_6 and NH_3/C_2H_5OH mixtures. In particular, the H-related reactions, such as $H+O_2=O+OH$ and $H+NH_3=H_2+NH_2$, emerge as significant players in promoting and inhibiting the reactivity of both additives. The underlying is straightforward that the reaction of $H+O_2$ is a typical process at high temperatures to consume fuel by yielding OH and O radicals, while the $H+NH_3$ reaction catches H radicals and mitigates the overall reactivity. Notable differences have been observed for the ammonia fuel blends (cf. Figure 5.3 for 10% ethane and Figure 5.6 for 10% ethanol in fuel) at high pressure and intermediate temperatures, where the peroxy radical (HO_2) serves as the primary chain carrier and its interactions with $NH_3/NH_2/C_2H_6/C_2H_5OH$ are pivotal reactions. Here, at high-temperature regimes (>1300 K), the activation energy barrier (E_a) of NH_3-related reactions will no longer limit the ammonia oxidation. Meanwhile, ammonia is the primary component in the fuel mixture. For this reason, the reactivity of the mixture is mainly determined by the reaction related to ammonia, e.g., the reactions of $NH_3+O_2/H/OH$ and N_2H_2+M, and shows minimal relevance to these C_2 chemistries, which can be reinforced by the similarity from the reaction pathway analysis for different C_2-blends.

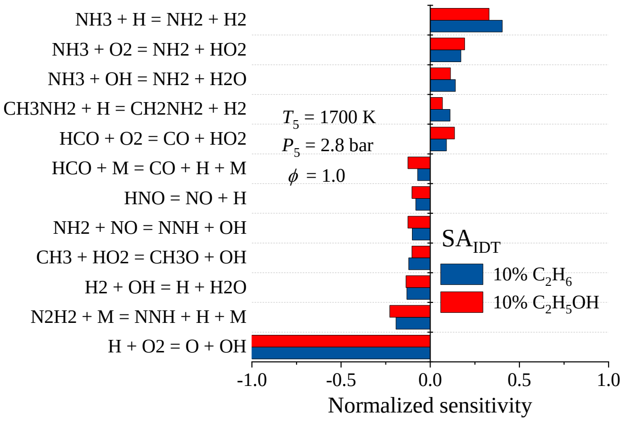

Fig. 6.5. Sensitivity analysis of IDT (Position of CO max.) for NH_3/C_2H_6 and NH_3/C_2H_5OH mixtures (T_5 = 1700 K, P_5 = 2.8 bar, $NH_3:C_2$ = 90:10, ϕ = 1.0). The negative value indicates the promotion of the reactivity while a positive value implies the inhibiting effect.

As discussed earlier, the ϕ-dependence of IDTs at high temperatures is in contrast to that at low temperatures. To explore the underlying reason, sensitivity analysis under different equivalence ratios have been conducted for 10% C_2H_6 in fuel mixtures, are shown in Figure 6.6, while similar conclusions can also be drawn for the case of NH_3/C_2H_5OH mixtures (cf. Figure A6.10 in the Appendix). At the elevated temperature of 1700 K, the comparison of sensitivity for fuel-lean and stoichiometric conditions (ϕ = 0.5, 1.0) reveals only a minimal difference. This is similar to the results from different equivalence at low-to-intermediate temperature conditions, such as JSR conditions at 1060 K (cf. Figure 4.5b), RCM conditions at 960 K (cf. Figure 5.3b), and ST conditions at 1100 K (cf. Figure 6.6b). However, under fuel-rich conditions (ϕ = 1.5), the situation is quite different. For instance, the reactions related to N_2H_2 and N–C chemistries exhibit the most promoting effect on mixture oxidation, while the H-related reactions of $H+O_2=O+OH$ and $H+NH_3=H_2+NH_2$ become less influential. One possible explanation for this phenomenon is that the temperature is sufficiently high to initiate reactions of nitrogen compounds with other nitrogen or carbon compounds, such as the reactions of NH_2+NH/NH_2 to form N_2H_2 as well as the reactions NH_2+CH_3 to introduce the N–C species (CH_3NH_2, HCN, etc.). Moreover, these reactions may inhibit the activation of normal H-formation reactions ($C/N+O_2/O/HO_2/OH$), consequently reducing the probability of the reactive $H+O_2=O+OH$ reaction. On the other hand, the stronger the H-C chemistry leads to more HCN accumulation. Its pronounced subsequent reaction pathway of HCN→CN →NCO→HNCO→CO generates CO continuously (cf. Figure 6.7), which can also explain why the CO remains nearly constant after reaching its peak. From the SA at 1100 K, it is evident that the O_2-related reactions, e.g., $NH_3+O_2=NH_2+HO_2$ and $H+O_2=O+OH$ dominate the reactivity of the mixtures. Besides, cross-reactions of NH_2 with $C_2H_6/C_2H_4/CH_3$ play a key player in the SA indicating the importance of introducing the N–C cross-system to obtain reasonable simulations.

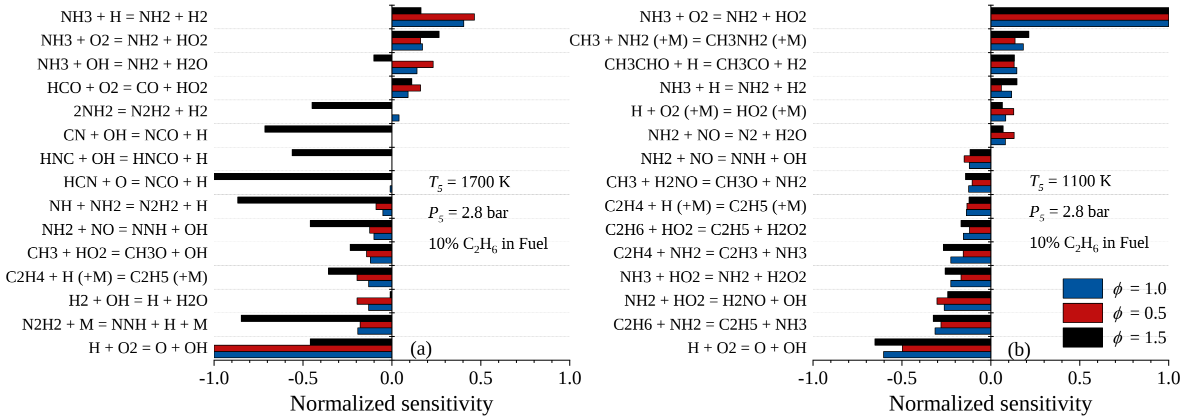

Fig. 6.6. Sensitivity analysis of IDT (Position of CO max.) for the mixtures with 10% C_2H_6 fractions and different equivalence ratios (ϕ) at 2.8 bar and a) 1700 K and b) 1100 K. The negative value indicates the promotion of the reactivity while a positive value implies the inhibiting effect.

Figure 6.7 shows the reaction pathways of NH_3/C_2H_6 and NH_3/C_2H_5OH mixtures at the location of the maximum derivative of pressure. Because C_2 species consume before the consumption of NH_3 (cf. Figure A6.11 in Appendix), the reaction paths are mainly NH_3-related, which can also be confirmed from the measured speciation profiles where the formation of CO is before the formation of NO (cf. Figure 2.11).

NH_3 is primarily consumed by OH/H/O radicals to form NH_2. These NH_2 radicals can either combine with NH/NH_2 (approximately 18%) through the reaction pathway of $NH_2 \rightarrow N_2H_2 \rightarrow H_2NN \rightarrow N_2$ or undergo further dehydrogenation to NH (around 66% to 68%) following the subsequent pathway $NH \rightarrow (HNO)N \rightarrow NO \rightarrow (N_2O)N_2$. While the typical oxidation step of NH_2 at low-to-intermediate temperatures (JSR conditions) through $NH_2 \rightarrow H_2NO \rightarrow HNO \rightarrow NO \rightarrow NO_2 \rightarrow N_2O \rightarrow N_2$, is absent in the present analyzed location of the reaction pathway. A mere 3% of NH_2 converts back to NH_3 by self-reaction, which contrasts with low-to-intermediate temperatures, where nearly 58% of NH_2 (cf. Figure 4.7) engages in cross-reaction with major C-species, e.g., $C_2H_6/CH_2O/C_2H_4$, to regenerate NH_3. As mentioned earlier, such differences are attributed to the rapid consumption and transformation of the C_2-additives and their intermediate species before the investigated location. These hydrocarbon oxidation processes introduce numerous small radicals, such as H, OH, and CH_3, facilitating the reactive radical pool. In the initial oxidation stage, some of the CH_3 radicals react with NH_2, leading to intersystem-crossing chemistry through $CH_3NH_2 \rightarrow CH_2NH_2 \rightarrow CH_2NH \rightarrow H_2CN \rightarrow HCN$. Consequently, these accumulated HCN species are well-pronounced at the test location, which will further be transformed into CN, NCO, HNCO, and CO.

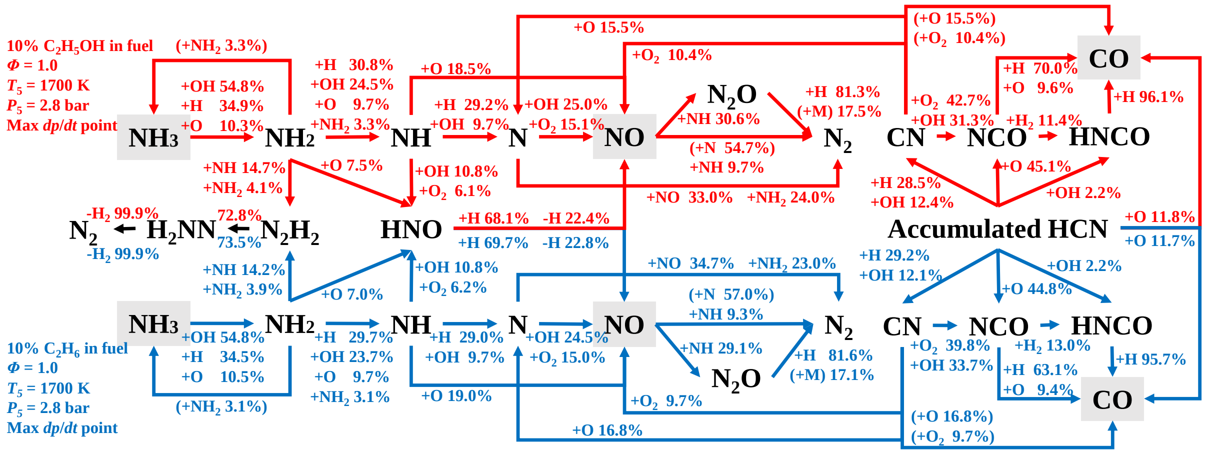

Fig. 6.7. Reaction pathways of NH_3/C_2H_6 (blue) and NH_3/C_2H_5OH (red) mixtures at the location of the maximum derivative of pressure (T_5 = 1700 K, P_5 = 2.8 bar, $NH_3:C_2$ = 90:10, ϕ = 1.0). Numbers indicate the ratio of the rate of a specific reaction to the total consumption rate of a species at the beginning of an arrow. Repeated reactions are shown in the bracket. Species experimentally measured are highlighted in grey.

https://doi.org/10.7795/110.20241024

6.2.3 Conclusion

Three Mid-IR lasers of QCL-NH_3, ICL-CO, and ICL-NO have been integrated into the shock tube. Using a fixed-wavelength laser absorption spectroscopy, time-resolved NH_3, NO, and CO profiles of both NH_3/C_2H_6 and NH_3/C_2H_5OH mixtures were measured in the shock tube for the first time, covering a temperature range of 1317-1957 K at around 2.8 bar, incorporating 5-20% C_2H_6 or C_2H_5OH in the fuel mixture, three equivalence ratios (0.5/1.0/1.5), and a constant argon dilution ratio of 0.9.

The experimental IDTs exhibit a typical Arrhenius temperature dependence. The promotional effect of adding either C_2H_6 or C_2H_5OH on ammonia ignition is consistently observed. The dependence of IDT on equivalence ratios for both NH_3/C_2H_6 and NH_3/C_2H_5OH mixtures remains consistent, i.e., IDT decreases as the equivalence ratios decrease. This trend contrasts with the results obtained in the rapid compression machine (5 - 10% C_2H_6/C_2H_5OH in the fuel mixtures). From the simulation and kinetic analysis, the opposite equivalence ratio-dependency is dominated by temperature rather than pressure.

The measured speciation profiles demonstrate reasonable relations between the consumption of NH_3 and the formation of NO and CO. The formation of CO initiates immediately with the oxidation process and continues to rise until reaching a peak value, which is prior to that of NO. For fuel-rich mixtures, CO reaches its peak and then remains almost unchanged. For NO profiles, the formation occurs and then levels off at a certain plateau. The maximum NO value decreases at lower temperatures and higher equivalence ratios, which is consistent with the observations for pure NH_3 and NH_3/H_2 oxidation in the shock tube [66,67].

The updated mechanism can satisfactorily reproduce the predictions of IDTs and speciation profiles under broad conditions. Addressing observed discrepancies, especially in fuel-rich mixtures, is crucial to enhance the predictive accuracy of the mechanism.

The kinetic analysis suggests that the C_2-hydrocarbon additives contribute additional OH/H/CH_3 radicals, which either build an N–C intersystem-crossing chemistry or facilitate the reactive radical pool. The promoting effect of C-chemistry from C_2H_6 and C_2H_5OH shows a comparable limited role since the high temperature of ST conditions eliminates the hindrance to ammonia oxidation by the activation energy barrier of NH_3-related reactions, leading to the dominance of N-chemistry in the oxidation. An additional sensitivity analysis under different equivalence ratios (ϕ) indicates that the reactions related to N_2H_2 and N–C chemistries contribute to the distinct dependence of IDTs on ϕ at high-temperature conditions. Furthermore, the N–C chemistries, particularly the pronounced reaction pathway of HCN→ CN→NCO→HNCO→CO play a crucial role in maintaining the CO level constant after reaching its peak position under fuel-rich conditions.

The main reaction pathway of NH_3 consumption at high temperatures is NH_3→NH_2→NH→N(HNO)→NO→(N_2O)N_2, differing from the typical oxidation step of NH_2 at low-to-intermediate temperatures in JSR conditions through NH_2→H_2NO→HNO→NO→NO_2→N_2O→N_2. The C_2-additives participate in the oxidation process by introducing additional OH/H/CH_3, thereby facilitating the reactive radical pool and developing the N–C intersystem-crossing pathways.

https://doi.org/10.7795/110.20241024

7. Summary and Perspective

7.1 Summary

Ammonia (NH_3) has gained attention as a potential carbon-free energy source, but its high auto-ignition temperature and low burning velocity present challenges. This thesis addresses these issues by blending ammonia with C_2-hydrocarbon fuels as additives, such as ethane (C_2H_6), ethanol (C_2H_5OH), and DME (CH_3OCH_3), offering a promising solution. In this work, the oxidation properties of NH_3/C_2 fuel blends have been investigated over a wide temperature (500 - 2000 K) and pressure (1 - 40 bar) range. Additionally, a comprehensive chemical kinetic model, PTB-NH_3/C_2 mech, has been systematically developed for ammonia fuel blends ranging from hydrogen to major C_2 hydrocarbons, which was validated against the experimental data including ignition delay times (global process reflection) and speciation measurements (molecule-scale process information). This validated and persuasive mechanism was then utilized for kinetic analysis to comprehend the combustion mechanisms of ammonia/C_2 fuel blends, which would further advance the application of ammonia as a fuel.

7.1.1 Ammonia/C_2 fuel blends at low-to-intermediate temperatures

The speciation experiments of NH_3/C_2H_6 and NH_3/C_2H_6O-isomers mixtures at atmospheric pressure (1 bar) and low-to-intermediate temperatures (700 - 1180 K for ethane cases and 450 - 1180 K for ethanol/DME cases) were performed by a jet-stirred reactor (JSR) coupled with a time-of-flight molecular-beam mass spectrometer (MBMS). The experimental results demonstrate that adding C_2-promoter fuels into NH_3 has a substantial effect on the reactivity of the ammonia oxidation. The newly developed model (PTB-NH_3/C_2 mech) can reasonably simulate the measured data, and reproduce both effects of C_2-promoter fraction and equivalence ratio on speciation under broad conditions.

For NH_3/C_2H_6 mixtures, the kinetic analysis indicates that the chain-branching reaction of $H+O_2=OH+O$ under the tested JSR conditions generates large amounts of reactive radicals triggering the early radical-initiated NH_3 consumption. As the temperature increases to a certain level (e.g., 1100 K for 10% C_2H_6 addition), the activation energy barrier (E_a) of the most NH_3-related reactions is exceeded, resulting in a fast NH_3 consumption. It was identified that the reactions associated with the C_2-promoter provide a more reactive radical pool already at relatively low temperatures through the decompositions of $C_2H_5/HCO/CH_3O$ generating H radical. These H radicals further form OH radicals via reactions such as $O_2+H=O+OH$, and its subsequent reactions of $C_2H_6/NH_3+O=C_2H_5/NH_2+OH$. The formed OH participates in the two NH_3 consumption stages leading to a more reactive ammonia fuel mixture. The investigation of NH_3/C_2H_6O-isomers (i.e., CH_3OCH_3/C_2H_5OH) mixtures reveals that the addition of both fuels influences ammonia oxidation differently, with three oxidation regimes (1^{st}, 2^{nd}, and 3^{rd}) as well as an NTC behavior observed for CH_3OCH_3 addition but only two regimes (2^{nd} and 3^{rd}) for C_2H_5OH addition (similar with the C_2H_6 case). In specific, the 1^{st} oxidation regime highlights the unique role of

https://doi.org/10.7795/110.20241024

CH_3OCH_3 in promoting NH_3 consumption at 600 K as well as the subsequent NTC phenomenon, through specific low-temperature kinetics and the influence of OH radical production. In the 2nd regime, the DME chemistry exhibits more importance in ammonia oxidation by competing for OH radicals with the NH_3 chemistry, which is less significant when adding ethanol. Nonetheless, NH_3 consumption with both promoter fuels follows identical chemical reaction paths initiated by the reaction of NH_3+OH. Moreover, nitrous acid HONO at 900 K tends to be a key species in NO and NO_2 formation. The 3rd oxidation regime is characterized by rapid NH_3 consumption primarily governed by NH_3 chemistry and independent from the promoter fuel.

7.1.2 Ammonia/C_2 fuel blends at intermediate temperatures

Ignition delay time measurements of NH_3/C_2H_6 and NH_3/C_2H_5OH fuel blends at intermediate temperatures (820 - 1120 K) and elevated pressures (20 - 40 bar) were conducted in a rapid compression machine (RCM). It is observed that the C_2-hydrocarbon addition has a substantial effect on ammonia ignition, with the following promotional effects compared to other blended fuels: 5% C_2H_5OH > 5% CH_3OH > 5% C_2H_6 > 5% H_2 > 10% CH_4. Besides, the PTB-NH_3/C_2 mech reproduces the measurements of IDT very well for most conditions. It is found that, the addition of cross-reactions to the mechanism between the two fuels is necessary to obtain reasonable simulations, especially in the case of NH_3/C_2H_5OH.

The kinetic analysis indicates that the addition of ethane/ethanol into ammonia provides N–C intersystem pathways and enriches the O/H radical pool, which will significantly promote the auto-ignition process leading to a lower ignition temperature than the observed for pure ammonia. Compared with the sensitive reactions under JSR conditions, notable changes were observed in the dominant reactions of the NH_3 oxidation at RCM conditions. Specifically, the HO_2 radical instead of the H radical plays an important role and its related reactions dominate the auto-ignition process across a wide temperature range, e.g., H- abstraction of C_2H_6 by HO_2 as well as the duplicated self-reaction of HO_2 becomes the most promoting and inhibiting reactions, respectively, while the important reaction of H+O_2 from JSR conditions show no influence in the autoignition process at RCM conditions.

7.1.3 Ammonia/C_2 fuel blends at intermediate-to-high temperatures

The oxidation of both NH_3/C_2H_6 and NH_3/C_2H_5OH mixtures at intermediate-to-high temperatures (1320 - 1960 K) and intermediate pressures (2.4 - 3.1 bar) was investigated in a shock tube (ST) using laser absorption spectroscopy (LAS). The promotional effect of adding either C_2H_6 or C_2H_5OH on ammonia ignition is consistently observed under ST conditions. Besides, it shows that the dependence of IDT on equivalence ratios for both NH_3/C_2H_6 and NH_3/C_2H_5OH mixtures remain consistent, i.e., IDT decreases as the equivalence ratios decrease, which trend contrasts with the results obtained in the rapid compression machine (5 - 10% C_2H_6/C_2H_5OH in the fuel mixtures). The measured speciation profiles

https://doi.org/10.7795/110.20241024

demonstrate reasonable relations between the consumption of NH_3 and the formation of NO and CO. In particular, CO forms immediately during the oxidation process, whose peak is before NO, and remains nearly constant at fuel-rich conditions after reaching its peak. The updated mechanism can satisfactorily reproduce the predictions of IDTs and speciation profiles under broad conditions.

The kinetic analysis suggests that the C_2-hydrocarbon additives contribute additional OH/H/CH_3 radicals, which either build an N–C intersystem-crossing chemistry or facilitate the reactive radical pool. However, the promoting effect of C-chemistry from C_2H_6 and C_2H_5OH shows a comparable limited role since the high temperature of ST conditions eliminates the hindrance to ammonia oxidation by the activation energy barrier of NH_3-related reactions, leading to the dominance of N-chemistry in the oxidation. Additionally, the sensitivity analysis under different equivalence ratios (ϕ) indicates that the reactions related to N_2H_2 and N–C chemistries contribute to the distinct dependence of IDTs on ϕ at high-temperature conditions. Moreover, N–C chemistries, particularly the pronounced reaction pathway of HCN→CN→NCO→HNCO→CO, play a crucial role in maintaining the CO level constant after reaching its peak position under fuel-rich conditions.

7.2 Perspective

7.2.1 Continuous development of the mechanism

Since the mechanism of the PTB-NH_3/C_2 mech has only been validated against the measured data from mixtures of NH_3/C_2H_6, NH_3/C_2H_5OH, and NH_3/CH_3OCH_3, it remains subject to continuous development. On one hand, the global process reflection from the laminar flame velocities (LBV) should be also used to test the overall performance of the mechanism for the ammonia/C_2 fuel blends. On the other hand, speciation experiments demonstrate the importance of intermediates such as CH_2O, C_2H_4, and CH_3CHO in the oxidation of the NH_3/C_2 mixture, while their predicted mole fractions do not perfectly match measurements, indicating that the sub-mechanism of these intermediates still requires improvement. For this reason, molecule-scale process information from speciation measurements of pure CH_2O, C_2H_4, and CH_3CHO fuels, as well as their blends with ammonia fuel mixtures in the JSR-MBMS setup, should be incorporated into future mechanism development efforts. Furthermore, it would be valuable to explore ammonia combustion (or its less pronounced oxidation) under extreme conditions, such as high temperatures with ultra-low pressure conditions similar to those on other planets. This research may also provide critical insights for future space exploration and the simulation of extraterrestrial environments.

7.2.2 Reactor with high-resolution diagnostics

In the current work, we have integrated a jet-stirred reactor with an electron ionization (EI) source mass spectrometer (MS), which has provided a large number of species information. However, utilizing EI as a source will bring challenges due to fragmentation reactions during the ionization process, leading to higher uncertainty in the raw spectrum data. Besides, the molecules with similar masses (e.g., N_2O and

https://doi.org/10.7795/110.20241024

CO_2 in this study) or isomers (e.g., CH_3OCH_3 and C_2H_5OH) are difficult to differentiate. To address these issues, photoionization (PI) can be utilized in the ionization process of MS. By selecting appropriate photon energies, fragmentation reactions can be significantly minimized, and isomers with distinct ionization energies can be distinguished. Moreover, combining laser absorption spectroscopy (LAS) with our current setup of MBMS is a feasible solution to enhance the visualization of specific molecules, such as NO_x, thereby compensating for the lack of accuracy in EI-MBMS detection.

7.2.3 Construction of a database on ammonia combustion

Increasing digitization and the associated production of data have propelled us into the era of information explosion. Numerous sectors are witnessing a rapid increment of information available such as economics, healthcare, and scientific research. Therefore, a science that focuses on leveraging and mining data has assumed paramount significance. Data science can take superficial data to a profound level by utilizing scientific methods and algorithms to provide forward-looking insights and knowledge. In the domain of combustion research, fundamental combustion experiment studies are indispensable tools for developing and validating intricate kinetic models. Over the past few decades, tremendous experimental data have been consistently available, which normally include the global process reflection such as ignition delay times and flame speeds, as well as the molecule-scale process information from speciation. However, most of these investigated studies merely focus on specific fuels (or fuel blends e.g., NH_3/C_2H_6 mixture) and individual conditions, which may lead to the inability to develop a comprehensive validated model. Consequently, utilizing database science techniques to analyze a wide range of combustion data from different flame studies becomes particularly important. This approach may help bridge gaps between individual studies and facilitate the development of comprehensive validated models.

https://doi.org/10.7795/110.20241024

Appendix

Chapter 2: Theoretical Basis and Experimental Method.

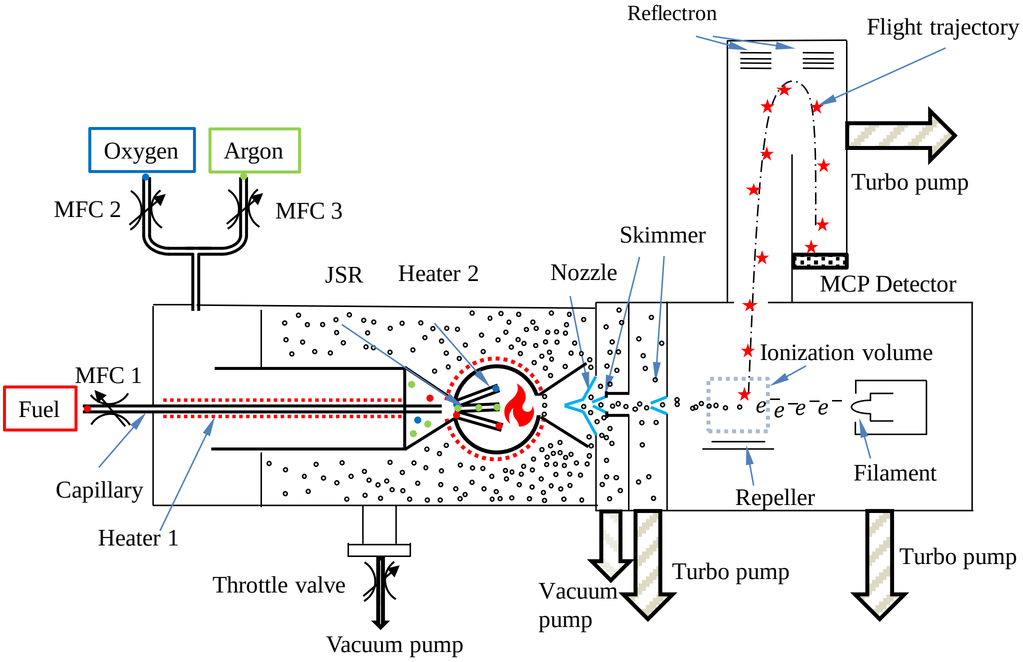

Fig. A2.1. The schematics of the JSR-MBMS system.

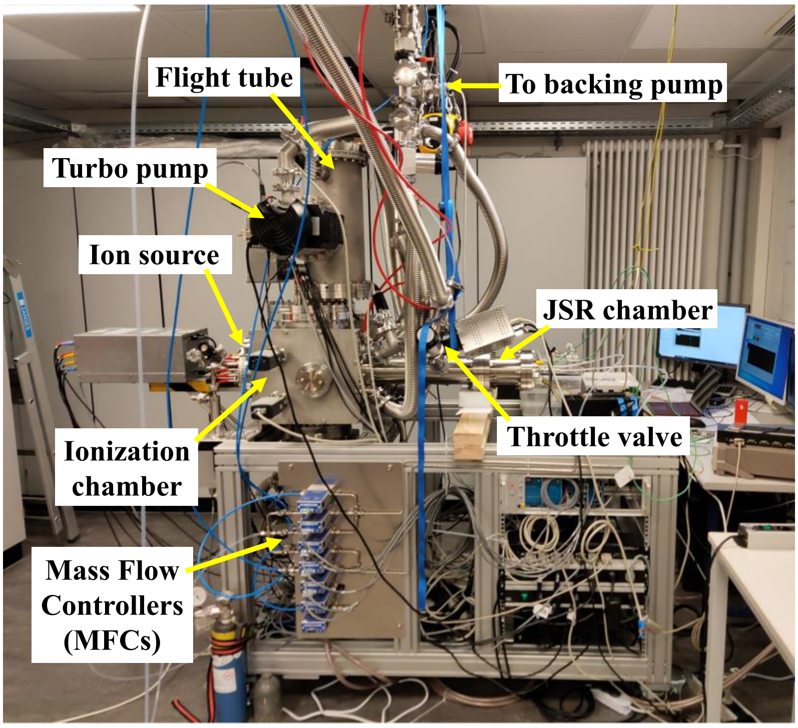

Fig. A2.2. The photo of the JSR-MBMS system.

https://doi.org/10.7795/110.20241024

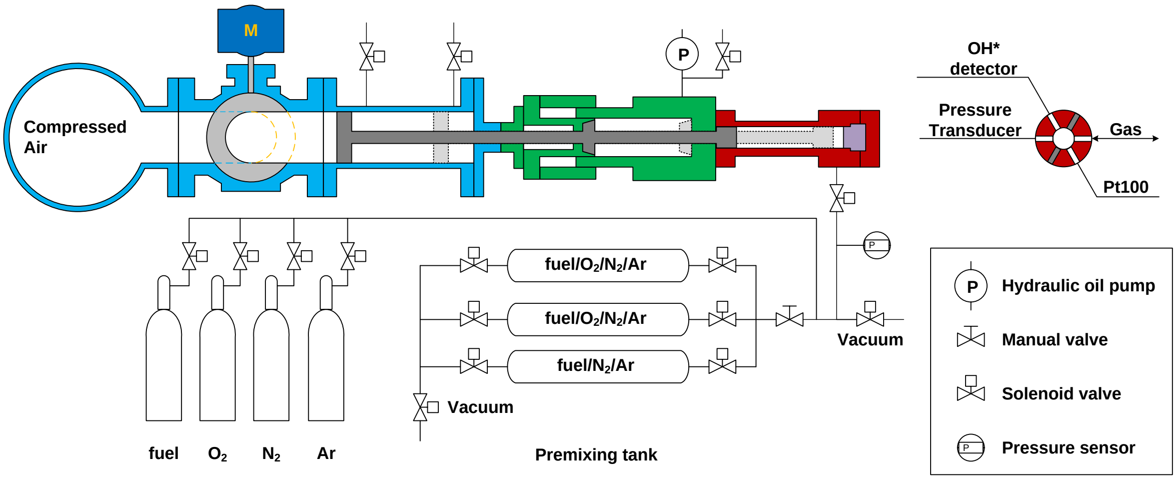

Fig. A2.3. The schematics of the RCM system.

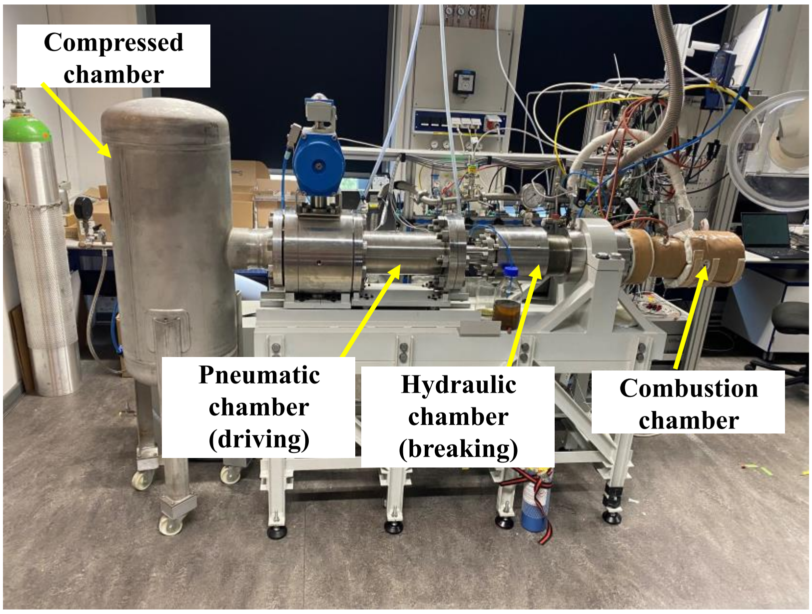

Fig. A2.4. The photo of the RCM system.

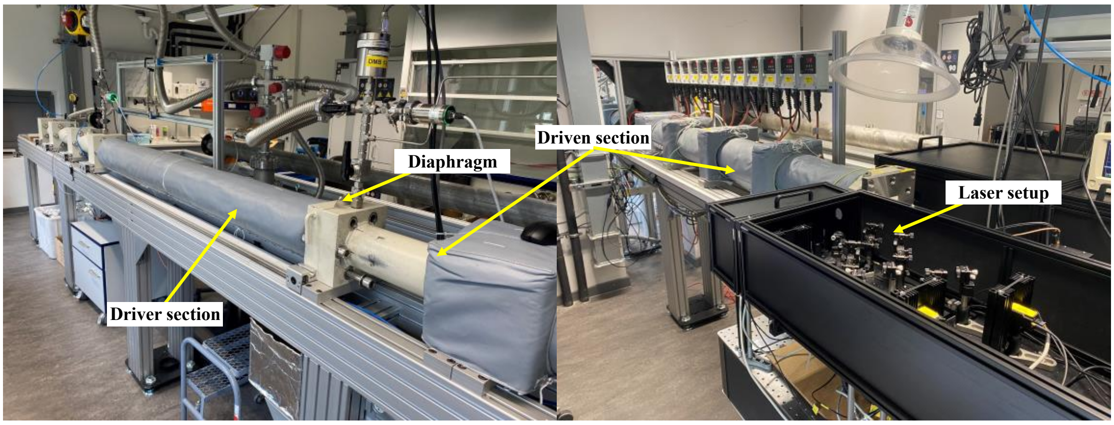

Fig. A2.5. The photo of the ST system.

https://doi.org/10.7795/110.20241024

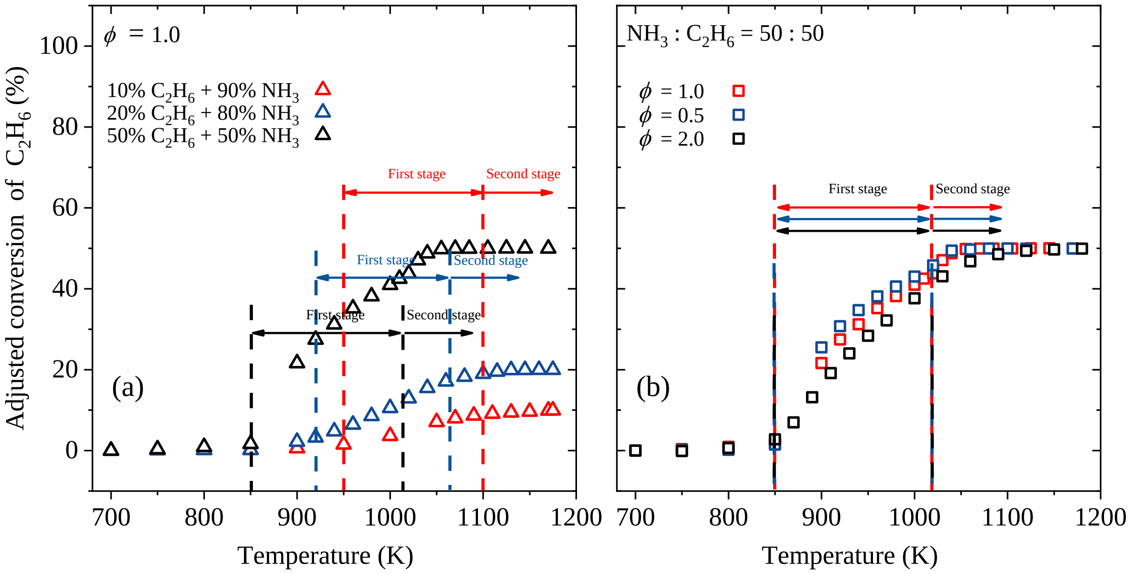

*Fig. A4.1. Adjusted conversion ratio of C_2H_6 for (a) different C_2H_6 mole fractions in fuel, at P_{JSR} = 1 bar, ϕ = 1.0; and (b) different equivalence ratio (ϕ), at P_{JSR} = 1 bar, with 50% C_2H_6 in fuel. The adjusted conversion ratio is defined as its conversion as a percentage of the overall fuel, namely adjusted conversion ratio of C_2H_6 = conversion ratio of C_2H_6 * C_2H_6 mole fraction in the fuel.*

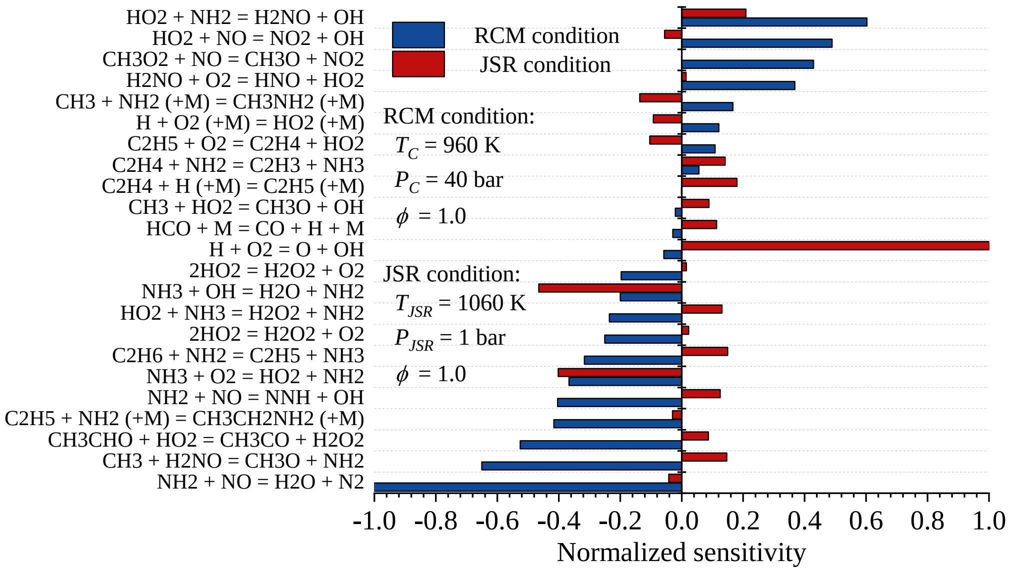

Fig. A4.2. Sensitivity analysis of OH radical at JSR and RCM conditions for the stoichiometric mixture with 10% C_2H_6 fractions. The positive value represents the promotion of OH formation and the negative value represents the opposite.

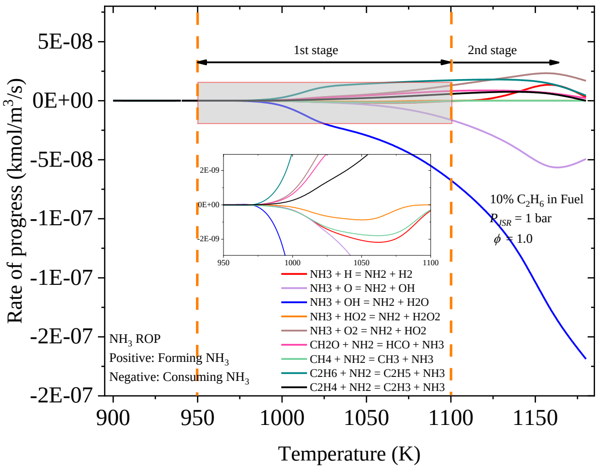

Fig. A4.3. Rate of production analysis for NH_3 at JSR condition for the stoichiometric mixture with 10% C_2H_6 fractions. The negative value represents consuming NH_3, and the positive value represents forming NH_3.

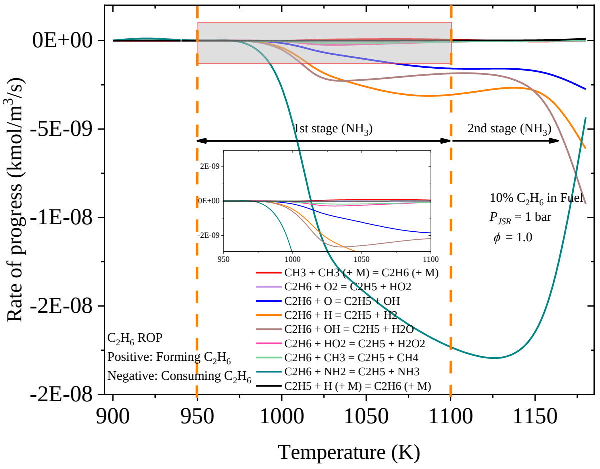

Fig. A4.4. Rate of production analysis for C_2H_6 at JSR condition for the stoichiometric mixture with 10% C_2H_6 fractions. The negative value represents consuming C_2H_6, and the positive value represents forming C_2H_6.

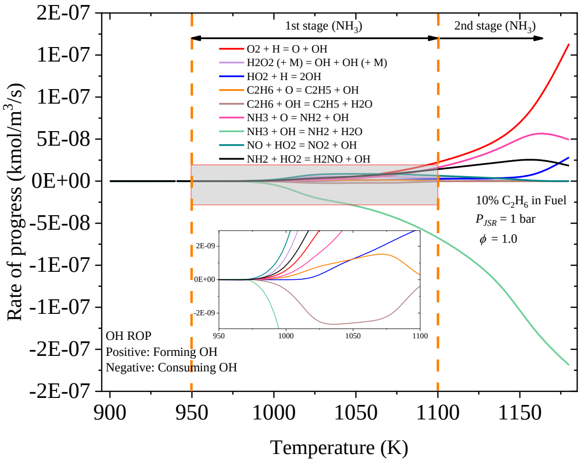

Fig. A4.5. Rate of production analysis for OH radical at JSR condition for the stoichiometric mixture with 10% C_2H_6 fractions. The negative value represents consuming OH radicals, and the positive value represents forming OH radicals.

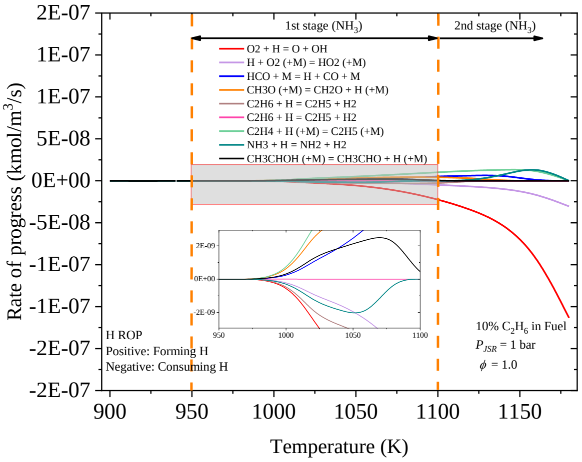

Fig. A4.6. Rate of production analysis for H radical at JSR condition for the stoichiometric mixture with 10% C_2H_6 fractions. The negative value represents consuming H radical, and the positive value represents forming H radical.

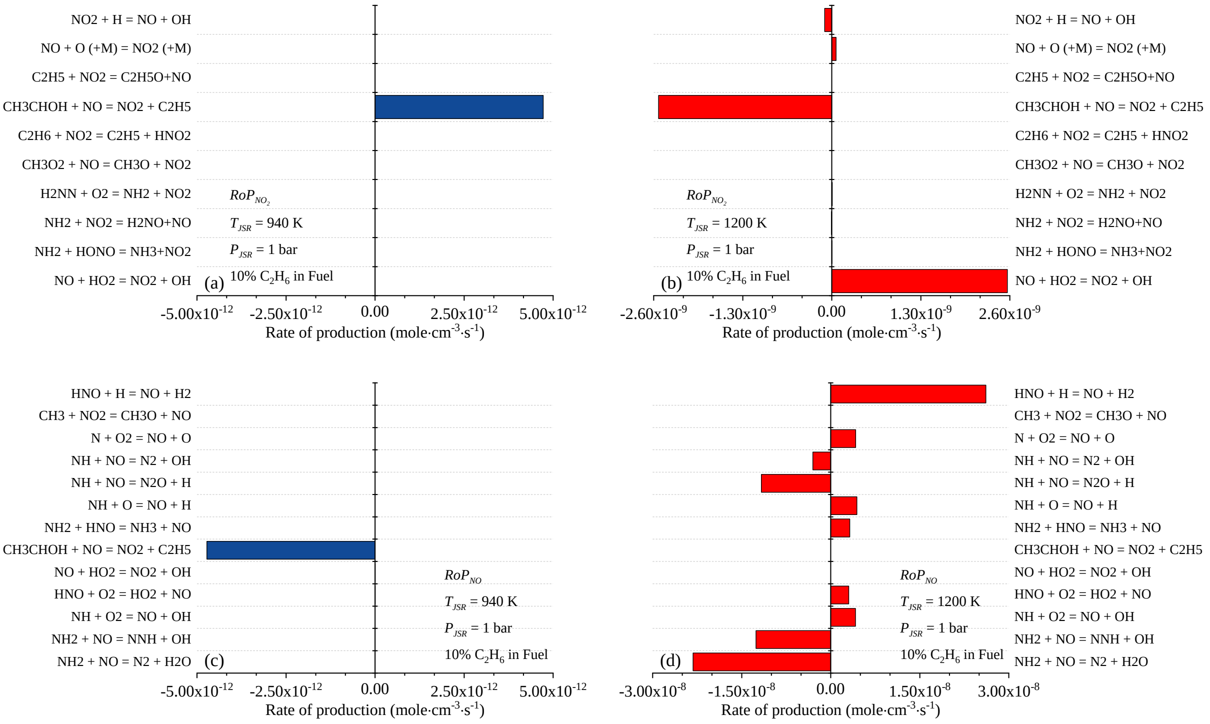

Fig. A4.7. Rate of production analysis for a) NO_2 at 940 K, b) NO_2 at 1200 K, c) NO at 940 K, and d) NO at 1200 K for the stoichiometric mixture with 10% C_2H_6 fraction. The negative value represents the consumption of NO_2/NO, and the positive value represents the formation of NO_2/NO. The ROP is based on the original PTB-NH_3/C_2 mech.

https://doi.org/10.7795/110.20241024

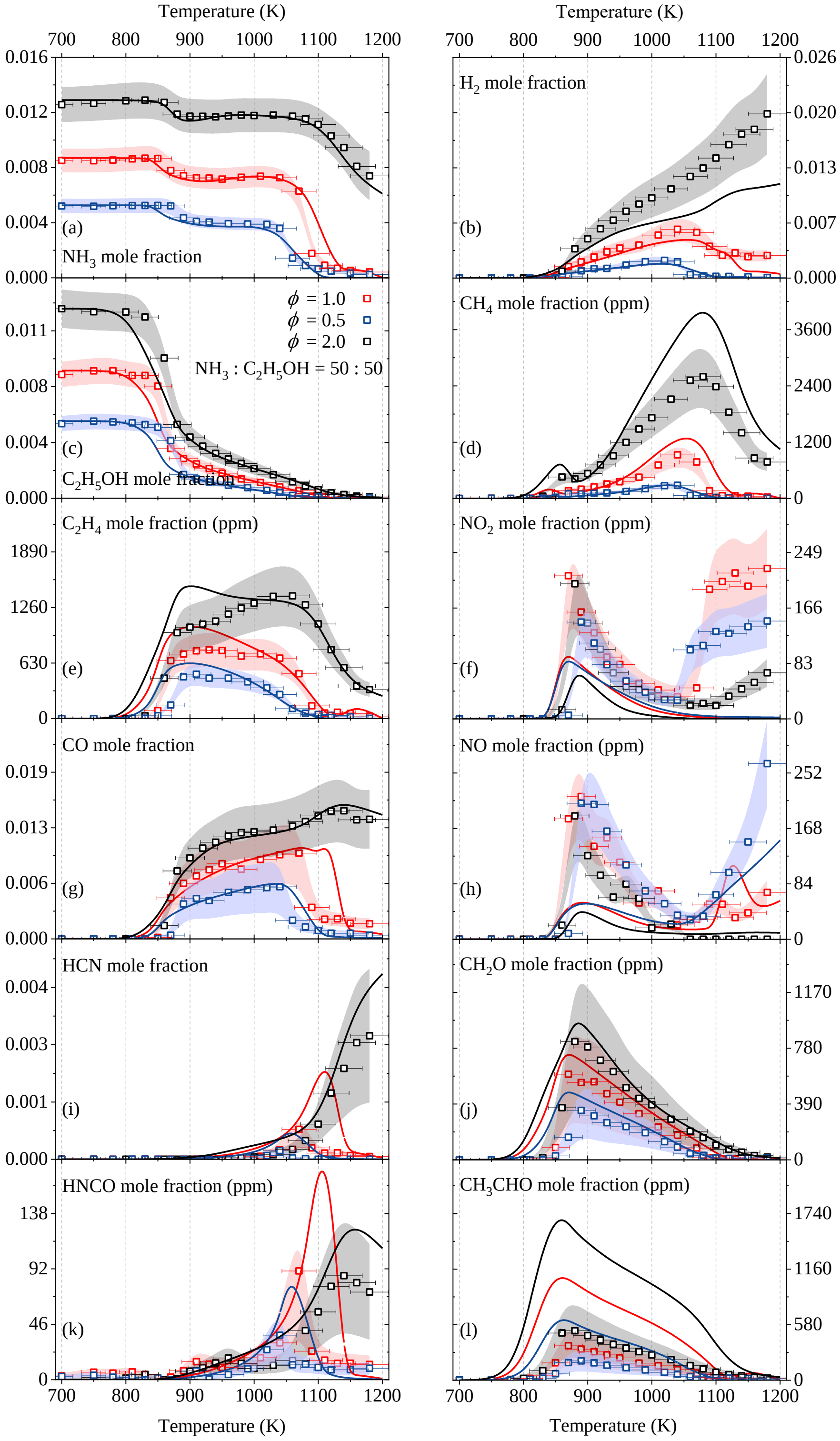

Fig. A4.8. Comparison of the measured (symbols) and simulated (lines) mole fraction profiles of a) NH_3, b) H_2, c) C_2H_5OH, d) CH_4, e) C_2H_4, f) NO_2, g) CO, h) NO, i) HCN, j) CH_2O, k) HNCO, l) CH_3CHO at P_{JSR} = 1 bar, with 50% C_2H_5OH in fuel, and different equivalence ratios (ϕ). The error bars of T_{JSR} (horizontal) and mole fraction (shade area, B-Spline) are indicated on all species.

https://doi.org/10.7795/110.20241024

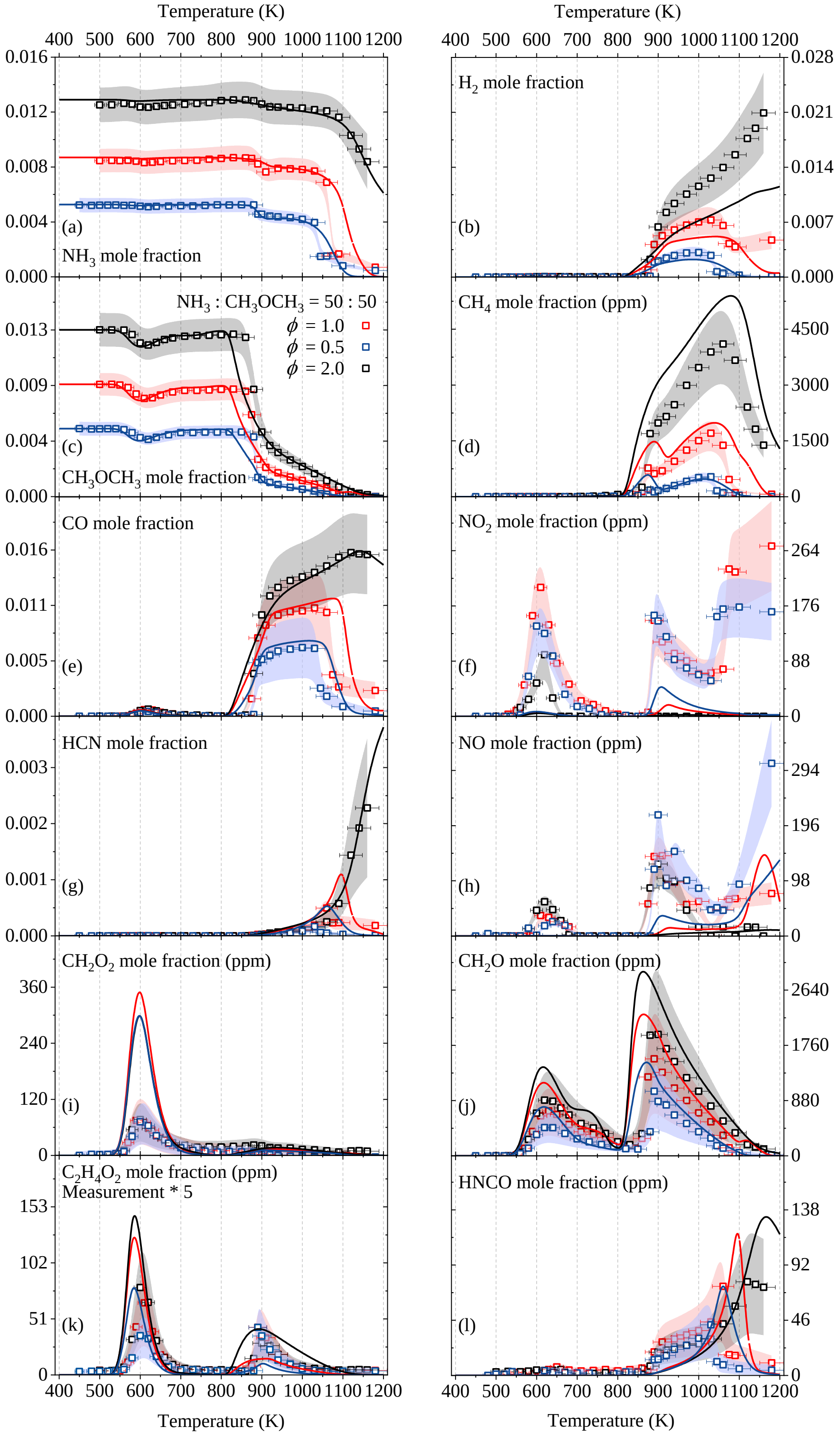

Fig. A4.9. Comparison of the measured (symbols) and simulated (lines) mole fraction profiles of a) NH_3, b) H_2, c) CH_3OCH_3, d) CH_4, e) CO, f) NO_2, g) HCN, h) NO, i) CH_2O_2, j) CH_2O, k) $C_2H_4O_2$, l) HNCO at P_{JSR} = 1 bar, with 50% CH_3OCH_3 in fuel, and different equivalence ratios (ϕ). The error bars of T_{JSR} (horizontal) and mole fraction (shade area, B-Spline) are indicated on all species.

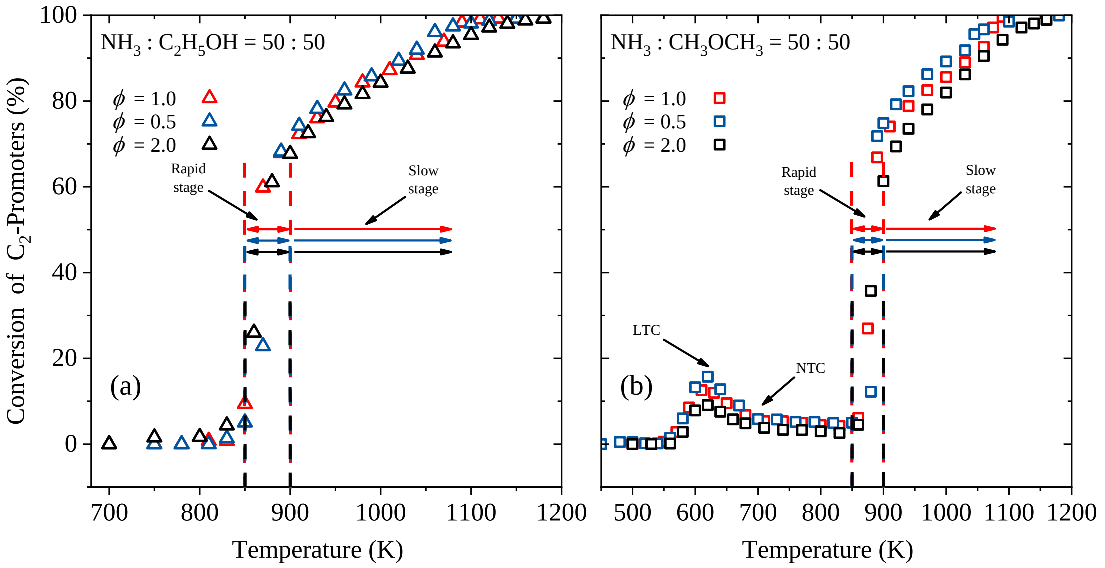

Fig. A4.10. Conversion ratio of (a) C_2H_5OH and (b) CH_3OCH_3 for different equivalence ratios (ϕ), at P_{JSR} = 1 bar, with 50% C_2-promoter in fuel.

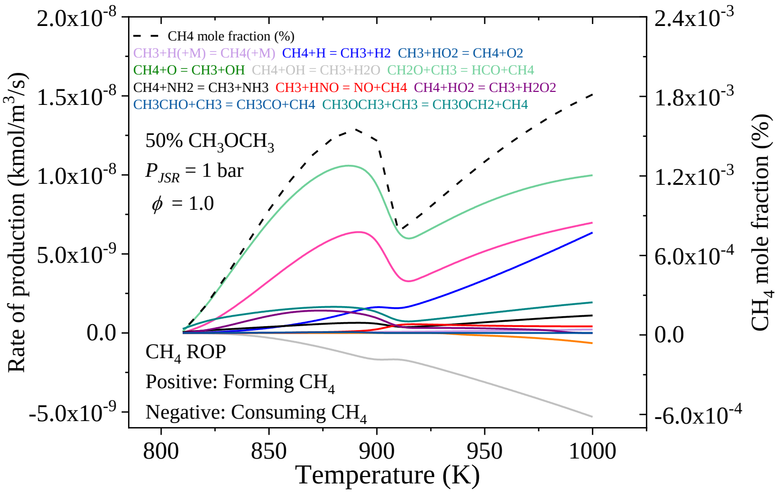

Fig. A4.11. Rate of production analysis of CH_4 radical for the exemplary NH_3/CH_3OCH_3 mixture at different temperatures. The negative value represents consuming CH_4, and the positive value represents forming CH_4.

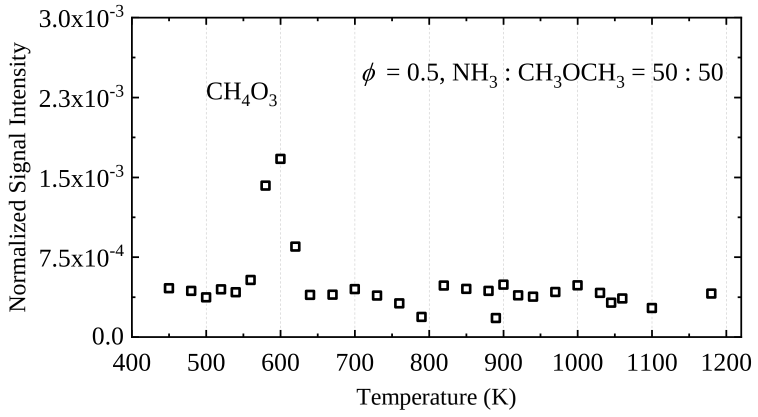

Fig. A4.12. Normalized signal intensity of CH_4O_3 for fuel-lean mixture with 50% CH_3OCH_3 in fuel, at P_{JSR} = 1 bar.

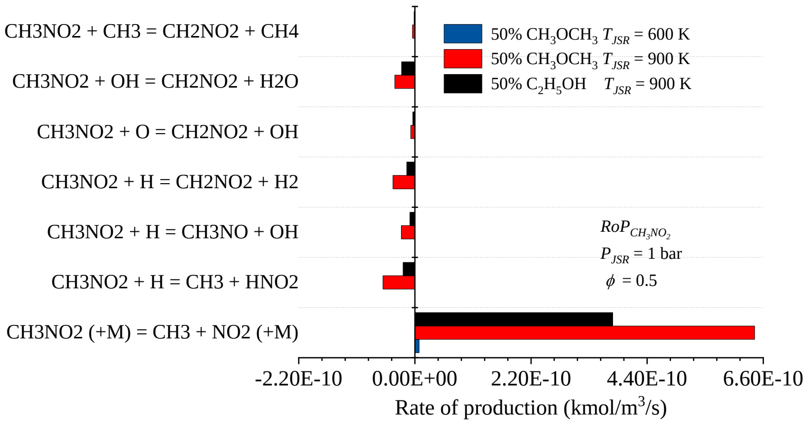

Fig. A4.13. Rate of production analysis of CH_3NO_2 for the fuel-lean mixture with 50% C_2-fuel fractions at different temperatures. The negative value represents consuming CH_3NO_2, and the positive value represents forming CH_3NO_2.

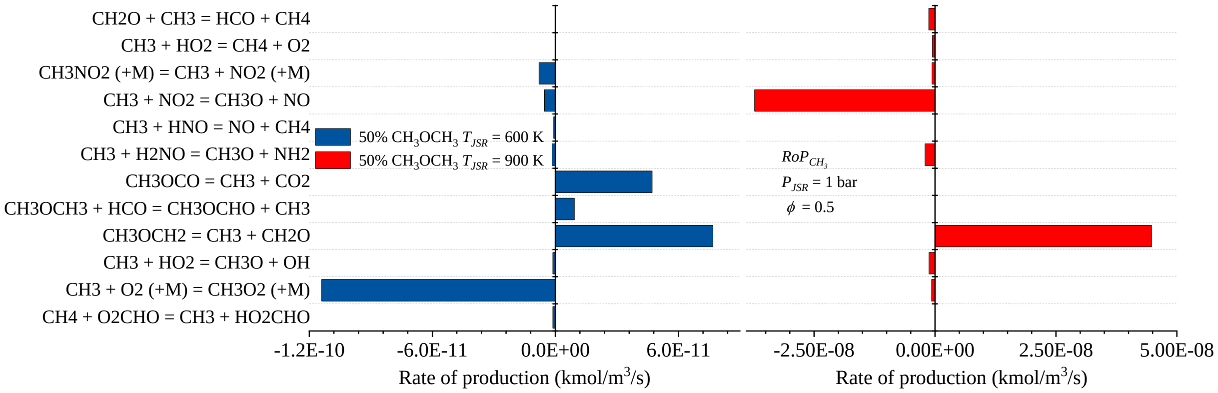

Fig. A4.14. Rate of production analysis of CH_3 for the fuel-lean mixture with 50% CH_3OCH_3 fractions at different temperatures. The negative value represents consuming CH_3, and the positive value represents forming CH_3.

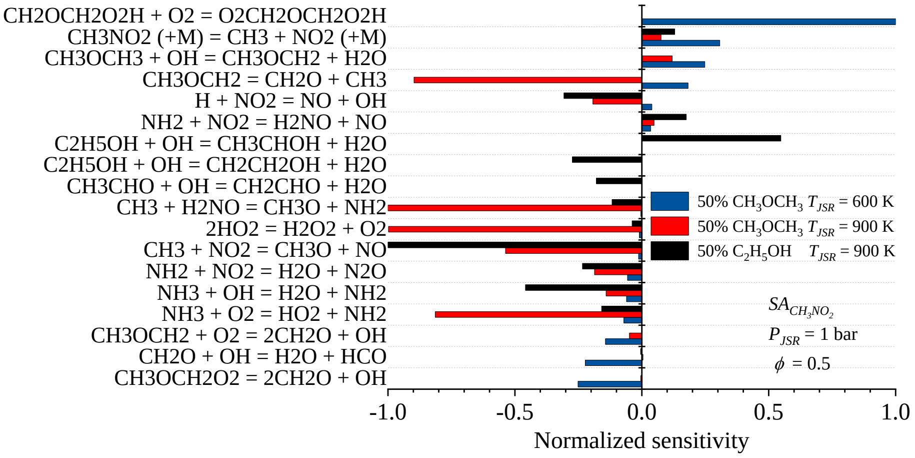

Fig. A4.15. Sensitivity analysis of CH_3NO_2 mole fraction for the fuel-lean mixture with 50% C_2-fuel fractions at different temperatures. The negative value indicates the promotion of CH_3NO_2 consumption while a positive value implies the inhibiting effect.

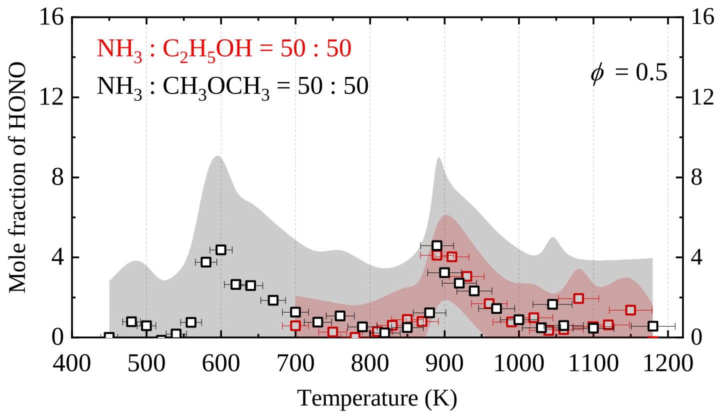

Fig. A4.16. Mole fraction profiles HONO for fuel-lean mixture with different 50% C_2 in fuel, at P_{JSR} = 1 bar. Uncertainties for mole fractions are illustrated by shaded areas and for temperature exemplary error bars are shown.

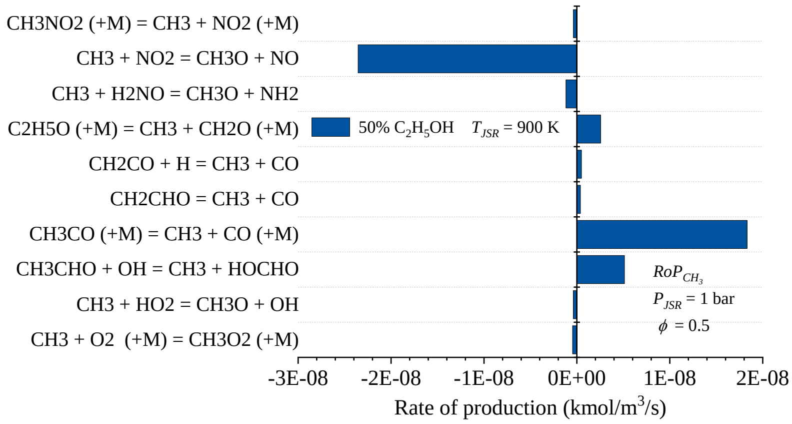

Fig. A4.17. Rate of production analysis of CH_3 for the fuel-lean mixture with 50% C_2H_5OH fractions at 900 K. The negative value represents consuming CH_3, and the positive value represents forming CH_3.

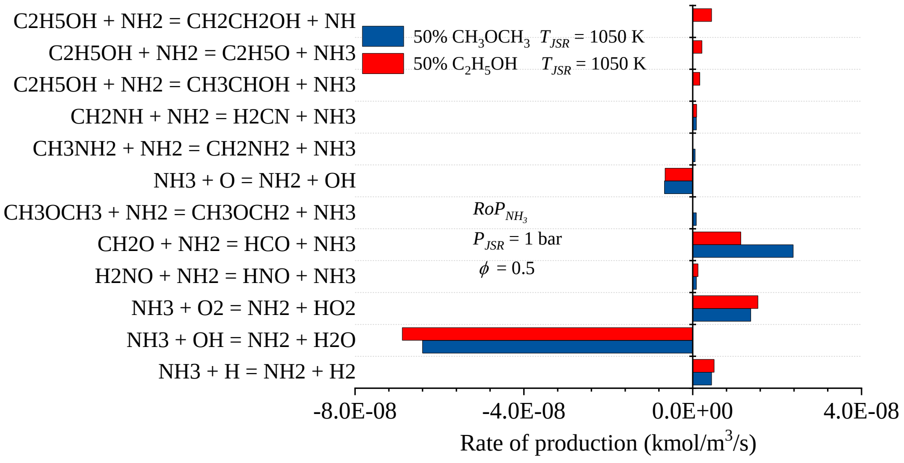

Fig. A4.18. Rate of production analysis of NH_3 for the fuel-lean mixture with 50% C_2-fuel fractions at different temperatures. The negative value represents consuming NH_3, and the positive value represents forming NH_3.

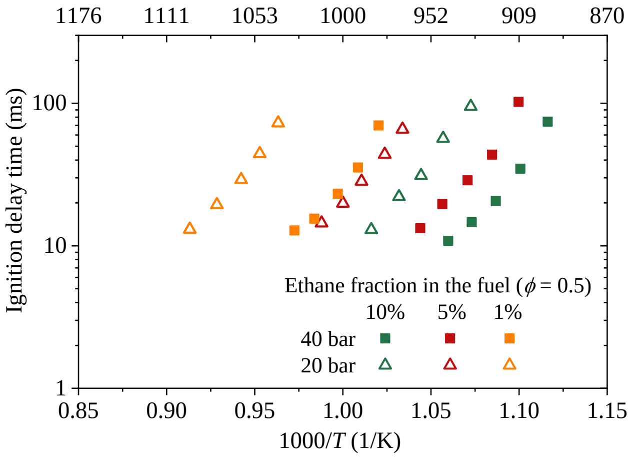

Fig. A5.1. Measured ignition delay times of NH_3/C_2H_6 fuel-lean mixtures for different C_2H_6 mole fractions in fuel at 20 and 40 bar.

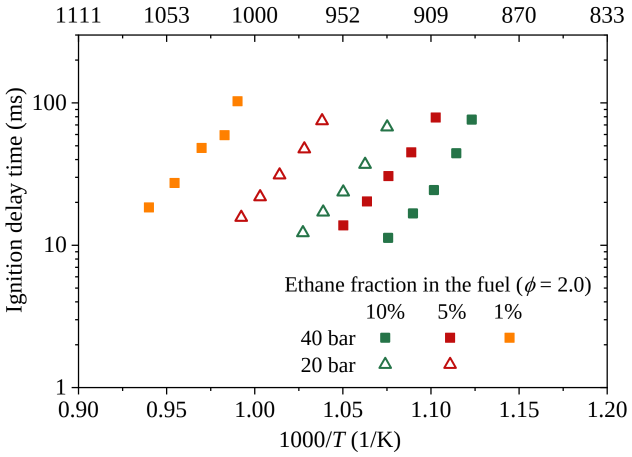

Fig. A5.2. Measured ignition delay times of NH_3/C_2H_6 fuel-rich mixtures for different C_2H_6 mole fractions in fuel at 20 and 40 bar.

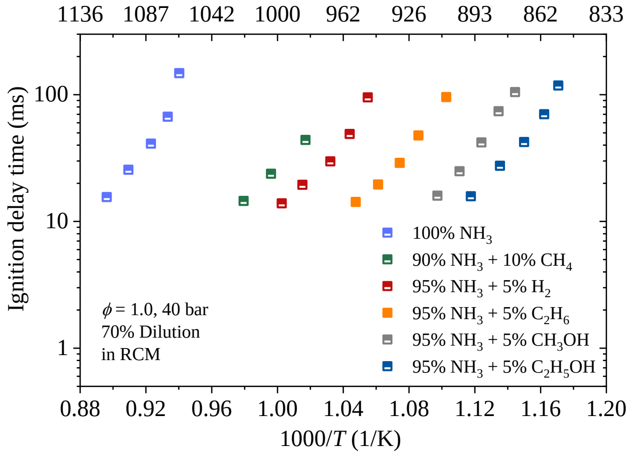

Fig. A5.3. Measured ignition delay times of the stoichiometric mixtures with pure NH_3, 10% CH_4 [9], *5% H_2* [11], *5% C_2H_6, 5% CH_3OH* [10], *5% C_2H_5OH in fuel at 40 bar.*

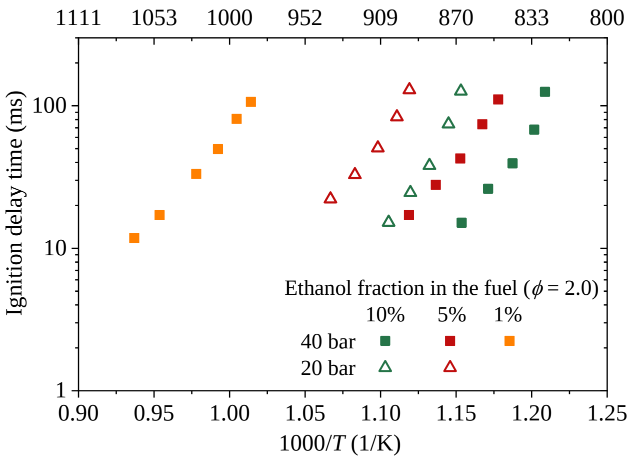

Fig. A5.4. Measured ignition delay time of NH_3/C_2H_5OH fuel-rich mixtures for different C_2H_5OH ratios at 20 and 40 bar.

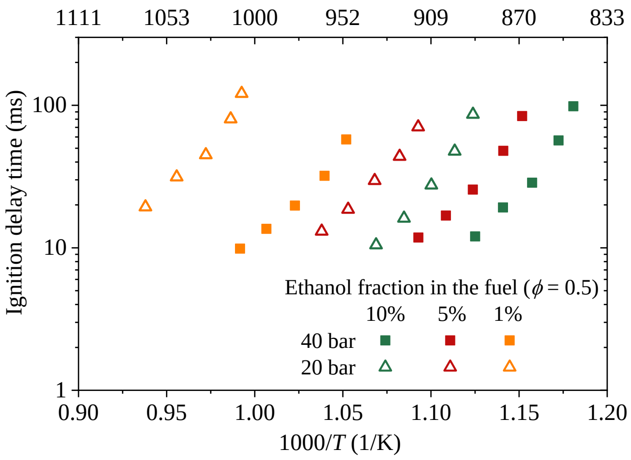

Fig. A5.5. Measured ignition delay time of NH_3/C_2H_5OH fuel-lean mixtures for different C_2H_5OH ratios at 20 and 40 bar.

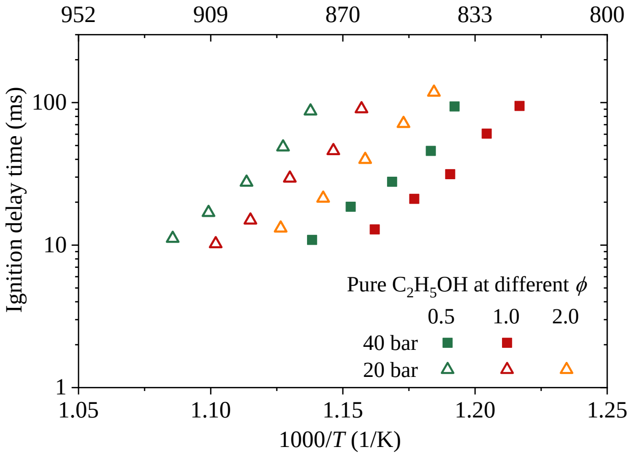

Fig. A5.6. Measured ignition delay time of pure C_2H_5OH mixtures for different equivalence ratios at 20 and 40 bar.

https://doi.org/10.7795/110.20241024

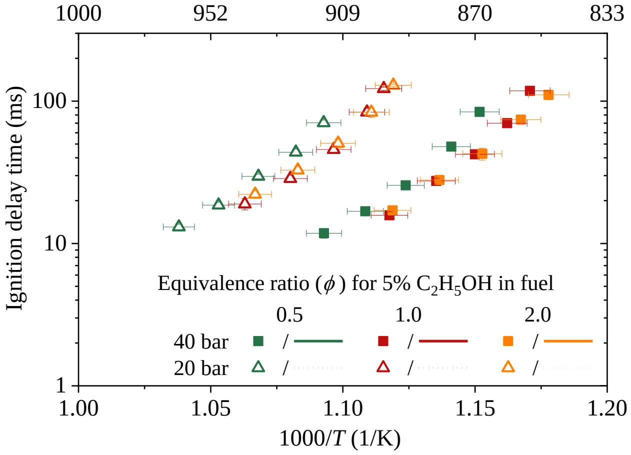

Fig. A5.7. Measured ignition delay time of the mixtures with 5% C_2H_5OH in fuel for different equivalence ratios at 20 and 40 bar. Missed lines of simulations because of less than two ignited points or no ignition.

Chapter 6: The experimental and kinetic study of NH_3/C_2 fuel blends oxidation at intermediate pressures and intermediate-to-high temperatures.

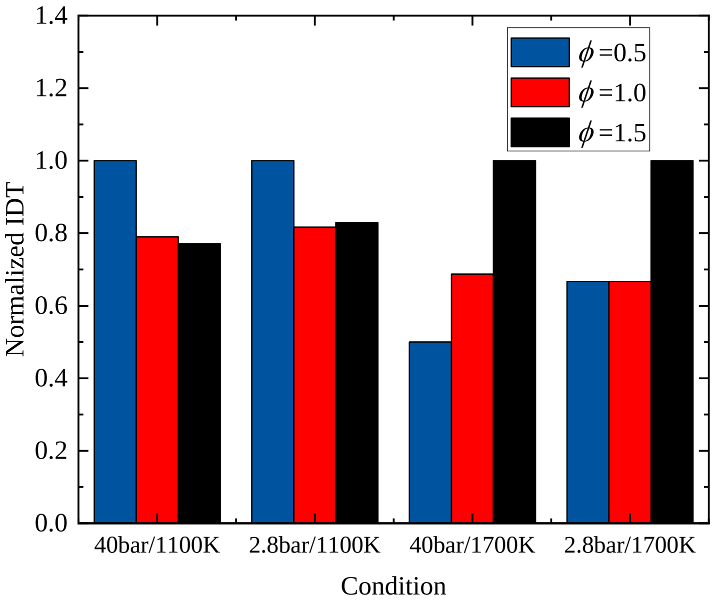

Fig. A6.1. Normalized simulated ignition delay time of the mixtures with 10% C_2H_6 in fuel for different equivalence ratios at various temperature and pressure conditions.

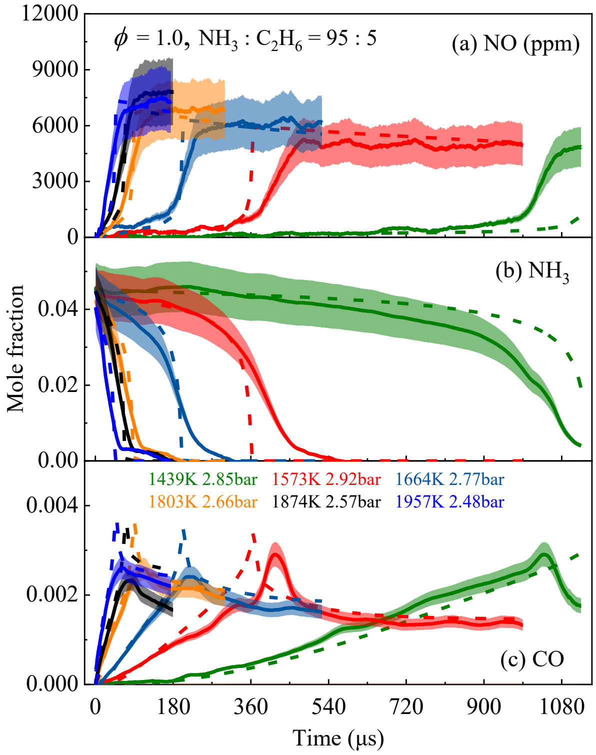

Fig. A6.2. *Comparison of the measurements (solid lines) and simulations (dash lines) for a) NO mole fraction profile, b) NH_3 mole fraction profile, and c) CO mole fraction profile from the stoichiometric mixture with 5% C_2H_6 fractions. The error bars of the measurements are indicated on all mixtures.*

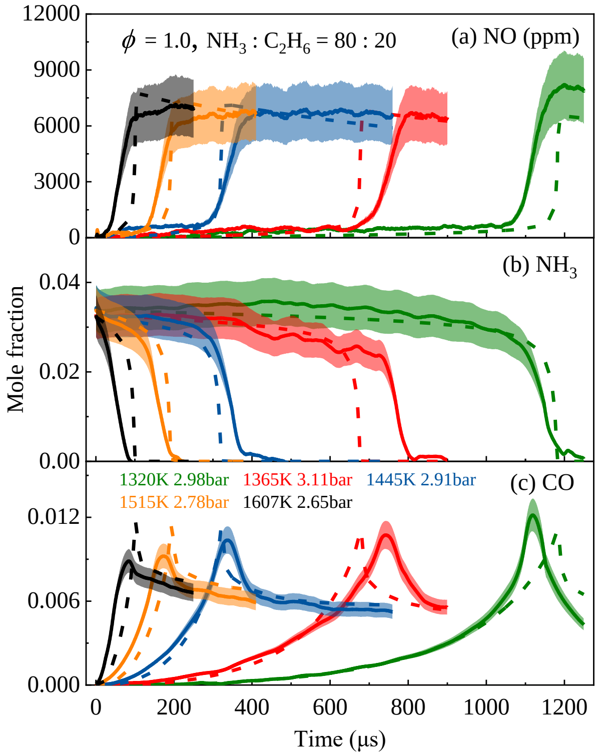

Fig. A6.3. *Comparison of the measurements (solid lines) and simulations (dash lines) for a) NO mole fraction profile, b) NH_3 mole fraction profile, and c) CO mole fraction profile from the stoichiometric mixture with 20% C_2H_6 fractions. The error bars of the measurements are indicated on all mixtures.*

https://doi.org/10.7795/110.20241024

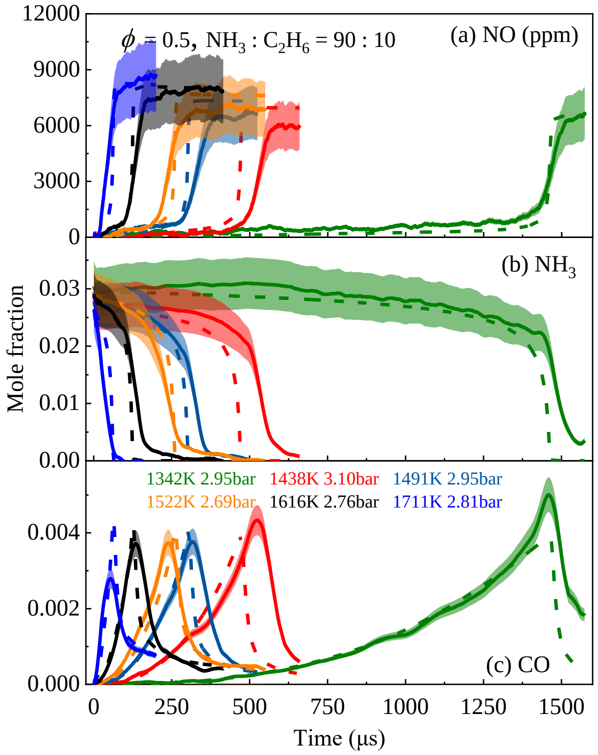

Fig. A6.4. Comparison of the measurements (solid lines) and simulations (dash lines) for a) NO mole fraction profile, b) NH_3 mole fraction profile, and c) CO mole fraction profile from the fuel-lean (ϕ = 0.5) mixture with 10% C_2H_6 fractions. The error bars of the measurements are indicated on all mixtures.

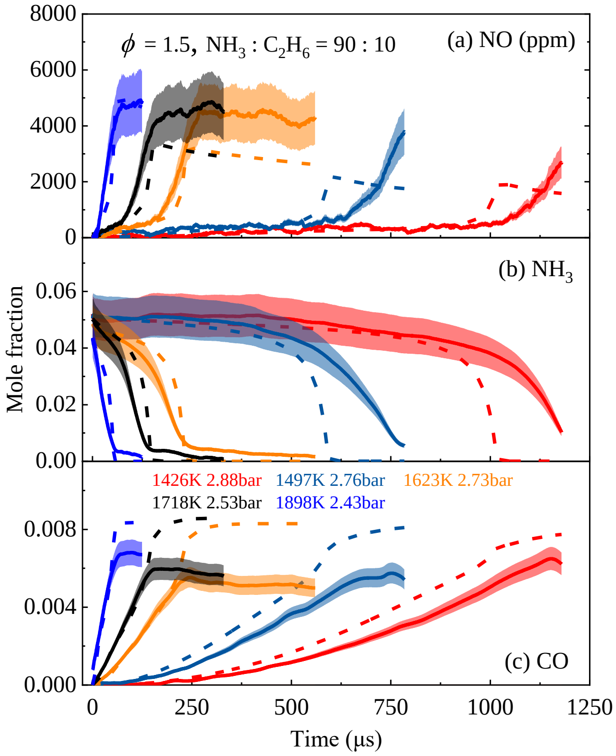

Fig. A6.5. Comparison of the measurements (solid lines) and simulations (dash lines) for a) NO mole fraction profile, b) NH_3 mole fraction profile, and c) CO mole fraction profile from the fuel-rich (ϕ = 1.5) mixture with 10% C_2H_6 fractions. The error bars of the measurements are indicated on all mixtures.

https://doi.org/10.7795/110.20241024

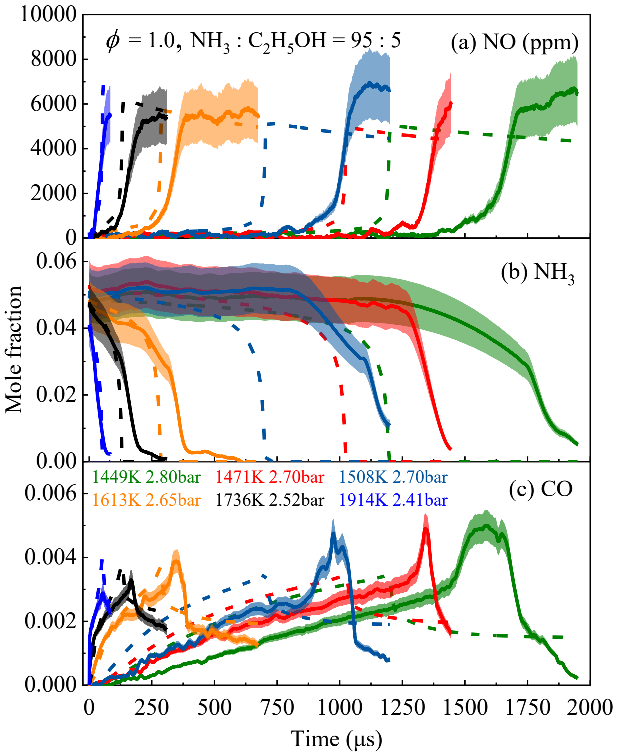

Fig. A6.6. Comparison of the measurements (solid lines) and simulations (dash lines) for a) NO mole fraction profile, b) NH_3 mole fraction profile, and c) CO mole fraction profile from the stoichiometric mixture with 5% C_2H_5OH fractions. The error bars of the measurements are indicated on all mixtures.

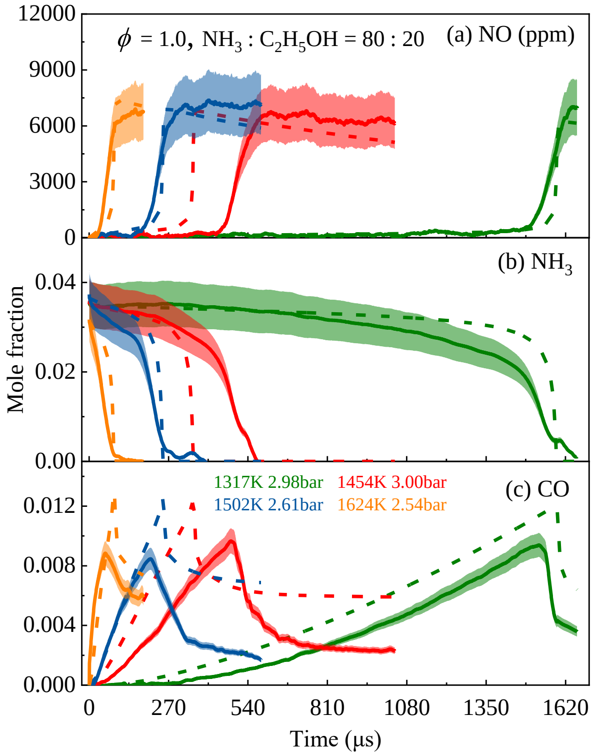

Fig. A6.7. Comparison of the measurements (solid lines) and simulations (dash lines) for a) NO mole fraction profile, b) NH_3 mole fraction profile, and c) CO mole fraction profile from the stoichiometric mixture with 20% C_2H_5OH fractions. The error bars of the measurements are indicated on all mixtures.

https://doi.org/10.7795/110.20241024

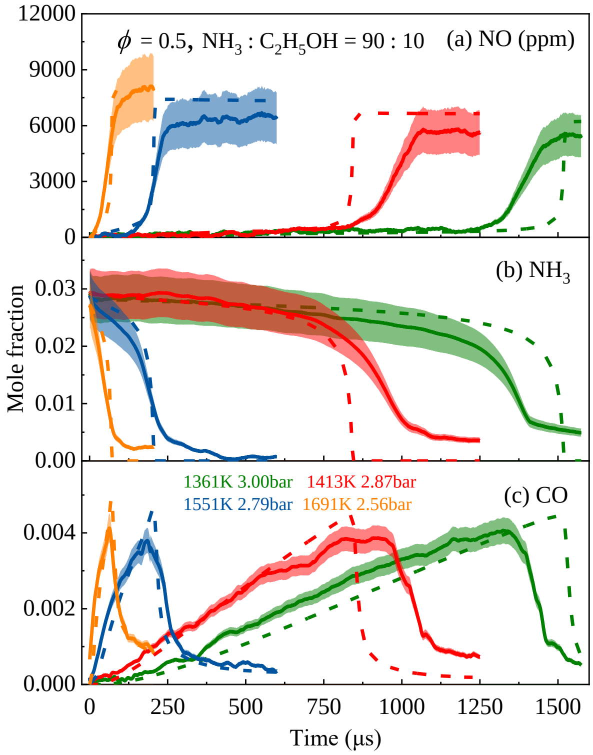

Fig. A6.8. Comparison of the measurements (solid lines) and simulations (dash lines) for a) NO mole fraction profile, b) NH_3 mole fraction profile, and c) CO mole fraction profile from the fuel-lean (ϕ = 0.5) mixture with 10% C_2H_5OH fractions. The error bars of the measurements are indicated on all mixtures.

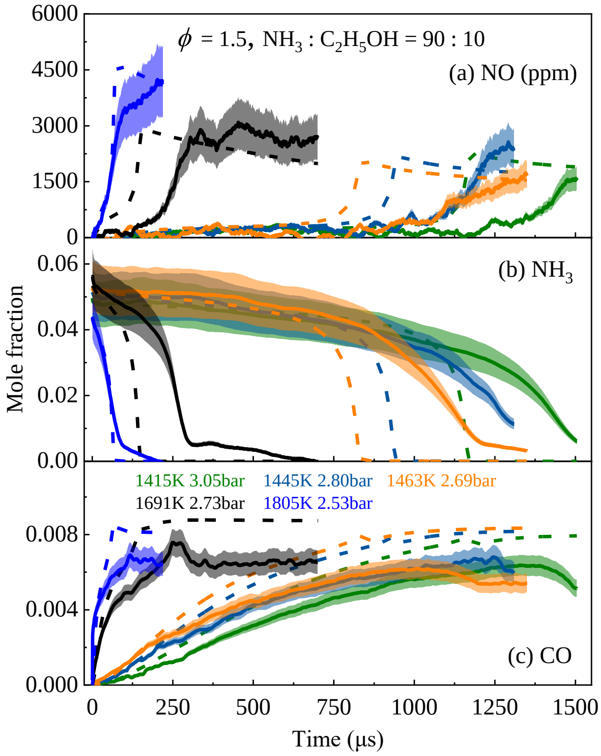

Fig. A6.9. Comparison of the measurements (solid lines) and simulations (dash lines) for a) NO mole fraction profile, b) NH_3 mole fraction profile, and c) CO mole fraction profile from the fuel-rich (ϕ =

https://doi.org/10.7795/110.20241024

1.5) mixture with 10% C_2H_5OH fractions. The error bars of the measurements are indicated on all mixtures.

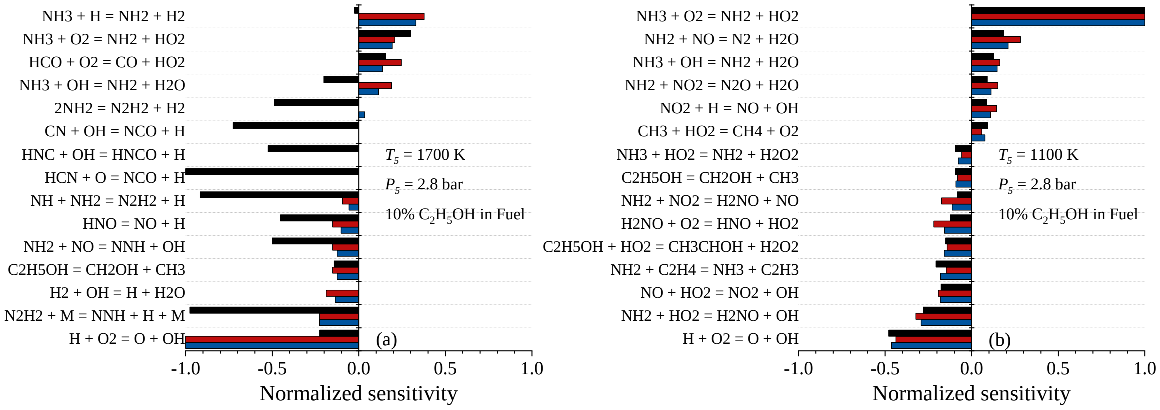

Fig. A6.10. Sensitivity analysis of IDT (Position of CO max.) for the mixtures with 10% C_2H_5OH fractions and different equivalence ratios (ϕ) at 2.8 bar and a) 1700 K and b) 1100 K.

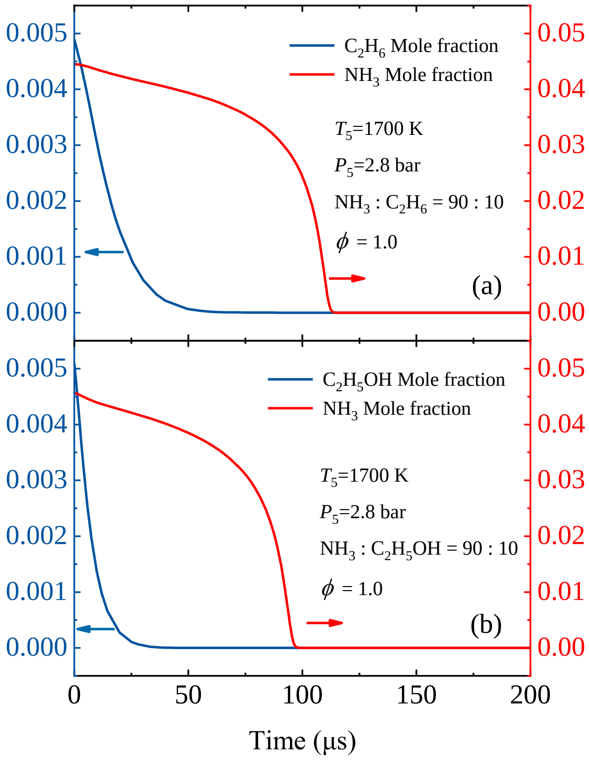

Fig. A6.11. a) Simulated consumption of C_2H_6 and NH_3 based on the updated mechanism (PTB-NH_3/C_2 mech, T_5 = 1700 K, P_5 = 2.8 bar, NH_3:C_2H_6 = 90:10, ϕ = 1.0); Simulated consumption of C_2H_5OH and NH_3 based on the updated mechanism (PTB-NH_3/C_2 mech, T_5 = 1700 K, P_5 = 2.8 bar, NH_3:C_2H_5OH = 90:10, ϕ = 1.0).

References

[1] Climate Change Indicators: Atmospheric Concentrations of Greenhouse Gases, United States Agency, Environmental Protection (2022).

[2] H. Hersbach, B. Bell, P. Berrisford, G. Biavati, A. Horányi, J. Muñoz Sabater, J. Nicolas, C. Peubey, R. Radu, I. Rozum, D. Schepers, A. Simmons, C. Soci, D. Dee, J.-N. Thépaut, ERA5 hourly data on single levels from 1940 to present. Copernicus Climate Change Service (C3S) Climate Data Store (CDS), (2023).

[3] A. Valera-Medina, H. Xiao, M. Owen-Jones, W.I.F. David, P.J. Bowen, Ammonia for power, Progress in Energy and Combustion Science 69 (2018) 63–102.

[4] H. Kobayashi, A. Hayakawa, K.D.K.A. Somarathne, E.C. Okafor, Science and technology of ammonia combustion, Proceedings of the Combustion Institute 37 (2019) 109–133.

[5] W.S. Chai, Y. Bao, P. Jin, G. Tang, L. Zhou, A review on ammonia, ammonia-hydrogen and ammonia-methane fuels, Renewable and Sustainable Energy Reviews 147 (2021) 111254.

[6] A. Valera-Medina, F. Amer-Hatem, A.K. Azad, I.C. Dedoussi, M. De Joannon, R.X. Fernandes, P. Glarborg, H. Hashemi, X. He, S. Mashruk, J. McGowan, C. Mounaim-Rouselle, A. Ortiz-Prado, A. Ortiz-Valera, I. Rossetti, B. Shu, M. Yehia, H. Xiao, M. Costa, Review on ammonia as a potential fuel: From synthesis to economics, Energy and Fuels 35 (2021) 6964–7029.

[7] M.C. Chiong, C.T. Chong, J.H. Ng, S. Mashruk, W.W.F. Chong, N.A. Samiran, G.R. Mong, A. Valera-Medina, Advancements of combustion technologies in the ammonia-fuelled engines, Energy Conversion and Management 244 (2021) 114460.

[8] X. He, B. Shu, D. Nascimento, K. Moshammer, M. Costa, R.X. Fernandes, Auto-ignition kinetics of ammonia and ammonia/hydrogen mixtures at intermediate temperatures and high pressures, Combustion and Flame 206 (2019) 189–200.

[9] B. Shu, X. He, C.F. Ramos, R.X. Fernandes, M. Costa, Experimental and modeling study on the auto-ignition properties of ammonia/methane mixtures at elevated pressures, Proceedings of the Combustion Institute 38 (2021) 261–268.

[10] M. Li, X. He, H. Hashemi, P. Glarborg, V.M. Lowe, P. Marshall, R. Fernandes, B. Shu, An experimental and modeling study on auto-ignition kinetics of ammonia/methanol mixtures at intermediate temperature and high pressure, Combustion and Flame 242 (2022) 112160.

[11] X. He, M. Li, B. Shu, R. Fernandes, K. Moshammer, Exploring the Effect of Different Reactivity Promoters on the Oxidation of Ammonia in a Jet-Stirred Reactor, Journal of Physical Chemistry A 127 (2023) 1923–1940.

[12] X. He, Experimental and modeling study on the oxidation of ammonia fuel blends at low-to-intermediate temperatures, PhD Thesis,Technische Universität Braunschweig (2022).

[13] M. Li, X. He, D. Zhu, R. Fernandes, K. Moshammer, Experimental and kinetic modeling study of the autoignition and oxidation of ammonia/ethane mixtures in a rapid compression machine and a jet-stirred reactor, Combustion and Flame 256 (2023) 11–13.

[14] C. Chen, Z. Wang, Z. Yu, X. Han, Y. He, Y. Zhu, A.A. Konnov, Experimental and kinetic modeling study of laminar burning velocity enhancement by ozone additive in NH_3+O_2+N_2 and NH_3+CH_4/C_2H_6/C_3H_8+air flames, Proceedings of the Combustion Institute 39 (2023) 4237–4246.

[15] Z. Jiang, S. Dong, W. Gao, B. Wang, H. Ding, J. Xie, C. Zou, X. Cheng, Probing the effect of fuel components on the auto-ignition behavior of ammonia/natural gas blends: A case study of ethane addition, Combustion and Flame 259 (2024) 113186.

[16] Z. Wang, X. Han, Y. He, R. Zhu, Y. Zhu, Z. Zhou, K. Cen, Experimental and kinetic study on the laminar burning velocities of NH_3 mixing with CH_3OH and C_2H_5OH in premixed flames, Combustion and Flame 229 (2021) 111392.

[17] P. Ronan, B. Pierre, M.-R. Christine, D. Guillaume, H. Fabien, Laminar flame speed of ethanol/ammonia blends–An experimental and kinetic study, Fuel Communications 10 (2022) 100052.

[18] M. Li, D. Zhu, X. He, K. Moshammer, R. Fernandes, B. Shu, Experimental and kinetic modeling study on auto-ignition properties of ammonia/ethanol blends at intermediate temperatures and high pressures, Proceedings of the Combustion Institute 39 (2022) 511–519.

[19] X. Li, X. Chu, Z. Ma, Y. Jin, X. Wang, Z. Xi, S. Hu, H. Chen, An experimental and kinetic modeling study on the ignition characteristics of ammonia/ethanol at high temperatures, Fuel 352 (2023) 129074.

[20] H. Yang, J. Tian, Z. Cui, M. Ye, X. Zhang, Q. Zhou, K. Wei, J. Wang, Experimental and numerical study of combustion characteristics of ammonia/ethanol mixture under high temperature and pressure, Fuel 367 (2024) 131350.

[21] D. Zheng, D. He, Y. Du, M. Zhang, J. Li, Y. Ding, Z. Peng, Mid-infrared absorption spectroscopy measurements and model improvements during the oxidation of ammonia/ethanol and ammonia/diethyl ether blends in a shock tube, Fuel 357 (2024) 129635.

[22] D. Wei, H. Fang, H. Tang, Y. Wang, G. Wei, H. Zhou, Experimental study of combustion instability and emission characteristics of ethanol/ammonia co-firing swirl flame, Fuel 362 (2024) 130786.

https://doi.org/10.7795/110.20241024

[23] L. Dai, H. Hashemi, P. Glarborg, S. Gersen, P. Marshall, A. Mokhov, H. Levinsky, Ignition delay times of NH_3/DME blends at high pressure and low DME fraction: RCM experiments and simulations, Combustion and Flame 227 (2021) 120–134.

[24] G. Issayev, B.R. Giri, A.M. Elbaz, K.P. Shrestha, F. Mauss, W.L. Roberts, A. Farooq, Ignition delay time and laminar flame speed measurements of ammonia blended with dimethyl ether: A promising low carbon fuel blend, Renewable Energy 181 (2022) 1353–1370.

[25] H. Xiao, H. Li, Experimental and kinetic modeling study of the laminar burning velocity of NH_3/DME/air premixed flames, Combustion and Flame 245 (2022) 112372.

[26] Y. Murakami, H. Nakamura, T. Tezuka, K. Hiraoka, K. Maruta, Effects of mixture composition on oxidation and reactivity of DME/NH_3/air mixtures examined by a micro flow reactor with a controlled temperature profile, Combustion and Flame 238 (2022) 111911.

[27] Y. Jin, X. Li, X. Wang, Z. Ma, X. Chu, Effect of dimethyl ether on ignition characteristics of ammonia and chemical kinetics, Fuel 343 (2023) 127885.

[28] S. Zhu, Q. Xu, R. Tang, J. Gao, Z. Wang, J. Pan, D. Zhang, A comparative study of oxidation of pure ammonia and ammonia/dimethyl ether mixtures in a jet-stirred reactor using SVUV-PIMS, Combustion and Flame 250 (2023) 112643.

[29] G. Yin, B. Xiao, H. Zhao, H. Zhan, E. Hu, Z. Huang, Jet-stirred reactor measurements and chemical kinetic study of ammonia with dimethyl ether, Fuel 341 (2023) 127542.

[30] J. Chen, X. Gou, Experimental and kinetic study on the extinction characteristics of ammonia-dimethyl ether diffusion flame, Fuel 334 (2023) 126743.

[31] X. Jiang, Q. Zhang, X. Liu, T. Zhang, Y. Zhang, Z. Huang, F. Deng, N. Zhao, H. Zheng, Y. Yan, A shock tube study of the ignition delay time of DME/ammonia mixtures: Effect of fuel blending from high temperatures to the NTC regime, Fuel 367 (2024) 131426.

[32] Y. Li, Y. Zhang, G. Yang, A. Fuentes, D. Han, Z. Huang, H. Lin, A comparative study on PAH characteristics of ethanol and ammonia as fuel additives in a premixed flame, Journal of the Energy Institute 101 (2022) 56–66.

[33] D. Matras, J. Villermaux, Un réacteur continu parfaitement agité par jets gazeux pour l'étude cinétique de réactions chimiques rapides, Chemical Engineering Science 28 (1973) 129–137.

[34] H. Zhao, C. Yan, T. Zhang, G. Ma, M.J. Souza, C.W. Zhou, Y. Ju, Studies of high-pressure n-butane oxidation with CO_2 dilution up to 100 atm using a supercritical-pressure jet-stirred reactor, Proceedings of the Combustion Institute 38 (2021) 279–287.

[35] P. Dagaut, M. Cathonnet, J.P. Rouan, R. Foulatier, A. Quilgars, J.C. Boettner, F. Gaillard, H. James, A jet-stirred reactor for kinetic studies of homogeneous gas-phase reactions at pressures up to ten atmospheres (~1 MPa), Journal of Physics E: Scientific Instruments 19 (1986) 207–209.

[36] W.W. Ayass, E.F. Nasir, A. Farooq, S.M. Sarathy, Mixing-structure relationship in jet-stirred reactors, Chemical Engineering Research and Design 111 (2016) 461–464.

[37] W. Chen, Q. Xu, H. Lou, Q. Di, C. Xie, B. Liu, J. Yang, H. Le Gall, L.S. Tran, X. Wang, Z. Xia, O. Herbinet, F. Battin-Leclerc, Z. Wang, Variable pressure JSR study of low temperature oxidation chemistry of n-heptane by synchrotron photoionization mass spectrometry, Combustion and Flame 240 (2022) 111946.

[38] J.H. Gross, Principles of Ionization and Ion Dissociation. In: Mass Spectrometry, Springer (2017) 21–66.

[39] E. Condon, A theory of intensity distribution in band systems, Physical Review 28 (1926) 1182–1201.

[40] J. Franck, E.G. Dymond, Elementary processes of photochemical reactions, Transactions of the Faraday Society 21 (1926) 536–542.

[41] S. Trajmar, D.F. Register, A. Chutjian, Electron scattering by molecules II. Experimental methods and data, Physics Reports 97 (1983) 219–356.

[42] H. Tawara, T. Kato, Total and partial ionization cross sections of NH_3 by electron impact, Atomic Data and Nuclear Data Tables 36 (1987) 167–353.

[43] O J Orient, S K Strivastava, Electron impact ionisation of H_2O, CO, CO_2 and CH_4, Journal of Physics B: Atomic and Molecular Physics 20 (1987) 3923.

[44] Y.K. Kim, M.E. Rudd, Binary-encounter-dipole model for electron-impact ionization, Physical Review A 50 (1994) 3954–3967.

[45] P. Oßwald, Systematische Analyse der Verbrennungsprozesse oxygenierter Brennstoffe mittels Molekularstrahlmassenspektrometrie, PhD Thesis, Universität Bielefeld (2009).

[46] M. Schenk, L. Leon, K. Moshammer, P. Oßwald, T. Zeuch, L. Seidel, F. Mauss, K. Kohse-Höinghaus, Detailed mass spectrometric and modeling study of isomeric butene flames, Combustion and Flame 160 (2013) 487–503.

[47] W.C. Wiley, I.H. McLaren, Time-of-flight mass spectrometer with improved resolution, Review of Scientific Instruments 26 (1955) 1150–1157.

[48] B.A. Mamyrin, Laser assisted reflectron time-of-flight mass spectrometry, International Journal of Mass Spectrometry and Ion Processes 131 (1994) 1–19.

[49] U. Struckmeier, P. Oßwald, T. Kasper, L. Böhling, M. Heusing, M. Köhler, A. Brockhinke, K. Kohse-Höinghaus, Sampling Probe Influences on Temperature and Species Concentrations in Molecular Beam Mass Spectroscopic Investigations of Flat Premixed Low-pressure Flames, Zeitschrift Fur Physikalische Chemie 223 (2009) 503–537.

[50] X. He, M. Giese, L. Ruwe, A. Lucassen, K. Moshammer, A detailed uncertainty analysis of EI-MBMS data from combustion experiments, Combustion and Flame 243 (2022) 112012.

[51] J.C. Biordi, Molecular beam mass spectrometry for studying the fundamental chemistry of flames, Progress in Energy and Combustion Science 3 (1977) 151–173.

[52] S.G. Lias, J.E. Bartmess, J.L. Liebman, R.D. Levin, W.G. Mallard, S.A. Kafafi, “Ion Energetics Data” in NIST Chemistry WebBook, National Institute of Standards and Technology, http://webbook.nist.gov, NIST Database (2024).

[53] Y.K. Kim, K.K. Irikura, M.E. Rudd, M.A. Ali, P.M. Stone, J.S. Coursey, R.A. Dragoset, A.R. Kishore, K.J. OLsen, A.M. Sansonetti, G.G. Wiersma, D.S. Zucker, M.A. Zucker, Electron-Impact Cross Sections for Ionization and Excitation, National Institute of Standards and Technology, https://physics.nist.gov/PhysRefData/Ionization/molTable.html, NIST Database (2024).

[54] S.S. Goldsborough, S. Hochgreb, G. Vanhove, M.S. Wooldridge, H.J. Curran, C.J. Sung, Advances in rapid compression machine studies of low- and intermediate-temperature autoignition phenomena, Progress in Energy and Combustion Science 63 (2017) 1–78.

[55] W.S. Affleck, A. Thomas, An Opposed Piston Rapid Compression Machine for Preflame Reaction Studies, Proceedings of the Institution of Mechanical Engineers 183 (1968) 365–387.

[56] C.J. Sung, H.J. Curran, Using rapid compression machines for chemical kinetics studies, Progress in Energy and Combustion Science 44 (2014) 1–18.

[57] D. Lee, S. Hochgreb, Rapid compression machines: Heat transfer and suppression of corner vortex, Combustion and Flame 114 (1998) 531–545.

[58] B.L. Wang, H. Olivier, H. Grönig, Ignition of shock-heated H_2-air-steam mixtures, Combustion and Flame 133 (2003) 93–106.

[59] C. Strozzi, A. Mura, J. Sotton, M. Bellenoue, Experimental analysis of propagation regimes during the autoignition of a fully premixed methane-air mixture in the presence of temperature inhomogeneities, Combustion and Flame 159 (2012) 3323–3341.

[60] R. Minetti, M. Carlier, M. Ribaucour, E. Therssen, L.R. Sochet, Comparison of oxidation and autoignition of the two primary reference fuels by rapid compression, Symposium (International) on Combustion 26 (1996) 747–753.

[61] J.F. Griffiths, P.A. Halford-Maw, C. Mohamed, Spontaneous ignition delays as a diagnostic of the propensity of alkanes to cause engine knock, Combustion and Flame 111 (1997) 327–337.

[62] M. Preußker, R.D. Büttgen, M.R. Noé, K.A. Heufer, Finding a common ground for RCM experiments. Part A: On the influences of facility effects regarding the reliability of experimental validations, Combustion and Flame 262 (2024) 113323.

[63] R.D. Büttgen, M. Preußker, D. Kang, S. Cheng, S.S. Goldsborough, G. Issayev, A. Farooq, H. Song, Y. Fenard, G. Vanhove, A.A.E.S. Mohamed, H.J. Curran, K.A. Heufer, Finding a common ground for RCM experiments. Part B: Benchmark study on ethanol ignition, Combustion and Flame 262 (2024).

[64] H. Hu, J. Keck, Autoignition of adiabatically compressed combustible gas mixtures, SAE Technical Papers (1987).

[65] G. Mittal, C.J. Sung, A rapid compression machine for chemical kinetics studies at elevated pressures and temperatures, 2007.

[66] D. Zhu, L. Ruwe, S. Schmitt, B. Shu, K. Kohse-Höinghaus, A. Lucassen, Interactions in Ammonia and Hydrogen Oxidation Examined in a Flow Reactor and a Shock Tube, Journal of Physical Chemistry A 127 (2022) 2351–2366.

[67] D. Zhu, Z. Qu, M. Li, S. Agarwal, R. Fernandes, B. Shu, Investigation on the NO formation of ammonia oxidation in a shock tube applying tunable diode laser absorption spectroscopy, Combustion and Flame 246 (2022) 112389.

[68] S. Agarwal, L. Seifert, D. Zhu, B. Shu, R. Fernandes, Z. Qu, Investigations on Pressure Broadening Coefficients of NO Lines in the 1←0 Band for N_2, CO_2, Ar, H_2, O_2 and He, Applied Sciences (Switzerland) 13 (2023).

[69] D. Zhu, S. Agarwal, L. Seifert, B. Shu, R. Fernandes, Z. Qu, NH_3 absorption line study and application near 1084.6 cm^{-1}, Infrared Physics and Technology 136 (2024) 105058.

[70] A. Vashishtha, Book Review: Applied Gas Dynamics, AIAA Journal 58 (2020) 1421–1422.

[71] H. Karas, Gas-phase investigation of ammonia-C_1 oxidation at the fuel-lean and rich condition in the shock tube using laser absorption spectroscopy, Master Thesis, Universidade de Lisboa (2023).

[72] W.J.M. Rankine, XV. On the thermodynamic theory of waves of finite longitudinal disturbance, Philosophical Transactions of the Royal Society of London 160 (1870) 277–288.

[73] H. Hugoniot, Mémoire sur la propagation du mouvement dans un fluide indéfini (première Partie), Journal de Mathématiques Pures et Appliquées 4e Série (1887) 477–492.

[74] A.G. Gaydon, I.R. Hurle, The Shock Tube in High-temperature Chemical Physics, Chapman and Hall, 1963.

[75] B. Shu, Mid-infrared absorption sensor for CO concentration and temperature measurements for pyrolysis and oxidation behind reflected shock waves, PhD Thesis, Universität Duisburg-Essen (2018).

[76] R.K. Hanson, R.M. Spearrin, C.S. Goldenstein, Spectroscopy and Optical Diagnostics for Gases, 2016.

[77] R.R. Gamache, S. Kennedy, R. Hawkins, L.S. Rothman, Total internal partition sums for molecules in the terrestrial atmosphere, Journal of Molecular Structure 517–518 (2000) 407–425.

[78] L.S. Rothman, History of the HITRAN Database, Nature Reviews Physics 3 (2021) 302–304.

[79] HITRANonline, https://hitran.org, (2024).

[80] R. V. Kochanov, I.E. Gordon, L.S. Rothman, K.P. Shine, S.W. Sharpe, T.J. Johnson, T.J. Wallington, J.J. Harrison, P.F. Bernath, M. Birk, G. Wagner, K. Le Bris, I. Bravo, C. Hill, Infrared absorption cross-sections in HITRAN2016 and beyond: Expansion for climate, environment, and atmospheric applications, Journal of Quantitative Spectroscopy and Radiative Transfer 230 (2019) 172–221.

[81] S. Agarwal, L. Sane, R.X. Fernandes, B. Shu, MID-IR laser absorption spectroscopy of 1- and 2-butanol in a shock tube facility, Combustion and Flame 243 (2022) 112087.

[82] M. Li, D. Zhu, H. Karas, S. Agarwal, Z. Qu, K. Moshammer, R. Fernandes, B. Shu, NH_3/C_2H_6 and NH_3/C_2H_5OH oxidation in a shock tube: Multi-speciation measurement, uncertainty analysis, and kinetic modeling, Chemical Engineering Journal 498 (2024) 155041.

[83] S.A. Alturaifi, C.R. Mulvihill, O. Mathieu, E.L. Petersen, Speciation measurements in shock tubes for validation of complex chemical kinetics mechanisms: Application to 2-Methyl-2-Butene oxidation, Combustion and Flame 225 (2021) 196–213.

[84] D. He, D. Zheng, Y. Du, J. Li, Y. Ding, Z. Peng, Laser-absorption-spectroscopy-based temperature and NH_3-concentration time-history measurements during the oxidation processes of the shock-heated reacting NH_3/H_2 mixtures, Combustion and Flame 245 (2022) 112349.

[85] S.R. Turns, An Introduction to Combustion, 2nd ed., McGraw-Hill Education, Singapore, McGraw-Hill, 2000.

[86] S. Arrhenius, Über die Dissociationswärme und den Einfluss der Temperatur auf den Dissociationsgrad der Elektrolyte, Zeitschrift Für Physikalische Chemie 4U (1889) 96–116.

[87] K.J. Laidler, A glossary of terms used in chemical kinetics, including reaction dynamics (IUPAC Recommendations 1996), 68 (1996) 149–192.

[88] P. Glarborg, J.A. Miller, B. Ruscic, S.J. Klippenstein, Modeling nitrogen chemistry in combustion, Progress in Energy and Combustion Science 67 (2018) 31–68.

[89] M. Quack, J. Troe, Specific Rate Constants of Unimolecular Processes II. Adiabatic Channel Model, Berichte Der Bunsengesellschaft Für Physikalische Chemie 78 (1974) 240–252.

[90] F.A. Lindemann, S. Arrhenius, I. Langmuir, N.R. Dhar, J. Perrin, W.C. McC. Lewis, Discussion on “the radiation theory of chemical action,” Trans. Faraday Soc. 17 (1922) 598–606.

[91] Y. Wu, S. Panigrahy, A.B. Sahu, C. Bariki, J. Beeckmann, J. Liang, A.A.E. Mohamed, S. Dong, C. Tang, H. Pitsch, Z. Huang, H.J. Curran, Understanding the antagonistic effect of methanol as a component in surrogate fuel models: A case study of methanol/n-heptane mixtures, Combustion and Flame 226 (2021) 229–242.

[92] S.J. Klippenstein, L.B. Harding, P. Glarborg, J.A. Miller, The role of NNH in NO formation and control, Combustion and Flame 158 (2011) 774–789.

[93] A. Stagni, C. Cavallotti, S. Arunthanayothin, Y. Song, O. Herbinet, F. Battin-Leclerc, T. Faravelli, An experimental, theoretical and kinetic-modeling study of the gas-phase oxidation of ammonia, Reaction Chemistry and Engineering 5 (2020) 696–711.

[94] X. Chen, M.E. Fuller, C. Franklin Goldsmith, Decomposition kinetics for HONO and HNO_2, React. Chem. Eng. 4 (2019) 323–333.

[95] M.U. Alzueta, M. Guerrero, Á. Millera, P. Marshall, P. Glarborg, Experimental and kinetic modeling study of oxidation of acetonitrile, Proceedings of the Combustion Institute 38 (2021) 575–583.

[96] P. Glarborg, C.S. Andreasen, H. Hashemi, R. Qian, P. Marshall, Oxidation of methylamine, International Journal of Chemical Kinetics 52 (2020) 893–906.

[97] M. Baigmohammadi, V. Patel, S. Martinez, S. Panigrahy, A. Ramalingam, U. Burke, K.P. Somers, K.A. Heufer, A. Pekalski, H.J. Curran, A comprehensive experimental and simulation study of ignition delay time characteristics of single fuel C_1-C_2 hydrocarbons over a wide range

https://doi.org/10.7795/110.20241024

of temperatures, pressures, equivalence ratios, and dilutions, Energy and Fuels 34 (2020) 3755–3771.

[98] A. Kéromnès, W.K. Metcalfe, K.A. Heufer, N. Donohoe, A.K. Das, C.-J. Sung, J. Herzler, C. Naumann, P. Griebel, O. Mathieu, M.C. Krejci, E.L. Petersen, W.J. Pitz, H.J. Curran, An experimental and detailed chemical kinetic modeling study of hydrogen and syngas mixture oxidation at elevated pressures, Combustion and Flame 160 (2013) 995–1011.

[99] W.K. Metcalfe, S.M. Burke, S.S. Ahmed, H.J. Curran, A Hierarchical and Comparative Kinetic Modeling Study of $C_1 - C_2$ Hydrocarbon and Oxygenated Fuels, International Journal of Chemical Kinetics 45 (2013) 638–675.

[100] Y. Zhang, H. El-Merhubi, B. Lefort, L. Le Moyne, H.J. Curran, A. Kéromnès, Probing the low-temperature chemistry of ethanol via the addition of dimethyl ether, Combustion and Flame 190 (2018) 74–86.

[101] U. Burke, W.K. Metcalfe, S.M. Burke, K.A. Heufer, P. Dagaut, H.J. Curran, A detailed chemical kinetic modeling, ignition delay time and jet-stirred reactor study of methanol oxidation, Combustion and Flame 165 (2016) 125–136.

[102] A.M. Mebel, Prediction of absolute rate constants for the reactions of NH_2 with alkanes from ab initio G2M/TST calculations, Journal of Physical Chemistry A 103 (1999) 2088–2096.

[103] K. Siddique, M. Altarawneh, J. Gore, P.R. Westmoreland, B.Z. Dlugogorski, Hydrogen Abstraction from Hydrocarbons by NH_2, The Journal of Physical Chemistry A 121 (2017) 2221–2231.

[104] C.L. Rasmussen, A.E. Rasmussen, P. Glarborg, Sensitizing effects of NO_x on CH_4 oxidation at high pressure, Combustion and Flame 154 (2008) 529–545.

[105] M. Wollenhaupt, J.N. Crowley, Kinetic Studies of the Reactions $CH_3 + NO_2 \rightarrow$ Products, $CH_3O + NO_2 \rightarrow$ Products, and $OH + CH_3C(O)CH_3 \rightarrow CH_3C(O)OH + CH_3$, over a Range of Temperature and Pressure, The Journal of Physical Chemistry A 104 (2000) 6429–6438.

[106] C.W. Gao, J.W. Allen, W.H. Green, R.H. West, Reaction Mechanism Generator: Automatic construction of chemical kinetic mechanisms, Computer Physics Communications 203 (2016) 212–225.

[107] V. Daële, A. Ray, I. Vassalli, G. Poulet, G. Le Bras, Kinetic study of reactions of $C_2H_5O_2$ with NO at 298 K and 0.55 – 2 torr, International Journal of Chemical Kinetics 27 (1995) 1121–1133.

[108] L. Batt, Reactions of alkoxy and alkyl peroxy radicals, International Reviews in Physical Chemistry 6 (1987) 53–90.

[109] J. Giménez-López, M.U. Alzueta, C.T. Rasmussen, P. Marshall, P. Glarborg, High pressure oxidation of C_2H_4/NO mixtures, Proceedings of the Combustion Institute 33 (2011) 449–457.

[110] A. Matsugi, H. Shiina, Thermal Decomposition of Nitromethane and Reaction between CH_3 and NO_2, Journal of Physical Chemistry A 121 (2017) 4218–4224.

[111] D.L. Baulch, C.T. Bowman, C.J. Cobos, R.A. Cox, T. Just, J.A. Kerr, M.J. Pilling, D. Stocker, J. Troe, W. Tsang, R.W. Walker, J. Warnatz, Evaluated kinetic data for combustion modeling: Supplement II, Journal of Physical and Chemical Reference Data 34 (2005) 757–1397.

[112] R. Zhu, M.C. Lin, The $CH_3 + HO_2$ reaction: First-principles prediction of its rate constant and product branching probabilities, Journal of Physical Chemistry A 105 (2001) 6243–6248.

[113] J. Mendes, C.-W. Zhou, H.J. Curran, Theoretical Chemical Kinetic Study of the H-Atom Abstraction Reactions from Aldehydes and Acids by $\dot{H}$ Atoms and $\dot{O}H$, $H\dot{O}_2$, and $\dot{C}H_3$ Radicals, The Journal of Physical Chemistry A 118 (2014) 12089–12104.

[114] S.A. Carr, T.J. Still, M.A. Blitz, A.J. Eskola, M.J. Pilling, P.W. Seakins, R.J. Shannon, B. Wang, S.H. Robertson, Experimental and Theoretical Study of the Kinetics and Mechanism of the Reaction of OH Radicals with Dimethyl Ether, The Journal of Physical Chemistry A 117 (2013) 11142–11154.

[115] Z. Zhao, M. Chaos, A. Kazakov, F.L. Dryer, Thermal decomposition reaction and a comprehensive kinetic model of dimethyl ether, International Journal of Chemical Kinetics 40 (2008) 1–18.

[116] Y. Yamaguchi, Y. Teng, S. Shimomura, K. Tabata, E. Suzuki, Ab Initio Study for Selective Oxidation of Methane with NO_x ($x = 1, 2$), The Journal of Physical Chemistry A 103 (1999) 8272–8278.

[117] W.-T. Chan, S.M. Heck, H.O. Pritchard, Reaction of nitrogen dioxide with hydrocarbons and its influence on spontaneous ignition. A computational study, Phys. Chem. Chem. Phys. 3 (2001) 56–62.

[118] Z. Wang, X. Zhang, L. Xing, L. Zhang, F. Herrmann, K. Moshammer, F. Qi, K. Kohse-Höinghaus, Experimental and kinetic modeling study of the low- and intermediate-temperature oxidation of dimethyl ether, Combustion and Flame 162 (2015) 1113–1125.

[119] J. de Vries, J.M. Hall, S.L. Simmons, M.J.A. Rickard, D.M. Kalitan, E.L. Petersen, Ethane ignition and oxidation behind reflected shock waves, Combustion and Flame 150 (2007) 137–150.

[120] O. Mathieu, L.T. Pinzón, T.M. Atherley, C.R. Mulvihill, I. Schoel, E.L. Petersen, Experimental

https://doi.org/10.7795/110.20241024

study of ethanol oxidation behind reflected shock waves: Ignition delay time and H_2O laser-absorption measurements, Combustion and Flame 208 (2019) 313–326.

[121] S. Nadiri, B. Shu, C.F. Goldsmith, R. Fernandes, Development of comprehensive kinetic models of ammonia/methanol ignition using Reaction Mechanism Generator (RMG), Combustion and Flame 251 (2023) 112710.

[122] L.H.S. Roblee, A technique for sampling reaction intermediates in a rapid compression machine, Combustion and Flame 5 (1961) 229–234.

[123] M.A. Mac Kinnon, J. Brouwer, S. Samuelsen, The role of natural gas and its infrastructure in mitigating greenhouse gas emissions, improving regional air quality, and renewable resource integration, Progress in Energy and Combustion Science 64 (2018) 62–92.

[124] B. Korb, K. Kuppa, H.D. Nguyen, F. Dinkelacker, G. Wachtmeister, Experimental and numerical investigations of charge motion and combustion in lean-burn natural gas engines, Combustion and Flame 212 (2020) 309–322.

[125] H. Hashemi, J.G. Jacobsen, C.T. Rasmussen, J.M. Christensen, P. Glarborg, S. Gersen, M. van Essen, H.B. Levinsky, S.J. Klippenstein, High-pressure oxidation of ethane, Combustion and Flame 182 (2017) 150–166.

[126] R.S. Tranter, R. Sivaramakrishnan, K. Brezinsky, M.D. Allendorf, High pressure, high temperature shock tube studies of ethane pyrolysis and oxidation, Physical Chemistry Chemical Physics 4 (2002) 2001–2010.

[127] L.D. Pfefferle, S.W. Churchill, NO_x production from the combustion of ethane doped with ammonia in a thermally stabilized plug flow burner, Combustion Science and Technology 49 (1986) 235–249.

[128] T. Cai, D. Zhao, Enhancing and assessing ammonia-air combustion performance by blending with dimethyl ether, Renewable and Sustainable Energy Reviews 156 (2022) 112003.

[129] X. Meng, M. Zhang, C. Zhao, H. Tian, J. Tian, W. Long, M. Bi, Study of combustion and NO chemical reaction mechanism in ammonia blended with DME, Fuel 319 (2022) 123832.

[130] R. Tang, Q. Xu, J. Pan, J. Gao, Z. Wang, H. Wei, G. Shu, An experimental and modeling study of ammonia oxidation in a jet stirred reactor, Combustion and Flame 240 (2022) 112007.

[131] K. Moshammer, A.W. Jasper, D.M. Popolan-Vaida, Z. Wang, V.S. Bhavani Shankar, L. Ruwe, C.A. Taatjes, P. Dagaut, N. Hansen, Quantification of the Keto-Hydroperoxide ($HOOCH_2OCHO$) and Other Elusive Intermediates during Low-Temperature Oxidation of Dimethyl Ether, Journal of Physical Chemistry A 120 (2016) 7890–7901.

[132] K. Moshammer, A.W. Jasper, D.M. Popolan-Vaida, A. Lucassen, P. Diévart, H. Selim, A.J. Eskola, C.A. Taatjes, S.R. Leone, S.M. Sarathy, Y. Ju, P. Dagaut, K. Kohse-Höinghaus, N. Hansen, Detection and Identification of the Keto-Hydroperoxide ($HOOCH_2OCHO$) and Other Intermediates during Low-Temperature Oxidation of Dimethyl Ether, Journal of Physical Chemistry A 119 (2015) 7361–7374.

[133] B. Yang, W. Sun, K. Moshammer, N. Hansen, Review of the Influence of Oxygenated Additives on the Combustion Chemistry of Hydrocarbons, Energy & Fuels 35 (2021) 13550–13568.

[134] J. Baeyens, Q. Kang, L. Appels, R. Dewil, Y. Lv, T. Tan, Challenges and opportunities in improving the production of bio-ethanol, Progress in Energy and Combustion Science 47 (2015) 60–88.

[135] S.O. Haputhanthri, T.T. Maxwell, J. Fleming, C. Austin, Ammonia and Gasoline Fuel Blends for Internal Combustion Engines, in: Asme Int. Conf. Energy Sustain. Collocated with Asme Int. Conf. Fuel Cell Sci., 2014.

[136] O. Mathieu, E.L. Petersen, Experimental and modeling study on the high-temperature oxidation of Ammonia and related NO_x chemistry, Combustion and Flame 162 (2015) 554–570.

[137] G. Issayev, B.R. Giri, A.M. Elbaz, K.P. Shrestha, F. Mauss, W.L. Roberts, A. Farooq, Combustion behavior of ammonia blended with diethyl ether, Proceedings of the Combustion Institute 38 (2021) 499–506.

[138] Y. Feng, J. Zhu, Y. Mao, M. Raza, Y. Qian, L. Yu, X. Lu, Low-temperature auto-ignition characteristics of NH_3/diesel binary fuel: Ignition delay time measurement and kinetic analysis, Fuel 281 (2020) 118761.

[139] S.J. Klippenstein, P. Glarborg, Theoretical kinetics predictions for $NH_2 + HO_2$, Combustion and Flame 236 (2022) 111787.

[140] L. Dai, S. Gersen, P. Glarborg, H. Levinsky, A. Mokhov, Experimental and numerical analysis of the autoignition behavior of NH_3 and NH_3/H_2 mixtures at high pressure, Combustion and Flame 215 (2020) 134–144.

[141] S. Cheng, S. Scott Goldsborough, C. Saggese, S.W. Wagnon, W.J. Pitz, New insights into fuel blending effects: Intermolecular chemical kinetic interactions affecting autoignition times and intermediate-temperature heat release, Combustion and Flame 233 (2021) 111559.

[142] S.A. Alturaifi, O. Mathieu, E.L. Petersen, An experimental and modeling study of ammonia pyrolysis, Combustion and Flame 235 (2022).

[143] S.A. Alturaifi, O. Mathieu, E.L. Petersen, Shock-tube laser absorption measurements of N_2O

time histories during ammonia oxidation, Fuel Communications 10 (2022) 100050.

[144] S.A. Alturaifi, O. Mathieu, E.L. Petersen, A shock-tube study of NH_3 and NH_3/H_2 oxidation using laser absorption of NH_3 and H_2O, Proceedings of the Combustion Institute 39 (2023) 233–241.

[145] D. Zheng, D. He, Y. Du, J. Li, M. Zhang, Y. Ding, Z. Peng, Experimental study of the methane/hydrogen/ammonia and ethylene/ammonia oxidation: Multi-parameter measurements using a shock tube combined with laser absorption spectroscopy, Combustion and Flame 254 (2023).

Herausgeber:
Physikalisch-Technische Bundesanstalt
ISNI: 0000 0001 2186 1887
Presse und Öffentlichkeitsarbeit
Bundesallee 100
38116 Braunschweig
Telefon: (05 31) 592-93 21
Telefax: (05 31) 592-92 92
www.ptb.de